P-ISSN 2525-2461 • E-ISSN 2615-9937

Vietnam Journal of Science, Technology and Engineering

MARCH 2022 • VOLUME 64 NUMBER 1

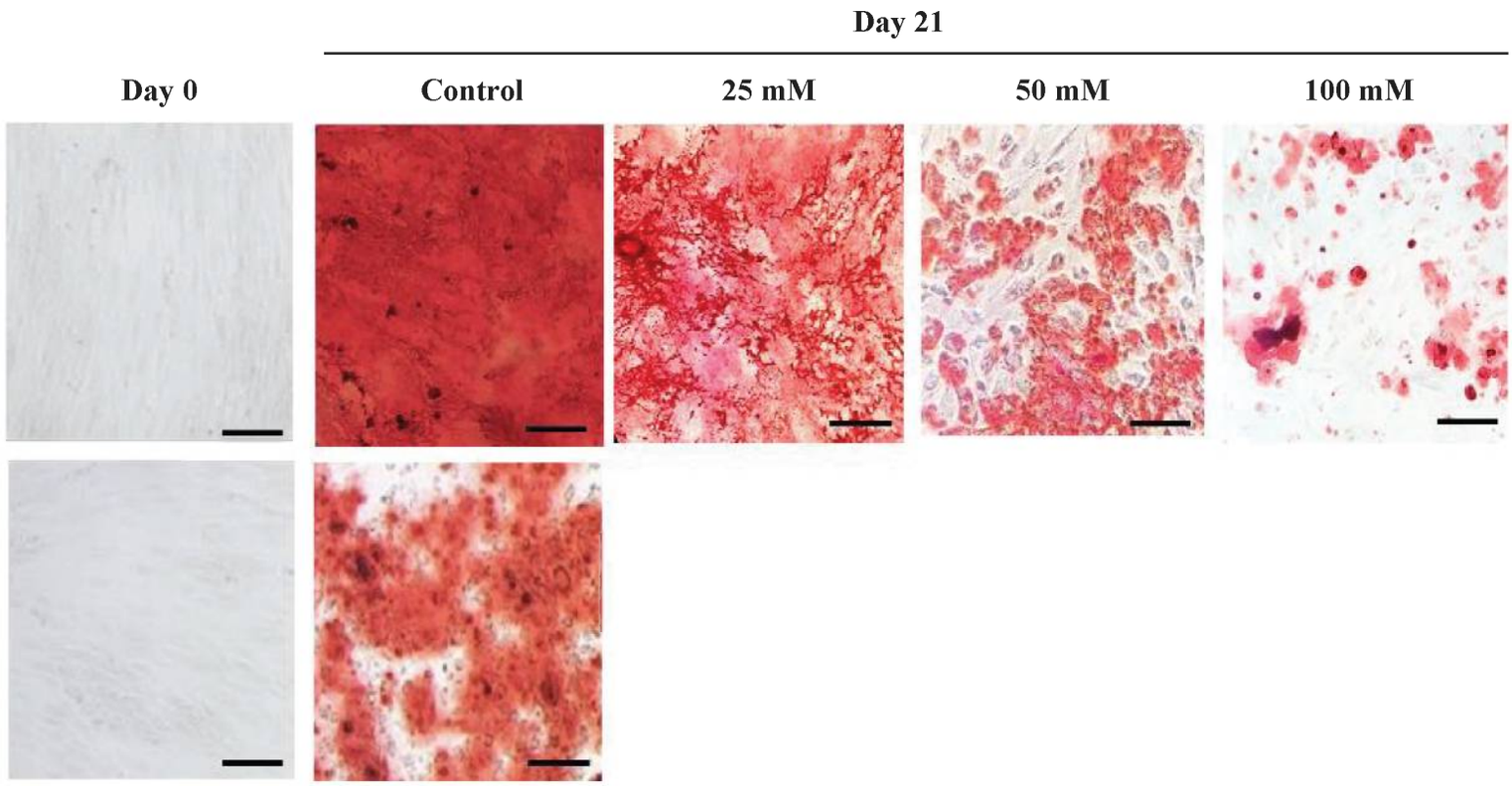

The impairment of osteogenic differentiation of human adipose tissue-derived mesenchymal stem cells under high D-glucose concentrations

VIETNAM JOURNAL OF SCIENCE, TECHNOLOGY AND ENGINEERING * MARCH 2022 * VOLUME 64 NUMBER 1

vietnamscience.vn or vietnamscience.vjst.vn

Vietnam Journal of Science, Technology and Engineering (VJSTE) **is a quarterly double-blind peer-reviewed academic journal. VJSTE publishes research articles and review articles in all areas of science, technology and engineering with the focus on the physical sciences, life sciences and environmental sciences including the following topics:**

- **Physical Sciences**
- **Agriculture**
- **Medicine**
- **Pharmacology**
- **Biology**
- **Biotechnology**
- **Biomedical Applications**
- **Ecology**
- **Climatology**
- **Environmental Science.**

CLASSIFICATION SCHEME

1. **Mathematics and Computer Science**
   - **1.1. Mathematics**
   - **1.2. Computer Science**
   - **1.3. Computational Science**
2. **Physical Sciences**
   - **2.1. Physics**
   - **2.2. Chemistry**
   - **2.3. Engineering**
3. **Life Sciences**
   - **3.1. Agriculture**
   - **3.2. Medicine**
   - **3.3. Pharmacology**
   - **3.4. Biology**
   - **3.5. Biotechnology**
   - **3.6. Biomedical Applications**
4. **Earth Sciences**
   - **4.1. Geography**
   - **4.2. Geology**
   - **4.3. Geophysics**
   - **4.4. Oceanography**
5. **Environmental Sciences**
   - **5.1. Ecology**
   - **5.2. Climatology**
   - **5.3. Environmental Science**

CONTENTS

MARCH 2022 • VOLUME 64 NUMBER 1

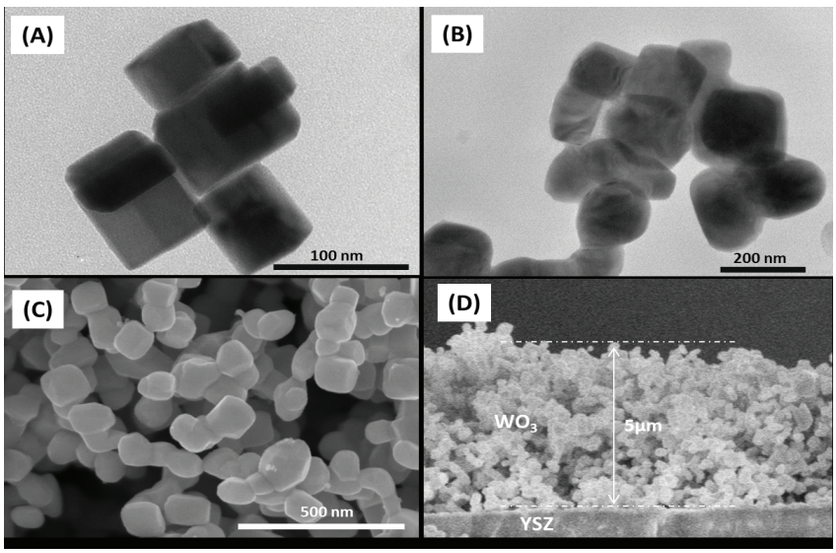

5

PHYSICAL SCIENCES

3 **Square-surface nanostructured tungsten oxide for a highly selective NO_2 gas sensing electrode in a YSZ mixed-potential sensor.**
Nguyen Truong Giang, Nguyen Quynh Nga

9 **Sulfolane as a co-solvent for carbonate-electrolytes in lithium-ion batteries using a $LiMn_2O_4$ cathode.**
Phuong Hue Luu, Phuong Hue Tran, Hoang Van Nguyen, An Le Bao Phan, Oanh Hoang Nguyen, Man Van Tran, Phung My Loan Le, Thanh Duy Vo

14 **Hemicellulose content in rice straws of several high-quality rice grains.**
Thuy-An Ngo, Dao-Chi Vo Thi, Nhan-Tanh Nguyen Tran

20 **Off-line ESI-MS/MS profiling of betalains and flavonoid glycosides isolated from (fruit) *Opuntia stricta var. dillenii* and (vegetable) *Atriplex hortensis var. rubra* by countercurrent chromatography.**
Thi Minh Thu Tran, Thanh Binh Nguyen, Peter Winterhalter, Gerold Jerz

27 **Chemical composition and antioxidant properties of ivy gourd (*Coccinia grandis*) wines prepared with different pretreatment techniques.**
Trang T. Dang, Thanh T.H. Le, Ngoc Lieu Le

LIFE SCIENCES

33 **Comparative analysis of overall survival in non-small cell lung cancer patients with and without different organ metastases.**
Tien Manh Hoang, Thi Thanh Nguyen

39 **Study on association between *SLC2A9* rs3733591 and Gout susceptibility in 481 Vietnamese individuals.**
Pham Quang Hung, Nguyen Xuan Canh, Nguyen Thuy Duong

43 **Phytochemical analysis and correlation of total polyphenol content and antioxidant properties of *Symplocos cochinchinensis* leaves.**
Hai Trieu Ly, Vu Khanh Trang Le, Van Minh Le, Cong Sanh Phan, Chau Tuan Vo, Minh Ly Nguyen, Thi Anh Dao Phan

CONTENTS

MARCH 2022 • VOLUME 64 NUMBER 1

68

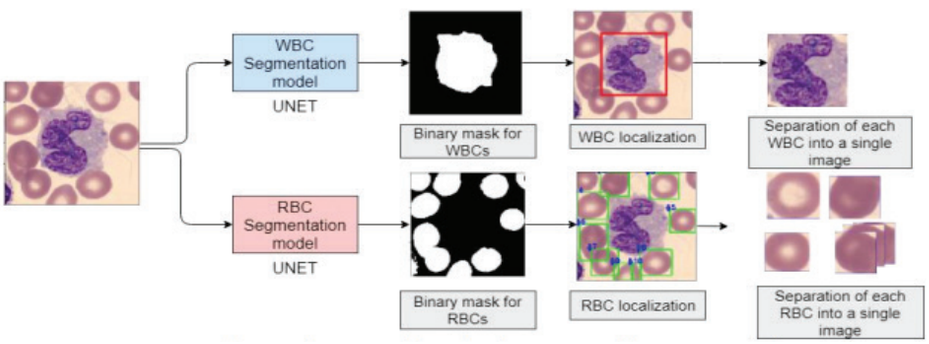

49 ***Aristolochia versicolor*** **S.M. Hwang (Aristolochiaceae), a new record for the flora of Vietnam**.
Van Truong Do, Thi Thao Hoang

53 **A review on injectable hydrogels from xanthan gum for biomedical applications.**
Thai Phuong Thao Nguyen, Phuong Hien Le, Thi-Hiep Nguyen

63 **A deep learning approach in detection of malaria and acute lymphoblastic leukemia diseases utilising blood smear microscopic images.**
Quyen Hoang Vo, Xuan-Hieu Le, Thanh-Hai Le, Thi-Thu-Hien Pham

72 **The impairment of osteogenic differentiation of human adipose tissue-derived mesenchymal stem cells under high D-glucose concentrations.**
Yen-Nhi Ha Nguyen, Long Binh Vong, Hong-Anh Pham, Dang-Quan Nguyen, Phan Ngoc Uyen Phuong, Huu-Phuong Mai, Nhu-Thuy Trinh

EARTH SCIENCES

78 **Radon concentrations and forecasting exposure risks to residents and workers in rare earth and copper mines containing radioactivity in northwest Vietnam.**
Van Dung Nguyen, Thi Lan Anh Vu, Dinh Huan Trinh, Thi Cuc Nguyen

85 **Tidal energy potential in coastal Vietnam.**
Huy Toan Do, Thanh Binh Nguyen, Tuan Minh Ly

ENVIRONMENTAL SCIENCES

90 **Applying the integrated model of GIS and AHP for evaluating ecological suitability of Ming aralia (*Polyscias fruticosa*): A case study of Hai Hau district, Nam Dinh province, Vietnam.**
Le Thuy Chau Ngoc, Truong Ngoc Kiem

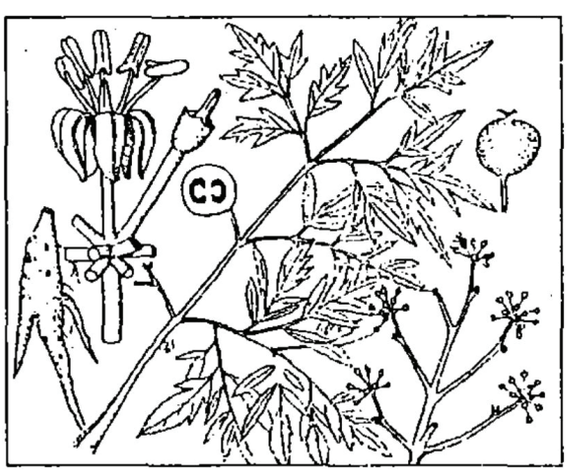

92

DOI: 10.31276/VJSTE.64(1).03-08

Square-surface nanostructured tungsten oxide for a highly selective NO_2 gas sensing electrode in a YSZ mixed-potential sensor

Truong Giang Nguyen[1*], Quynh Nga Nguyen[2]

[1]*University of Transport and Communications, 3 Cau Giay Street, Lang Thuong Ward, Dong Da District, Hanoi, Vietnam*
[2]*Vietnam Centre for Science and Technology Evaluation, Vietnam Ministry of Science and Technology, 113 Tran Duy Hung Street, Trung Hoa Ward, Cau Giay District, Hanoi, Vietnam*

Received 18 December 2020; revised 3 March 2021; accepted 16 March 2021

Abstract:

In this work, a YSZ mixed-potential sensor was fabricated utilising square-surface nanostructured tungsten oxide (WO_3) as an NO_2 gas sensing-electrode. YSZ (ZrO_2+8% mol Y_2O_3) was used as the high temperature electrolyte layer of the sensor. The square-surface nanostructured WO_3 was synthesised by a hydrothermal treatment and used to fabricate the NO_2 gas sensing-electrode. The sensor with a configuration of Pt/YSZ/(Pt-WO_3) was investigated at operating temperatures ranging from 320 to 600°C to monitor sensing performance to NO_2, NO, CO, CH_4, and CO_2 gases. The Pt/YSZ/(Pt-WO_3) sensor presented a high selectivity to NO_2 gas. This behaviour is suggested to occur due to the specific high catalytic activity of the square-surface nanostructured WO_3 to NO_2 gas. The highest gas-sensing response (ΔU_{emf}) of the sensor was about 40.9 mV for 50 ppm NO_2 at 450°C. The sensor also had a short response time and recovery time (τ_{90}) of approximately 15 and 39 s, respectively, for 50 ppm NO_2 at 450°C.

Keywords: **gas sensing-electrode, mixed-potential gas sensors, square-surface nanostructured tungsten oxide (WO_3), YSZ (Yttria-stabilised zirconia).**

Classification number: **2.1**

1. Introduction

Highly toxic gases such as NO_2, NO, CO, and SO_2, etc., are typically released from fuel combustion. These gases can cause adverse human health effects and severe air pollution. In fuel combustion, nitrogen oxides (NO_x = NO_2 + NO) are mainly formed from a chemical-reaction between N_2 and O_2 in high temperature conditions. Therefore, in-situ or direct analysis of NO_2 concentration from exhaust gas environments plays an important role in the feedback control of fuel combustion process to not only reduce toxic gas emission into the air but also optimise fuel consumption. Two typical types of gas sensors for analysing NO_x gases in combustion environments include electrochemical gas sensors and optical gas sensors (e.g., a nondispersive infrared gas sensor or NDIR). However, the NDIR gas sensor has been met with major difficulties in selectivity due to the partial overlap of the IR absorption band of H_2O vapour and that of NO_x gases [1]. Moreover, it is also difficult to design the NDIR gas sensor for direct or in-situ operation in the high temperature processes of fuel combustions. In contrast, a high temperature electrochemical sensor like the YSZ-based gas sensor can directly operate in these hazardous environments, thus it has been considered as a promising candidate [1, 2]. Actually, some commercial YSZ-based electrochemical sensor devices have been developed to directly measure NO_2 gas in high temperature processes [2, 3].

High temperature electrochemical sensors using the solid electrolyte YSZ (Yttria-stabilised zirconia) and a metal-oxide sensing electrode to detect various gases (such as NO_2, NO, CO, HC, NH_3) have been explored in hazardous environments with high temperature and corrosive agents. In this case, the YSZ mixed-potential gas sensors with a metal-oxide auxiliary sensing electrode have been of great interest to NO_2 gas detection. Numerous metal-oxides such as NiO, WO_3, ZnO, SnO_2, In_2O_3, CeO_2, Nb_2O_5, $LaFeO_3$, and $MnCr_2O_4$, etc., have been mostly investigated with the aim of finding highly selective gas-sensing electrodes for NO_2 (as reviewed in Refs. [3-5]). Potentiometric sensors based a configuration of WO_3/YSZ/Pt for high NO_2 sensing responses have

*Corresponding author: Email: ntgiang@utc.edu.vn

been reported in Refs. [6, 7]. A. Dutta, et al. (2003) [8] also indicated that the WO_3 electrode of a YSZ-based gas sensor had the high sensing performance to NO_2 gas. Most of the WO_3 nanostructures for the sensing electrode of the YSZ-based electrochemical sensor were used with a type of nanoparticles. However, the NO_2 gas sensing electrode-based YSZ sensor remains in need of sensitivity and selectivity improvement to achieve the best performance in application requirements.

Additionally, WO_3 nanostructure-based conductive sensors have been reported to possess the highest sensing performance to NO_2 gas [9-14]. Square-surface WO_3 nanostructures were especially reported to exhibit very high or even ultra-high sensitivity to NO_2 gas. This characteristic was considered to occur due to the contribution of well-oriented crystalline structure of tungsten oxide after square-surface nanostructuring to NO_2 catalytic activity. For example, L. You, et al. (2011) [13] synthesised square-like nanosheets of WO_3 by hydrothermal treatment and reported having a very high selectivity and sensitivity to NO_2 gas with R_g/R_a=92 for 100 ppb at 125°C when compared to various gases including Cl_2, SO_2, H_2S, NH_3, and C_2H_5OH. Similarly, nanosheets assembled from hierarchical flower-like WO_3 nanostructures fabricated by hydrothermal treatment presented a high sensing performance to NO_2 gas when compared with Cl_2, CO, H_2S, NH_3, acetone, and ethanol were proposed by C. Wang, et al. (2015) [14]. A. Boudiba, et al. (2012) [10] also reported two-dimensional WO_3 nanostructures synthesised by hydrothermal treatment for very high sensitivity in ppb of NO_2.

In this work, square-surface nanostructured WO_3 was investigated as the NO_2 sensing electrode in a YSZ (ZrO_2 doped 8% mol Y_2O_3) mixed-potential sensor. The main ideal of this work is utilizing the high NO_2 catalytic activity of the square-surface WO_3 nanostructures for the auxiliary sensing electrode of a YSZ mixed-potential sensor to obtain high NO_2 selectivity performance.

2. Experimental design

The square-surface nanostructured WO_3 used to fabricate the auxiliary sensing electrode was synthesized by a hydrothermal process as shown in detail in our previous work [15]. Briefly, $(NH_4)_{10}W_{12}O_{41}\cdot 5H_2O$ was dissolved in distilled water and then $(NH_2)_2CO$ solution was added and stirred continuously at 80°C for 1 h to achieve a homogeneous solution. Hydrochloric acid (1.5 M) was gradually dropped into the homogeneous solution until the appearance of a light-yellow precipitate. After that, this mixture was transferred to a Teflon autoclave for hydrothermal treatment at 180°C for 24 h. Finally, the precipitate after hydrothermal treatment was filtered and washed by distilled water and then calcined at 300°C for 2 h to achieve a powder of square-surface nanostructured WO_3. The WO_3 nanostructured powder was mixed with an organic binder (α-terpineol) to achieve a paste for creating the thick sensing electrode film.

Powder YSZ (ZrO_2 doped 8% mol Y_2O_3), as shown in Ref. [16], synthesised by a sol-gel citric route was used to fabricate the electrolyte substrate. Therein, the powder YSZ was pressed at 5 tons/cm^2 and then sintered at 1300°C for 4 h to realise YSZ plate. Then, the YSZ plate was sharpened and laser-cut into square substrate with widths of 3×3 mm and thickness of 0.1 mm.

To fabricate the mixed-potential sensor, two Pt porous electrodes (size of each electrode was width of 1×1 mm and thickness about 3 μm, as similarly reported in our previous work [16]) were created by screen-printing on two sides of the YSZ substrate using the Pt paste (ESL 5545) and then sintered at 1000°C for 1 h to obtain a structure of Pt/YSZ/Pt. One Pt electrode of the Pt/YSZ/Pt structure was coated by the paste of square-surface

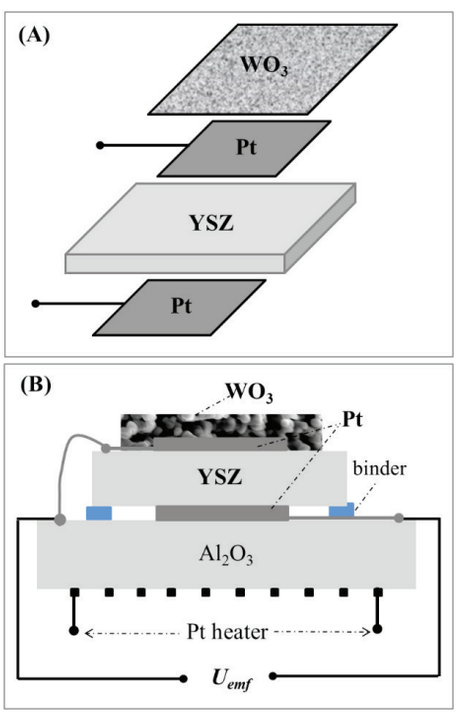

Fig. 1. (A) Illustration of compositional layers and (B) Cross-sectional view structure of the mixed-potential sensor Pt/YSZ/(Pt-WO_3) on Al_2O_3 substrate.

nanostructured WO_3, after that sintered at 700°C for 10 h to get the sensing electrode with WO_3 thick film of approximately 2×2 mm in size and 5 µm in thickness. The structure Pt/YSZ/(Pt-WO_3) was adhered on the front side of an Al_2O_3 substrate integrated with a Pt heater on its rear side to control the operating temperature. Pt wires with a diameter of 25 µm were connected to both Pt and Pt-WO_3 electrodes by sealing with the Pt paste (ESL 5545). The complete mixed-potential sensor consists of the electrode (Pt), electrolyte layer (YSZ), and NO_2 auxiliary sensing electrode (Pt-WO_3). Fig. 1 illustrates this configuration including the compositional layers (Fig. 1A) and structure of the mixed-potential sensor Pt/YSZ/(Pt-WO_3) on Al_2O_3 substrate (Fig. 1B).

Gas sources (including NO_2 and NO from Air Liquide America Specialty Gases - LLC and CO, CH_4, and CO_2 from Singapore Oxygen Air Liquide Pte Ltd.) were used in mixture with dry air (80% N_2+20% O_2) by using the flow-through mixing method [17] for gas-sensing performance. A measuring chamber of 50 ml in volume was used and the total gas flow rate through the chamber was fixed at 300 ml/min. Changes in electromotive force or mixed-potential voltage (U_{emf}) between the electrodes of the sensor Pt/YSZ/(Pt-WO_3) were recognised by a voltmeter (Keithley, model 2700). The gas sensing response (ΔU_{emf}) was calculated with the following equation:

$$\Delta U_{emf} = U^{g}_{emf} - U^{a}_{emf} \quad (1)$$

where U^{g}_{emf} and U^{a}_{emf} are the mixed-potential voltages measured between the two electrodes of the sensor in air containing the desired gases and pure air, respectively.

Scanning electron microscopy (SEM, Hitachi S-4800), X-ray diffractometry (Miniflex Rigaku) with a Cu-Kα radiation source (λ=1.5405 Å), and transmission electron microscopy (TEM, JEOL 2100) were used to examine morphologies and crystalline structures of the sensing electrode of the square-surface nanostructured WO_3.

3. Results and discussion

Figs. 2A and 2B show TEM images of the as-synthesised WO_3 nanoparticles and WO_3 nanoparticles originating from the sensing electrode after sintering at 700°C, respectively. The results indicate that the synthesised WO_3 nanoparticles from the hydrothermal treatment presented square-surface nanostructures approximately 60×80 nm in size. It can also be seen that the WO_3 nanoparticles almost retain their morphological structure after sintering at 700°C (Fig. 2B). This characteristic is further defined by the SEM image of the surface of the WO_3 sensing electrode as shown in Fig. 2C. The thickness of the WO_3 sensing electrode on the YSZ substrate was defined to be about 5 µm by the cross-sectional SEM image in Fig. 2D.

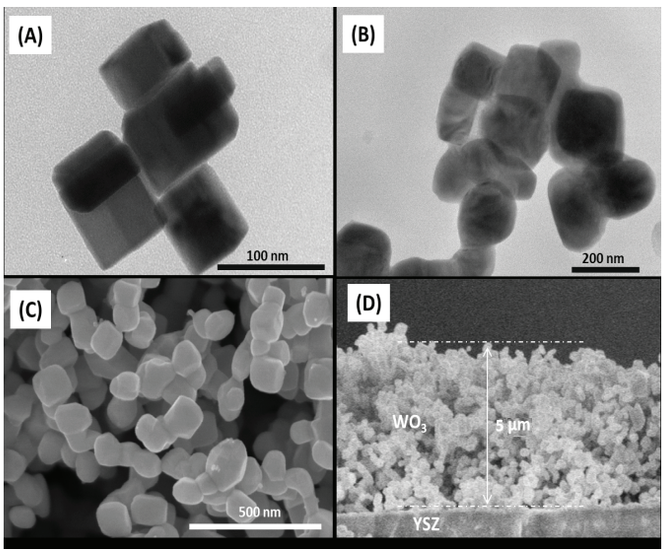

Fig. 2. (A) TEM images of as-synthesised WO_3 nanoparticles, (B) WO_3 nanoparticles originated from the sensing electrode after sintering at 700°C, (C) SEM images of surface, and (D) Cross-sectional view of the WO_3 sensing electrode on YSZ substrate.

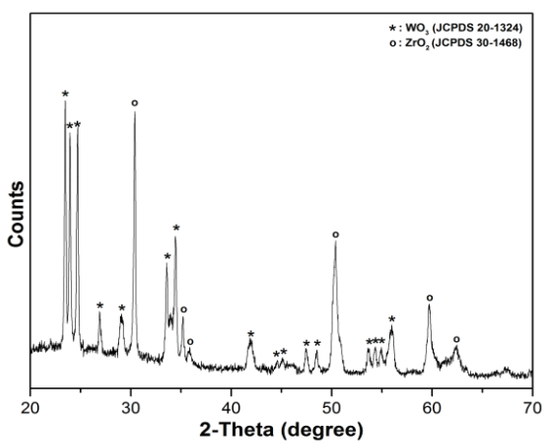

Fig. 3. XRD pattern of the WO_3 square-surface nanostructure-based sensing electrode on YSZ substrate after sintering process at 700°C.

The X-ray diffraction pattern of the WO_3 nanoparticle sensing electrode on YSZ substrate after the sintering process at 700°C is shown in Fig. 3. The result indicated that the peaks of the pattern likely belong to the typical crystalline structures of orthorhombic WO_3 (JCPDS 020-1324, denoted '*') and cubic zirconia (JCPDS 30-1468, denoted 'o').

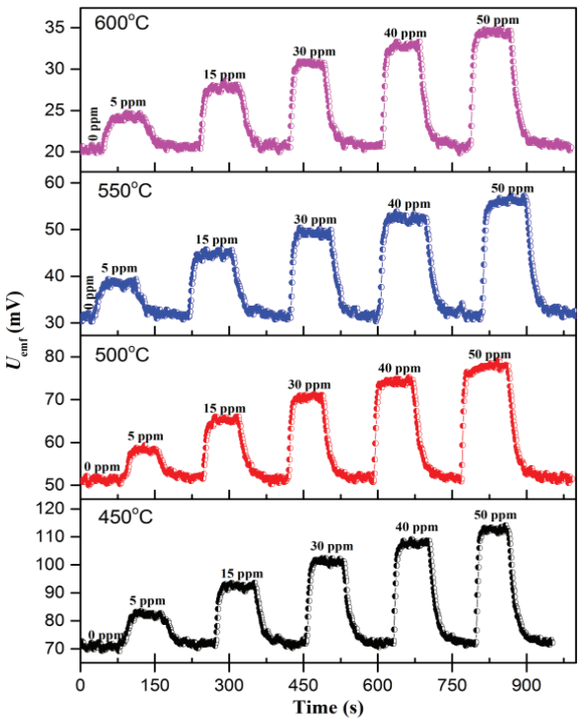

Fig. 4. Electromotive voltage (U_{emf}) of the sensor Pt/YSZ/(Pt-WO_3) responding to 5, 15, 30, 40, and 50 ppm NO_2 at operating temperatures of 450, 500, 550, and 600°C.

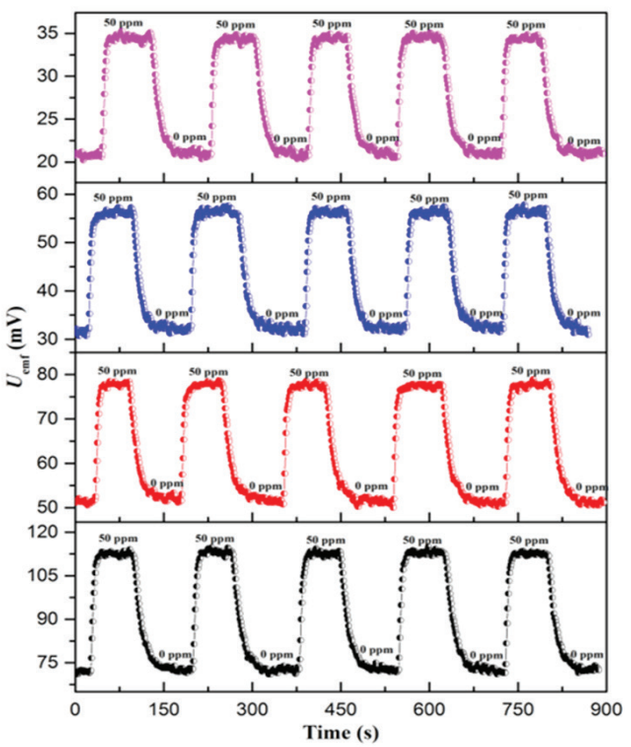

Fig. 5. Electromotive voltage (U_{emf}) of the sensor Pt/YSZ/(Pt-WO_3) responding to 50 ppm NO_2/air cycles at operating temperatures of 450, 500, 550, and 600°C.

For the gas sensing investigation, the Pt/YSZ/(Pt-WO_3) sensor was examined when responding to NO_2 gas at different operating temperatures of 320, 390, 450, 500, 550, and 600°C. From this measured data, the sensing response (ΔU_{emf}) and the response-recovery times (τ_{90}) were calculated. Fig. 4 shows typical results of electromotive voltage (U_{emf}) of the Pt/YSZ/(Pt-WO_3) sensor responding to 5, 15, 30, 40, and 50 ppm NO_2 at operating temperatures of 450, 500, 550, and 600°C. It was observed that the electromotive voltage U_{emf} clearly changed according to the cycles of exposure to different NO_2 gas concentrations. Fig. 5 shows highly repeatable and stable characteristics of the electromotive voltage U_{emf} responding to 50 ppm NO_2/air cycles under working temperatures of 450, 500, 550, and 600°C.

With the each NO_2 concentration, the sensing response ΔU_{emf} of the Pt/YSZ/(Pt-WO_3) sensor slightly increased with operating temperatures from 320 to 450°C and then strongly reduced from 450 to 600°C.

For example, ΔU_{emf} values for 50 ppm NO_2 of the sensor Pt/YSZ/(Pt-WO_3) were found about 35.2, 39.9, 40.9, 27.6, 25.2, and 13.7 mV for operating temperatures of 320, 390, 450, 500, 550, and 600°C, respectively. These values were significant for YSZ mixed potential gas sensor as compared with recent reports [4]. In more detail, Table 1 showed a typical gas sensing performance of the Pt/YSZ/(Pt-WO_3) sensor to 50 ppm NO_2 when operating at 320, 390, 450, 500, 550, and 600°C. The highest response was about 40.9 mV for 50 ppm NO_2 at 450°C. The sensor presented quite short response/recovery times (τ_{90}) of only approximately several tenths of seconds. Fig. 6 indicates the dependences of the sensing response ΔU_{emf} on NO_2 gas concentration when operating at 320, 390, 450, 500, 550, and 600°C. The dependences presented a similar shaped curve with the sensing response ΔU_{emf} increasing with the increase of NO_2 gas concentration. However, one disadvantage was found: the sensing response (ΔU_{emf}) sharply reduced in the high operating temperature region. This behaviour presents an obstacle for high temperature applications.

Table 1. Gas sensing performance of the sensor Pt/YSZ/(Pt-WO_3) to 50 ppm NO_2.

Operating temperature	Gas sensing response (ΔU_{emf})	Response time (τ_{90})	Recovery time (τ_{90})
320°C	35.2 mV	17 s	40 s
390°C	39.9 mV	16 s	39 s
450°C	40.9 mV	15 s	39 s
500°C	27.5 mV	14 s	37 s
550°C	25.2 mV	13 s	35 s
600°C	13.7 mV	13 s	34 s

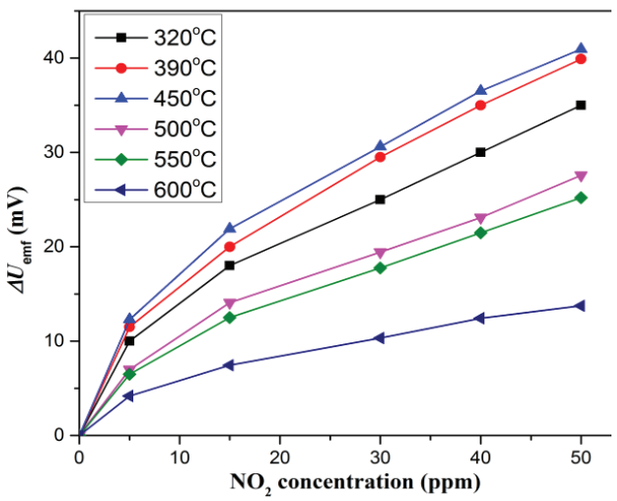

Fig. 6. Dependence of sensing response (ΔU_{emf}) of the Pt/YSZ/(Pt-WO_3) sensor on NO_2 concentration at operating temperatures of 320, 390, 450, 500, 550, and 600°C.

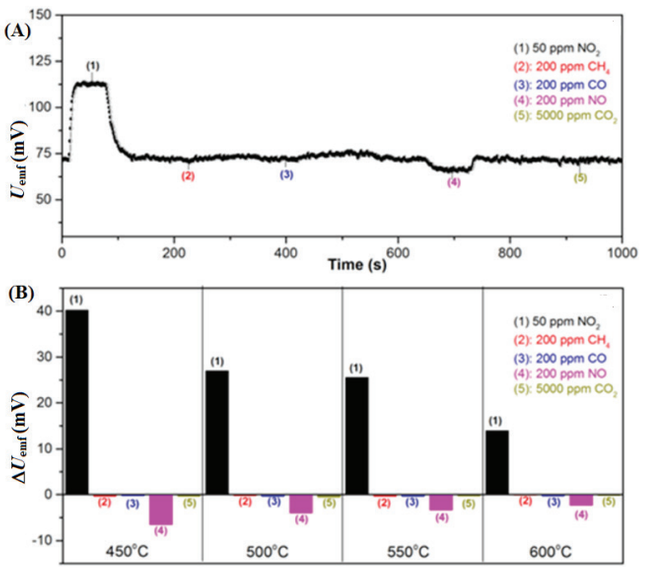

Fig. 7. (A) Typical electromotive voltage (U_{emf}) of the Pt/YSZ/(Pt-WO_3) sensor responding to 50 ppm NO_2, 200 ppm CH_4, 200 ppm CO, 200 ppm NO, and 5000 ppm CO_2 450°C and (B) Comparison of the sensing response (ΔU_{emf}) for these gas concentrations at operating temperatures of 450, 500, 550, and 600°C.

To evaluate selectivity, we have investigated and compared the gas sensing responses of the Pt/YSZ/(Pt-WO_3) sensor to some common combustion gases including NO_2, NO, CO, CH_4, and CO_2. The selective gas sensing characteristics of the Pt/YSZ (Pt-WO_3) sensor are shown in Fig. 7. Typically, the electromotive voltage U_{emf} responding to 50 ppm NO_2, 200 ppm CH_4, 200 ppm CO, 200 ppm NO, and 5000 ppm CO_2 at operating temperatures of 450°C are illustrated in Fig. 7A. A comparison chart of the gas sensing response (ΔU_{emf}) for these gas concentrations at different operating temperatures of 450, 500, 550, and 600°C is presented in Fig. 7B. The result indicated that the gas sensing response ΔU_{emf} of the Pt/YSZ/(Pt-WO_3) sensor was small for NO gas and almost negligible for CO, CH_4, and CO_2 gases. It was concluded that the Pt/YSZ/(Pt-WO_3) sensor presented a very high selectivity to NO_2 gas in compared with the gases of NO, CO, CO_2, and CH_4.

The gas sensing mechanism of the mixed potential sensor Pt/YSZ/(Pt-metal-oxide) when exposed to gas mixtures occurs by simultaneous electrochemical reactions at the triple phase boundary of the gas-electrolyte-electrode and then reaches an equilibrium state resulting in the formation of the mixed potential or electromotive force (U_{emf}) as proposed in Refs. [3, 18, 19]. The triple phase boundary, considered as a key factor explaining the NO_2 sensing performance of the Pt/YSZ/(Pt-metal-oxide) mixed potential sensor, can be described as:

In air: O_2, Pt/YSZ/(Pt-metal-oxide), O_2

In air containing NO_2: $O_2 + NO_2$, Pt/YSZ/(Pt-metal-oxide), $O_2 + NO_2$

The electrochemical reactions can be assumed as following:

Anodic for O_2: $O^{2-} \rightarrow \frac{1}{2}O_2 + 2e^-$ (2)

Cathodic for NO_2: $NO_2 + 2e^- \rightarrow NO + O^{2-}$ (3)

The changes of ionic (O^{2-}) and electronic (e^-) forms the electrochemical potentials (U_{emf}) at the electrodes. Differences in the cathodic/anodic catalytic reactions in the interfaces of Pt/YSZ and (Pt-metal-oxide)/YSZ makes the sensing response (ΔU_{emf}) change in correspondence with the NO_2 gas concentration. The magnitude of the sensing response (ΔU_{emf}) is mainly dominated by the catalytic activity properties of (Pt_metal-oxide)/YSZ interfaces with reducing/oxidising gases. Thus, in this work, the specific characteristic of the high catalytic activity to NO_2 gas of the square-surface nanostructured WO_3, as mentioned in Refs. [10, 13-15], could play an important role in the high selectivity performance of the Pt/YSZ/(Pt-WO_3) sensor to NO_2 gas.

4. Conclusions

In summary, the mixed-potential gas sensor Pt/YSZ/(Pt-WO_3) exhibited very high selectivity to NO_2 in comparison with NO, CO, CO_2, and CH_4 gases. The high sensing selectivity of the Pt/YSZ/(Pt-WO_3) mixed-potential gas sensor to NO_2 could be related to the high catalytic activity of the square-surface nanostructured

WO_3. The sensor Pt/YSZ/(Pt-WO_3) exhibited the high NO_2 sensing performance with the gas sensing response (ΔU_{emf}) and response/recovery times (τ_{90}) of 40.9 mV and 15/39 s, respectively, for 50 ppm at 450°C. It can be expected that the square-surface nanostructured WO_3 will be developed for the gas sensing electrode of YSZ-based gas sensors for the detection of NO_2.

CRediT author statement

Truong Giang Nguyen: Conceptualization, Methodology, Writing, Reviewing. Quynh Nga Nguyen: Conceptualization, Writing and Editing.

ACKNOWLEDGEMENTS

This research is funded by University of Transport and Communications (UTC) under grant number T2020-CB-002. The group of authors would like to thank to Dr. Ho Truong Giang - Institute of Materials Science, for the experimental setup on the gas sensing investigation.

COMPETING INTERESTS

The authors declare that there is no conflict of interest regarding the publication of this article.

REFERENCES

[1] J. Hodgkinson, R.P. Tatam (2013), "Optical gas sensing: A review", *Measurement Science and Technology*, **24(1)**, DOI: 10.1088/0957-0233/24/1/012004.

[2] U. Guth, P. Shuk, C. McGuire (2020), "Gas sensing technologies in combustion: A comprehensive review", *Journal of Electrochemical Science and Engineering*, **10(2)**, pp.103-110, DOI: 10.5599/jese.743.

[3] S. Zhuiykov, N. Miura (2007), "Development of zirconia-based potentiometric NO_x sensors for automotive and energy industries in the early 21st century: What are the prospects for sensors?", *Sensors and Actuators B: Chemical*, **121(2)**, pp.639-651, DOI: 10.1016/j.snb.2006.03.044.

[4] K.P. Ramaiyan, R. Mukundan (2020), "Review-recent advances in mixed potential sensors", *Journal of the Electrochemical Society*, **167(3)**, DOI: 10.1149/1945-7111/ab67ab.

[5] N. Miura, T. Sato, S.A. Anggraini, et al. (2014), "A review of mixed-potential type zirconia-based gas sensors", *Ionics*, **20**, pp.901-925, DOI: 10.1007/s11581-014-1140-1.

[6] J. Yoo, S. Chatterjee, E.D. Wachsman (2007), "Sensing properties and selectivities of a WO_3/YSZ/Pt potentiometric NO_x sensor", *Sensors and Actuators B: Chemical*, **122(2)**, pp.644-652, DOI: 10.1016/j.snb.2006.07.024.

[7] J. Yoo, F.V. Assche, E.D. Wachsman (2006), "Temperature-programmed reaction and desorption of the sensor elements of a WO_3/YSZ/Pt potentiometric sensor", *Journal of the Electrochemical Society*, **153(6)**, DOI: 10.1149/1.2188248.

[8] A. Dutta, N. Kaabbuathong, M.L. Grilli, et al. (2003), "Study of YSZ-based electrochemical sensors with WO_3 electrodes in NO_2 and CO environments", *Journal of the Electrochemical Society*, **150(2)**, DOI: 10.1149/1.1533044.

[9] M. Horprathum, K. Limwichean, A. Wisitsoraat, et al. (2013), "NO_2-sensing properties of WO_3 nanorods prepared by glancing angle DC magnetron sputtering", *Sensors and Actuators B: Chemical*, **176**, pp.685-691, DOI: 10.1016/j.snb.2012.09.077.

[10] A. Boudiba, C. Zhang, C. Bittencourt, et al. (2012), "Hydrothermal synthesis of two dimensional WO_3 nanostructures for NO_2 detection in the ppb-level", *Procedia Engineering*, **47**, pp.228-231, DOI: 10.1016/j.proeng.2012.09.125.

[11] A. Afzal, N. Cioffi, L. Sabbatini, et al. (2012), "NO_x sensors based on semiconducting metal oxide nanostructures: Progress and perspectives", *Sensors and Actuators B: Chemical*, **171-172**, pp.25-42, DOI: 10.1016/j.snb.2012.05.026.

[12] P.V. Tong, N.D. Hoa, V.V. Quang, et al. (2013), "Diameter controlled synthesis of tungsten oxide nanorod bundles for highly sensitive NO_2 gas sensors", *Sensors and Actuators B: Chemical*, **183**, pp.372-380, DOI: 10.1016/j.snb.2013.03.086.

[13] L. You, Y.F. Sun, J. Ma, et al. (2011), "Highly sensitive NO_2 sensor based on square-like tungsten oxide prepared with hydrothermal treatment", *Sensors and Actuators B: Chemical*, **157(2)**, pp.401-407, DOI: 10.1016/j.snb.2011.04.071.

[14] C. Wang, X. Li, C. Feng, et al. (2015), "Nanosheets assembled hierarchical flower-like WO_3 nanostructures: Synthesis, characterization, and their gas sensing properties", *Sensors and Actuators B: Chemical*, **210**, pp.75-81, DOI: 10.1016/j.snb.2014.12.020.

[15] D.T. Thu, D.V. Huong, P.Q. Ngan, et al. (2016), "NO_2 sensing performance of nanosheet tungsten oxide with square-like surface structure synthesized by hydrothermal process", *Journal of Nanoscience and Nanotechnology*, **16(8)**, pp.7935-7941, DOI: 10.1166/jnn.2016.12746.

[16] H.T. Giang, H.T. Duy, P.Q. Ngan, et al. (2013), "High sensitivity and selectivity of mixed potential sensor based on Pt/YSZ/$SmFeO_3$ to NO_2 gas", *Sensors and Actuators B: Chemical*, **183**, pp.550-555, DOI: 10.1016/j.snb.2013.04.035.

[17] H.E. Endres, H.D. Jander, W. Gottler (1995), "A test system for gas sensors", *Sensors and Actuators B: Chemical*, **23(2-3)**, pp.163-172, DOI: 10.1016/0925-4005(94)01272-J.

[18] J.W. Yoon, M.L. Grilli, E.D. Bartolomeo, et al. (2001), "The NO_2 response of solid electrolyte sensor made using nano-sized $LaFeO_3$ electrode", *Sensors and Actuators B: Chemical*, **76(1-3)**, pp.483-488, DOI: 10.1016/S0925-4005(01)00594-9.

[19] X. Liang, S. Yang, J. Li, et al. (2011), "Mixed-potential-type zirconia-based NO_2 sensor with high-performance three-phase boundary", *Sensors and Actuators B: Chemical*, **158(1)**, pp.1-8, DOI: 10.1016/j.snb.2011.02.051.

Sulfolane as a co-solvent for carbonate-electrolytes in lithium-ion batteries using a $LiMn_2O_4$ cathode

Phuong Hue Luu[1], Phuong Hue Tran[1], Hoang Van Nguyen[1, 2], An Le Bao Phan[3], Oanh Hoang Nguyen[1], Man Van Tran[1, 2], Phung My Loan Le[1, 2], Thanh Duy Vo[2*]

[1]Department of Physical Chemistry, Faculty of Chemistry, University of Science, Vietnam National University, Ho Chi Minh City, 227 Nguyen Van Cu Street, Ward 4, District 5, Ho Chi Minh City, Vietnam

[2]Applied Physical Chemistry Laboratory, Faculty of Chemistry, University of Science, Vietnam National University, Ho Chi Minh City, 227 Nguyen Van Cu Street, Ward 4, District 5, Ho Chi Minh City, Vietnam

[3]University of Maryland, Virginia, United States, College Park, Maryland State, USA

Received 12 February 2020; revised 28 April 2020; accepted 11 May 2020

Abstract:

In this study, we aimed to evaluate the effect of sulfolane (SL) as a co-solvent in conventional carbonate-based electrolytes and its compatibility with a $LiMn_2O_4$ (LMO) cathode. The amount of SL was varied from 10 to 50 vol.% in an EC-DMC mixture (1:1 vol. ratio) within a 1.0-M lithium bis(trifluoromethanesulfonyl)imide (LiTFSI) salt. The thermal properties of the electrolytes were studied using thermogravimetric analysis (TGA). Solvent flammability was measured via self-extinguishing time (SET) and ignition time indexes while viscosity was gauged by the Ostwald method. Ionic conductivity was evaluated by electrochemical impedance spectroscopy (EIS). Electrochemical techniques such as cyclic voltammetry (CV) and galvanostatic cycling with potential limitation (GCPL) were carried out to evaluate battery performance with the selected electrolytes. The results indicated that an increasing proportion of SL leads to an enhancement of the thermal and oxidation stability of the electrolytes. At 20-vol.% SL and below, the as-synthesized electrolytes exhibited a high ionic conductivity of 7.45 $mS.cm^{-1}$ (25°C) and enabled LMO to deliver a specific capacity of 103 $mAh.g^{-1}$ with a capacity retention of 92% after 20 cycles at C/10 rate. Due to such favourable properties, SL can be used as a co-solvent in EC-DMC systems to enhance the safety of lithium-ion batteries under high voltage conditions.

Keywords: **conductivity, electrolytes, lithium-ion batteries, sulfolane, viscosity.**

Classification number: **2.2**

1. Introduction

Sulfolane (SL), also known as thiolane 1,1-dioxane, is a sulfur-organic compound with a highly polar double bond S=O as shown in Fig. 1.

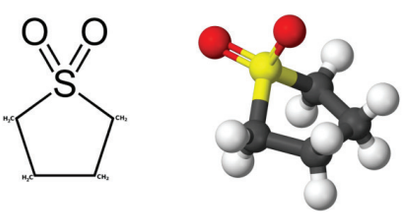

Fig. 1. Chemical formula and structure of SL.

The key features of SL are good thermal stability (decomposed at 220°C), high ignition temperature of 528°C, high flash point (FP) of 165°C, excellent oxidation resistance (above 5.0 V vs. Li^+/Li), and high polarity (water solubility of 1.266 $g.l^{-1}$ at 20°C) [1, 2]. Owing to these advantages, SL derivatives have been considered promising electrolytes for high working potentials and the improvement ofthelithium-ion battery safety. Specifically, Xu's group utilized pure SL as a non-carbonate solvent with a cathode material of $LiNi_{0.5}Mn_{1.5}O_4$ for half and full-cell tests a nd obtained a capacity of about 110 $mAh.g^{-1}$ in the first 10 cycles [3]. However, SL-based electrolytes have high viscosity and an inability to stabilize solid electrolyte interphase layers on the surface of a graphite anode. Indeed, SL has been often used in combination with carbonate-based electrolytes like diethyl carbonate (DEC), dimethyl carbonate (DMC), and ethylene carbonate (EC) to improve the electrochemical properties of electrolytic mixtures [4]. In particular, Cai, et al. (2017) [5] added 2 vol.% SL to 1.0 M $LiPF_6$/EC-DMC (1:1) and demonstrated that the SL additive enabled oxidation resistance as well as enhanced the charge-discharge performance of $LiNi_{1/3}Co_{1/3}Mn_{1/3}O_2$ (NMC111)/ graphite batteries. As a result, the solution containing SL had an oxidation potential up to 5.0 V (vs. Li^+/ Li), 4.25 V higher than electrolytes without SL. Furthermore, the long-term cycling stability of electrolytes containing SL was significantly improved in specific capacity and Coulombic efficiency as well. Abouimrane, et al. (2009) [6] tested the

*Corresponding author: Email: vodthanh@hcmus.edu.vn

ignition of the two electrolytes 1.0-M $LiPF_6$/EC-EMC (3:7) and 1.0 M $LiPF_6$/SL-EMC (1:1) exposed to a 1200°C flame in the air. The EC electrolyte ignited vigorously within 2 s while the electrolyte containing SL needed about 45 s to become weakly flamed, which indicates significantly reduced flash points. Highly concentrated sulfone-based electrolytes with lithium bis(fluorosulfonylimide) were recently suggested for a high voltage cathode such as $LiNi_{0.5}Mn_{1.5}O_4$ or $LiCoPO_4$ because of synergistic interphase (CEI/SEI) in LiF [3]. Ren, et al. (2018) [7] also worked on localized high-concentration sulfone-based electrolytes and found lithium-metal cells with high efficiency.

Herein, our work aims to investigate the thermal properties, physico-chemical, and electrochemical properties of SL substitution in 1:1 EC-DMC-based electrolytes as well as their compatibility to the high voltage cathode material $LiMn_2O_4$ (LMO).

2. Experimental

2.1. Preparation of electrolytes and physico-chemical characterization

SL, EC, DMC, and LiTFSI were purchased from Sigma-Aldrich with high purity (>99%) and stored inside an Argon filled-glovebox with controlled oxygen and water concentration less than 5 ppm.

The electrolytes were prepared by dissolving a lithium salt in mixtures of EC: DMC: SL (EDS) at different volume ratios and was kept stirring for 12 h in the glovebox. The composition of the prepared electrolytes is described in Table 1.

Table 1. The solvent composition of prepared electrolytes.

Abbreviation	vol.% EC	vol.% DMC	vol.% SL	C_{LiTFSI} (M)
EDS550	50	50	0	1
EDS541	50	40	10	1
EDS532	50	30	20	1
EDS523	50	20	30	1
EDS514	50	10	40	1
EDS505	50	0	50	1

The weight loss of as-prepared electrolytes at different temperatures were analysed by TGA between 0°C and 600°C with a heating rate of 10°C.min^{-1} in an N_2 atmosphere on a thermal analysis LABSYS Evo (Setaram, France).

SET is widely applied to assess the fired resistance of electrolytes. In a typical measurement, a fixed amount of solvent was immobilized on a 14-mm diameter Whatman separator piece then exposed to a burner for 3 s. The distance between a burner and sample was 13 cm. The SET value (s/g) was recorded by measuring the burning time of sample after removal from the flame source, which was then normalized with solvent mass [8]. Each as-prepared sample was measured 3 times in order to get an average value.

The absolute viscosity of the electrolyte solution was determined by an Ostwald viscometer (Canon, Japan) using the following equation:

$$\eta = K.d.t \quad (1)$$

where K is a viscometer constant (K=0.035), d is the electrolyte's density, and t is the time it takes for the electrolyte to flow entirely through the capillary of the viscometer. The sample temperature was adjusted by a temperature-controlled chamber.

The specific ionic conductivity of an electrolyte solution is calculated by the following equation:

$$\kappa = \frac{L}{S}.\frac{1}{R} = K.\frac{1}{R} \quad (2)$$

where κ is the specific conductivity (S/cm), K is the cell constant (cm^{-1}), R is resistance of the solution (Ω), S is the surface area of the Pt electrode (cm^2), and L is the distance between two electrodes (cm). To measure the electrolyte resistance, 0.5 ml of as-prepared solution was added into a dip-type glass conductivity cell (CDC749 conductivity cell, Radiometer) and then kept at the desired temperature for 120 min before each measurement. The conductivity cell was connected to an electrochemical device VSP (Biologics, France) to perform the measurement. A 10-mV AC potential was applied to the cell over a frequency range of 10 mHz to 1 MHz. The cell was initially calibrated using a 0.1 M KCl solution at 25°C to measure the K value.

2.2. Coin cell assembling and electrochemical performance

The cathode slurry was prepared by mixing commercial LMO material (MTI, USA), conductive carbon AB/graphite (Japan) and PVDF-HFP (10% in N-methyl pyrrolidone or NMP) as a binder in a mass ratio of 80:15:5. The as-prepared slurry was cast on aluminium foil, dried at 80°C for 15 h in vacuum, and finally cut out in 14-mm diameter circles.

Electrochemical measurements were conducted on the electrochemical device MPG-2 (Biologics, France). CV sweeping was performed to determine the electrochemical window of the electrolytes using a 1.0-ml three-electrode cell consisting of Pt wire and Ni grid as the working electrode and counter electrode, respectively. The reference electrode was an Ag wire embedded in a solution of 0.01 M $AgNO_3$ + 0.1 M tetrabutylammonium perchlorate (TBAP) in acetonitrile.

3. Results and discussion

3.1. Thermal properties of the electrolytes

In Fig. 2, the samples containing DMC revealed three weight loss stages based on the evaporation temperature of the three pure solvents in the mixture. Specifically, the first stage is the evaporation of DMC at 90°C. The second stage at 243°C could be involved with the evaporation of both EC and SL because their boiling temperatures are quite

close (T_b=243°C and 270°C for EC and SL, respectively). Finally, the weight loss step at 430°C consists of both SL evaporation and the decomposition of the LiTFSI salt. The weight loss percentages of these electrolytes and the corresponding onset temperature are detailed in Table 2. The practical boiling temperature values obtained from thermogravimetric curves closely coincided with those of the pristine solvents [9, 10].

Overall, the non-DMC electrolyte EDS505 shows only two mass loss stages at 243°C and 430°C that correspond to EC-SL evaporation and LiTFSI decomposition, respectively. This electrolyte also exhibits relatively high thermal stability (up to 270°C) due to the absence of the volatile solvent DMC (T_b=90°C).

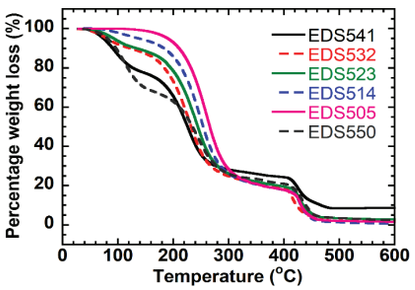

Fig. 2. Thermogravimetric curves of EC:DMC:SL+1 M LiTFSI with different volume ratios between SL and DMC.

In contrast, when adding SL to the EC-DMC electrolytes, the temperature associated with the first weight loss decreases sharply. Typically, the decomposition temperature of EDS550 (0 vol.% SL) and EDS523 (30 vol.% SL) are 112°C and 94°C, respectively. This could be attributed to different solvent polarization, for example, DMC has poor polarity (ε=3.20) while the polarity of EC and SL (ε_{EC}=90, ε_{SL}=43) are strong [10, 11], which leads to micro-phase separation in these electrolyte systems. The samples with increasing SL amount in the electrolyte, namely, EDS541, EDS532, and EDS523, exhibited lower thermal stability owing to significant micro-phase separation. Interestingly, with an SL amount higher than 40 vol.%, the sample EDS514 reveals the first weight loss temperature higher than the other ones. This increase is ascribed to the hysteresis of DMC evaporation due to the significant increase of viscosity.

Table 2. The onset temperature at different stages of weight loss of SL mixed carbonate-based electrolytes.

Electrolyte	T_{onset} (°C)			Weight loss (%)		
	Step 1	*Step 2*	*Step 3*	*Step 1*	*Step 2*	*Step 3*
EDS550	112	244	428	31.4	44.0	20.0
EDS541	98	227	426	27.2	50.6	16.3
EDS532	96	230	428	21.4	59.9	16.5
EDS523	94	235	426	12.1	67.6	17.1
EDS514	109	250	428	7.5	74.7	17.2
EDS505	-	266	427	-	80.4	16.8

Besides, the effect of SL on the flammability of electrolytes was evaluated by the value of SET in Table 3. The addition of a moderate amount of SL (≤20 vol.%) in the carbonate mixtures enhances their thermal stability. With the increase of SL content from 0 to 20 vol.%, the self-extinguishing time of the electrolytes reduced from 45 to 32 $s.g^{-1}$. When a small amount of SL was added to the electrolyte, the volatile DMC that had separated from the mixture ignited first, which lead to a combustion occurring in the gas or vapor phase followed by immediate self-extinguishing. Despite SL's high evaporation temperature and flash point compared to EC and DMC, low concentrations of SL had a negligeable contribution to the combustion property of the electrolytes.

Table 3. SET values of SL-mixed electrolyte systems.

Electrolyte	% vol. SL	SET ($s.g^{-1}$)
EDS550	0	45
EDS541	10	34
EDS532	20	32
EDS523	30	59
EDS514	40	63
EDS505	50	67

When increasing the SL content from 30 to 50 vol.%, the SET value rose from 59, to 67 $s.g^{-1}$. As a fire-retardant, SL has a slow rate of ignition and low heat generation, which minimizes the amount of heat radiating to the surrounding environment. Indeed, SLs are mostly difficult to burn; however, once it was burnt, the fire lasted a very long time. This phenomenon has been similarly observed in previous studies [8, 11].

3.2. Viscosity and ionic conductivity of the electrolytes

The density, viscosity, and ionic conductivity of the carbonate electrolytes mixed with different vol.% SL are presented in Table 4. Ionic conductivity is one of the most critical properties of the application of electrolytes to Li-ion batteries. As shown in Fig. 3, two opposite directions of conductivity could be observed when increasing the SL content.

Figure 3 shows the relationship between ionic conductivity and viscosity for all the electrolytes. As SL content increases, the density and viscosity of these mixtures rose due to the high density and viscosity of SL (d_{SL}=1.6 $g.cm^{-3}$) compared with that of DMC and EC solvents (d_{DMC}=1.069 $g.cm^{-3}$, d_{EC}=1.32 $g.cm^{-3}$). The electrolyte EDS505 with 50 vol.% SL and no DMC solvent had the highest viscosity of 22.6 mPa.s.

The conductivity first increased with increasing SL content from 0 to 20 vol.%, then suddenly decreased with more SL content. The complicated change in conductivity can be explained by the combination of two factors: ionic solvation and viscosity. In principal, the high dielectric constant of SL (ε_{SL}=43.3) could improve the solvating ability

of the solvent mixtures and reduce ion-ion interaction, resulting in enhanced lithium-ion mobility under the effect of electric fields. In parallel, due to the high viscosity of SL compared to EC and DMC, SL amounts greater than 20 vol.% significantly increase the viscosity of electrolytes, which mitigates lithium-ion mobility and dominates the effect of ion solvation. Thus, the ionic conductivity was totally penalized at high SL content. The sample EDS532 that contains 20 vol.% SL exhibited the highest conductivity (7.45 $mS.cm^{-1}$ at 25°C). The viscosity and ionic conductivity need to be optimized in these carbonate-based electrolytes when adding SL.

Table 4. Density, viscosity, ionic conductivity, and oxidation limit potential (E_{ox}) of SL-based electrolytes.

Mixture	Density ($g.cm^{-3}$)	Viscosity (mPa.s)	Ionic conductivity ($mS.cm^{-1}$)	E_{ox} (V) vs. Li^+/Li
EDS550	1.196	6.38	4.82	4.57
EDS541	1.215	7.52	6.10	4.68
EDS532	1.234	10.40	7.45	4.72
EDS523	1.254	15.88	5.37	4.77
EDS514	1.273	20.93	3.22	4.89
EDS505	1.291	22.62	2.03	4.97

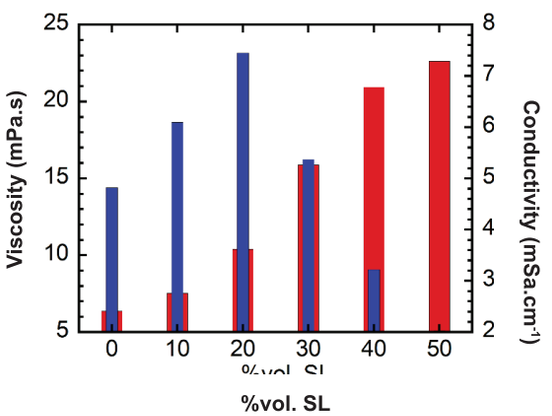

Fig. 3. Relationship between ionic conductivity and viscosity of SL-based electrolytes.

3.3. Electrochemical stability of the electrolytes

Cyclic voltammograms were performed to determine the oxidation stability of the SL-based electrolytes in the range 3.5-5.6 V (Fig. 4). The oxidation limit potential of the electrolytes were determined in the forward scan where the current reaches 0.0025 mA. The oxidation limit potential of the electrolytes containing SL reaches about 4.8 V vs. Li^+/Li, which is superior to conventional carbonate solvents or electrolytes containing only EC-DMC (EDS550). The oxidation stability rose quickly as SL content was gradually increased. Therefore, the highest electrochemical oxidation (E_{ox}) value of about 5.0 V belongs to the EDS505 electrolyte containing 50 vol.% SL (Table 4).

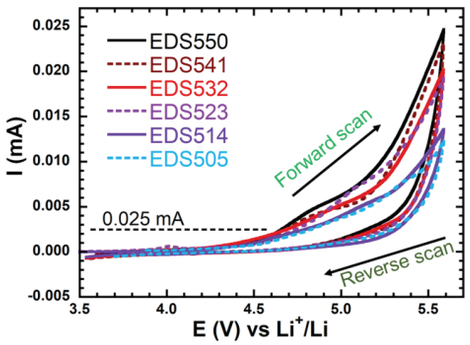

Fig. 4. Cyclic voltammograms of SL-mixed carbonate solvents + 1 M LiTFSI electrolytes.

3.4. Cycling performance of Li/LMO half-cell in the prepared electrolytes

Samples EDS532 and EDS523 with 20 and 30 vol.% SL were selected for cycling tests in a Li|LMO half-cell and compared to the cell with non-SL electrolyte (ESD550). Charge-discharge profiles of the cells showed two small plateaus at about 3.9 V and 4.1 V with a small shoulder corresponding to the two-step embedding and removal of lithium ions in different stages of the electrochemical reaction, which are also consistent with the CV curves. According to Fig. 5, EDS532 reveals the highest capacity of about 103 $mAh.g^{-1}$ (theoretical capacity is 148 $mAh.g^{-1}$) and its Coulomb efficiency reaches over 95%, indicating a good compatibility between cathode materials and the investigated electrolytes.

In terms of discharge capacity, the LMO cell with the EDS532 electrolyte shows the best value at the first cycle and remains at 95 $mAh.g^{-1}$ after 20 cycles. Both EDS550 and EDS523 have the same initial reversible capacity of 95 $mAh.g^{-1}$. While the capacity of EDS550 decreased to less than 85 $mAh.g^{-1}$ after only 5 cycles, that of EDS523 remained around 90 $mAh.g^{-1}$. After the fifth cycle, EDS523 demonstrated a linear decrease in discharge capacity. In contrast, EDS550 showed a stable range for only 8 cycles, then continuously decreased at the same rate as EDS523 to 75 $mAh.g^{-1}$ after 20 cycles.

Regarding Coulombic efficiency, all electrolyte systems showed various degrees of fluctuation from mild (EDS523) to high (EDS550) and remained at over 90% through 20 cycles.

The primary factor determining the discharge capability of EDS550 is ionic conduction and solvation phenomena. The sample with the lowest dielectric constant and highest DMC proportion, like EDS550, showed the electrolyte weakly solvated Li^+ resulting in low ionic conductivity and low specific discharge capacity. In the SL-based electrolyte, the highest dielectric constant of SL compared to other solvents is beneficial to ion dissociation leading to an increase of mobile Li^+ ions. However, its high viscosity penalizes the

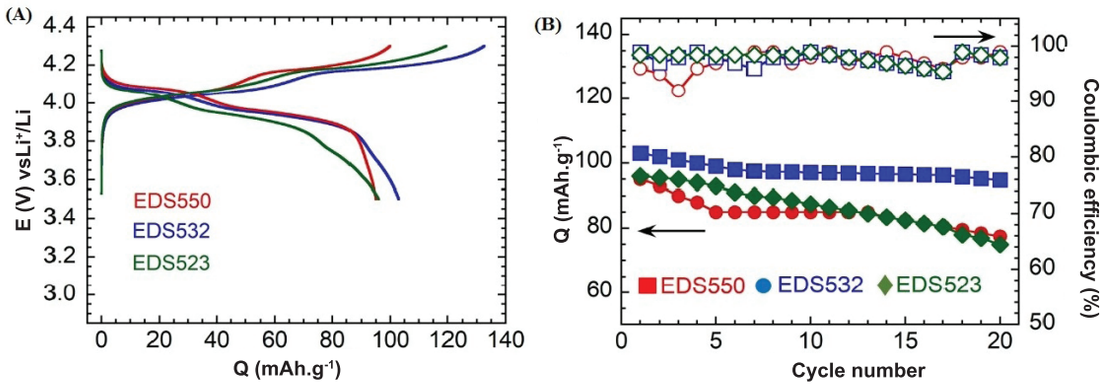

Fig. 5. First charge-discharge profiles (A) and plot of capacity and Coulombic efficiency against cycle number (B) of half-cells containing EDS550, EDS523 and EDS532 electrolyte.

movement of Li^+ ions, which means a decrease of charge mobility rate and discharge ability. Indeed, the EDS523 with 30 vol.% SL shows a linear decrease in capacity due to high viscosity resulting in hindered ionic mobility.

With an average proportion of SL (about 20 %wt.), EDS532 show a good stability after 20 cycles. The capacity loss is as low as 8%, and the Coulombic efficiency ranges from 100 to 93%.

4. Conclusions

We have studied electrolytes with different vol.% of SL in EC-DMC (1:1)/1.0 M LiTFSI. The electrolytes are thermally stable up to 100°C and their thermal stability increased with increasing SL content. The SL addition significantly enhanced the flammability resistance of the carbonate-based electrolytes. The oxidation limit of the electrolyte systems enlarged to 4.8 V vs. Li^+/Li. Although SL addition increased the viscosity of the electrolytes, the optimized amount of SL could be as low as 20 vol.% to reach the highest ionic conductivity for a mixed SL-carbonate electrolyte. Thus, the EDS532 sample exhibited the highest capacity (103 $mAh.g^{-1}$) and the most stable cycling after 20 cycles (efficiency above 90%).

CRediT author statement

Phuong Hue Luu: Conceptualization, Methodology, Software; Phuong Hue Tran: Data curation, Writing-Original draft preparation; Hoang Van Nguyen: Visualization, Investigation; An Le Bao Phan: Software, Validation; Oanh Hoang Nguyen: Software, Validation; Man Van Tran: Writing and Reviewing; Phung My Loan Le: Conceptualisation, Methodology and Writing; Thanh Duy Vo: Writing - Reviewing and Editing.

ACKNOWLEDGEMENTS

This research is funded by Vietnam National University, Ho Chi Minh city through the project grant number: C2019-18-18.

COMPETING INTERESTS

The authors declare that there is no conflict of interest regarding the publication of this article.

REFERENCES

[1] O. Stewart (2010), *Sulfolane Technical Assistance and Evaluation Report*, Alaska Department of Environmental Conversation, 43pp.

[2] V.S. Kolosnitsyn, L.V. Sheina, S.E. Mochalov (2008), "Physicochemical and electrochemical properties of sulfolane solutions of lithium salts", *Russ. J. Electrochem.*, **44(5)**, pp.575-578, DOI: 10.1134/S102319350805011X.

[3] J. Alvarado, M.A. Schroeder, M. Zhang, et al. (2018), "A carbonate-free, sulfone-based electrolyte for high-voltage Li-ion batteries", *Materials Today*, **21(4)**, pp.341-353, DOI: 10.1016/j.mattod.2018.02.005.

[4] E. Clark (2000), "Sulfolane and sulfones", *Encyclopedia of Chemical Technology*, pp.1-11, DOI: 10.1002/0471238961.1921120603120118.a01.

[5] H. Cai, H. Jing, X. Zhang, et al. (2017), "Improving high-voltage performance of Lithium-ion batteries with sulfolane as an electrolyte additive", *J. Electrochem. Soc.*, **164**, pp.A714-A720, DOI: 10.1149/2.0801704jes.

[6] A. Abouimrane, I. Belharouak, K. Amine (2009), "Sulfone-based electrolytes for high-voltage Li-ion batteries", *Electrochem. Commun.*, **11**, pp.1073-1076, DOI: 10.1016/j.elecom.2009.03.020.

[7] X. Ren, S. Chen, H. Lee, et al. (2018), "Localized high-concentration sulfone electrolytes for high-efficiency lithium-metal batteries", *Chem. Cell Press.*, **4**, pp.1877-1892, DOI: 10.1016/j.chempr.2018.05.002.

[8] S. Hess, M. Wohlfahrt-Mehrens, M. Wachtler (2015), "Flammability of Li-ion battery electrolytes: Flash point and self-extinguishing time measurements", *J. Electrochem. Soc.*, **162**, pp.A3084-A3097, DOI: 10.1149/2.0121502jes.

[9] G.G. Eshetu, S. Grugeon, S. Laruelle, et al. (2013), "In-depth safety-focused analysis of solvents used in electrolytes for large scale lithium ion batteries", *Phys. Chem. Chem. Phys.*, **15(23)**, pp.9145-9155, DOI: 10.1039/C3CP51315G.

[10] U. Tilstam (2012), "Sulfolane: A versatile dipolar aprotic solvent", *Org. Process Res. Dev.*, **16(7)**, pp.1273-1278, DOI: 10.1021/op300108w.

[11] R. Naejus, D. Lemordant, R. Coudert, et al. (1997), "Excess thermodynamic properties of binary mixtures containing linear or cyclic carbonates as solvents at the temperatures 298.15 K and 315.15 K", *J. Chem. Thermodyn.*, **29(12)**, pp.1503-1515, DOI: 10.1006/jcht.1997.0260.

DOI: 10.31276/VJSTE.64(1).14-19

Hemicellulose content in rice straws of several high-quality rice grains

Thuy-An Ngo*, Dao-Chi Vo Thi, Nhan-Tanh Nguyen Tran

An Giang University, Vietnam National University, Ho Chi Minh city (VNU-HCM),
18 Ung Van Khiem Street, Dong Xuyen Ward, Long Xuyen City, An Giang Province, Vietnam

Received 2 June 2021; revised 22 June 2021; accepted 6 July 2021

Abstract:

A by-product of rice farming, rice straw is made up of lignin, cellulose, and hemicellulose and comprises lignocellulosic biomass. Particularly rich in this biomass are rice-producing nations like Vietnam, which ranks sixth in the world for rice exports. Because 30-40% of this bioresource is burned to make way for new rice fields for cultivation, its use has not been optimum. Air pollution has been linked to this, particularly in Vietnam. Indeed, burning half of the world's rice straw produces almost 100 million tons of carbon dioxide emissions. Therefore, to increase the benefits of rice and reduce environmental pollution, lignocellulosic biomass reuse is crucial. This paper reports the hemicellulose content in three rice straw types (OM5451, IR50404, and 6976 commons from An Giang province, Vietnam). Alkaline extraction assisted with ultrasound was employed. In this process, samples were mixed with 2 M sodium hydroxide and ultrasonicated for 30 min at 90°C. Then, the mixture was continuously heated at 90°C and stirred at 40 rpm for 1.5 h. Ethanol was used to precipitate hemicellulose. The highest yields obtained of crude hemicellulose were 23.17% in OM5451, 23.1% in IR50404, and 22.94% in 6976 at pH 4.0, however, there was no significant difference at a 95% confidence level as determined by a two-way ANOVA with p-values >0.05. The extracted hemicellulose was confirmed using Fourier-transform infrared spectroscopy (FTIR), X-ray diffraction (XRD), and thermo-gravimetric analysis (TGA).

Keywords: **alkaline extraction, biomass, circular agriculture engineering (CAE), gravimetry, hemicellulose, rice straw.**

Classification number: **2.2**

1. Introduction

Rice straw, a by-product of rice cultivation, contains lignocellulosic biomass and is composed of lignin (5-24%), cellulose (32-47%), and hemicellulose (19-27%) [1, 2]. This biomass is particularly abundant in rice countries such as Vietnam (the fifth in global rice exportation) [3]. However, utilizing this bioresource has not been optimized as 30-40% is burned to clear rice fields for the next cultivation seasons. This has been known to cause air pollution, especially in Vietnam [4]. Indeed, approximately 100 million tons of carbon oxide is emitted from burning 50% of global rice straw [5]. Therefore, the reuse of lignocellulosic biomass is much needed to improve rice benefits and mitigate environmental pollution [6].

Hemicellulose is the second-most abundant class of short-chain polysaccharides, which is different from cellulose and is branched in nature [7, 8]. As a non-crystalline heteropolysaccharide, hemicellulose is made of pyranoses and furanoses sugar including xylans (predominant materials in plant cell walls), xyloglucans, manans, and other compounds of linkage β-glucans. The main acid groups of hemicellulose make them very hydrophilic and soluble in alkaline. Hemicellulose is easily hydrolysed by dilute acid, i.e., HCl and H_2SO_4, or bases [9]. Hydrolysis of hemicellulose can produce xylans that are widely used in commercial products such as various pharmaceuticals, food, and biofuels [10].

Hemicellulose from plant cells can be isolated by ionic liquid extraction, organic solvent solution, alkaline treatment, and liquid hot water extraction. Of these methods, the alkaline method is most commonly used in industries and labs due to its efficiency. While sodium hydroxide solution is applied for the hydrolysis of the soft plant cell wall, potassium hydroxide solution is usually used for hardwood [11-13]. After hydrolysis, ester linkages will be cut and this process produces hemicelluloses. Then, ethanol can be used to precipitate hemicelluloses from the alkaline extraction [14]. The efficiency of hemicellulose can be increased by using ultrasound, which can help reduce the extraction time down to 1.5-2.5 h. The ultrasound waves easily break rice straw cells by disturbing the cells of the biomass and thus promote hemicellulose extraction [15-17].

*Corresponding author: Email: ntan@agu.edu.vn

An Giang is a province of Vietnam with the largest rice production in the Mekong delta with approximately 4 million tons in 2017 [18, 19]. Common rice varieties in An Giang with high yield and good grain quality are OM5451, IR50404, and 6976 [20]. The amount of rice straw generated was about 3891 thousand tons, of which 62% was used for composting, cattle feed, and selling while 36.36% was open-burned. As reported, the highest emission of open-burning is CO_2 with 5.7 million tons while other emissions are CO, SO_2, NO_2, $PM_{2.5}$ and PM_{10} with 135.1, 7.78, 0.28, 54.4, and 14.4 thousand tons, respectively [21]. Since rice straw is a bioresource rich in carbon, nitrogen, and potassium, such open-burning contributes to global air pollution. Therefore, recycling rice straw is necessary to reduce negative environmental impacts.

The temperature and concentration of the alkaline solution in the hemicellulose extraction process significantly affects hemicellulose yield [22]. For example, high yields of lignin, hemicellulose, and nanocellulose fibres separated from rice straw were collected with a 2 M NaOH solution at 90°C. Another work indicated a higher extraction yield versus pH conditions [23]. On the other hand, hemicellulose is a group of polysaccharides in biomass and they possess different properties depending on the variety of biomass [24]. Therefore, the effect of pH values on hemicellulose precipitation in ethanol and the comparison of hemicellulose characteristics generated from sources were two factors investigated in this study. Knowing the hemicellulose concentration in rice straws can aid in optimizing their benefits and recycling. Rice straw from the rice cultivars in An Giang may contain various hemicellulose concentrations, which have not been well studied. Therefore, this research focused on revealing the hemicellulose contents in rice straws generated from those cultivars to provide background data for rice straw hemicellulose studies.

2. Materials and methods

2.1. Sample preparation and materials

Rice straws of OM5451, IR50404, and 6976 were collected from paddy fields in Cho Moi district, An Giang province. All samples (10 kg) were firstly washed by distilled water (room temperature) to remove fine sand particles, then sun-dried for seven days to have the average sample moisture of 4-5.5%. The samples were milled to a size of 1 mm to obtain dried rice straw (DRS) for all the experiments as suggested by Kim, et al. (2020) [25]. After that, the samples were cut into small forms, finely ground (sieve screen: φ=0.08 mm), kept in airtight containers, and stored at room temperature [26].

The chemicals of acid hydrochloric, ethanol 99,5%, sodium hydroxide, acid perchloric, and acetone were purchased from Merck, Germany.

2.2. Extraction of hemicellulose

First, 360 ml of acetone 5% was added to 15 g DRS in a Soxhlet system controlled at 70°C for 4 h, which then became the extracted rice straw (ERS). After 4 h, the ERS was dried in an oven at 105-110°C to constant mass [27].

Each ERS sample (10 g) was first mixed with NaOH 2 M by the ratio of 1 g straw ratio: 20 ml NaOH 2 M and ultrasonicated for 30 min at 90°C. An S100-Elmasonic was used to create the ultrasound waves. After that, the mixture was heated at 90°C and continuously stirred at 40 rpm for 1.5 h. At the end of the 1.5 h period, vacuum filtration was used to collect the filtrate containing hemicellulose. Then, hydrochloric acid 6 M was added to adjust the filtrate pH to the values of 3.5; 4.0; 4.5; and 5.0. The mixture was maintained to stand at 4°C for 24 h. Then, three volumes (500 ml) of ethanol 95% were added to the liquid fraction and this mixture was kept at 4°C for 6 h to precipitate hemicelluloses at the bottom. Vacuum suction was employed to remove the clear solution above the hemicellulose precipitate. The precipitate was washed 3 times with 70% ethanol to remove the others. The extracted hemicellulose was dried under sunlight to constant mass. The crude hemicellulose (CH) yield was the difference between the dried CH and ERS. All samples are presented in Table 1.

Table 1. Hemicellulose extraction samples.

pH values	3.5	4.0	4.5	5.0
Extracted rice straw types	OM5451	OM5451	OM5451	OM5451
	IR50404	IR50404	IR50404	IR50404
	6976	6976	6976	6976
The fixed factors in the extraction experiments:				
Sodium hydroxide concentration (mol/l):	2 M			
Ultrasonication time (min):	30			
Reaction temperature (°C):	90			
Hydrochloric acid concentration (mol/l):	6 M			
Replicates:	3			

2.3. Hemicellulose characterization

Hemicellulose yields:

The yield of pH was determined regarding the reported study and calculated by using Eq. (1) [28]:

$$\text{Yield} = \frac{m_1}{m_0} \text{x}100\% \quad (1)$$

where m_1: the mass of crude hemicellulose; m_0: the mass of extracted rice straw (ERS) employed in above section.

Hemicellulose characteristics:

This study used XRD and TGA to assess hemicellulose characteristics [29, 30]. Hemicelluloses were characterized using FTIR with an Alpha Bruker spectrophotometer with a resolution of 4 cm^{-1} in the range of 400-4500 cm^{-1}.

XRD was performed with an Aeris Benchtop X-ray Diffractometer Malvern PANalytical to investigate the phase and crystallinity of the hemicelluloses, of which the XRD patterns were recorded in the region of 2θ from 5-40° [31].

Thermogravimetric analyses were applied to investigate hemicellulose thermal degradation [32]. In this paper, the thermal decompositions of samples were measured on a TGA instrument Q5000 with temperature ranging from ambient temperature (28°C) to 600°C with nitrogen as the purge gas at a rate of 40 ml/min.

Statistical analysis:

All experiments were performed in triplicate. Data were analysed using a two-way ANOVA to determine the significant differences of variance.

3. Results and discussion

3.1. Hemicellulose extraction

Results of raw hemicellulose yields were showed in Table 2. The total crude hemicellulose obtained varied in the range of 15.12-23.09% for all samples. A two-way ANOVA was used to analyse the hemicellulose yield variance with one dependent variable (yield) and two factors (pH and grains). ANOVA test results showed a statistically significant difference in average hemicellulose yield according to pH values at the 95% significance level ($p<0.05$), whereas there was no significant difference at 95% confidence level between experiments of grains in the same treatment of pH level ($p=0.330$).

Table 2. Hemicellulose yields from three rice straw grains

Classes	pH value			
	3.5	*4.0*	*4.5*	*5.0*
OM5451	18.05 ± 0.07^{a}	23.17 ± 0.48^{b}	20.07 ± 0.29^{c}	15.21 ± 0.32^{d}
IR50404	17.97 ± 0.07^{a}	23.11 ± 0.13^{b}	19.98 ± 0.11^{c}	15.06 ± 0.06^{d}
6976	18.10 ± 0.14^{a}	22.94 ± 0.08^{b}	20.02 ± 0.11^{c}	15.08 ± 0.11^{d}
Average yields	18.04±0.09	23.09±0.23	20.09±0.17	15.12±0.17

Note: F-value: 455.762, CV: 1.3, Means±SE^{a,b,c,d} (i.e 18.05 ± 0.07^{a}) with difference letters are significantly different at 95% confidence level.

Hemicelluloses are soluble in the dilute alkali because of the deprotonated hydroxyl groups on hemicelluloses. The yield of hemicellulose started to increase from 15.12 and 20.09% at pH 5 and pH 4.5, respectively. This could be explained when the pH of the liquid started to decrease, the pronation dominated and hemicellulose precipitation occurred. At pH 4.0, hydroxyl groups on hemicelluloses were neutralized, so the yield of raw hemicellulose was 23.09%. However, at pH 3.5, the average yield of three rice straw grains was 18.04% because the glycosidic bonds of hemicellulose can be broken in an acidic medium and promote hemicellulose degradation with lower pH [33]. The hemicellulose yields can increase from pH 5-4.5 because of the high lignin contents released due to lower pH (Fig. 1) [34].

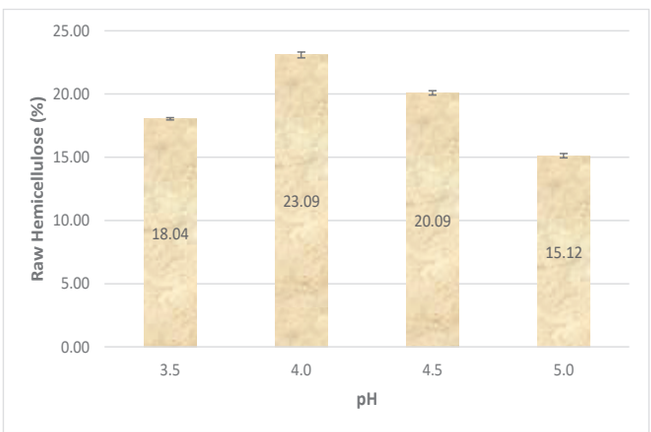

Fig. 1. Effect of pH on the yield of hemicellulose.

3.2. Hemicellulose characteristics

Figure 2 obtained from FTIR shows that the structures of the three hemicelluloses (OM5451, IR50404, 6976) within the spectra of 500-4000 cm^{-1} were similar, but the contents of functional groups were different. The broadbands were between 3453.37 and 3451.76 cm^{-1}, at which signals of hydroxyl groups were present in the hemicellulose components [35]. The presence of

an absorption band at 2362.13 cm^{-1} was understood as the stretching vibrations of O=C=O. The carbonyl stretching region was at 1644.13 cm^{-1} from 1326.54 to 1476.54 cm^{-1}, which was the appearance of OH or CH_2 linkage [36]. As shown in Fig. 2, the typical spectrum region of hemicellulose ranged from 850 to 1200 cm^{-1} encompassing the absorption band at about 1157.71-1159.13 cm^{-1}, which indicated the presence of C–O vibration, while the absorption band at 1093 and 1095 cm^{-1} was that of the C–O–C stretching glycosidic bonds in the xylan groups [37, 38]. The absorption at 471 to nearly 800 cm^{-1} was low because the samples contained lignin components. In general, the three rice straw samples' FTIR spectra had similar functional groups and bands as the hemicelluloses extracted from the different varieties of the rice straw carried out by previous studies mentioned.

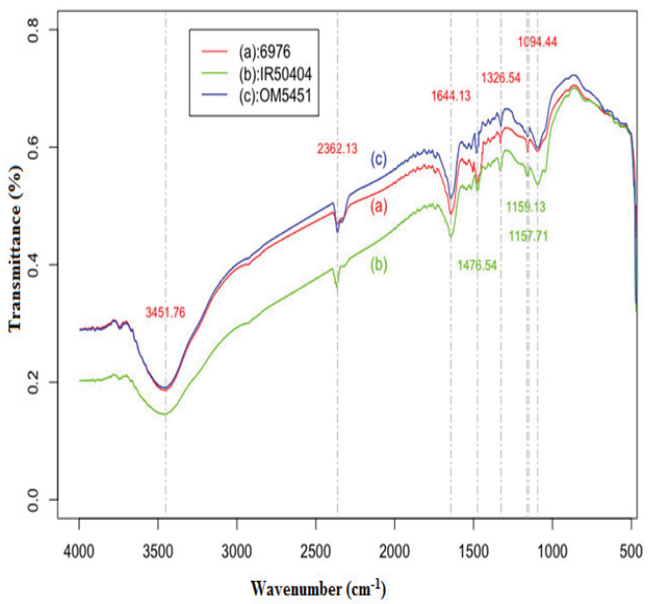

Fig. 2. FTIR spectra of hemicellulose extracted from rice straw.

The XRD patterns (Fig. 3) of the hemicellulose samples had a wide peak at a 2θ angle close to 22°, which indicates the amorphous nature of hemicellulose [39]. The height of the peaks at 2θ=22° was clearly. They had a non-crystalline structure related to their heterogeneous chemical structure [40]. These structures were similar among the samples. Compared to the XRD analysis of hemicelluloses from untreated rice straws investigated by [41], the crystallinity regions of this study were broader.

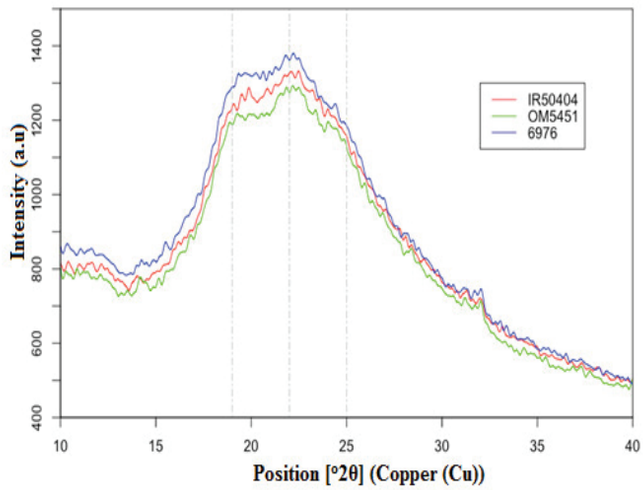

Fig. 3. XRD analysis of rice straw hemicelluloses.

Figure 4 shows the TGA curves of OM5451, IR50404, and 6976, respectively. The initial weight loss at about 50°C was related to the release of moisture in the samples. The decomposition of hemicellulose started easily, with weight loss commonly occurring between 270 and 300°C. The weights of the three samples suddenly decreased from 250 to 300°C. At 280°C, the weight loss of the three samples was approximately 15 to 42%. When the temperature was raised to 400°C, the weight loss reached nearly 53%. The TGA characteristics of the three hemicellulose samples were the same, which were not stable at higher temperatures (>250°C). The experiment outcome indicated that the thermal degradation of rice straw hemicellulose occurred at about 250°C, which agrees with previous studies [42].

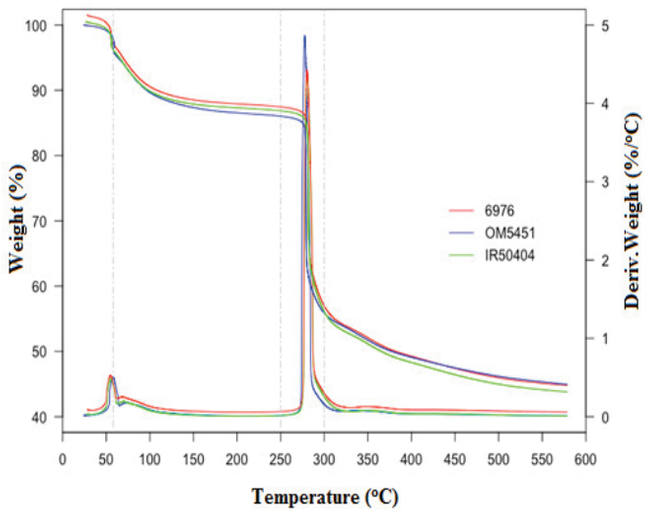

Fig. 4. TGA of rice straw hemicelluloses.

Conclusions

The hemicellulose contents of three rice straws did not significantly differ at each pH. We were able to obtain the highest yield of hemicellulose of 23.09% at pH 4.0. The FTIR results showed lignin in the samples, which could affect the purity of the extracted hemicellulose. XRD revealed the amorphous region was at 2θ=22°. TGA indicated the weight loss of hemicellulose samples was nearly 53% at 400°C. This study is a comprehensive demonstration of hemicellulose in rice straws of common rice grains from the An Giang Province. We highlight that the application of the simple techniques used in our study efficiently extract hemicellulose.

CRediT author statement

Thuy-An Ngo: Conceptualization, Methodology, Software, Writing and Editing; Dao-Chi Vo Thi: Data curation, Writing - Original draft preparation; Nhan-Tanh Nguyen Tran: Conceptualisation, Methodology and Writing.

ACKNOWLEDGEMENTS

This research is funded by Vietnam National University, Ho Chi Minh city (VNU-HCM) under grant number "C2020-16-01".

COMPETING INTERESTS

The authors declare that there is no conflict of interest regarding the publication of this article.

REFERENCES

[1] C. Harada, Y. Nakamura, H. Minato (1999), "Effect of sodium hydroxide treatment of rice straw on cell wall composition and digestibility of dry matter", *Animal Science Journal*, **70(2)**, pp.61-66, DOI: 10.2508/chikusan.70.61.

[2] A. Guzman, S. Delvasto, E. Sanchez (2015), "Valorization of rice straw waste: An alternative ceramic raw material", *Ceramica*, **61**, pp.126-136, DOI: 10.1590/0366-69132015613571888.

[3] T.T. Do (2017), "A review of the role of collectors in Vietnam's rice value network", *Review of Socio-Economic Perspectives*, **2(2)**, pp.85-98, DOI: 10.19275/RSEP019.

[4] T.D. Pham, H. Yoshiro (2015), "Current situation and possibilities of rice straw management in Vietnam", *Semantic Scholar*, pp.1-7.

[5] B. Gadde, S. Bonnet, C. Menke, et al. (2009), "Air pollutant emissions from rice straw open field burning in India, Thailand and the Philippines", *Journal of Environmental Pollution*, **157(5)**, pp.1554-1558, DOI: 10.1016/j.envpol.2009.01.004.

[6] N. Nadiha, B. Jamilah (2020), "Hemicellulose extraction and characterization of rice straw and *Leucaena Leucocephal*a", *Knowledge E Social Sciences*, pp.46-54, DOI: 10.18502/kss.v4i9.7314.

[7] L. Hu, M. Du, J. Zhang (2018), "Hemicellulose based hydrogels present status and application prospects: A brief review", *Open Journal of Forestry*, **8**, pp.13-28, DOI: 10.4236/ojf.2018.81002.

[8] B.C. Saha (2003), "Hemicellulose bioconversion", *Journal of Industrial Microbiology and Biotechnology*, **30(5)**, pp.279-291, DOI: 10.1007/s10295-003-0049-x.

[9] J.P. Patel, P.H. Parsania (2018), "Characterization, testing, and reinforcing materials of biodegradable composites", *Biodegradable and Biocompatible Polymer Composites*, pp.55-79, DOI: 10.1016/B978-0-08-100970-3.00003-1.

[10] S.S. Hanim, A.M.S. Norsafurah (2012), "Physical properties of hemicellulose films from sugarcane bagasse", *Procedia Engineering*, **42**, pp.1390-1395, DOI: 10.1016/j.proeng.2012.07.532.

[11] S.L. Sun, J.L. Wen, M.G. Ma, et al. (2013), "Successive alkali extraction and structural characterization of hemicelluloses from sweet sorghum stem", *Carbohydrate Polymers*, **92(2)**, pp.2224-2231, DOI: 10.1016/j.carbpol.2012.11.098.

[12] C. Froschauer, M. Hummel, M. Lakovlev, et al. (2013), "Separation of hemicellulose and cellulose from wood pulp by means of ionic liquid/cosolvent systems", *Biomacromolecules*, **14(6)**, pp.1741-1750, DOI: 10.1021/bm400106h.

[13] P. Peng, F. Peng, J. Bian, et al. (2011), "Isolation and structural characterization of hemicelluloses from the bamboo species *phyllostachys incarnata* Wen", *Carbohydrate Polymers*, **86(2)**, pp.883-890, DOI: 10.1016/j.carbpol.2011.05.038.

[14] R.J. Stoklosa, D.B. Hodge (2012), "Extraction, recovery, and characterization of hardwood and grass", *Industrial & Engineering Chemistry Research*, **51(34)**, pp.11045-11053, DOI: 10.1021/ie301260w.

[15] C. Wang, C. Tallian, J. Su, et al. (2018), "Ultrasound-assisted extraction of hemicellulose and phenolic compounds from bamboo bast fiber powder", *PLOS ONE*, **13(6)**, DOI: 10.1371/Journal.pone.0197537.

[16] D.V. Ngo, T.H. Tran, D.N. Bui, et al. (2017), "Lignin and cellulose extraction from Vietnam's rice straw using ultrasound-assisted alkaline treatment method", *International Journal of Polymer Science*, **2017(2)**, pp.1-8, DOI: 10.1155/2017/1063695.

[17] R.M. Fuentes, A. Femenia, M.C. Garau, et al. (2016), "Ultrasound-assisted extraction of hemicelluloses from grape pomace using response surface methodology", *Carbohydrate Polymers*, **138**, pp.180-191, DOI: 10.1016/j.carbpol.2015.11.045.

[18] H.V. Vo, N.K. Dang, T.N. Le, et al. (2013), "Assessment of a farmer base network in promoting an integrated farming system at the Mekong delta in Vietnam", *Asian Journal of Agriculture and Development*, **10(1)**, pp.39-58.

[19] D.K. Do (2017), "The technologies to make rice husk into materials", *Vietnam Agriculture Journal*, **23**, pp.23-29 (in Vietnamese).

[20] T.N.C. Truong, T.T.A. Tran, T. Paris, et al. (2015), "Farmers' feedback on rice varieties tested under farmer - managed trials", *Omonrice*, **20**, pp.93-108.

[21] T.M.T. Pham (2019), "Research on emissions inventory for rice straw open burning in An Giang province", *Journal of Science and Technology in Civil Engineering Nuce*, **13(1)**, pp.100-108, DOI: 10.31814/stce.nuce2019-13(1)-10.

[22] N.H. Zulyadi, S.H. Saleh, S.H. Sarijo (2016), "Fractionation of hemicellulose from rice straw by alkaline extraction and ethanol precipitation", *Malaysian Journal of Analytical Sciences*, **20(2)**, pp.329-333, DOI: 10.17576/mjas-2016-2002-15.

[23] T. Song, A. Pranovich, I. Sumerskiy, et al. (2008), "Extraction of galactoglucomannan from spruce wood with pressurised hot water", *Holzforschung*, **62**, pp.659-666, DOI: 10.1515/HF.2008.131.

[24] Z. Jin, K.S. Katsumata, T.B.T. Lam, et al. (2006), "Covalent linkages between cellulose and lignin in cell walls of coniferous and nonconiferous woods", *Biopolymers*, **83(2)**, pp.103-110, DOI: 10.1002/bip.20533.

[25] T.H. Kim, H. Kwak, T.H. Kim, et al. (2020), "Extraction behaviors of lignin and hemicellulose-derived sugars during organosolv fractionation of agricultural residues using a bench-scale ball milling reactor", *Energies*, **13(2)**, pp.1-15, DOI: 10.3390/en13020352.

[26] L.M.F. Bardo, A.G. Cordoba, J.E.L. Galan (2018), "Evaluation of different methods for efficient extraction of hemicelluloses leaves and tops of sugarcan", *Dyna (Medellin, Colombia)*, **85(204)**, pp.18-27, DOI: 10.15446/dyna.v85n204.66626.

[27] A.M. Mansora, J.S. Lima, F.N. Anib, et al. (2019), "Characteristics of cellulose, hemicellulose and lignin of mD2 pineapple biomass", *Chemical Engineering Transactions*, **72**, pp.79-84, DOI: 10.3303/CET1972014.

[28] K. Luo, Y. Wang, H. Xiao, et al. (2019), "Preparation of convertible cellulose from rice straw using combined organosolv fractionation and alkaline bleaching", *Earth and Environmental Science*, **237**, pp.1-6, DOI: 10.1088/1755-1315/237/5/052053.

[29] I. Carrillo, R.T. Mendonca, M. Ago, et al. (2018), "Comparative study of cellulosic components isolated from different eucalyptus species", *Hindawi International Journal of Polymer Science*, **25**, pp.1011-1029, DOI: 10.1007/s10570-018-1653-2.

[30] Z. Ahmad, I. Sopyan, Z. Halim, et al. (2011), "Effect of fiber length variations on properties of coir fiber reinforced cementalbumen composite", *International Islamic University Malaysia (IIUM) Engineering Journal*, **12(1)**, pp.63-76, DOI: 10.31436/iiumej.v12i1.116.

[31] T. Liang, L. Wang (2017), "Thermal treatment of poplar hemicelluloses at 180 to 220°C under nitrogen atmosphere", *BioResources*, **12(1)**, pp.1128-1135, DOI: 10.15376/biores.12.1.1128-1135.

[32] M.V. Ramiah (1970), "Thermogravimetric and differential thermal analysis of cellulose, hemicellulose, and lignin", *Journal of Applied Polymer Science*, **14(5)**, pp.1323-1337, DOI: 10.1002/app.1970.070140518.

[33] S. Mhiri, N. Mignard, M. Abid, et al. (2017), "Thermally reversible and biodegradable polyglycolicacid-based networks", *European Polymer Journal*, **88**, pp.292-310, DOI: 10.1016/j.eurpolymj.2017.01.020.

[34] W. He, P. Fatehi (2015), "Preparation of sulfomethylated softwood kraft lignin as a dispersant for cement admixture", *The Royal Society of Chemistry* (*RSC Advances)*, **58**, pp.1-19, DOI: 10.1039/c5ra04526f.

[35] Y. He, Y. Pang, Y. Liu, et al. (2008), "Physicochemical characterization of rice straw pretreated with sodium hydroxide in the solid state for enhancing biogas production", *Energy & Fuels,* **28(4)**, pp.2775-2781, DOI: 10.1021/ef8000967.

[37] R.C. Suna, J. Tomkinsona, P.L. Mab, et al. (1999), "Comparative study of hemicelluloses from rice straw by alkali and hydrogen peroxide treatments", *Carbohydrate Polymers*, **42(2)**, pp.111-122, DOI: 10.1016/S0144-8617(99)00136-8.

[38] F. Peng, J.L. Ren, F. Xu, et al. (2009), "Comparative study of hemicelluloses obtained by graded ethanol precipitation from sugarcane bagasse", *Journal of Agricultural and Food Chemistry*, **57(14)**, pp.6305-6317.

[39] L. Huang, Z. Yang, M. Li, et al. (2020), "Effect of pre-corrected pH on the carbohydrate hydrolysis of bamboo during hydrothermal pretreatment", *Polymers*, **12(3)**, DOI: 10.3390/polym12030612.

[40] D. Gautam, S. Kumari, B. Ram, et al. (2018), "A new hemicellulose-based adsorbent for malachite green", *Journal of Environmental Chemical Engineering*, **6(4)**, pp.3889-3897, DOI: 10.1016/j.jece.2018.05.029.

[41] Z. Yang, L. Cao, Y. Li, et al. (2020), "Effect of pH on hemicellulose extraction and physicochemical characteristics of solids during hydrothermal pretreatment of eucalyptus", *Bioresources*, **15(3)**, pp.6627-6635, DOI: 10.15376/biores.15.3.6627-6635.

[42] X.N. Nie, J. Liu, D. She, et al. (2013), "Physicochemical and structural characterization of hemicelluloses isolated by different alcohols from rice straw", *Bioresources*, **3(8)**, pp.3817-3832, DOI: 10.15376/biores.8.3.3817-3832.

DOI: 10.31276/VJSTE.64(1).20-26

Off-line ESI-MS/MS profiling of betalains and flavonoid glycosides isolated from (fruit) *Opuntia stricta var. dillenii* and (vegetable) *Atriplex hortensis var. rubra* by countercurrent chromatography

Thi Minh Thu Tran[1, 2*], Thanh Binh Nguyen[1], Peter Winterhalter[1], Gerold Jerz[1]

[1]*Institute of Food Chemistry, Technical University of Braunschweig, 20 Schleinitzstrasse Street, Braunschweig City, Germany*

[2]*Food Technology and Bioengineering Faculty, Cantho University of Technology, Area II, 3/2 Street, Xuan Khanh Ward, Ninh Kieu District, Can Tho City, Vietnam*

Received 23 December 2020; revised 2 March 2021; accepted 19 March 2021

Abstract:

***Opuntia stricta var. dillenii* and *Atriplex hortensis var. rubra,* two plant species with abundant betalain and flavonoid content, were studied by high performance countercurrent chromatography (HPCCC) coupled with ESI-MS/ MS in an off-line detection process. Both CCC runs used *tert.*-butyl-methyl-ether/n-butanol/acetonitrile/water 1% trifluoroacetic acid (v/v/v/v, 2:2:1:5) as a biphasic solvent system within an elution-extrusion mode. The resulting fractions were scanned by an off-line sequential injection to ESI-MS/MS approach. The separation of *Opuntia stricta var. dillenii* extract showed a partial isolation of principal betalains (betanin) from their derivatives (betanidin, phyllocactin, feruloyl-betanin, betaxanthin), degraded products (hydroxyl-neobetanin, mono decarboxy-betanins), and flavonoid glycosides (isorhamnetin-rutinoside, kaempferol-rutinoside). In case of *Atriplex hortensis var. rubra,* this study confirmed the coexistence of several flavonoids (quercetin-Omalonyl glucoside, kaempferol-O-malonyl glucoside) and generated few pure pigment fractions (celosianin II) for structural elucidation. These findings are consistent with earlier research on the use of CCC for the separation of flavonoids and betalain from these two plants. This work also shows that the CCC all-liquid separation technology may be used to recover bioactive chemicals on a larger scale from plant materials of *Atriplex hortensis* and *Opuntia stricta*.**

Keywords: ***Atriplex hortensis var. rubra,* betalains, countercurrent chromatography (CCC), ESI-MS/MS, *Opuntia stricta var. dillenii.***

Classification number: **2.2**

1. Introduction

Red-purple and yellow-orange pigment betalains including betacyanins and betaxanthins are known worldwide as food colorants with positive health properties [1]. This group of pigments abundantly occurs in some families of *Caryophyllales* and their antioxidative effects are numerously reported such as inhibition of tumours (*in-vitro*), reduction of radiation damage [2-6]. Nevertheless, betalains are vulnerable to many exogenic conditions as well as processing techniques such as high temperatures, pH, light, oxygen, and metal ions, etc., making this is a limitation to larger scale betalain recovery and use. The high demand for natural pigments requires innovative research to explore new betalain sources and large-scale purification processes [5-8].

Historically, inorganic silica gel or organic cation-exchangers having high adsorption capacity of plant pigments were used for pigment extraction [9]; however, these resins induce a rapid degradation of labile betalain. Meanwhile, betalain quantification is normally accomplished by UV-Vis spectrophotometry although underestimations and limitations in structural information derived from this method have been reported [10]. The introduction of HPLC-UV-Vis analysis together with LC-MS/MS structural analysis opens a new chapter for betalain investigation [10, 11]. Nevertheless, their unstable nature makes pure betalains (including authentic reference compounds) unavailable and causes problems for comprehensive phytochemical studies [12-16].

All-liquid countercurrent chromatography (CCC) is a robust purification technique that uses a variety of biphasic solvent systems in which complex crude extracts are partially distributed between immiscible solvent phase layers and fractionated according to the polarities of the metabolites. The liquid stationary phase layer is kept

*Corresponding author: Email: ttmthu@ctuet.edu.vn

on the coil system due to a strong Archimedean screw force. CCC is a method consisting of multiple continuous liquid-liquid extraction processes and has been widely applied to larger-scale separations of metabolites from various natural product classes. In general, this method of liquid chromatography prevents irreversible sample loss that occurs in solid chromatography; therefore, it is gentle enough for sensitive compounds like the natural pigments betalain and carotenoid [17-19]. Moreover, a variety of available operation modes allow CCC to be flexible for many samples (in term of polarities) and the solvent system has the capability to connect up-to-date monitoring methods such as UV-Vis, ESI-MS/MS, or ACPI-MS/MS. For instance, the combination of CCC with ESI-MS/MS profiling technique has been applied in the discovery many bioactive compounds such as flavonoids, propolis metabolites, and betacyanins from *Impatiens glandulifera Royle* flowers, Saudi-Arabian propolis metabolites, and *Bougainvillea glabra* flowers, respectively [20-22].

In this study, the pre-purified pigment extracts from the cactus fruits of *Opuntia stricta var. dillenii (Opuntia)* and vegetable leaves from *Atriplex hortensis var. rubra* (*Atriplex*) were fractionated by high performance CCC (HPCCC) using the ion-pair solvent system of *tert*.-butyl-methyl-ether/n-butanol/acetonitrile/water,trifluoroacetic acid (TBMe/n-BuOH/ACN/water) (v/v/v/v, 2:2:1:5, 1% TFA). The recovered fractions were selected and monitored by off-line sequential injections to the ESI-MS/MS for the direct identification of eluting betalain pigments and flavonoid glycosides from each cultivar.

2. Material and method

2.1. Samples and chemicals

Samples: Opuntia stricta var. dellini (fruit, Egypt) and *Atriplex hortensis var. rubra* (leaves, Germany) were harvested and stored below -20ºC in dark until analysis.

Chemical: acetonitrile (ACN, LC-MS and HPLC grade, honeywell-Germany), formic acid (LC-MS grade, Sigma-Aldrich-Germany), C18 resin for pigment enrichment (40-63 µm pore, Merck), acetic acid (AcOH ≥ 99.8%, Sigma), ethanol (EtOH, HPLC grade, Sigma). Nanopure water (0.2 µm spore, Wilhelm Werner, Leverkusen). *Tert.*-butyl-methyl-ether and n-butanol (TBMe and n-BuOH, HPLC grade, Honeywell); trifluoroacetic acid (TFA, 99%, Sigma-Aldrich-Germany); propionic acid (LC-MS grade, Sigma-Aldrich-Germany).

2.2. Pigment extraction and enrichment

Extraction: Each material was treated separately by a similar processing protocol. Briefly, the frozen materials were blended before maceration several times with solvents. Five hundred grams of *Opuntia* was extracted with 1 l ACN:water 0.7% AcOH (1:9, v:v) while 250 g *Atriplex* was extracted with 0.5 l ACN:water (1:1, v:v). The crude extracts were filtered by cotton and paper filters before enrichment by 500 g C18 material in the next step. These steps were done quickly in the dark at room temperature to limit betalain degradation.

Betalain enrichment by C18 adsorption: Reversed phase C18 resin was cleaned (three times) by 0.5 l ACN then conditioned (four times) by 0.5 l aqueous AcOH 0.7%. The activated resin was then incubated with each crude extract for 1 h. The pigmented resin was rinsed several times with AcOH 0.7% to remove un-adsorbed sugar, acids, amino acid, etc. The pigment desorption was done by incubating the colored resin with 0.5 l EtOH:AcOH 0.7% (v/v, 2:8) until the purple color was completely released. The colored supernatants were combined, filtered, and immediately freeze dried. The dried powders were stored in the dark at -20ºC to prevent pigment degradation before CCC experiments.

2.3. HPCCC operation and offline ESI-MS/MS flow-injection analysis

HPCCC apparatus: The two separations were done on a J-type HPCCC model (Dynamic Extractions, Gwent, UK) that was fabricated with two-connected semi-preparative polytetrafluoroethylene coil columns (total volume of 63+62.5 ml, 1.6 mm internal diameter tube). These columns were mounted on a two-bobbin system. The machine allowed a maximum speed of 1600 rpm under stable temperatures. During operation, the temperature was kept at 30ºC by an external cooling system. The system used a preparative LC pump for solvent delivery.

HPCCC operation: The biphasic solvent system of TBMe/1-BuOH/ACN/water/TFA (0.1%) (v/v/v/v, 2:2:1:5) was poured sequentially into a separatory funnel (at 20ºC) before being mixed vigorously until equilibrium was reached. The system was left to form two clear layers (upper layer or organic layer worked as stationary phase while lower layer or aqueous layer used as mobile phase), which were then collected separately and de-gassed shortly before use. In this study of betalains, the '*head to*

tail' and '*elution - extrusion*' modes were applied. Briefly, the stationary phase was firstly pumped to fill the 125-ml coil column. Then, the HPCCC was set to maximum rotation at 1600 rpm. When the temperature reached 30°C, 4 ml/min mobile phase was delivered to the system until only the mobile phase was released (hydrodynamic equilibrium condition). The *stationary phase retention value* S_f was calculated by the ratio of *stationary phase volume* V_S (retained in the system at equilibrium) divided by the *column coil volume* V_C.

Sample preparation and injections: Two separations were performed using lyophilized enriched pigment extract (500 mg *Opuntia* and 460 mg *Atriplex*). For each separation, the sample was dissolved in 5 ml of biphasic solvent mixture (2.5 ml aqueous phase and 2.5 ml organic phase), de-gassed, and then filtered (Chromafil Xtra GF-100/25, Macherey & Nagel, Düren, Germany) before delivered into a 5 ml injection loop. When the CCC system was stable at 30ºC, a low-pressure injection port (Reodyne, Cotati, CA, USA) was used to inject the sample into the system to begin the separation. The released fractions were collected at 1 min intervals by a Superfrac (Pharmacia, Uppsala, Sweden) fraction collector. The stationary phase was replaced after the mobile phase passed two coil volumes (approximately 250 ml). The separation was complete when one-coil volume of stationary phase (around 125 ml) was carried through.

ESI-MS/MS profiling by sequential offline injection of collected fractions: For every HPCCC separation, an exact amount of each collected fraction was sequentially injected to the ESI ion trap-MS/MS system (HCT-Ultra ETD II, Bruker Daltonics, Bremen, Germany) through an AS-2000A auto-sampler device (Merck-Hitachi, Japan). For preparation, 300 µl of each fraction was diluted with 1 ml make-up solvent (ACN:water:formic acid (0.1%), v:v, 50:50) and 20 µl propionic acid into a single HPLC vial. Propionic acid was used to eliminate the strong ESI-MS ion signal quenching effect of TFA in the HPCCC fractions. The same volume from each vial (10 µl depending on initial concentration) was injected sequentially into the ESI-MS/MS system within 2 min time intervals to generate a 'mass' selective chromatography profile in the positive ionization mode. Each injection was pumped together with 0.5 ml/min make-up solvent by a binary HPLC-pump (G1312 A, 1100 Series, Agilent Technologies, Waldbronn, Germany). For each ESI-MS/MS injection profile, a base peak ion intensity around 1.0×10^6- to 10^8 was necessary for the relevant ion intensity of a single peak.

ESI-MS/MS set up: ESI detection was set to alternating ionization mode, the *m/z* scan range was 100-2000, the "ultra"-mode and mass scanning rate were 26.000 *m/z* per second, 10.0 l/min nitrogen was used at 320°C for the drying gas, and the nebuliser pressure was set at 60 psi. The high ionization voltage (HV) capillary was -3500 V, HV end plate offset was -500 V, trap drive 79.2, octopole radiofrequency (RF) amplitude was 187.1 V_{pp}, lens 2 60.0 V, Cap Ex 115.0 V, and maximum accumulation time 200 ms. Other notable parameters include averages of five spectra, trap drive level 120%, target mass range *m/z* 500, compound stability 80%, Smart ICC target 100000, ICC charge control "on" and smart parameter setting "active". The most intensive precursor ions (5 to 7 ions) were selected for fragmentation. The remaining MS/MS fragmentation amplitude value was 1 V.

Betalains and flavonoid glycosides identification: The identification of betalains and flavonoid glycosides from each separation were done based on ESI-MS/MS data of the compounds (summarized in Tables 1 and 2) in comparison to that of standard compounds found in literature.

3. Results and discussion

3.1. HPCCC-off-line ESI-MS/MS profile of Opuntia pigment extract

There were many studies to compare the bioactivities of the most common prickly pear metabolites, which indicate that pigments and flavonoid glycosides from *Opuntia stricta* show the highest antioxidant activities, especially that of *Opuntia dillenii* [23, 24]. Therefore, this prompted us to investigate the pigment and polyphenolic metabolites of this cultivar for a potential process for natural pigment. The hyphenation of preparative HPCCC with an off-line ESI-MS/MS as the molecular-weight-visualization method enabled the fractionation and identification of around 500 mg of pre-cleaned pigment extract. In general, the colored betalains were nicely fractionated from non-colored flavonoid glycosides. From there, a few minor pigments and degradation products were significantly concentrated into a few fractions although they were not detected in the crude extract by LC-ESI-MS (data not shown). Table 1 summarizes the principle phytochemistry from *Opuntia fruits* pigment

extract and their MS data elucidated from this study. Fig. 1 illustrates the dried sequential injected vials (upper) and the generated injection ESI-MS/MS profile (lower) of this HPCCC run with selected single ion traces.

Table 1. ESI-MS/MS data of betalains in *Opuntia stricta var. dillenii* fruits (positive ionization mode).

No	*m/z*	MS^2	Compounds	References
1	551	389	15*S*/15*R* betanin 15*S*/15*R* gomphrenin	[11-16]
2	637	551, 389	15*S*/15*R* phyllocactin	[11-16]
3	568	549, 387	Hydroxyl-neobetanin	[25-27]
4	309	263	Indicaxanthin	[14]
5	689	645, 603	Unknown	
6	389	345	15*S*/15*R* betanidin	[11-16]
7	625	317, 257, 479	(Isorhamnetin-O-rutinoside	[26]
8	595	449, 287	Kaempferol-O-rutinoside	[26]
9	506	268	Unknown	
10	620	602, 342	Unknown	
11	563	-	Unknown	
-	727	389	15*S*/15*R* feruloyl betanin	[26]
-	507	345	Degraded betacyanins (mono decarboxy-betanins)	[11-16, 25]
-	358	196, 150	Degraded betacyanins (cyclo-dopa 5-O-β-glucoside)	[11-16, 25]

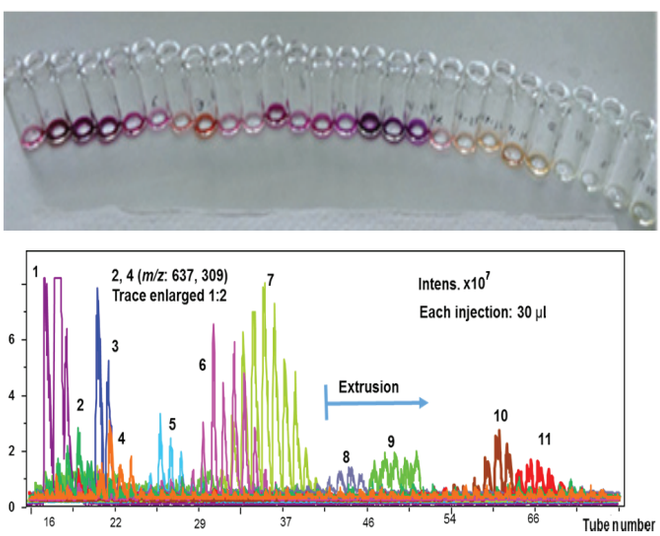

Fig. 1. The dried sequential injected vials and sequential ESI-MS/MS off-line injection profile of C18 purified *Opuntia* pigment extract fractionated by preparative HPCCC (pos. ionization mode) with visualized selected single target ion traces (*m/z* 100-1500).

The diastereomeric pair *15S/15R* betanin (**1**) in Fig. 1 eluted initially at low retention volumes (fraction 15) after the so-called break-through of solvents until fraction 14. Subsequently, they appeared as the most intensive ion signal with $[M+H]^+$ at *m/z* 551 in the initial fractions 16 to 18 together with cyclo-dopa-5-O-β-glucoside (*m/z* 358), which is one precursor molecular of betanin. On the other hand, traces of betalamic acid ($[M+H]^+$ at *m/z* 212), the other betanin precursor, appeared later at larger elution volumes and apart in tube 46 to 50 (data not shown in Fig. 1). Similarly, the three most abundant degradation products of betanin, including neobetanin (or dehydro betanin, $[M+H]^+$ at *m/z* 549), mono decarboxy betanin ($[M+H]^+$ at *m/z* 507), and decarboxy neobetanin (*m/z* 505), were also found in traces within these initial tubes fractions. These degraded products of betanin mixed together made a distinct dark red color for fraction 14. Interestingly, these red compounds or betanin artifacts were not detected in the *Opuntia dillenii* crude extract scanned by LC-ESI-MS experiment before (data not shown). The presence of betanin artifacts in these HPCCC fractions suggest that the separation process could provoke pigment degradation. These degradative effects were seen in previous works on betalain purification using the CCC technique as an usual result of processing steps by impacts of solvents, oxygen contact, and separation time [25, 27].

The ESI-MS/MS data of the following fractions from tube 18-21 showed high concentrations of phyllocactin epimeric mixture (**2**, *15S/15R*). These epimers were partly fractionated from the betanin epimers. The higher elution time, and therefore higher affinity to the liquid stationary phase, could be related to the slightly decreased polarity of phyllocactin by the malonyl-substitution at the glucose unit. The strong ion signal of **3** (*m/z* 568), indicating a neobetanin derivative, was found close to **2** (tube 21 and 22). This compound was reported before as hydroxy-neobetanin, which is a neobetanin structured with an additional hydroxyl group bound to the C14-C15 double bond (K.M. Herbach, et al. (2005) [25]). This red derivative was well separated from betanins although it mixed with phyllocactins. Betanidin epimers (**6,** *m/z* 389), the aglycone of betanin, were either eluted at much longer elution times or much later than betanins (from tube 31 to 37) in this HPCCC run. This could be related to the neutral loss Δm/z 162, which was identical to the cut-off of one glucose unit from betanin structure. Thus, the missing hydrophilic glucose group implies that betanidin

is more lipophilic and remained longer in the organic stationary phase. These later fractions also carried more polar epimers of *15S/15R* feruloyl-betanin (*m/z* 727, MS^2 389), which could be identified as lampranthin II or gomphrenin III based on a neutral loss cleavage of the feruloyl unit (Δm/z 176). These betacyanin derivatives have been seen in *O. ficus indica* before [26]. Surprisingly, Jerz, et al. (2013) [26] detected very polar betanidin 5-O-β-sophoroside epimers (*15S/15R, m/z* 713, MS/MS 389) from their IPHSCCC purification of *O. ficus* pigments while these compounds were not found in this study of *O. stricta*. Moreover, *15S/15R* hylocerenins (*m/z* 695, MS/MS 389) are typical cactus betacyanins but were not recognized in these separations, which is in agreement with the report of Jerz, et al. (2013) [26] on *O. ficus* pigments using CCC technique.

Beside betacyanins, the only betaxanthin found after the C18 cleaning step was indicaxanthin (**4**, *m/z* 309). This yellow pigment was isolated completely from the purple betanin although it was partly mixed with a neobetanin derivative (**3**). Meanwhile, isorhamnetin-rutinoside and kaempferol-O-rutinoside (**7**, *m/z* 625, MS/MS 317 and **8**, *m/z* 595, MS/MS 287, respectively) were seen as the two major concentrated flavonoid glycosides from the extract and they eluted apart from each other. However, **7** partly mixed with betanidin (**6**). Interestingly, there were several novel minor concentrated compounds, namely, **5**, **9**, **10,** and **11,** which were detected by higher ion intensities in the extrusion mode (from fraction 42 to the end). These structures could be metabolites from the fruits that need further CCC studies to verify. In general, this HPCCC off-line ESI-MS/MS approach could partly purify the pigment betanin from its derivatives and flavonoid glycosides, resulting in some fractions of a few pure *15S/15R*-betanin and isorhamnetin-rutinoside for further NMR experiments (NMR data not shown).

3.2. HPCCC off-line ESI-MS/MS profile of Atriplex pigments extract

Atriplex hortensis var. rubra is known for its high content of celosianin II and flavonoid glycosides (particularly sulphated flavonoids), which gives the plant its typical purple color and shows a strong antioxidant capacity [28]. The HPCCC run of this enriched *Atriplex* pigment and polyphenol extract was performed using the same procedure as the *Opuntia* pigment above. As a result, the pigments (betalains) and non-pigmented compounds (flavonoids) were effectively fractionated. Table 2 summarizes the principle compounds elucidated from this separation and their MS/MS data. Fig. 2 indicates the adjusted ESI-MS/MS profile of recovered fractions eluting from this HPCCC run, which is displayed by selected single ion traces using the positive ionization mode.

Table 2. ESI-MS/MS data of betalains and flavonoids from *Atriplex* leaves (positive ionization mode).

No	*m/z*	MS^2	Compounds	References
1	727	551, 389	*15S/15R* amaranthin	[11-17, 29]
2	551	389	*15S/15R* betanin	[11-17, 29]
3	903	551, 389	*15S/15R* celosianin II ((2”-O-E-feruloyl)-amaranthine)	[28, 29]
4	551	302.7	Quercetin-O-malonyl glucoside	[22, 28, 29]
5	535	287	Kaempferol-O-malonyl glucoside	[22, 28, 29]
6	419	287	Kaempferol-O-pentoside	[22, 28, 29]
7	499	367, 287	Kaempferol-3-O-sulphate-7-O α-arabinopyranoside	[22, 28, 29]
-	265	248, 177	Unknown	
-	611	455, 302.7	Quercetin-rhamnose-glucose	[22, 28, 29]
-	667	535, 287	Kaempferol-arabino-glucose-malonyl	[22, 28, 29]
-	595	449, 287	Kaempferol-rhamnose-glucose	[22, 28, 29]

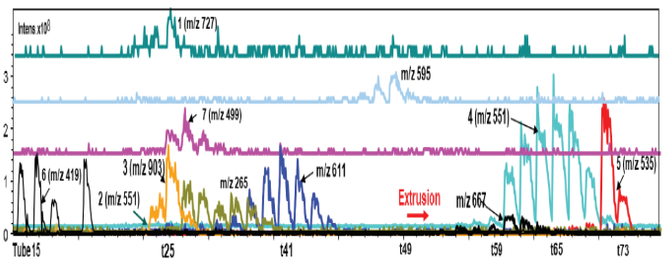

Fig. 2. Adjusted off-line ESI-MS/MS profile of *Atriplex* pigment extract eluted from HPCCC (possitive ionization mode).

The high content of the epimeric mixture of celosianin II (*15S/15R-(2”-O-E-feruloyl)-amaranthine*, (**3**), was represented by a strong molecular ion signal $[M+H]^+$ at *m/z* 903. In contrast, celosianin I, a typical betacyanin from this cultivar, was not found. Meanwhile, signals from amaranthin (*15S/15R*, **1**, *m/z* 727) and betanin (*15S/15R*, **2**, *m/z* 551) were found only in trace amounts. Similarly, these betacyanins were identified by the abundant fragmented ion signals at *m/z* 551 (betanin) and *m/z* 389 (betanidin). As can be seen from the profile, amaranthin (**1**) started eluting early, followed by betanin (**2**), then celosianin II (**3**) in which (**3**) was apart from (**2**) but (**3**) mixed completely with (**1**). Because celosianin II was recovered in some specific fraction, a few fractions were selected for NMR structural elucidation (data not shown). Notably, the degraded betacyanins, together

with the unidentified pigment (traces, *m/z* 889), have been found before within the HSCCC run of *Atriplex* extract but they were not detected in this HPCCC run [29]. This indicates the lighter effect of this new HPCCC approach to vulnerable betalains as compared to the HSCCC approach.

In addition to the pigments, these initial HPCCC fractions also contained the hydrophilic flavonoid glycosides kaempferol 3-O-sulphate-7-O α-arabinopyranoside (**7**, *m/z* 499) and kaempferol-O-pentoside (**6**, *m/z* 419). These two kaempferol derivatives were identified based on their MS/MS fragmentation signal at *m/z* 287 and their sulphated linkage, which makes the structure more polar and better bound to the mobile phase. While compound **6** appeared far away from amaranthin and celosianin II, flavonoid **7** was partly co-eluted with both of these major pigments. On the other hand, some flavonoid-O-glycosides appeared to be slightly more lipophilic and concentrated in the stationary phase within the *extrusion-mode*. For instance, there was effective fractionation of quercetin-O-malonyl-glucoside (**4**, *m/z* 551) and kaempferol-O-malonyl glucoside (**5**, *m/z* 535) from the rest of compounds and from each other. This is because they were the two flavonoid glycosides released at the end of the separation, which indicates their low polarities. Besides, the 'unknown' structures $[M+H]^+$ at *m/z* 265 and *m/z* 611 were also partly fractionated from each other and from the pigments since they came in the middle of the MS profile. However, their quantities were not sufficient for further investigation by NMR experiments. Therefore, their structural identification was tentatively accomplished by comparisons with the flavonoid MS/MS fragmentation data available in literature [22, 28, 29]. Similarly, kaempferol-O-rhamnosyl-O-glucoside (*m/z* 595) was well isolated and concentrated in several center fractions of the HPCCC while kaempferol-O-arabinosyl-O-malonyl-glucoside (*m/z* 667) was completely co-eluted with part of major compound **4** in several early fractions within *extrusion-mode* (the recovered amount was limited). These end fractions of *extrusion* also contained traces of other unknown ion signals at *m/z* 565, 435, etc. (data not shown), which were supposed to be flavonoid glycosides based on MS/MS fragmentation and indicative of neutral loss differences, namely, Δ*m/z* 86, Δ*m/z* 80, Δ*m/z* 132, and Δ*m/z* 146 representing malonyl, sulphate, pentose, and desoxy-hexose, respectively.

Recently, the similar application of LC-MS/MS coupled with IPHPCCC to investigate the whole betalain metabolome of Vietnamese red dragon fruit (*Hylocereus polyrhizus*) was reported [30]. While this ESI - MS/MS profiling and IPHPCCC method was used to study the polar metabolites from of *Opuntia stricta var. dillenii* in detail, analytical and semi-preparative IPHPCCC separations were done to compare and evaluate the reproductivity of the method [31].

4. Conclusions

This report contributes to the basic phytochemical knowledge of betalains and flavonoid constituents of *Atriplex hortensis var. Rubra* and *Opuntia stricta var. dillenii* by application of the all-liquid chromatography technique HPCCC. The off-line hypenation of semi-preparative HPCCC separations with the sensitive ESI-MS/MS profiling was able to fractionate principal pigments from its derivatives and from most of the flavonoids glycosides. This approach supplies molecular weight data and fragmentation data of all ionizable molecules available in every single injected HPCCC fraction. From then, the compounds of interest can be directly pooled for further analysis. These results are in agreement with previous studies about the applications of CCC on betalain and flavonoid purification from these two plants. This work also demonstrates the potential for larger scale recoveries of bioactive compounds from plant materials of *Atriplex hortensis* and *Opuntia stricta* using CCC all-liquid separation methodology.

CRediT author statement

Thi Minh Thu Tran: Conceptualisation, Writing and Editing; Thanh Binh Nguyen: Conceptualisation, Methodology, Writing and Editing; Peter Winterhalter: Conceptualisation, Methodology, Writing and Editing; Gerold Jerz: Conceptualisation, Data curation, Reviewing.

COMPETING INTERESTS

The authors declare that there is no conflict of interest regarding the publication of this article.

REFERENCES

[1] K.M. Herbach, F.C. Stintzing, R. Carle (2006), "Betalain stability and degradation - structural and chromatic aspects", *Journal of Food Science*, **71(4)**, pp.41-50, DOI: 10.1111/j.1750-3841.2006.00022.x.

[2] G.T. Sigurdson, P. Tang, M.M. Giusti (2017), "Natural colorants - food colorants from natural sources", *Annual Review Food Science Technology*, **8**, pp.261-280, DOI: 10.1146/annurev-food-030216-025923.

[3] F.C. Stintzing, K.M. Herbach, M.R. Mosshammer, et al. (2008), "Betalain pigments and color quality", *ACS Symposium Series*, **983**, pp.82-101, DOI: 10.1021/bk-2008-0983.ch007.

[4] I.B. Slimen, T. Najar, M. Abderrabba (2017), "Chemical and antioxidant properties of betalains", *Journal of Agricultural and Food Chemistry*, **65(4)**, pp.675-689, DOI: 10.1021/acs.jafc.6b04208.

[5] H. Azeredo (2009), "Betalains: Properties, sources, applications, and stability - a review", *International Journal of Food Science Technology*, **44(12)**, pp.2365-2376, DOI: 10.1111/j.1365-2621.2007.01668.x.

[6] F.C. Stintzing, R. Carle (2004), "Functional properties of anthocyanins and betalains in plants, food, and in human nutrition", *Trends in Food Science and Technology*, **15**, pp.19-38, DOI: 10.1016/j.tifs.2003.07.004.

[7] A. Downham, P. Collins (2000), "Colouring our foods in the last and next millennium", *International Journal of Food Science and Technology*, **35**, pp.5-22, DOI: 10.1046/j.1365-2621.2000.00373.x.

[8] J.A. Fernandez-lopez, P.J. Gimenez, J.M. Angosto, et al. (2012), "A process of recovery of a natural yellow colourant from *Opuntia* fruits", *Food Technology and Biotechnology*, **50(2)**, pp.246-251.

[9] A.T. Serra, J. Poejo, A.A. Matias, et al. (2013), "Evaluation of *Opuntia spp*. derived products as antiproliferative agents in human colon cancer cell line (HT29)", *Food Research International*, **54(1)**, pp.892-901, DOI: 10.1016/j.foodres.2013.08.043.

[10] S.J. Schwartz, B.E. Hildenbrand, J.H. Elbe (1981), "Comparison of spectrophotometric and HPLC methods to quantify betacyanins", *Journal of Food Science*, **46(1)**, pp.296-297, DOI: 10.1111/j.1365-2621.1981.tb14587.x.

[11] F.C. Stintzing, A. Schieber, R. Carle (2003), "Evaluation of colour properties and chemical quality parameters of cactus juices", *European Food Research and Technology*, **213(4)**, pp.303-311, DOI: 10.1007/s00217-002-0657-0.

[12] F.C. Stintzing, R. Carle (2007), "Betalains - emerging prospects for food scientists", *Trends in Food Science and Technology*, **18(10)**, pp.514-525, DOI: 10.1016/j.tifs.2007.04.012.

[13] F.C. Stintzing, J. Conrad, I. Klaiber, et al. (2004), "Structural investigations on betacyanin pigments by LC NMR and 2D NMR spectroscopy", *Phytochemistry*, **65**, pp.415-422, DOI: 10.1016/j.phytochem.2003.10.029.

[14] F.C. Stintzing, F. Kugler, R. Carle, et al. (2006), "First ^{13}C-NMR assignments of betaxanthins", *Helvetica Chimica Acta*, **89**, pp.1008-1016, DOI: 10.1002/hlca.200690077.

[15] S. Wybraniec, B. Nowak-Wydra, Y. Mizrahi (2006), "^{1}H and ^{13}C NMR spectroscopic structural elucidation of new decarboxylated betacyanins", *Tetrahedron Letter*, **47**, pp.1725-1728, DOI: 10.1016/j.tetlet.2006.01.046.

[16] S. Wybraniec, Y. Mizrahi (2002), "Fruit flesh betacyanin pigments in *Hylocereus* cacti", *Journal of Agricultural and Food Chemistry*, **50**, pp.6086-6089, DOI: 10.1021/jf020145k.

[17] P. Winterhalter (2007), "Application of countercurrent chromatography (CCC) to the analysis of natural pigments", *Trends in Food Science and Technology*, **18(10)**, pp.507-513, DOI: 10.1016/j.tifs.2007.04.013.

[18] A. Marston, K. Hostettmann (2006), "Developments in the application of counter-current chromatography to plant analysis", *Journal of Chromatography A*, **1112(1-2)**, pp.181-194, DOI: 10.1016/j.chroma.2005.10.018.

[19] Y. Ito (2005), "Golden rules and pitfalls in selecting optimum conditions for high-speed counter-current chromatography", *Journal of Chromatography A*, **1065(2)**, pp.145-168, DOI: 10.1016/j.chroma.2004.12.044.

[20] G. Jerz, S. Wybraniec, N. Gebers, et al. (2010), "Target-guided separation of *Bougainvillea glabra* betacyanins by direct coupling of preparative ion-pair high-speed countercurrent chromatography and electrospray ionization mass-spectrometry", *Journal of Chromatography A*, **1217(27)**, pp.4544-4554, DOI: 10.1016/j.chroma.2010.04.061.

[21] G. Jerz, Y.A. Elnakady, A. Braun, et al. (2014), "Preparative massspectrometry profiling of bioactive metabolites in Saudi-Arabian propolis fractionated by high-speed countercurrent chromatography and off-line atmospheric pressure chemical ionization massspectrometry injection", *Journal of Chromatography A*, **1347**, pp.17-29, DOI: 10.1016/j.chroma.2014.04.068.

[22] M.N. Vieira, P. Winterhalter, G. Jerz (2016), "Flavonoids from the flowers of *Impatiens glandulifera Royle* isolated by high performance countercurrent chromatography", *Phytochemical Analysis*, **27(2)**, pp.116-125, DOI: 10.1002/pca.2606.

[23] D.M. Jimenez-Aguilar, H. Mujica-Paz, J. Welti-Chanes (2014), "Phytochemical characterization of prickly pear (*Opuntia spp*.) and of its nutritional and functional properties: A review", *Current Nutrition & Food Science*, **10(1)**, pp.57-69, DOI: 10.2174/1573401310011403281209 52.

[24] O. Osorio-Esquivel, A. Ortiz-Moreno, V.B. Alvarez, et al. (2011), "Phenolics, betacyanins and antioxidant activity in *Opuntia joconostle* fruits", *Food Research International*, **44(7)**, pp.2160-2168, DOI: 10.1016/j.foodres.2011.02.011.

[25] K.M. Herbach, F.C. Stintzing, R. Carle (2005), "Identification of heat-induced degradation products from purified betanin, phyllocactin and hylocerenin by high-performance liquid chromatography/electrospray ionization mass spectrometry", *Rapid Communications in Mass Spectrometrty*, **19**, pp.2603-2616, DOI: 10.1002/rcm.2103.

[26] G. Jerz, B. Klose, S. Wybraniec, et al. (2013), "Preparative separation and pigment profiling of betalains from fruits of *Opuntia ficus* by ion-pair high-speed countercurrent chromatography (IP-HSCCC) and off-line LC-ESIMS/MS", *Tropical and Subtropical Fruits: Flavors, Color, and Health Benefits*, ACS Symposium Series, pp.3-27, DOI: 10.1021/bk-2013-1129.

[27] S. Wybraniec, P. Stalica, G. Jerz, et al. (2009), "Separation of polar betalain pigments from cacti fruits of *Hylocereus polyrhizus* by ion-pair high-speed countercurrent chromatography", *Journal of Chromatography A*, **1216(41)**, pp.6890-6899, DOI: 10.1016/j.chroma.2009.08.035.

[28] W. Bylka, M. Stobiecki, R. Frahski (2001), "Sulphated flavonoid glycosides from leaves of *Atriplex hortensis*", *Acta Physiologiae Plantarum*, **23(3)**, pp.285-290, DOI: 10.1007/s11738-001-0035-8.

[29] G. Jerz, N. Gebers, P. Stalica, et al. (2008), "Preparative isolation of polar and acylated betalains from Atriplex hortensis var. rubra by ion-pair high-speed countercurrent chromatography (IP-HSCCC)", Conference Materials, *Institute of Inorganic Chemistry and Technology*, pp.38-41, https://suw.biblos.pk.edu.pl/resourceDetailsBPP&rId=35752, accessed 18 August 2020.

[30] T.T.M. Thu, G. Jerz, P. Winterhalter (2019), "The application of ion-pair high performance countercurrent chromatography monitored by off-line LC-ESI-MS/MS injections to study betalain metabolite from Vietnamese red dragon fruit (*Hylocereus polyrhizus*)", *Vietnam J. Chem.*, **57(5)**, pp.531-537, DOI: 10.1002/vjch.201900049.

[31] T.M.T. Tran, B.N. Thanh, T.E. Moussa-Ayoub, et al. (2019), "Profiling of polar metabolites in fruits of *Opuntia stricta var. dillenii* by ion-pair high-performance countercurrent chromatography and off-line electrospray mass-spectrometry injection", *Journal of Chromatography A*, **1601**, pp.274-287, DOI: 10.1016/j.chroma.2019.06.009.

Chemical composition and antioxidant properties of ivy gourd (*Coccinia grandis*) wines prepared with different pretreatment techniques

Trang T. Dang[1, 2], Thanh T.H. Le[1, 2], Ngoc Lieu Le[1, 2*]

[1]*International University, Area 6, Linh Trung Ward, Thu Duc City, Ho Chi Minh City, Vietnam*
[2]*Vietnam National University - Ho Chi Minh City, Area 6, Linh Trung Ward, Thu Duc City, Ho Chi Minh City, Vietnam*

Received 14 December 2020; revised 19 February 2021; accepted 3 March 2021

Abstract:

Ivy gourd (*Coccinia grandis*), which is said to possess a variety of health benefits, may find use in the food processing sector. Numerous alkaloids, flavonoids, tannins, steroids, glycosides, saponins, ellagic acid, and triterpenoids have all been reported to be present in the plant. This study proposes the winemaking of ivy gourd and investigates the influence of microwave, thermovinification, and enzymatic pretreatments on the total flavonoid content (TFC), total phenolic content (TPC), and antioxidant capacity of the wines. The results showed that the pretreatments had no negative effects on the chemical composition of the products. Instead, there were positive changes in antioxidant content and activities when different processing techniques were employed. The wines pre-treated with enzymatic treatment contained much higher TPC (up to 39.37 µg GAE/ml), TFC (18.61 µg CE/ml), and 1,1-diphenyl-2-picrylhydrazyl (DPPH) radical scavenging activity (28.98 µg AAE/ml) than the untreated wines. Microwave and thermovinification also exhibited positive effects but to lesser extents. A fermentation process helped increase the TPC and antioxidant capacity of the wine samples while reducing their TFC values as compared to those of the musts.

Keywords: **antioxidant, chemical composition, fermentation, flavonoid content, ivy gourd fruits, phenolic content.**

Classification numbers: **2.2, 3.5**

1. Introduction

Reported to contain numerous beneficial health compounds, ivy gourd (*Coccinia grandis*) can potentially be utilised in the food processing industry. The plant has been known to provide a variety of alkaloids, flavonoids, tannins, steroids, glycosides, saponins, ellagic acid, and triterpenoids [1]. Along with phytonutrients, the fruit also contains a certain amount of pectin that is considered as important as soluble fiber, which control lipid concentrations in human body. Due to its prominent nutritional content and properties, ivy gourd fruit has been used and studied as medicine for the treatment of diabetes [2, 3]. Though beneficial for human health and readily available as a raw ingredient, the fruit has not been made use of and thus remains unfamiliar to most consumers. In order to promote and enhance its usage, this research aims to study the wine fermentation of ivy gourd fruit and assess its antioxidant content and capacity.

One of the most concerning matters in fruit wine processing is nutritional quality. Some studies have shown that the nutritional benefits of wines not only depend on types of fruits but are also strongly affected by winemaking techniques [4]. Some winemaking techniques have been reported to increase the phenolic concentration such as high-temperature fermentation, thermovinification, must freezing, microwave treatments, enzymatic treatments, and extended maceration. Thermovinification can be used for red wines to increase the contents of some phenolics and volatile compounds during fermentation. For wines that are to be consumed young, and when the colour intensity is a problem, thermovinification may help to enhance the colour [5]. Microwave treatment is a novel red wine pre-treatment process that has shown potential results in improving phenolic extraction of the finished wines [6]. Microwave has been demonstrated to be efficient in terms of both rate and effectiveness of extraction for a range of plant compounds. By conducting the pre-fermentation maceration with microwave radiation, the heated water within the cells of grapes are transformed into vapours, which increases the pressure inside and hence the content of intracellular constituents were released. The use of commercial enzymes as a pre-treatment in winemaking is also a common and well-known practice. Pectinases obtained from *Aspergillus* sp. are commonly used in red winemaking to enhance the extraction of free-run juice

*Corresponding author: Email: lnlieu@hcmiu.edu.vn

during maceration, to aid in clarification and filtration, and to facilitate the processes [7]. Some reports on the effect of pectinases demonstrated an increase in extraction of phenolic compounds, especially anthocyanins that are the red pigments of grapes, and thus wine colour intensity is enhanced. These enzyme preparations degrade the structural polysaccharides of grape skin cell walls, which facilitates the release of phenolic compounds.

Therefore, the purpose of this research was to conduct wine fermentation of ivy gourd fruit to promote its usage. Effects of pretreatments including thermovinification, microwave, and enzymes on the nutritional values and health benefits of the fruit wine were also studied to compare among these methods and find out the most suitable treatment technique for the production of ivy gourd fruit wine.

2. Materials and methods

2.1. Materials and chemicals

Ripe ivy gourd fruits (*Coccinia grandis*) with bright red colour were harvested from Tay Ninh province, Vietnam. They were transported to the laboratory within a day for processing. Commercial yeast *Saccharomyces cerevisiae* RV100 was purchased from Angel Yeast Co., Ltd, China. The enzyme used was Pectinex Ultra SP-L supplied by Novozyme, Denmark. Chemicals required were of analytical grade including diammonium phosphate ($(NH_4)_2HPO_4$), potassium metabisulfite ($K_2S_2O_5$), sodium hydroxide, Folin-Ciocalteau's reagent, anhydrous sodium carbonate, 1,1-diphenyl-2-picrylhydrazyl (DPPH), methanol, ethanol, aluminium chloride, and potassium acetate obtained from various suppliers. Standards including gallic acid, catechin, and L-ascorbic acid were purchased from Sigma Aldrich, Singapore.

2.2. Sample preparation

After being collected, ivy gourd fruits were washed and crushed by a mechanical grinder (Philips HR2118, Japan). The mixture was then mixed with water at 1:1 (w/w) ratio. The final fruit musts were stored frozen at -20°C until further processing. At this temperature, deterioration reactions as well as enzymatic activities of fruit was reported to be negligible, and thus, the fruit's nutritional values were hardly altered [8].

2.3. Thermovinification

Thermovinification process was performed according to M. Atanacković, et al. (2012) [5] with minor modifications. The ivy gourd fruit musts (200 ml per sample) were heated to 85°C in a water bath (WiseCircu, Germany) for 2 min then cooled down to 40°C in an ice bath. After that, the musts were held at 40°C for 12 h in a sterilised incubator (Memmert, Denmark) before being cooled down to 27°C for fermentation.

2.4. Microwave treatment

Microwave treatment was done following the method of A.L. Carew, et al. (2014) [6]. Each 200 ml of ivy gourd fruit musts was microwave-macerated using an 800 W microwave oven (Sharp R-209VN, China) at the maximum power level for three periods of time including 2 min, 1 min, and 15-40 s, respectively (final heating time was varied according to temperature reading). The stop time between two treatment periods was 5 min to stir and evaluate the temperature using a thermometer. The temperature for all treated samples would be in the range of 70-71°C and held there for 10 min. After that, the musts were cooled down in an ice bath until reaching 27°C for fermentation.

2.5. Enzymatic treatment

Enzymatic treatment was prepared according to M.A. Zaker, et al. (2014) [7]. The commercial enzyme Pectinex Ultra SP-L was added to 200 ml of the musts at a concentration of 0.03% (w/w) before the incubation for 90 min at 40°C in a shaking water bath (WiseBath, Germany). Enzyme was deactivated at 90°C for 5 min. After maceration, the musts were cooled down in ice bath to 27°C for fermentation.

2.6. Wine fermentation

The wine fermentation process was performed according to the method of [9] with modifications. The ivy gourd fruit musts (200 ml each) were adjusted to pH 4.0 by adding acetic acid 10% and adjusted to 22°Brix by adding sucrose. The musts were also added with 1 g/l diammonium phosphate for enhancement of yeast growth as well as with 0.1 g/l sodium metabisulfite as preservation additive. The fermentation was then proceeded with pre-activated *Saccharomyces cerevisiae* at 8% (v/v), which was approximately $8x10^6$ cells/ml, with the expectation for the final products to reach 10% (v/v) in alcohol content. Fermentation was performed anaerobically in a closed bottle at 25°C for 10 days in a dark incubator (Memmert, Denmark). The cap of the bottle was slightly loosened every day for the first 3 days to release gases. The ivy gourd fruit wines produced were filtered by using cheese cotton cloth and then centrifuged (Hettich Zentrifugen Universal 320 R, Germany) at 2500g and 4°C for 20 min and stored at -20°C for analyses within

one month. The storage at freezing conditions minimises the nutritional changes because deterioration reactions as well as enzymatic activities of the fruit are reported to be negligible at this temperature [8]. All experiments were carried out in triplicate.

2.7. Analytical methods

Total soluble solid (TSS) content was determined by measuring the Brix value using a refractometer. The pH was measured using a pH meter. Ethanol content was measured by using the distillation method. Briefly, 20 ml of wine samples were put in a rotary evaporator (Steroglass 300, Italy) for 15 min at 40°C. The obtained distillates were made up to 20 ml with distilled water and then measured using an alcohol refractometer.

Titratable acidity (TA) was measured using the titration method, where 5 ml of ivy gourd fruit wine was mixed 45 ml of distilled water before the titration with 0.1 N NaOH until a pH of 8.2 (endpoint) was reached. TA was expressed as g malic acid equivalent (MAE) per litre.

The TPC was determined by the Folin-Ciocalteu method and expressed as micrograms of gallic acid equivalents per ml (µg GAE/ml) [9]. The TFC was determined using the colorimetric method described by L. Wang, et al. (2015) [10] and expressed as micrograms of catechin equivalents per ml (µg CE/ml). The antioxidant capacity was evaluated through 1,1-diphenyl-2-picrylhydrazyl (DPPH) assay modified from the method of [10] and expressed as micrograms of L-ascorbic acid equivalent per ml (µg AAE/ml).

2.8. Data analysis

All measurements were done in triplicate and results were expressed as the average value ± standard deviation. Statistical analyses were determined using one-way ANOVA by the SPSS software version 22.0 with a 95% confident interval. The differences among samples were assessed by Post-hoc's multiple test. Sample letters in value indicated no significant differences.

3. Results and discussion

3.1. Physicochemical properties of the ivy gourd fruit musts and wines

Table 1 shows that three studied pretreatment methods did not significantly influence the TSS content (mainly sugar) of the musts ($p>0.05$). After fermentation, the initially adjusted TSS values of approximate 22°Brix for all types of treatments decreased to 6.14-7.17°Brix. This was due to the conversion of sugar into ethanol by yeast activity. The ethanol contents of all wine samples after fermentation were not significantly different ($p>0.05$), which varied from 10.87 to 11.52 (% v/v). The insignificant variation in ethanol concentration for all ivy gourd wines was due to the same fermentation condition of temperature and pH among the tested samples. These two parameters were reported to govern the yeast growth and fermentation capacity and thus no differences in these parameters led to no significant changes in ethanol content [11].

The pH value and TA content of the wines noticeably changed in comparison with those of the musts (Table 1). Particularly, the pH values of the wines decreased significantly with corresponding increases in TA content. These values are approximate to those reported by J. Foong, et al. (2012) [12]. The reduction in pH was caused by the alternation of buffer capacity in wine, adsorption of bases, and excretion of organic acids during fermentation [13]. Consequently, TA values increased with the releases of more organic acids into the fermented samples. Meanwhile, the wines with pretreatments had slightly lower pH values and higher TA contents than the control wine. These results were consistent with their slightly higher ethanol contents observed, which imply that pretreatments may slightly increase wine fermentability. Beside the main substrates, i.e., sugar, yeasts also need minor nutrients for their growth and fermentation such as certain vitamins (e.g., thiamine and pantothenic acid) [13] or nitrogen-carrying compounds (e.g., amino acids) [14]. Therefore, although pretreatments did exhibit the additional extraction of soluble solids, they might induce the release of certain minor nutrients that promote the fermentation of yeasts.

Table 1. Physicochemical properties of ivy gourd fruit musts and wines with different pretreatments.

Pretreatment	Fermentation	TSS (°Brix)	Ethanol content (% v/v)	pH	TA (g MAE/ 100 ml)
Control	Before	1.66±0.01^{c}	-	4.51±0.08^{a}	0.23±0.01^{c}
	After	6.73±0.12^{ab}	10.87±0.66^{a}	3.96±0.03^{b}	0.49±0.02^{b}
Microwave	Before	1.70±0.02^{c}	-	4.38±0.02^{a}	0.23±0.01^{c}
	After	6.14±0.33^{b}	11.37±0.83^{a}	3.88±0.01^{bc}	0.53±0.01^{ab}
Thermo-vinification	Before	1.69±0.03^{c}	-	4.53±0.13^{a}	0.23±0.01^{c}
	After	6.81±0.62^{ab}	11.17±0.62^{a}	3.80±0.05^{bc}	0.55±0.02^{a}
Enzyme	Before	1.69±0.02^{c}	-	4.48±0.09^{a}	0.24±0.02^{c}
	After	7.17±0.10^{a}	11.52±0.68^{a}	3.71±0.03^{c}	0.54±0.02^{a}

Values are expressed as mean ± SD (n=3).
Same letters in the same row express that values are not significantly different ($p>0.05$).

3.2. Antioxidant contents and capacity of the ivy gourd fruit musts and wines

TPC: it is shown in Fig. 1 that the TPC of the control must was less affected by microwave and thermovinification methods while the enzymatic treatment displayed a major enhancement of the compounds ($p<0.05$). This trend is similar to the results obtained in a report for black currant juice [15]. The reason is that the pectinase family in the Pectinex Ultra SP-L could damage the skin cell membranes releasing phenolic substances into the musts. The wine samples after fermentation had TPC ranging from 30.15 to 39.37 µg GAE/ml. There was an increase in TPC after fermentation ($p<0.05$) for the enzyme-treated sample while there were no significant differences for others ($p>0.05$). One of reasons of the observed increase could be due to their greater solubility in ethanol (in wine) than in purely aqueous solutions (in juice) [16]. As a result, the phenolic compounds in fruit mash were continuously extracted into wine during fermentation. Another reason may be attributed to the fact that less oxidation of polyphenols occurred during the fermentation process [17]. Phenolic compounds can act as antioxidants and also can easily be oxidized leading to its loss. As reported by J.M. Salmon (2006) [18], the yeast *Saccharomyces cerevisiae* used in the alcoholic fermentation requires oxygen for lipid synthesis and can consume much oxygen with no detrimental effect on the fermentation process. As yeasts have much higher affinities for oxygen than phenolic compounds, their further extracted amount during fermentation could be protected from oxidation leading to their high content in wine.

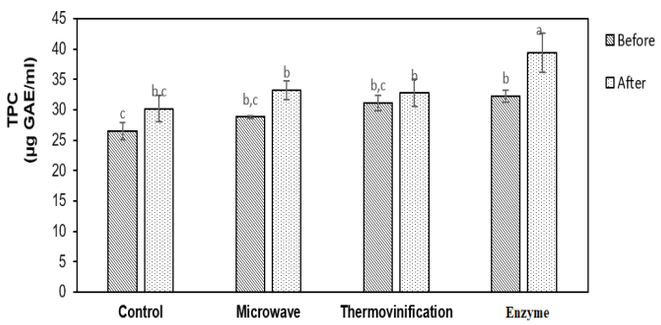

Values are expressed as mean ± SD (n=3).
Same letters in the same row express that values are not significantly different ($p>0.05$).

Fig. 1. TPC of ivy gourd fruit musts before and after wine fermentation.

Amongst all wine samples, the highest value of TPC was found in the wines with enzymatic pretreatment. Although the values of the wine pretreated with microwave and thermovinification were not statistically different ($p>0.05$) from that of the control wine, there existed obvious differences between them and the value of the control musts (while the control wine was not), which indicates the efficiency of these pretreatment techniques in winemaking. During the thermovinification process, heat could damage the hypodermal cell membranes and denature polyphenol oxidases [16]. The first effect facilitated the release of phenolic compounds and the second prevented their loss, especially during the long duration of fermentation. The positive effect of thermovinification in winemaking was also reported by M. Atanackovic, et al. (2012) [5] for grape wines. On the other hand, microwaves are considered similar to thermal treatment but with shortened duration. Enhanced extraction of phenolic compounds during fermentation by pretreating the must with microwaves was also reported by other authors [6] for grape wines. The application of enzymatic treatment in juice, however, still produced more phenolic compounds in wine than microwave treatment and thermovinification techniques in this study ($p<0.05$). Various studies have pointed out that pectolytic enzymes have been used to slow fermentation and increase phenolic extraction [19] because they could break down skin cell walls for substance release [16].

TFC: similar to the results for TPC, enzymatic treatment enhanced the TFC of ivy gourd musts the most while microwave and thermovinification methods only showed a minor but statistically insignificant ($p>0.05$) (Fig. 2) increase. After fermentation, the TFC of the wine samples decreased substantially in all four samples. Flavonoids are certain polyphenolic compounds known for their high antioxidant properties and free radical scavenging ability [20]. It has been reported that during fermentation, polyphenolic compounds of wine change significantly due to the combinative effects of their adsorption on solids, proteins, or even yeasts; their extraction from the mash into the wine; their polymerisation, degradation or oxidation; and their release from bound polyphenolic complexes with other substances induced by micro-organisms [21].

Depending on which reactions dominate, an increasing or decreasing trend could be observed. Among three studied pretreatments, enzymatic treatment again exhibited the best efficiency.

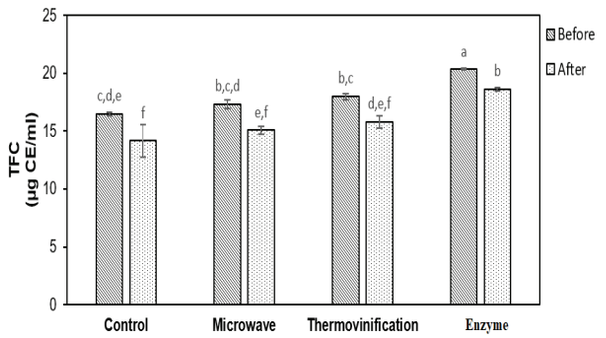

Values are expressed as mean ± SD (n=3).
Same letters in the same row express that values are not significantly different (p>0.05).

Fig. 2. TFC of ivy gourd fruit musts before and after wine fermentation.

3.3. Antioxidant capacity by the DPPH assay

As shown in Fig. 3, the differences in antioxidant capacity of the thermovinification-treated and enzymatically-treated musts were significant compared to that of the control. In addition, the antioxidant capacity of the wines after fermentation was slightly higher than the initial musts, however the deviations were not large enough to produce a statistically significant difference ($p>0.05$). Further interpretation reveals that although there were no significant differences in DPPH scavenging activity among the wines pre-treated with microwave and thermovinification compared to the control wine ($p>0.05$), the former did create a significance with the control must while the control wine did not. This again verifies the possibly positive effects of microwave and thermovinification in winemaking. In fact, the trend of DPPH scavenging activity followed that of TPC, which confirms that the antioxidant activity of wine depended mainly on phenolic compounds. Some previous studies also demonstrated a positive correlation between the TPC and the antioxidant activities of wines [22]. On the other hand, the content of total flavonoids, another group of antioxidants did not exhibit the correlation with DPPH scavenging activity in this study. Similar negative correlation between total flavonoids and DPPH scavenging activity were also reported by A. Meda, et al. (2005) [23].

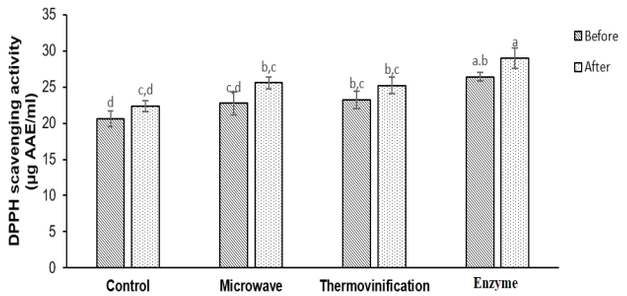

Values are expressed as mean ± SD (n=3).
Same letters in the same row express that values are not significantly different (p>0.05).

Fig. 3. Total antioxidant capacity of ivy gourd fruit musts before and after wine fermentation.

4. Conclusions

The total flavonoid, total phenolic, and antioxidant contents contribute to the health benefits of wines. The development of procedures and techniques that contribute to these characteristics is important for improvement of their quality. In this study, the physicochemical and antioxidant properties of the ivy gourd fruit wines under three different pretreatment winemaking techniques including microwave, thermovinification, and enzymatic treatment were evaluated. Results showed that fermentation of ivy gourd fruit musts increased the content of certain antioxidants and the antioxidant capacity in wines. Enzymatic treatment was shown to be the best pretreatment amongst the three applied methods. With these primary data, further investigation is needed to determine the optimal conditions of each technique.

CRediT author statement

Trang T. Dang: Conceptualisation, Methodology, Software, Writing and Editing; Thanh T.H. Le: Data curation, Writing - Original draft preparation; Ngoc Lieu Le: Conceptualisation, Methodology, Writing, Reviewing and Editing.

ACKNOWLEDGEMENTS

This paper was supported by International University.

COMPETING INTERESTS

The authors declare that there is no conflict of interest regarding the publication of this article.

REFERENCES

[1] S.Z. Shaheen, K. Bolla, K. Vasu, et al. (2009), "Antimicrobial activity of the fruit extracts of *Coccinia indica*", *African Journal of Biotechnology*, **8(24)**, pp.7073-7076.

[2] E. Wasantwisut, T. Viriyapanich (2003), "Ivy gourd (*Coccinia grandis* Voigt, *Coccinia cordifolia*, *Coccinia indica*) in human nutrition and traditional applications", *World Review of Nutrition and Dietetics*, **91**, pp.60-66, DOI: 10.1159/000069929.

[3] A. Attanayake, K. Jayatilaka, L. Mudduwa (2016), "Anti-diabetic potential of ivy gourd (*Coccinia grandis*, family: Cucurbitaceae) grown in Sri Lanka: A review", *Journal of Pharmacognosy and Phytochemistry*, **5(6)**, pp.286-289.

[4] A. Baiano, C. Terracone, G. Gambacorta, et al. (2009), "Phenolic content and antioxidant activity of Primitivo wine: Comparison among winemaking technologies", *Journal of Food Science*, **74(3)**, pp.258-267, DOI: 10.1111/j.1750-3841.2009.01101.x.

[5] M. Atanackovic, A. Petrovic, S. Jovic, et al. (2012), "Influence of winemaking techniques on the resveratrol content, total phenolic content and antioxidant potential of red wines", *Food Chemistry*, **131(2)**, pp.513-518, DOI: 10.1016/j.foodchem.2011.09.015.

[6] A.L. Carew, A.M. Sparrow, C.D. Curtin, et al. (2014), "Microwave maceration of Pinot Noir grape must: Sanitation and extraction effects and wine phenolics outcomes", *Food and Bioprocess Technology*, **7**, pp.954-963, DOI: 10.1007/s11947-013-1112-x.

[7] M.A. Zaker, K. Syed, R. Harkal (2014), "Pre-treatment of pectinase and amylase on production of banana based wine", *International Journal of Processing and Post Harvest Technology*, **5(2)**, pp.145-150, DOI: 10.15740/HAS/IJPPHT/5.2/145-150.

[8] A. Alhamdan, B. Hassan, H. Alkahtani, et al. (2018), "Cryogenic freezing of fresh date fruits for quality preservation during frozen storage", *Journal of the Saudi Society of Agricultural Sciences*, **17(1)**, pp.9-16, DOI: 10.1016/j.jssas.2015.12.001.

[9] U.B. Jagtap, V.A. Bapat (2015), "Phenolic composition and antioxidant capacity of wine prepared from custard apple (*Annona squamosa* L.) fruits", *Journal of Food Processing and Preservation*, **39(2)**, pp.175-182, DOI: 10.1111/jfpp.12219.

[10] L. Wang, X. Sun, F. Li, et al. (2015), "Dynamic changes in phenolic compounds, colour and antioxidant activity of mulberry wine during alcoholic fermentation", *Journal of Functional Foods*, **18**, pp.254-265, DOI: 10.1016/j.jff.2015.07.013.

[11] G.M. Heard, G.H. Fleet (1988), "The effects of temperature and pH on the growth of yeast species during the fermentation of grape juice", *Journal of Applied Bacteriology*, **65(1)**, pp.23-28, DOI: 10.1111/j.1365-2672.1988.tb04312.x.

[12] J. Foong, W. Hon, C. Ho (2012), "Bioactive compounds determination in fermented liquid dragon fruit (*Hylocereus polyrhizus*)", *Broneo Science*, **31(1)**, pp.37-56.

[13] X. Wang, J. Bohlscheid, C. Edwards (2003), "Fermentative activity and production of volatile compounds by *Saccharomyces* grown in synthetic grape juice media deficient in assimilable nitrogen and/or pantothenic acid", *Journal of Applied Microbiology*, **94(3)**, pp.349-359, DOI: 10.1046/j.1365-2672.2003.01827.x.

[14] J.O.V. Rodriguez, G.H. Cortes, J. Cordova, et al. (2012), "Fermentation of *Agave tequilana* juice by *Kloeckera africana*: Influence of amino-acid supplementations", *Antonie Van Leeuwenhoek*, **101(2)**, pp.195-204, DOI: 10.1007/s10482-011-9622-x.

[15] A.K. Landbo, A.S. Meyer (2004), "Effects of different enzymatic maceration treatments on enhancement of anthocyanins and other phenolics in black currant juice", *Innovative Food Science & Emerging Technologies*, **5(4)**, pp.503-513, DOI: 10.1016/j.ifset.2004.08.003.

[16] K.L. Sacchi, L.F. Bisson, D.O. Adams (2005), "A review of the effect of winemaking techniques on phenolic extraction in red wines", *American Journal of Enology and Viticulture*, **56**, pp.197-206, DOI: 10.5344/ajev.2005.56.3.197.

[17] H.D. Jang, K.S. Chang, T.C. Chang, et al. (2010), "Antioxidant potentials of buntan pumelo (*Citrus grandis* Osbeck) and its ethanolic and acetified fermentation products", *Food Chemistry*, **118(3)**, pp.554-558, DOI: 10.1016/j.foodchem.2009.05.020.

[18] J.M. Salmon (2006), "Interactions between yeast, oxygen and polyphenols during alcoholic fermentations: Practical implications", *LWT-Food Science and Technology*, **39(9)**, pp.959-965, DOI: 10.1016/j.lwt.2005.11.005.

[19] C. Ough, A. Noble, D. Temple (1975), "Pectic enzyme effects on red grapes", *American Journal of Enology and Viticulture*, **26**, pp.195-20, DOI: 10.5344/ajev.1975.26.4.195.

[20] R. Scherer, H.T. Godoy (2009), "Antioxidant activity index (AAI) by the 2, 2-diphenyl-1-picrylhydrazyl method", *Food Chemistry*, **112(3)**, pp.654-658, DOI: 10.1016/j.foodchem.2008.06.026.

[21] F.O. Adetuyi, T.A. Ibrahim (2014), "Effect of fermentation time on the phenolic, flavonoid and vitamin C contents and antioxidant activities of okra (*Abelmoschus esculentus*) seeds", *Nigerian Food Journal*, **32(2)**, pp.128-137, DOI: 10.1016/S0189-7241(15)30128-4.

[22] P. Simonetti, P. Pietta, G. Testolin (1997), "Polyphenol content and total antioxidant potential of selected Italian wines", *Journal of Agricultural and Food Chemistry*, **45(4)**, pp.1152-1155, DOI: 10.1021/jf960705d.

[23] A. Meda, C.E. Lamien, M. Romito, et al. (2005), "Determination of the total phenolic, flavonoid and proline contents in Burkina Fasan honey, as well as their radical scavenging activity", *Food Chemistry*, **91(3)**, pp.571-577, DOI: 10.1016/j.foodchem.2004.10.006.

DOI: 10.31276/VJSTE.64(1).33-38

Comparative analysis of overall survival in non-small cell lung cancer patients with and without different organ metastases

Tien Manh Hoang[1*], Thi Thanh Nguyen[2]

[1]*Vietnam Military Medical University, 160 Phung Hung Street, Phuc La Ward, Ha Dong District, Hanoi, Vietnam*

[2]*E Hospital, 89 Tran Cung Street, Nghia Tan Ward, Cau Giay District, Hanoi, Vietnam*

Received 14 June 2021; revised 1 September 2021; accepted 12 September 2021

Abstract:

Lung cancer is the leading cause of cancer death globally. Non-small cell lung cancer (NSCLC) constitutes more than 80% of all lung cancers, and patients with distant metastasis have much higher mortality. The survival times of NSCLC patients with metastasis have been reported in early studies, however, it remains unclear whether there are variations or patterns in survival times of patients with different metastases. Therefore, we assessed risk factors for distant metastases and the effects of different organ metastasis on overall survival (OS) in patients with NSCLC. Methods: demographics and clinical data of NSCLC patients with and without distant metastasis were collected from the Surveillance, Epidemiology, and End Result (SEER) database between 2010 and 2016. Results: a total of 3849 patients diagnosed with NSCLC were screened from the SEER database with 41% (1577) of the patients having distant metastasis. During the follow-up period, 3221 (83.7%) patients died and, of all the deceased patients, 2935 (88.4%) died of lung cancer while only 286 (11.6%) died from other diseases or causes. The occurrence of distant metastasis was closely related to the patient's age, primary tumour site, tumour grade, T stage, N stage, surgery of primary site, radiation therapy, and chemotherapy ($p<0.05$). Conclusions: distant metastasis indicates a poor prognosis in NSCLC patients. There were significant differences in the prognosis of different metastatic sites and the order of their OS from high to low was: no metastasis > lung metastasis, liver metastasis, bone metastasis > brain metastasis, multiple organ metastasis.

Keywords: **metastasis, non-small cell lung cancer, overall survival, SEER.**

Classification number: **3.2**

1. Introduction

Lung cancer is a malignant tumour with the highest morbidity and mortality rates in the world for both men and women, which claims more lives than prostate, breast, and colon cancers combined [1]. Statistics from the Vietnam Ministry of Health show that lung cancer is the second leading cause of cancer death in Vietnam, and more than 20,000 new lung cancer patients are diagnosed across the country every year with up to 17,000 fatalities [2]. The age-standardised incidence rate for males is 40.2/100,000 while for women it is 10.6 per 100,000 people [2]. The 1-year survival rate of patients diagnosed with lung cancer is less than 50%, and over four-fifths of those die within 5 years of diagnosis [3]. According to histopathology, lung cancer has two major subtypes, namely, small cell lung cancer and NSCLC, with the latter constituting more than 80% of all lung cancers [4]. Despite noticeable advances in targeted therapy, the survival rates of NSCLC patients have not improved. Approximately 80% of all lung cancer patients have metastases in their lifetime, and once distant metastases occur, the 5-year survival rate drops to <5%, which indicates that metastasis has much higher mortality in NSCLC [5].

*Corresponding author: Email: tienmanhhoang@outlook.com

The lung, liver, bone, and brain are common distant metastasis sites of NSCLC. While many studies have evaluated the survival time of NSCLC patients with metastasis to each of these organs, it remains unclear whether there is a difference in the survival times of each case. Therefore, the purpose of this study is to determine the risk factors for distant metastasis as well as the impact of metastasis in different organs on patient OS.

2. Materials and methods

2.1. Patient population and data collection

Patients were identified from the SEER database of the National Cancer Institute between 2010 and 2016. SEER*Stat Software 8.3.8 (National Cancer Institute, Bethesda, MD) was used to extract information from the SEER database.

The SEER database was developed by the National Cancer Institute and is supported by the Surveillance Research Program in the Division of Cancer Control and Population Science of the National Cancer Institute. This is one of the largest cancer epidemiological databases in the world and it collects information on demographic characteristics, clinical characteristics, and follow-up after diagnosis and treatment of cancer patients from 18 registries representing 28% of the US population. Researchers are granted permission to access this database for study after completing the registration and approval process.

Inclusion and exclusion criteria: Among the NSCLC patients pathologically diagnosed from 2010 to 2016, patients with previous malignant tumours were excluded, and 21,985 cases were finally selected. We extracted the age, gender, race, marital status, pathology, degree of differentiation, surgery, T-staging, N-staging, survival time, radiation therapy, chemotherapy, metastasis site, etc., of each patient from the database. Pathological staging was based on American Joint Committee on Cancer (AJCC) 6th edition staging.

The inclusion criteria were as follows: (1) NSCLC patients diagnosed between 2010 and 2016; (2) patients with complete baseline and treatment information; and (3) patients with a complete follow-up and known survival time. The exclusion criteria were as follows: (1) more than one primary tumour; (2) unknown site and grade of primary neoplasm; (3) unknown N stage or T stage; (4) incomplete therapy information, which includes primary tumour surgery, radiation therapy, and chemotherapy; (5) unknown survival time; and (6) lack of metastasis information.

Grouping: The extracted NSCLC patients were divided into two groups. The NSCLC patients who did not have metastasis between 2010 and 2016 were placed into the non-metastasis group and the patients who had distant metastases during or after NSCLC was diagnosed from 2010 to 2016 were divided into the metastasis group.

We further divided the patients in the metastasis group into 5 subgroups based on the location of metastasis including the brain metastasis subgroup, bone metastasis subgroup, liver metastasis subgroup, lung metastasis subgroup, and multi-organ metastasis subgroup.

2.2. Demographics and clinical characteristics

Demographic characteristics of patients included age at diagnosis, sex, and marital status. To facilitate the evaluation and comparison, we converted the age of patients when diagnosed from a measurement variable into an ordinal categorical variable (≤60, 61-70, 71-80, and >80 years old). Marital status was characterised as married, unmarried, or unknown. It should be noted that the unmarried status included single or never married, separated, divorced, widowed, and domestic partner.

Clinical characteristics included primary tumour site, tumour grade, T and N stage, primary tumour surgery, chemotherapy, and radiation therapy. The primary tumour site was classified as main bronchus, upper lobe, middle lobe, lower lobe, or overlapping lesion of lung. There are 4 different types of tumour grades, which are grade I, grade II, grade III, and grade IV representing well differentiated, moderately differentiated, poorly differentiated, and undifferentiated, respectively. The tumour grade assists clinicians with determining how aberrant cancer cells and tissue appear under a microscope, as well as how rapidly cancer cells are expected to develop and spread. Low-grade cancer cells have a more natural appearance than high-grade cancer cells and develop and spread more slowly. T stage and N stage are based on the 7th edition of the AJCC. Regarding radiation therapy and chemotherapy, whether these were given preoperatively or postoperatively are both considered for NSCLC patients.

The survival time in this study is understood as the OS time, which was the period beginning from the time the patient was diagnosed to the time the patient died from

any cause. Follow-up was conducted at regular follow-up visits and/or through tele-communication.

2.3. Statistical analysis

The software SPSS 25.0 (Statistical Package for the Social Sciences, IBM Corporation, Armonk, NY, USA) was used for all statistical analyses in this study. Regarding the differences between groups and subgroups, a Chi-squared test was used to evaluate the categorical variables and the Log-rank test was used for the difference test of OS. The fraction of patient survival after treatment was measured by using the Kaplan-Meier estimator. A statistical test was considered statistically significant if its corresponding two-tailed P-value was less than 0.05.

2.4. Ethical considerations

The SEER database is an open-access database, hence, after signing the Data Use Agreement for the SEER 1975-2016 Research Data, we were allowed to access to the database to abstract the data. Thus, we did not need to acquire patients' informed consent or an ethical review committee statement.

3. Results

3.1. Characteristics of metastasis in NSCLC patients

As shown in the study design flowchart (Fig. 1), 21,985 patients diagnosed with NSCLC from January 2010 to December 2016 were initially identified. Based on the criteria outlined above, 18,136 ineligible patients were excluded, and a total of 3,849 patients remained both with and without distant metastases.

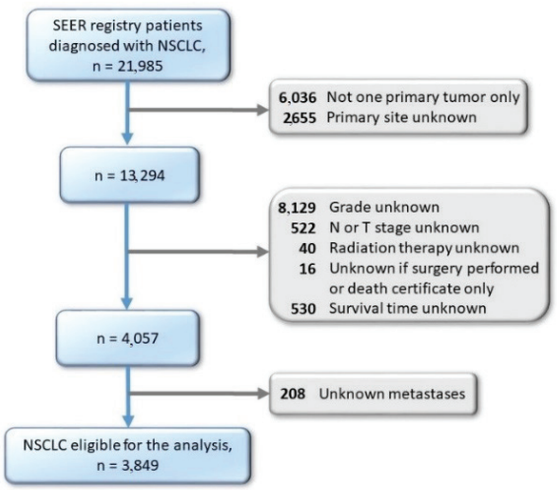

Fig. 1. Study design flowchart of the specific patient screening process.

There were a total of 1,577 out of 3,849 NSCLC patients with distant metastasis, which accounts for approximately 41.0%. The organ with the most cancer metastasis is bone (n=713), followed by brain (n=664), lung (n=563), and liver (n=349). Details of the number of patients with or without metastases are shown in Fig. 2. Among patients with metastasis, up to 561 patients had metastatic conditions in more than one organ making the rate more than one-third.

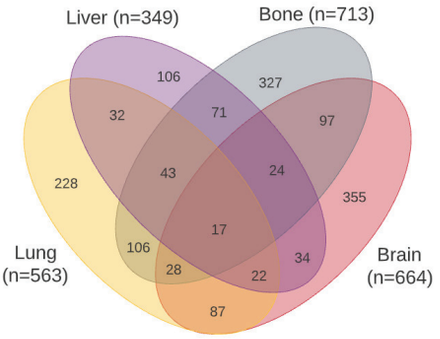

Fig. 2. Venn diagram of the distribution of metastatic sites in NSCLC patients.

3.2. Demographics and clinical characteristics

The start time was January 1, 2010, and the cut-off time was December 31, 2016. During the follow-up period, 3,221 patients (83.7%) died, and the overall median OS was 8.00 (3.00-20.00) months. Of all deceased patients, 2,935 (91.1%) died of lung cancer, and only 286 (8.9%) died from other diseases or causes.

The basic clinical characteristics are shown in Table 1. Whether the patient had distant metastasis was closely related to the patient's age, tumour primary site, tumour grade, T stage, N stage, surgery of primary site, radiation therapy, and chemotherapy ($p<0.05$).

With the increase of age, the probability of distant metastasis in lung cancer patients gradually decreased i.e., the metastasis rate for those ≤60 years old was 46.8% while those >80 years old was 33.0%. The upper lobe was the most common primary site with 2,445 individuals (approximately 63.5%), however, cancer at this site had the least metastasis (40.0%) followed by middle lobe (40.6%), lower lobe (42.1%), main bronchus (46.5%), and overlapping lesion of lung (47.5%), which had the highest risk of metastasis. With respect to tumour grade, the majority of patients with or without distant metastasis was represented as grade III (poorly differentiated) (89.1%); patients with distant metastasis were, in descending order, dedifferentiated (35.1%), poorly differentiated (42.3%), moderately

Table 1. Baseline of the demographics and clinical characteristics for patients diagnosed with NSCLC.

Characteristics	Non-metastasis	Single organ metastasis				Multiple-organ metastasis	P
		Bone	*Brain*	*Liver*	*Lung*		
Age							<0.001
≤60	578 (53.2%)	99 (9.1%)	139 (12.8%)	29 (2.7%)	66 (6.1%)	175 (16.1%)	
>60~70	740 (58.3%)	104 (8.2%)	132 (10.4%)	30 (2.4%)	69 (5.4%)	194 (15.3%)	
>70~80	641 (62.4%)	85 (8.3%)	68 (6.6%)	34 (3.3%)	58 (5.6%)	141 (13.7%)	
>80	313 (67.0%)	39 (8.4%)	16 (3.4%)	13 (2.8%)	35 (7.5%)	51 (10.9%)	
Sex							0.369
Male	999 (60.4%)	142 (8.6%)	153 (9.2%)	49 (3.0%)	93 (5.6%)	219 (13.2%)	
Female	1,273 (58.0%)	185 (8.4%)	202 (9.2%)	57 (2.6%)	135 (6.2%)	342 (15.6%)	
Primary site							0.041
Main bronchus	100 (53.5%)	16 (8.6%)	17 (9.1%)	5 (2.7%)	12 (6.4%)	37 (19.8%)	
Upper lobe	1,467 (60.0%)	193 (7.9%)	242 (9.9%)	64 (2.6%)	144 (5.9%)	335 (13.7%)	
Middle lobe	114 (59.4%)	27 (14.1%)	17 (8.9%)	1 (0.5%)	9 (4.7%)	24 (12.5%)	
Lower lobe	570 (57.9%)	86 (8.7%)	75 (7.6%)	35 (3.6%)	58 (5.9%)	161 (16.3%)	
Overlapping lesion	21 (52.5%)	5 (12.5%)	4 (10.0%)	1 (2.5%)	5 (12.5%)	4 (10.0%)	
Grade							0.005
Grade I	32 (80.0%)	1 (2.5%)	2 (5.0%)	0 (0.0%)	3 (7.5%)	2 (5.0%)	
Grade II	141 (72.7%)	12 (6.2%)	13 (6.7%)	3 (1.5%)	10 (5.2%)	15 (7.7%)	
Grade III	1,979 (57.7%)	300 (8.7%)	324 (9.4%)	97 (2.8%)	204 (5.9%)	526 (15.3%)	
Grade IV	120 (64.9%)	14 (7.6%)	16 (8.6%)	6 (3.2%)	11 (5.9%)	18 (9.7%)	
T stage							<0.001
T0	0 (0.0%)	1 (100.0%)	0 (0.0%)	0 (0.0%)	0 (0.0%)	0 (0.0%)	
T1	435 (79.2%)	33 (6.0%)	36 (6.6%)	7 (1.3%)	10 (1.8%)	28 (5.1%)	
T2	718 (62.8%)	97 (8.5%)	128 (11.2%)	36 (3.1%)	35 (3.1%)	129 (11.3%)	
T3	520 (55.1%)	86 (9.1%)	90 (9.5%)	25 (2.6%)	76 (8.1%)	147 (15.6%)	
T4	478 (48.5%)	84 (8.5%)	75 (7.6%)	29 (2.9%)	101 (10.2%)	219 (22.2%)	
Tx	121 (53.5%)	26 (11.5%)	26 (11.5%)	9 (4.0%)	6 (2.7%)	38 (16.8%)	
N stage							<0.001
N0	909 (74.0%)	65 (5.3%)	89 (7.2%)	20 (1.6%)	53 (4.3%)	93 (7.6%)	
N1	218 (61.4%)	35 (9.9%)	35 (9.9%)	9 (2.5%)	18 (5.1%)	40 (11.3%)	
N2	832 (51.5%)	158 (9.8%)	175 (10.8%)	54 (3.3%)	107 (6.6%)	288 (17.8%)	
N3	259 (47.5%)	52 (9.5%)	46 (8.4%)	17 (3.1%)	48 (8.8%)	123 (22.6%)	
Nx	54 (50.9%)	17 (16.0%)	10 (9.4%)	6 (5.7%)	2 (1.9%)	17 (16.0%)	
Surgery of primary site							<0.001
No	1,776 (53.5%)	320 (9.6%)	341 (10.3%)	106 (3.2%)	222 (6.7%)	556 (16.7%)	
Yes	496 (93.9%)	7 (1.3%)	14 (2.7%)	0 (0.0%)	6 (1.1%)	5 (0.9%)	
Radiation therapy							<0.001
No	1,112 (65.2%)	120 (7.0%)	67 (3.9%)	73 (4.3%)	151 (8.9%)	182 (10.7%)	
Yes	1,160 (54.1%)	207 (9.7%)	288 (13.4%)	33 (1.5%)	77 (3.6%)	379 (17.7%)	
Chemotherapy							<0.001
No	1,073 (61.7%)	114 (6.6%)	181 (10.4%)	47 (2.7%)	93 (5.3%)	231 (13.3%)	
Yes	1,199 (56.8%)	213 (10.1%)	174 (8.2%)	59 (2.8%)	135 (6.4%)	330 (15.6%)	

differentiated (27.3%), and well differentiated (20.0%). Regarding T and N stage, cancer staging was positively correlated with the probability of metastasis (except T0). Those who underwent surgery at the primary site had an extremely low metastasis rate (6.1% only). Patients with distant metastasis received more radiation therapy and chemotherapy than those without metastasis.

3.3. Survival analysis

Table 2. The median OS of the NSCLC patients with different metastatic sites.

Metastatic sites	Median OS (months)	Patients alive at the cut-off time	95% CI*	
			Lower bound (months)	*Upper bound (months)*
No	13.00 (5.00-41.00)	546 (24.03%)	12.04	13.96
Lung	6.00 (2.00-17.00)	23 (10.09%)	4.62	7.38
Liver	5.00 (2.00-13.00)	6 (5.66%)	3.56	6.44
Bone	5.00 (2.00-11.00)	18 (5.5%)	4.38	5.62
Brain	4.00 (2.00-8.00)	16 (4.51%)	3.47	4.53
Multi-organ	3.00 (2.00-7.00)	19 (3.39%)	2.59	3.41

*95%: confidence interval for the median OS.

As shown in Table 2, the median OS of patients without distant metastasis was 13 months, which is much higher than that of patients with distant metastases. Among patients with distant metastasis of lung cancer, the median OS of patients with lung metastasis was the highest (6 months), followed by liver metastasis and bone metastases, which were 5 months. The median OS of patients with brain metastasis and multiple-organ metastases was the worst with 4 months and 3 months, respectively.

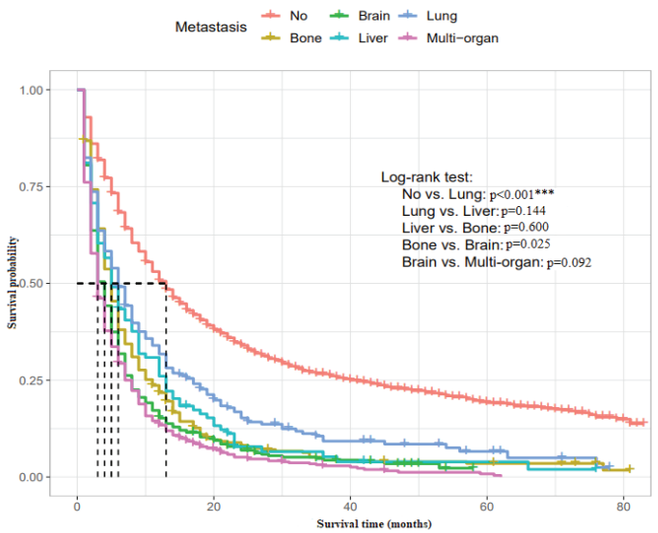

Fig. 3. Kaplan-Meier curves of the NSCLC patients without metastasis or with different metastatic sites.

It can also be seen from Fig. 3 that the prognosis of patients with NSCLC in descending order is without metastasis, lung metastasis, liver metastasis, bone metastasis, brain metastasis, and multiple-organ metastases. According to the result of the Log-rank test, the difference between the survival curves of patients without metastasis and patients with lung metastasis, as well as between bone metastasis and brain metastasis was statistically significant ($p<0.001$ and $p=0.025$, respectively).

4. Discussion

In recent years, with the advancement of new medical technologies, the treatment of lung cancer has rapidly developed and the OS of NSCLC patients has been significantly prolonged. However, most patients with lung cancer are at an advanced stage when they are first diagnosed and may have metastases in different sites. The process of distant metastasis of lung cancer is complex; the cancer cells leave the primary tumour and invade the blood and lymphatic system until the tumour cells grow in the distance with each step closely related to biological characteristics [6]. There are many types of metastases in advanced NSCLC patients such as single lesion, single organ, multiple lesions, and multiple organs. In this study, we mainly compared the OS of patients with lung metastasis, brain metastasis, bone metastasis, liver metastasis, and multiple-organ metastases in their medical history.

From the entire medical history of the lung cancer patients in this study, the median OS of patients without distant metastasis reached 13 (12.04-13.96) months, which was significantly higher than that of patients with distant metastases.

Among patients with distant metastasis, the median OS of patients with lung metastasis is the longest, reaching 6 (4.62-7.38) months. The prognosis is good, which may be related to the large respiratory reserve function of humans.

Following lung metastasis, the median OS of patients with liver metastasis is 5 (3.56-6.44). In contrast, R. Kitadai, et al. (2020) [7] revealed that the median OS of patients with advanced liver metastasis was 3.12 (1.71-9.03). The prognosis of patients with liver metastasis was better than those with bone metastasis. This may be related to rapid progress in the treatment of liver metastasis in recent years, and the treatment effect continues to improve.

The median OS of patients with bone metastasis was also 5 (4.38-5.62) months. Patient survival was affected by many factors such as single bone metastasis or multiple bone metastases, whether it was combined with pathological fracture, and whether it was combined with metastasis of other sites. H. Rief, et al. (2014) [8] found that the 6-month and 12-month OS of patients with single bone metastasis were 76.7 and 47.2%, respectively, and their OS was significantly higher than that of patients with other metastases by 60.0 and 34.0%, respectively. In general, patients with multiple bone metastases and with pathological fractures had poor OS.

Brain metastasis had the worst prognosis among single-organ metastases of NSCLC, with a median OS of only 4 (3.47-4.53) months. Previous studies [9, 10] have found that the factors affecting the survival of patients with brain metastasis included age, physical status, metastasis interval time, number of metastases, treatment methods, course of therapy, brain metastasis symptoms, extracranial metastases, gene mutations, programmed death receptor-1, etc. Patients with multiple organ metastases had the worst prognosis, with a median OS of 3 (2.59-3.41) months. Similar to previous research data [11], distant metastases of NSCLC were dominated by multiple organ metastases (64.4 vs 35.6%), and patients with multiple organ metastases generally had a higher tumour burden than single-organ metastasis, and their prognosis was relatively poor [12].

As mentioned above, distant metastasis suggests that patients with lung cancer have a poor prognosis, and there are many influencing factors for its occurrence. It can be seen from Table 1 that age was inversely proportional to the probability of distant metastasis. This may be because younger patients have good physical fitness, good tolerance to various treatments, and long OS time, thus, the probability of distant metastasis in the medical history increased. Same as previous clinical experience, the worse the degree of differentiation, the worse the T stage and the N stage, and the more likely the patient to develop distant metastases.

Due to the poor prognosis and many risk factors of distant metastasis of NSCLC, research on the treatment of metastasis of different organs has progressed rapidly in recent years and the prognosis has gradually improved. NSCLC patients with metastatic disease require systemic treatment. Before immunotherapy was commonly available, a platinum doublet with either carboplatin or cisplatin with gemcitabine, vinorelbine, or taxanes was widely used as the standard treatment. After the introduction of chemoimmunotherapy, the treatment landscape of NSCLC has changed significantly [13].

M. Tönnies, et al. (2012) [14] stated that patients with solitary pulmonary metastasis (outside of the tumour-bearing lobe) and otherwise operable NSCLC may benefit from surgical intervention comprising resection of the primary tumour, lymphadenectomy, and resection of the solitary pulmonary metastasis. Also, three-dimensional radiotherapy for metastases is relatively effective.

For NSCLC patients with liver metastases, M. Reck, et al. (2019) [15] reported that the survival of patients treated with atezolizumab plus bevacizumab plus carboplatin plus paclitaxel had better improvement than those given bevacizumab plus carboplatin plus paclitaxel. P.C. Tumeh, et al. (2017) [16] proposed that liver metastatic patients with NSCLC who had been treated with pembrolizumab were associated with reduced responses and progression-free survival, and liver metastases were associated with reduced marginal CD8 + T-cell infiltration, which provides a potential mechanism for this outcome.

Bone metastasis was associated with a significant increase in skeletal-related events including pathological fractures, hypercalcaemia, spinal cord injury, and uncontrolled pain requiring bone surgery and/or radiotherapy [17]. Currently, there are opioid analgesic treatments, zoledronic acid, and ibandronic acid, while some patients are treated with radiation therapy and a small number of patients are treated with surgery.

Regarding brain metastases in NSCLC, the former primary treatment selection included surgical resection, stereotactic radiosurgery, and whole-brain radiation therapy. With the finding of targetable molecular drivers and the increase of an enormous number of tyrosine kinase inhibitors, treatments have become complicated [18].

There were also several limitations in the study. First, selection bias in retrospective data could not be entirely avoided. Second, we were unable to obtain more specific data such as laboratory results and treatment drugs. Finally, if a patient moved to a different part of the United States where SEER data was not gathered, patient follow-up may have come to an end.

5. Conclusions

In summary, this study suggested that the occurrence of distant metastases of NSCLC patients had a great impact on the prognosis. There were significant differences in the prognosis of different metastatic sites and the order of their OS from high to low was: no metastasis > lung metastasis, liver metastasis, bone metastasis > brain metastasis, multiple organ metastasis. For patients diagnosed with NSCLC, early assessment of the systemic condition and clear staging are conducive to a more accurate prognosis.

CRediT author statement

Tien Manh Hoang: Conceptualisation, Methodology, Writing, Reviewing and Editing; Thi Thanh Nguyen: Conceptualisation, Writing and Editing.

ACKNOWLEDGEMENTS

The authors would like to thank all of members of the SEER Program tumour registries for their efforts in the establishment of the SEER database.

COMPETING INTERESTS

The authors declare that there is no conflict of interest regarding the publication of this article.

REFERENCES

[1] R.L. Siegel, K.D. Miller, H.E. Fuchs, et al. (2021), "Cancer statistics", *CA: A Cancer Journal for Clinicians*, **71(1)**, pp.7-33, DOI: 10.3322/caac.21654.

[2] D.H. Pham, V.T. Tran, T.C. Dang, et al. (2009), "Cancer registry results in some regions in Vietnam in the 2006-2007 period", *Ho Chi Minh City Medicine*, **13(5)**, pp.53-64 (in Vietnamese).

[3] National Cancer Institute (2016), "SEER cancer statistics review, 1975-2013", https://seer.cancer.gov/archive/csr/1975_2013/, accessed 25 April 2021.

[4] T. Sher, G.K. Dy, A.A. Adjei (2008), "Small cell lung cancer", *Mayo Clin. Proc.*, **83(3)**, pp.355-367, DOI: 10.4065/83.3.355.

[5] V.W. Chen, B.A. Ruiz, M.C. Hsieh, et al. (2014), "Analysis of stage and clinical/prognostic factors for lung cancer from SEER registries: AJCC staging and collaborative stage data collection system", *Cancer*, **120(S23)**, pp.3781-3792, DOI: 10.1002/cncr.29045.

[6] S.L. Wood, M. Pernemalm, P.A. Crosbie, et al. (2014), "The role of the tumor-microenvironment in lung cancer-metastasis and its relationship to potential therapeutic targets", *Cancer Treat. Rev.*, **40(4)**, pp.558-56, DOI: 10.1016/j.ctrv.2013.10.001.

[7] R. Kitadai, Y. Okuma, T. Hakozaki, et al. (2020), "The efficacy of immune checkpoint inhibitors in advanced non-small-cell lung cancer with liver metastases", *J. Cancer Res. Clin. Oncol.*, **146(3)**, pp.777-785, DOI: 10.1007/s00432-019-03104-w.

[8] H. Rief, T. Muley, T. Bruckner, et al. (2014), "Survival and prognostic factors in non-small cell lung cancer patients with spinal bone metastases: A retrospective analysis of 303 patients", *Strahlenther. Onkol.*, **190(1)**, pp.59-63, DOI: 10.1007/s00066-013-0431-1.

[9] E. Schapira, H. Hubbeling, B.Y. Yeap, et al. (2018), "Improved overall survival and locoregional disease control with concurrent PD-1 pathway inhibitors and stereotactic radiosurgery for lung cancer patients with brain metastases", *Int. J. Radiat. Oncol. Biol. Phys.*, **101(3)**, pp.624-629, DOI: 10.1016/j.ijrobp.2018.02.175.

[10] S.Y. Sung, S.W. Lee, Y.K. Kwak, et al. (2018), "Intracranial control and survival outcome of tyrosine kinase inhibitor (TKI) alone versus TKI plus radiotherapy for brain metastasis of epidermal growth factor receptor-mutant non-small cell lung cancer", *J. Neurooncol.*, **139(1)**, pp.205-213, DOI: 10.1007/s11060-018-2861-1.

[11] Y.F. He, H.Q. Luo, W. Wang, et al. (2015), "Clinical features and prognosis-associated factors of non-small cell lung cancer exhibiting symptoms of bone metastasis at the time of diagnosis", *Oncol. Lett.*, **9(6)**, pp.2706-271, DOI: 10.3892/ol.2015.3081.

[12] C. Zhang, C. Liao, B.C. Penney, et al. (2015), "Relationship between overall survival of patients with non-small cell lung cancer and whole-body metabolic tumor burden seen on postsurgical fluorodeoxyglucose PET images", *Radiology*, **275(3)**, pp.862-869, DOI: 10.1148/radiol.14141398.

[13] N. Duma, R.S. Davila, J.R. Molina (2019), "Non-small cell lung cancer: Epidemiology, screening, diagnosis, and treatment", *Mayo Clin. Proc.*, **94(8)**, pp.1623-1640, DOI: 10.1016/j.mayocp.2019.01.013.

[14] M. Tonnies, J. Kollmeier, T.T. Bauer, et al. (2012), "Curative surgical treatment options for patients with non-small cell lung cancer (NSCLC) and solitary pulmonary metastasis", *Pneumologie*, **66(4)**, pp.218-223, DOI: 10.1055/s-0032-1308917.

[15] M. Reck, T.K. Mok, M. Nishio, et al. (2019), "Atezolizumab plus bevacizumab and chemotherapy in non-small-cell lung cancer (IMpower150): Key subgroup analyses of patients with EGFR mutations or baseline liver metastases in a randomised, open-label phase 3 trial", *Lancet. Respir. Med.*, **7(5)**, pp.387-401, DOI: 10.1016/S2213-2600(19)30084-0.

[16] P.C. Tumeh, M.D. Hellman, O. Hamid, et al. (2017), "Liver metastasis and treatment outcome with anti-PD-1 monoclonal antibody in patients with melanoma and NSCLC", *Cancer Immunol. Res.*, **5(5)**, pp.417-424, DOI: 10.1158/2326-6066.CIR-16-0325.

[17] C. Kan, G. Vargas, F.L. Pape, et al. (2016), "Cancer cell colonisation in the bone microenvironment", *Int. J. Mol. Sci.*, **17(10)**, DOI: 10.3390/ ijms17101674.

[18] V. Ernani, T.E. Stinchcombe (2019), "Management of brain metastases in non-small-cell lung cancer", *J. Oncol. Pract.*, **15(11)**, pp.563-570, DOI: 10.1200/JOP.19.00357.

DOI: 10.31276/VJSTE.64(1).39-42

Study on association between *SLC2A9* rs3733591 and Gout susceptibility in 481 Vietnamese individuals

Pham Quang Hung[1], Nguyen Xuan Canh[2], Nguyen Thuy Duong[1, 3*]

[1]*Institute of Genome Research, Vietnam Academy of Science and Technology, 18 Hoang Quoc Viet Street, Nghia Do Ward, Cau Giay District, Hanoi, Vietnam*

[2]*Vietnam National University of Agriculture, Trau Quy Town, Gia Lam District, Hanoi, Vietnam*

[3]*Graduate University of Science and Technology, Vietnam Academy of Science and Technology, 18 Hoang Quoc Viet Street, Nghia Do Ward, Cau Giay District, Hanoi, Vietnam*

Received 4 December 2021; revised 3 January 2022; accepted 26 January 2022

Abstract:

Gout is a common form of inflammatory arthritis that is strongly associated with elevated uric acid concentration in the blood. The development of the disease is not only triggered by environmental factors but also genetic variations. Previous studies demonstrated that the genetic associations with gout vary in different populations in the world. This study aimed to identify the relationship between *SLC2A9* rs3733591 and gout susceptibility in the Vietnamese population. Total DNAs were extracted from 481 blood samples including 160 patients with gout and 321 age-matched healthy controls. The genotyping of *SLC2A9* rs3733591 was performed using polymerase chain reaction-restriction fragment length polymorphism (PCR-RFLP). Chi-squared test was used to test whether the genotypes frequencies of rs3733591 follow Hardy-Weinberg equilibrium (HWE) and to check its association with gout in three models (additive, recessive, dominant) and allele form. The result showed that *SLC2A9* rs3733591 was in agreement with Hardy-Weinberg equilibrium (p>0.05). However, there was no association between the rs3733591 and gout in any tested models (p>0.05). This study will contribute to the genetic study of gout susceptibility in Vietnam.

Keywords: **Gout, PCR-RFLP, rs3733591, *SLC2A9*, Vietnam.**

Classification numbers: **3.2, 3.5**

1. Introduction

Gout is common inflammatory arthritis associated with severe co-morbidities including cardiovascular diseases, chronic kidney diseases, obesity, and type 2 diabetes [1]. Gout might result from high serum urate levels (hyperuricemia) and accumulation of monosodium urate crystals in the joints and soft tissues. Based on the patient's fractional excretion of urate clearance (urate clearance/creatinine clearance ratio, FEUA) and urinary urate excretion (UUE), gout is classified into two distinct types: renal overload (ROL) and renal underexcretion (RUE) [2]. Gout patients often suffer from throbbing, burning, pain, swelling, warmth, redness, and difficulty moving the affected joint due to inflammation. Besides, gout is commonly encountered in middle-aged male patients. In Vietnam, the rate of gout was 0.14% of the population in 2003 [3]; 1.0% of the population (940,000 patients) in 2014 include: 96% were men, 38% were in their 40s, with 75% in the working age. In addition, the development of gout disease is caused not by only environmental factors, a high protein diet, and alcohol use, but also genetic factors. Therefore, research on the inherited cause of gout is extremely important especially when the disease significantly impacts the working-age population's performance and work quality. For the last two decades, Genome-Wide Association Studies (GWAS), replication studies, and meta-analyses have broadened our knowledge of common genetic variants with a predisposition to gout. The discovery of these novel genes has substantially increased our understanding of the role of renal urate transporters in the pathogenesis of gout [4]. In particular, the solute carrier family 2 member 9 (also known as SLC2A9) plays an important role in the cause of gout.

SLC2A9, located on chromosome 4p16.1, contains 12 exons spanning over 195 Kb. The gene product is a member of the GLUT family of transport facilitators, consisting of monosaccharides and polyol transporters that can carry other small carbon compounds across the plasma membranes [5]. The SLC2A9 gene encodes

*Corresponding author: Email: tdnguyen@igr.ac.vn

GLUT9, which is a membrane-spanning protein from the significant facilitator transporter superfamily and includes elements of sugar transporters. In one study, GLUT9 proteins behave as an exchange transporter exchanging uric acid for glucose and fructose [6]. Still, it most likely mediates the efflux of urate under physiological circumstances in the proximal tubule cells [7]. The effect of variations in SLC2A9 is most pronounced in females, in whom it accounts for approximately 6% of the variance of serum urate compared to 2% in males [8]. Besides, multiple genetic studies suggest that mutations in the SLC2A9 gene are linked with gout risk in different populations. For example, rs16890979 (V253I) was associated with gout in a GWAS of US Caucasian population [9], which was replicated in several studies of New Zealand Māori, Pacific island, Caucasian [10], Spanish [11], and Chinese populations [12]. Another variant, rs6449213, was associated with gout in Germany [13] and the US populations [9]. Among the studied polymorphisms, rs3733591 was frequently investigated and generated inconsistent results in different populations (Chinese, Solomon Islanders, Japanese, New Zealander, Maylay). To the best of our knowledge, no study has been performed to assess the correlation between *SLC2A9* rs3733591 and gout susceptibility in the Vietnamese population. Therefore, to understand the relationship of *SLC2A9* rs3733591 with gout in the Vietnamese population, we conducted a case-control association study of this variant in Vietnamese people.

2. Materials and methods

2.1. Study subjects

A total of 481 subjects, including 160 male patients with gout and 321 healthy controls, were enrolled at Dai Phuoc general clinic, Ho Chi Minh city. Gout patients were diagnosed following the criteria of the American College of Rheumatology [14]. Controls were males, age-matched healthy individuals, and recruited randomly from annual health checks with no family history of diabetes or gout. The study was approved by the Institutional Review Board of the Institute of Genome Research, Vietnam Academy of Science and Technology (No. 1-2017/NCHG-HDDD).

2.2. Methods

DNA extraction: total DNA was extracted from blood samples using the Kit GeneJET Whole Blood Genomic DNA Purification (Thermo Fisher Scientific) following the manufacturer's protocol. After isolation, total DNA samples were checked by electrophoresis in agarose gel. Additionally, the quality and quantity of total DNA were assessed using a Nanodrop 2000c spectrophotometer (Thermo Scientific). DNA samples were then diluted to a concentration of 10 ng/µl to obtain standard working samples that were stored at -20°C.

Genotyping of SLC2A9 rs3733591 using PCR-RFLP: to genotype *SLC2A9* rs3733591, polymerase chain-reaction-restriction fragment length polymorphism (PCR-RFLP) was performed using specific primers. The primer sequences will be provided upon request. Reaction components included 10 ng DNA, 0.25 mmol each dNTP (Thermo Fisher Scientific), 0.25 U Taq DNA polymerase (Thermo Fisher Scientific), 5 pmol primers (per each direction), Dream Taq Buffer (Thermo Fisher Scientific). The PCR cycle was as follows: 94°C - 4 min; 30 cycles of 94°C - 15 s, 62°C - 15 s, 72°C - 30 s; 72°C - 8 min; kept at 4°C.

PCR products were then digested with restriction enzyme *Bst*UI (Thermo Fisher Scientific). Reaction components included 1 µl of Buffer R, 3 µl of PCR product, 1U *Bst*UI, and water added to 10 µl. The mixture was incubated at 37°C in a water bath for 4-6 h. Digested products were further assessed using electrophoresis of 2.5% agarose gel. Depending on the number of DNA bands acquired from enzymatic digestion of PCR products, the genotypes of *SLC2A9* rs3733591 are summarized and given in Table 1. In addition, 10% of randomly selected subjects were confirmed by Sanger sequencing.

Table 1. Number and size of DNA bands of 3 genotypes of *SLC2A9* rs3733591.

Genotypes	Number of DNA bands	Size of DNA bands (bp)
CC	2	219, 177
CT	3	396, 219, 177
TT	1	396

Statistical analysis: the obtained data were analysed using SPSS version 20. Chi-squared test (χ^2) was used to test whether allele distribution follows Hardy-Weinberg equilibrium (HWE). Association between polymorphic genotype with gout was assessed in three test models (additive, dominant, and recessive) and estimated by OR (odds ratio) with 95% confidence intervals. The estimation was considered to be statistically significant if the p-value was less than 0.05.

3. Results

3.1. Genotype identification of polymorphism SLC2A9 rs3733591

A total of 481 subjects, including 160 gout patients and 321 controls, were used to amplify the region containing polymorphism rs3733591 using PCR. The PCR products were digested with the restriction enzyme *Bst*UI (Fig. 1).

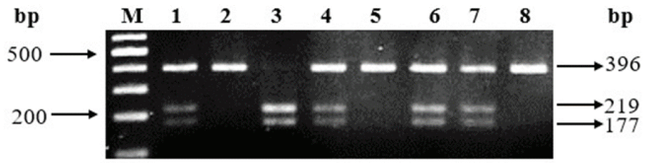

Fig. 1. Image of eight *Bst*UI-digested PCR products on 2.5% agarose gel. M: marker 100 bp; 1,4,6,7: genotype CT (3 bands with 396 bp, 219 bp and 177 bp); 2,5,8: genotype TT (396 bp); 3: genotype CC (two bands with 219 bp and 177 bp).

The frequencies of genotypes and alleles *SLC2A9* rs3733591 from all 481 samples were summarized in Table 2. Allele C (minor allele) was less common than allele T in the studied population with frequencies of 0.353 and 0.647. The distribution of 3 genotypes of polymorphism *SLC2A9* rs3733591 followed Hardy-Weinberg equilibrium (HWE) with a *p*-value of 0.07.

Table 2. Information on *SLC2A9* rs3733591 genotypes and allele frequency.

	Genotype			Allele		HWE in the studied population
	CC	*CT*	*TT*	*C*	*T*	
Case	19	72	69	0.344	0.656	
Control	50	130	141	0.358	0.642	0.07
Total	69	202	210	0.353	0.647	

Note: Hardy-Weinberg equilibrium (HWE) checked by Chi-squared test.

After genotyping using RFLP, 10% of samples were verified using Sanger sequencing. The results showed 100% concordance of observed genotypes obtained from PCR-RFLP and Sanger sequencing (Fig. 2).

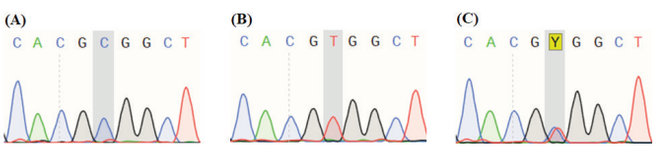

Fig. 2. Genotyping *SLC2A9* rs3733591 using Sanger sequencing. (A) genotype CC; **(B)** genotype TT; **(C)** genotype CT.

3.2. Analysis of the correlation between SLC2A9 rs3733591 and gout

To evaluate the association between the genotypes and alleles of *SLC2A9* rs3733591 and gout, we performed statistical analyses in 3 test models: additive, dominant, and recessive (Table 3). The results showed that the *p*-values of the three models were all higher than 0.05 ($p>0.05$) meaning no significant difference was detected. Furthermore, when analysing the correlation between alleles of *SLC2A9* rs3733591 with gout, the *p*-value obtained was 0.658, so the allele of rs3733591 was not associated with gout risk in the studied population.

Table 3. Association of *SLC2A9* rs3733591 with gout.

Test model	Controls (n=321)	Gout patients (n=160)	OR	95% CI	*p*-value
		Additive			
CC	50 (15.6%)	19 (11.9%)	1.000		
CT	130 (40.5%)	72 (45%)	1.458	0.799-2.66	0.220
TT	141 (43.9%)	69 (43.1%)	1.269	0.695-2.318	0.438
		Recessive			
CC	50 (15.6%)	19 (11.9%)	1.000		
CT + TT	271 (84.4%)	141 (88.1%)	1.369	0.777-2.411	0.277
		Dominant			
CC + CT	180 (56.1%)	91 (56.9%)	1.000		
TT	141 (43.9%)	69 (43.1%)	1.033	0.705-1.515	0.868
		Allele			
C	230 (35.8%)	110 (34.4%)	1.000		
T	412 (64.2%)	210 (65.6%)	1.065	0.804-1.412	0.658

Note: n: number of participants; 95% CI: 95% confidence interval of odds ratio; *p*-values calculated from Chi-squared test, OR: odds ratio.

4. Discussion

Gout is a common form of arthritis in Vietnam and around the world. In addition to environmental factors such as risks from alcohol use, drugs, high-protein diets, obesity, hypertension, *etc.*, genetic factors also play an important role in the development of gout. Genome-wide association studies (GWAS) and meta-analyses have identified several genes associated with gout susceptibility such as *ABCG2, SLC22A12, SLC17A1, etc.* Among these, the *SLC2A9 (GLUT9)* gene is a known risk factor for gout among different populations worldwide. *SLC2A9*, a facilitated glucose transporter family member, is a voltage-dependent urate transporter with a not yet fully elucidated role in uric acid homeostasis. In humans, the main function of the *SLC2A9* gene is in the efflux of reabsorbed uric acid from the proximal tubule cells of the kidney toward the blood. Therefore, when a mutation occurs in the *SLC2A9* gene, it is likely to increase uric acid reabsorption and blood uric acid level. In *SLC2A9*, the variant R265H (rs3733591) occurs in many populations in different regions worldwide, with the highest allele frequency in the East Asian populations (T=0.6692) followed by the South Asian populations (T=0.3625) and the lowest in the European populations (T=0.2388). Besides that, R265H has previously been demonstrated

to be associated with gout among Han Chinese in Taiwan (p=0.008) and Solomon Islanders (p=0.0045) [15]. It was also associated with the development of gout in Japanese males (OR=1.52, 95% CI 1.19-1.95, p=7.3×10^{-4}) [16]. In contrast, rs3733591 was not associated with gout susceptibility in New Zealander populations [17], Chinese Han [18], Minnan populations in China [19], or Maylay populations [20]. Similarly, we did not find any association of the polymorphism with gout susceptibility in the current study of the Vietnamese population (p>0.05). Such inconsistency could be explained by genetic background, environmental factors, or lifestyle differences.

5. Conclusions

In the current study, we identified the genotypes of *SCL2A9* rs3733591 in the Vietnamese population using PCR-RFLP. Statistical analysis showed that rs3733591 was not associated with gout disease. This data could be used for further in-depth studies on the relationship between polymorphisms and gout in the Vietnamese population.

CRediT author statement

Pham Quang Hung: Data curation, Writing - Original draft preparation, Editing; Nguyen Xuan Canh: Conceptualisation, Methodology and Writing; Nguyen Thuy Duong: Conceptualisation, Methodology, Software, Writing and Editing.

ACKNOWLEDGEMENTS

This study was conducted with funding from Vietnam Academy of Science and Technology under project NCVCC 40.01/21-21 and with support from Institute of Genome Research, Vietnam Academy of Science and Technology.

COMPETING INTERESTS

The authors declare that there is no conflict of interest regarding the publication of this article.

REFERENCES

[1] P.C. Robinson, S. Horsburgh (2014), "Gout: Joints and beyond, epidemiology, clinical features, treatment and co-morbidities", *Maturitas*, **78(4)**, pp.245-251, DOI: 10.1016/j.maturitas.2014.05.001.

[2] A. Nakayama, H. Nakaoka, K. Yamamoto, et al. (2017), "GWAS of clinically defined gout and subtypes identifies multiple susceptibility loci that include urate transporter genes", *Ann. Rheum. Dis.*, **76(5)**, pp.869-877, DOI: 10.1136/annrheumdis-2016-209632.

[3] T.T.M. Hoa, J. Darmawan, S.L. Chen, et al. (2003), "Prevalence of the rheumatic diseases in urban Vietnam: A WHO-ILAR COPCORD study", *Journal of Rheumatology*, **30(10)**, pp.2252-2256.

[4] A.M. Reginato, D.B. Mount, I. Yang, et al. (2012), "The genetics of hyperuricaemia and gout", *Nature Reviews Rheumatology*, **8(10)**, pp.610-621, DOI: 10.1038/nrrheum.2012.144.

[5] B. Thorens, M. Mueckler (2014), "The SLC2 (GLUT) family of membrane transporters", *Mol. Aspects Med.*, **34(2-3)**, pp.121-138, DOI: 10.1016/j.mam.2012.07.001.

[6] M.J. Caulfield, P.B. Munroe, D. O'Neill, et al. (2008), "SLC2A9 is a high-capacity urate transporter in humans", *PLoS Med.*, **5(10)**, pp.1509-1523, DOI: 10.1371/journal.pmed.0050197.

[7] N. Anzai, K. Ichida, P. Jutabha, et al. (2008), "Plasma urate level is directly regulated by a voltage-driven urate efflux transporter URATv1 (SLC2A9) in humans", *J. Biol. Chem.*, **283(40)**, pp.26834-26838, DOI: 10.1074/jbc.C800156200.

[8] T.R. Merriman (2019), "Genetics of hyperuricemia and gout", *Gout*, Elsevier, pp.9-27.

[9] A. Dehghan, A. Kottgen, Q. Yang, et al. (2008), "Association of three genetic loci with uric acid concentration and risk of gout: A genome-wide association study", *Lancet*, **372(9654)**, pp.1953-1961, DOI: 10.1016/S0140-6736(08)61343-4.

[10] J.E. Hollis-Moffatt, X. Xu, N. Dalbeth, et al. (2009), "Role of the urate transporter SLC2A9 gene in susceptibility to gout in New Zealand Māori, Pacific island, and Caucasian case-control sample sets", *Arthritis Rheum.*, **60(11)**, pp.3485-3492, DOI: 10.1002/art.24938.

[11] R.J. Torres, E. de Miguel, R. Bailen, et al. (2014), "Tubular urate transporter gene polymorphisms differentiate patients with gout who have normal and decreased urinary uric acid excretion", *J. Rheumatol.*, **41(9)**, pp.1863-1870, DOI: 10.3899/jrheum.140126.

[12] Z. Dong, J. Zhou, S. Jiang, et al. (2017), "Effects of multiple genetic loci on the pathogenesis from serum urate to gout", *Sci. Rep.*, **7(1)**, DOI: 10.1038/srep43614.

[13] K. Stark, W. Reinhard, K. Neureuther, et al. (2008), "Association of common polymorphisms in GLUT9 gene with gout but not with coronary artery disease in a large case-control study", *PLoS One*, **3(4)**, DOI: 10.1371/journal.pone.0001948.

[14] T. Neogi, T.L.T.A. Jansen, N. Dalbeth, et al. (2015), "2015 goutclassification criteria: An American college of Rheumatology/European league against Rheumatism collaborative initiative", *Arthritis Rheumatol.*, **67(10)**, pp.2557-2568, DOI: 10.1002/art.39254.

[15] H.P. Tu, C.J. Chen, S. Tovosia, et al. (2010), "Associations of a non-synonymous variant in SLC2A9 with gouty arthritis and uric acid levels in Han Chinese subjects and Solomon Islanders", *Ann. Rheum. Dis.*, **69(5)**, pp.887-890, DOI: 10.1136/ard.2009.113357.

[16] W. Urano, A. Taniguchi, N. Anzai, et al. (2010), "Association between GLUT9 and gout in Japanese men", *Annals of the Rheumatic Diseases*, **69(5)**, pp.932-933, DOI: 10.1136/ard.2009.111096.

[17] J.E. Hollis-Moffatt, P.J. Gow, A.A. Harrison, et al. (2011), "The SLC2A9 nonsynonymous Arg265His variant and gout: Evidence for a population-specific effect on severity", *Arthritis Res. Ther.*, **13(3)**, DOI: 10.1186/ar3356.

[18] W. Wan, X. Xu, D.B. Zhao, et al. (2015), "Polymorphisms of uric transporter proteins in the pathogenesis of gout in a Chinese Han population", *Genet. Mol. Res.*, **14(1)**, pp.2546-2550, DOI: 10.4238/2015.March.30.13.

[19] C. Zheng, H. Yang, Q. Wang, et al. (2016), "Association analysis of five SNP variants with gout in the Minnan population in China", *Turkish J. Med. Sci.*, **46(2)**, pp.361-367, DOI: 10.3906/sag-1409-58.

[20] W.R.W. Taib, A. Mahfudzah, M.Y. Nazihah, et al. (2018), "Association of solute carrier family 2, member 9 (SLC2A9) genetic variant rs3733591 with gout in a Malay sample set", *Med. J. Malaysia*, **73(5)**, pp.307-310.

DOI: 10.31276/VJSTE.64(1).43-48

Phytochemical analysis and correlation of total polyphenol content and antioxidant properties of *Symplocos cochinchinensis* leaves

Hai Trieu Ly[1], Vu Khanh Trang Le[2], Van Minh Le[1], Cong Sanh Phan[3], Chau Tuan Vo[2], Minh Ly Nguyen[2], Thi Anh Dao Phan[4*]

[1]*Research Center of Ginseng and Medicinal Materials, National Institute of Medicinal Materials, 41 Dinh Tien Hoang Street, Ben Nghe Ward, District 1, Ho Chi Minh City, Vietnam*

[2]*University of Science and Education, The University of Danang, 459 Ton Duc Thang Street, Hoa Khanh Nam Ward, Lien Chieu District, Da Nang City, Vietnam*

[3]*Management Board of Cham Islands MPA, 3 Nguyen Hue Street, Minh An Ward, Hoi An City, Quang Nam Province, Vietnam*

[4]*Faculty of Chemical and Food Technology, Ho Chi Minh City University of Technology and Education, 1 Vo Van Ngan Street, Thu Duc City, Ho Chi Minh City, Vietnam*

Received 28 January 2021; revised 17 February 2021; accepted 15 March 2021

Abstract:

This study successfully screened phytochemicals to determine their total polyphenols content (TPC) by Folin-Ciocalteu reagents and to evaluate antioxidant activity using DPPH scavenging, ABTS cation decolorization, and reducing power assays of various extracts of *Symplocos cochinchinensis* leaves. A correlation between TPC and antioxidant activity was analysed by Pearson's method. The results indicated that *S. cochinchinensis* leaves contained triterpenoids, alkaloids, anthraglycosides, flavonoids, anthocyanosides, proanthocyanidins, polyphenols, tannins, saponins, polyuronics, and reducing agents. All extracts had antioxidant properties with the ethyl acetate fraction exhibiting the highest antioxidant capacity, which had the lowest IC_{50} in DPPH (83.33 µg/ml), an ABTS of 46.21 µg/ml, and EC_{50} of 69.10 µg/ml in reducing power. There was a significant negative correlation between the TPC in *S. cochinchinensis* leaf extracts and their IC_{50} and EC_{50} values of antioxidant activity. It was suggested that *S. cochinchinensis* leaves have a great potential for antioxidant activity based on its high total polyphenol content and potential for use as a traditional treatment.

Keywords: **antioxidant activity, correlation, phytochemicals, polyphenols, *S. cochinchinensis* leaves.**

Classification number: **3.3**

1. Introduction

Oxidative damage is initiated by free radicals and reactive oxygen species (ROS) or reactive nitrogen species (RNS) that are produced by the normal aerobic metabolism of organisms. The oxidative reaction causes protein and lipid oxidation as well as DNA damage related to various diseases such as age-associated degenerative psychological disorders, atherosclerosis, cirrhosis, cancer, arthritis, diabetes, and haemorrhagic shock [1]. Molecular antioxidants have the ability to inhibit oxidation and these natural antioxidant sources have been receiving much attention not only because they lack the toxicity of synthetic ones such as butylated hydroxyanisole (BHA) and butylated hydroxytoluene (BHT) but also they bring positive health effects [2]. Therefore, antioxidants not only protect ourselves against the products of oxidative damage to DNA, proteins, or lipids; but also play a vital role in the prevention of diseases such as cancer, cardiovascular disease, Alzheimer's disease, and muscular degeneration by scavenging free radicals [3]. Recently, there has been increasing interest in plant-derived extracts or compounds with antioxidant capacity for an alternative treatment with minor side effects. Medicinal plants that are especially rich in their polyphenol content have been widely recognized as potent antioxidants [4, 5]. Polyphenols, a secondary metabolite found abundantly in plants, play an important role in the defence against free radicals. Several parts of medicinal plants, such as flavonoids, tannins, stilbenes, and coumarins, are rich in phenolic compounds. The antioxidant properties of polyphenols are due to their redox properties, which allow them to act as reducing agents, hydrogen donators, metal chelators, and single oxygen quenchers [6]. Polyphenols possess a wide range of biological activities including antioxidant, anti-inflammatory, antidiabetic, antiallergic, hepatoprotective, anticancer, and other effects and many

*Corresponding author: Email: daopta@hcmute.edu.vn

of these biological functions have been attributed to their free radical quenching and antioxidant activity. Because of these beneficial effects for health, research on natural antioxidants derived from plants has intensified [7, 8].

Symplocos cochinchinensis (Lour.) Moore ssp. *Laurina* (Retz.) Nooteb. Symplocos laurina (*S. cochinchinensis*) belonging to the family Symploceaceae is widely distributed in many tropical and subtropical areas around the world including Vietnam. The plant is commonly used in folk medicine for the treatment of various disorders like leprosy, tumours, diarrheal, dysentery, menorrhagia, inflammation, and uterine problems [9]. Many plants in the *Symplocos* species have been used to treated various diseases based on their biological activities that include anti-diabetic, anti-HIV, antimicrobial, anti-inflammatory, antioxidant, and antitumor applications [4]. However, scientific reports on the biological potential of this indigenous Vietnamese plant are not widely available. Therefore, the present study was conducted to comprehensively study both chemical composition and biological activities of *S. cochinchinensis* collected from Cham island, Quang Nam province, Vietnam. Specifically, this study systematically evaluated *in vitro* antioxidant activities as well as determined the total polyphenol content of crude extracts and different fractions of *S. cochinchinensis* extracts to screen for potential medicinal application. Furthermore, the present study is the first to investigate the correlation between polyphenol content and the antioxidant activities of various extracts from *S. cochinchinensis* leaves.

2. Materials and methods

2.1. Plant materials

The plant samples were collected in August 2019 from Cham island, Quang Nam province, and identified and authenticated by BSc. Tran Ngoc Toan of the Greenviet Biodiversity Conservation Centre and checked again by the Southern Institute of Ecology, Vietnam Academy of Science and Technology where a voucher specimen was deposited for *Symplocos cochinchinensis* (Lour.) Moore ssp. *Laurina* (Retz.) Nooteb. Before grinding into the fine powder, the leaves were cleaned with tap water followed by distilled water, then they were air dried to the standard of loss on drying (LOD) following the Vietnam Pharmacopoeia 5th edition. The samples were stored in a sealed bag (Sample code: TTS-SC-0819) at the Research Center of Ginseng and Medicinal Materials in Ho Chi Minh city, Vietnam.

2.2. Chemicals

Gallic acid, Folin-Ciocalteu's phenol reagent, DPPH reagent (1,1-diphenyl-2-picrylhydrazyl), ABTS reagent (2,2′-azino-bis(3-ethylbenzothiazoline-6-sulfonic acid) diammonium salt), trichloroacetic acid, and ascorbic acid were purchased from Sigma-Aldrich® Co. Ltd (USA). Potassium ferricyanide and sodium carbonate were purchased from China of the highest grade. *n*-hexane, chloroform, ethyl acetate, *n*-butanol, and methanol were obtained from Chemsol, Co. Ltd, Vietnam. Ethanol 96% was collected from OPC Pharmaceutical Company, Vietnam.

2.3. Extraction and fractionation

The crude extract (SCT) was obtained by using 45% ethanol to extract dried to a powdered material (Moisture is 9.73±0.41%) with a material/solvent ratio of 1/15 (g/ml) at room temperature for 24 h in a percolator apparatus. Then, the extract was collected at a rate of 2 ml/min and concentrated using a rotary evaporator at 60°C under reduced pressure.

To prepare fractionated extracts, the crude extract (moisture 15.50±0.34%) was solubilized in distilled water and sequentially extracted with solvents of increasing polarity (*n*-hexane, chloroform, ethyl acetate, and *n*-butanol). Then, the extract solutions were evaporated under reduced pressure conditions to dry and recover fractionated extract including *n*-hexane (SCH), chloroform (SCC), ethyl acetate (SCE), *n*-butanol (SCB), and water (SCW) extracts were obtained as fractional extracts. The percentage yield of crude and fractionated extracts of *S. cochinchinensis* leaves was 23.04% (SCT), 10.91% (SCH), 12.64% (SCC), 25.46% (SCE), 23.97% (SCB), 17.17% (SCW). The crude and fractionated extracts were preserved in sterilized vials and stored at 4°C.

The extraction yield of SCT was estimated using the expression: $H(\%)=(m\times(1-a))/(M\times(1-A))\times100$, where H is the extraction yield (%), m is the mass of the crude extract (g), M is the mass of the dried powder (g), a is the moisture of the crude extract (%), and A is the moisture of the dried powder (%). The extraction yield of fractionated extracts was estimated using the expression: $H(\%)=m/(M\times(1-A))\times100$, in which H is the extraction yield (%), m is the mass of the fractionated extract (g), M is mass of the crude extract (g), and A is the moisture of the crude extract (%).

2.4. Preliminary qualitative phytochemical screening

Preliminary qualitative phytochemical screening proceeded to identify the presence of phytochemicals in *S. cochinchinensis* leaves. The preliminary screening was carried out by I. Ciulei's method (1982) [10] with some modifications. The extracts of *S. cochinchinensis* leaves including diethyl ether, ethanol, and aqueous extracts were tested for secondary compounds like alkaloids, flavonoids, tannins, triterpenoids, saponins,

coumarins, anthraquinones, anthocyanosides, proanthocyanidins, lipids, volatile oils, carotenoids, reducing agents, polyuronics, and organic acids.

2.5. Determination of total polyphenol content

The total polyphenol content (TPC) of *S. cochinchinensis* leaf extracts were determined by a previously described method using Folin-Ciocalteu's reagent and gallic acid was used as a standard [11]. Briefly, 200 µl of test extract was mixed with 500 µl of Folin-Ciocalteu's reagent in 6 ml of double-distilled water. After 5 min, 1.5 ml of 20% *w/v* sodium carbonate solution was poured into this mixture and the volume was topped off to 10 ml with distilled water. The reaction was kept for 2 h at room temperature in the dark. The absorbance was measured at 758 nm and all measurements were made in triplicate. The TPC was calculated using the linear regression equation of gallic acid and expressed as mg gallic acid equivalent per 1 gram of dry weight (mg GAE/g d.w.).

2.6. In vitro antioxidant activity assay

DPPH radical scavenging assay: A DPPH free radical quenching assay was used to evaluate the antioxidant activity of *S. cochinchinensis* leaf extracts based on a previously described method [12]. Briefly, 4 ml of reaction mixture consisting of 0.5 ml of different concentrations of test extract or positive control and 0.5 ml of 0.6 mM DPPH reagent in methanol was incubated at room temperature for 30 min in the dark. The absorbances were measured at 515 nm using a Spectro UV-2550 spectrophotometer. DPPH inhibitory activity was expressed as the percentage inhibition (I%) of DPPH and calculated as (1-B/A)×100, where A and B are the absorbance of the blank (without test extract) and the sample (with test extract), respectively. IC_{50} (inhibitory concentration, 50%) values were calculated from the mean values of data from three trials. Ascorbic acid (vitamin C) at various concentrations (62.5, 125, 250, 500, 1000 µM) was used as a positive control.

ABTS radical cation decolorization assay: The ABTS antioxidant test was carried out according to the following description [13]. To start, a 7 mM ABTS solution was added to a 2.45 mM potassium persulfate solution and the mixture was incubated in the dark for 16 h at room temperature. Then, the solution was diluted by mixing 1 ml of ABTS solution with 50 ml of methanol to obtain an absorbance of 0.70±0.05 units at 734 nm using a spectrophotometer (Spectro UV-2550). Next, 20 µl of the test sample at various concentrations or the positive control was mixed with 980 µl of ABTS solution. The absorbance was measured at 734 nm after 6 min at room temperature. All samples were done in triplicate and the average of each sample was calculated. The results were expressed as an IC_{50} value for each sample from the proportion of the radical quenching activity, which was calculated by the formula: (%ABTS quenching activity)=(1-B/A)×100, where A and B are the absorbance of the blank (without test extract) and the sample (with test extract), respectively. Again, ascorbic acid at various concentrations (125, 250, 500, 750, 1000 µM) was used as a positive control.

Reducing power assay: The reducing property of all extracts was determined by assessing the ability of the extracts to reduce a $FeCl_3$ solution as described by M. Oyaizu [14]. The mixture including 0.2 ml aliquot, 0.5 ml of 200 mM sodium phosphate buffer (pH 6.6), and 0.5 ml potassium ferricyanide 1% was incubated at 50°C for 30 min, then 0.5 ml trichloroacetic acid 10% was added and centrifuged at 3000 rpm for 10 min. A volume of 0.5 ml of supernatant was mixed with equal volume double-distilled water and 0.1 ml ferric chloride 0.1%. The absorbance was measured at 700 nm. Ascorbic acid at various concentrations (31.25, 62.5, 125, 250, 500 µM) was used as a positive control. The reducing power activity was subsequently analysed via optical density and EC_{50} values. The lower the optical density value, the weaker the reduction activity of the sample. The EC_{50} value is the concentration of effective antioxidants for an absorbance of 0.5, which was calculated through the equation illustrating the correlation between the concentration of the sample and its optical density.

2.7. Data analysis

All experiments were carried out in triplicate. The obtained results were expressed in terms of mean ± SD (standard deviation) and the data were analysed by Graphpad Prism software (version 8, Inc., La Jolla, CA, USA) using the T-test and one-way ANOVA. The correlation coefficient (r) and coefficient of determination (R^2) were determined by the Pearson test, using Graphpad Prism software (version 8, Inc., La Jolla, CA, USA). P values <0.05 were considered statistically significant.

3. Results and discussion

3.1. Phytochemical analysis of S. cochinchinensis leaves

Phytochemical screening gives an idea concerning the chemical nature of the constituents that have biological effects present in extracts of medicinal materials. Therefore, it is useful for predicting the existence of crude products and also valuable for the detection of constituents present in samples. The presence of such essential phytochemical groups in this medicinal herb indicates its therapeutic properties and validates some its wide range of ethnomedicinal uses. Three extracts consisting of diethyl ether, ethanol, and aqueous were screened for

qualitative chemical tests to identify various secondary metabolites presenting in the leaf of *S. cochinchinensis*. The results in Table 1 showed that *S. cochinchinensis* leaves collected from Cham island, Quang Nam province, Vietnam contains secondary metabolites including triterpenoids, alkaloids, anthraglycosides, flavonoids, anthocyanosides, proanthocyanidins, tannins, saponins, polyuronics, and reducing agents.

Table 1. Preliminary phytochemical analysis of *S. cochinchinensis* leaves.

No.	Metabolites	Diethyl ether	Ethanol	Aqueous
1	Lipids	–	–	–
2	Carotenoids	–	–	–
3	Volatile oils	–	–	–
4	Triterpenoids	+	+	+
5	Alkaloids	+	+	–
6	Coumarins	–	–	–
7	Anthraglycosides	+	+	+
8	Flavonoids	+	+	+
9	Anthocyanosides	–	+	+
10	Proanthocyanidins	–	+	+
11	Polyphenols	+	+	+
12	Tannins	–	+	+
13	Saponins	–	+	–
14	Organic acids	–	–	–
15	Reducing agents	–	+	+
16	Polyuronics	–	–	+

Note: (+) indicates the presence and (−) the absence of a metabolite.

3.2. Determination of TPC in S. cochinchinensis leaves

Phytochemicals could contribute to potential biological activities, which is promising to the production of natural, new drugs. Important medicinal and pharmacological properties have been demonstrated in recent research that could be attributed to the phenolic compounds present in many plant extracts, for instance, anti-oxidant, anti-inflammatory, anti-microorganism, anti-carcinogenic, cardiovascular protection, improvement of endothelial function, inhibition for angiogenesis, and cell proliferation activities [8]. Our results show that the crude extract and its fractions of *S. cochinchinensis* leaves in Vietnam contain high levels of polyphenols, which is higher than the previously reported results [4], especially for the ethyl acetate fraction.

In detail, TPC was expressed as mg of gallic acid equivalent (GAE)/g of dry weight (d.w.) that was calculated using an equation obtained from a standard gallic acid graph ($y=0.0024x–0.2135$, $R^2=0.9907$). The results showed that the highest concentration of TPC was in the ethyl acetate fraction (852.74±13.28 mg GAE/g SCE d.w.), followed by the *n*-butanol fraction at 757.51±21.24 mg GAE/g SCB d.w., and then the total extract with 738.47±15.28 mg GAE/g SCT d.w., which are nearly double compared to that of the chloroform fraction (397.08±8.86 mg GAE/g SCC d.w.). By contrast, the *n*-hexane fraction was recorded as containing the lowest content of TPC (320.90±10.19 mg GAE/g SCH d.w.). Meanwhile, the TPC of the aqueous fraction is 511.35±8.86 mg GAE/g SCW d.w. Thus, these inconsistent results seem to imply that different extraction solvents can affect total phenolic content and the composition of extracts.

3.3. Antioxidant activity of crude and fractionated extracts of S. cochinchinensis leaves

A couple of methods had been utilized to determine the antioxidant property *in vitro* and using more than one method to evaluate antioxidant properties will accommodate more comprehensive information. In the present study, the antioxidant ability of different *S. cochinchinensis* leaf extracts was evaluated via an array of assays including a DPPH radical scavenging assay, ABTS radical cation decolorization assay, and a reducing power assay with ascorbic acid used as a positive control.

The DPPH method has been widely used to test the ability of compounds to act as free radical scavengers or hydrogen donors, where a purple-coloured solution bleaching acts like an indicator to evaluate antioxidant capacity [15]. At a concentration of 100 µg/ml, the ethyl acetate fraction had the highest activity with an inhibition percentage of 58.15% (Table 2). Of the six total extracts, five showed IC_{50} values ranging from 100 to 200 µg/ml. The SCE exhibited the strongest capacity compared with the lowest IC_{50} value (83.33±1.26 µg/ml). The order of the IC_{50} values in this test was VitC<SCE<SCB<SCW<SCT<SCC<SCH (Table 3).

The ABTS assay measures the loss of colour when an antioxidant is added to the blue-green chromophore $ABTS^{\bullet+}$. The antioxidant reduces $ABTS^{\bullet+}$ to ABTS and decolorizes it. Table 2 shows that the SCE also exhibited the highest activity with an inhibition percentage of 82.45% at 100 µg/ml. The scavenging of ABTS by the studied extracts increased with increasing content of the samples. When extracts were assessed at various concentrations, IC_{50} values in these assays were also calculated and the *S. cochinchinensis* leaf extracts exhibited IC_{50} values in the following order: VitC<SCE<SCT<SCB<SCW<SCC<SCH (Table 3).

In the reducing power assay, the ability to change colour will depend on the reducing capability of the test extract. The existence of reducing agents in the extract will react with Fe^{3+}/ferricyanide complex to its ferrous specimen. Thus, Fe^{2+} is determined by measuring the absorbance of the mixture after the reaction at a wavelength of 700 nm. In this test, antioxidant activity is generated via the reduction ability by giving away a hydrogen atom from the reducing compounds present in the investigated sample thereby inhibiting the propagation of a free radical chain. The reducing power

assay of all studied *S. cochinchinensis* leaf extracts at 100 µg/ml is given in Table 2 and shows that all extracts had a potent reducing power. Similar to the two aforementioned activities, the reducing power also depended on the content of extracts and increased with increasing amounts of extracts. Besides, for the IC_{50} value, there were significant differences between SCB (75.76 µg/ml) compared to SCE (69.10 µg/ml) and SCW (80.75 µg/ml). Accordingly, this belongs to the extract group with high reducing power and are nearly 2.5 times higher than those of SCC and SCH (Table 3). The ranking order for reducing power was similar to the DPPH scavenging activity.

All values are expressed as mean ±SD (*n*=3). SCT, SCH, SCC, SCE, SCB, and SCW indicate crude ethanol extract, *n*-hexane, chloroform, ethyl acetate, *n*-butanol, and aqueous fractions, respectively.

Table 2. Antioxidant capacity of crude extract and its fractions of *S. cochinchinensis* leaves at a concentration of 100 µg/ml.

No.	Samples	% Scavenging		Absorbance at 700 nm
		DPPH assay	*ABTS assay*	*Reducing power assay*
1	SCT	41.46±2.13	76.73±1.92	0.422±0.023
2	SCH	33.46±0.51	31.38±0.80	0.306±0.003
3	SCC	34.88±0.59	50.80±0.54	0.310±0.003
4	SCE	58.15±0.67	82.54±0.22	0.611±0.006
5	SCB	49.90±0.51	64.05±2.73	0.579±0.006
6	SCW	42.29±0.45	49.15±0.69	0.555±0.008

Table 3. The IC_{50} and EC_{50} values for antioxidant activities of crude extract and its fractions of *S. cochinchinensis* leaves.

No.	Samples	IC_{50} and EC_{50} (µg/ml)		
		DPPH assay	*ABTS assay*	*Reducing power assay*
1	SCT	174.33±3.12^{c}	60.67±1.09^{e}	138.16±5.69^{c}
2	SCH	244.23±1.94^{a}	127.53±0.9^{a}	175.64±2.86^{a}
3	SCC	195.50±7.49^{b}	118.93±0.3^{b}	169.43±0.65^{b}
4	SCE	83.33±1.26^{f}	46.21±0.70^{f}	69.10±2.28^{f}
5	SCB	114.23±2.56^{e}	84.30±2.13^{d}	75.76±1.27^{e}
6	SCW	148.70±2.84^{d}	106.03±0.47^{c}	80.75±0.39^{d}
7	VitC	4.20±0.07^{g}	9.59±1.57^{g}	4.20±0.19^{g}

All values are expressed as mean ±SD (*n*=3). SCT, SCH, SCC, SCE, SCB, SCW, and VitC indicate crude ethanol extract, *n*-hexane, chloroform, ethyl acetate, *n*-butanol, aqueous fractions, and vitamin C, respectively. Means with different letters in each column indicate significant differences (p<0.05).

3.4. Correlation between total polyphenols content and antioxidant activities

The results of this study also showed that there was a significant correlation between the studied antioxidant properties (IC_{50}/EC_{50} values) and the estimated total polyphenol content of *S. cochinchinensis* leaves. The total antioxidant capacity determined through ABTS, DPPH, and reducing power assays and TPC was significantly correlated with R^2 values of 0.7495, 0.9091, and 0.5510, respectively (Table 4). These correlation studies indicated that the evaluated antioxidant properties may be related to the presence of antioxidant bioactives such as polyphenols.

Table 4. The results of regression analysis between total polyphenol content and antioxidant activity (IC_{50}/EC_{50}).

Antioxidant values	Total polyphenol content			
	Linear regression	R^2	*r*	*p*
IC_{50} of DPPH assay	y=-0.2306x+297.6	0.7495	-0.8657	<0.0001****
IC_{50} of ABTS assay	y=-0.1433x+176.0	0.9091	-0.9534	<0.0001****
EC_{50} of reducing power assay	y=-0.1674x+217.9	0.5510	-0.7423	0.0004***

Note: ***: p<0.001 and ****: p<0.0001 are statistically significance.

The present study showed that TPC in *S. cochinchinensis* leaf extracts had significant and negative correlation with their IC_{50} of DPPH, ABTS, and EC_{50} of reducing power assays (r=-0.8657, r=-0.9534, and r=-0.7423, respectively, p<0.05) (Table 4). It can be predicted that phenolic compounds are the main contributor in antioxidant activities of *S. cochinchinensis* leaves by DPPH, ABTS, and reducing power assays.

In this study, the crude and fraction extracts were found to contain polyphenols with various concentrations, which resulted in different antioxidant levels. The ethyl acetate fraction (SCE) was recorded as the extract having the strongest antioxidant properties in all three assays including radical scavenging (DPPH and ABTS) potency and reducing power when compared to the lowest (the *n*-hexane fraction (SCH)), which were consistent with the highest and lowest polyphenol content of SCE and SCH, accordingly. Other findings also proved that there was a significant correlation between antioxidant activities and the polyphenol level of extracts, which could present a great number of polyphenols contributing to the evaluated antioxidant properties of *S. cochinchinensis* leaves. These obtained results were in agreement with the research of C. Sunil, et al. (2011) [4] which also supported the vital role of polyphenols derived from *S. cochinchinensis* leaf and bark extracts in India. The antioxidant activity was measured through reductive ability, scavenger of DPPH, nitric oxide, or inhibition of lipid peroxidation.

Phenolic compounds are secondary metabolites that are ubiquitously found in plants. The high phenolic content of *S. cochinchinensis* leaf extracts may be a good parameter of their antioxidant proficiency. The antioxidant properties of polyphenol compounds have been investigated, which is mainly owing to their redox characteristics and chemical structure allowing the neutralization of free

radicals, chelating metal ions, and singlet and triplet oxygen quenching activity [7, 8]. In this study, Pearson's method was applied to investigate *in silico* the correlation between polyphenols and the antioxidant activity of *S. cochinchinensis* leaf extracts, thereby providing additional information about the relationship between them. The highly remarkable correlations attained in the present study is consistent with the proven hypothesis that polyphenol composition significantly contribute to the antioxidant efficiency of plant extracts. Similar to some previous studies, a linear correlation between polyphenols content in the total extract and the antioxidant capacity was detected of some plants [16, 17]. Hence, polyphenol compounds could make a substantial contribution in the antioxidant activity of *S. cochinchinensis* leaves.

4. Conclusions

In this study, *S. cochinchinensis* leaves were proven to be a potential source of natural antioxidants. A linear correlation between polyphenol content and antioxidant capacity was demonstrated, which suggests that polyphenols could be applied as a marker for antioxidant properties of the *S. cochinchinensis* leaves. However, for a clearer view, further studies should be conducted on polyphenol composition and the *in vivo* effects of the *S. cochinchinensis* leaves.

CRediT author statement

Hai Trieu Ly: Conceptualisation, Methodology, Software; Vu Khanh Trang Le: Data curation, Writing - Original draft preparation; Van Minh Le: Software, Validation, Writing and Editing; Cong Sanh Phan: Conceptualisation, Methodology and Writing; Chau Tuan Vo: Writing - Reviewing and Editing; Minh Ly Nguyen: Conceptualisation, Methodology and Writing and Editing; Thi Anh Dao Phan: Conceptualisation, Methodology and Editing.

ACKNOWLEDGEMENTS

The authors express the gratitude to People's Committee of Hoi An city, Quang Nam province, Vietnam has maintained the project on sustainable development of Tan Hiep island ward based on preserving and promoting the value of Cu Lao Cham's world biosphere reserve, Hoi An city, in the period of 2017-2025. We are also grateful to BSc. Tran Ngoc Toan, the GreenViet Biodiversity Conservation Centre - Da Nang city, and the Southern Institute of Ecology, Vietnam Academy of Science and Technology for timely authentication of herbs under study. We express our sincere gratitude to MSc. Lam Bich Thao (Research Center of Ginseng and Medicinal Materials Ho Chi Minh city) for supporting laboratory in the phytochemical investigation.

COMPETING INTERESTS

The authors declare that they have no conflict of interest regarding the publication of this article.

AUTHORS' CONTRIBUTION

Hai Ly Trieu and Vu Khanh Trang Le contributed equally as co-first authors to this work.

REFERENCES

[1] A. Phaniendra, D.B. Jestadi, L. Periyasamy (2015), "Free radicals: Properties, sources, targets, and their implication in various diseases", *Indian J. Clin. Biochem.*, **30(1)**, pp.11-26, DOI: 10.1007/s12291-014-0446-0.

[2] M. Taghvaei, S.M. Jafari (2015), "Application and stability of natural antioxidants in edible oils in order to substitute synthetic additives", *J. Food Sci. Technol.*, **52(3)**, pp.1272-1282, DOI: 10.1007/s13197-013-1080-1.

[3] C.C. Winterbourn (1995), "Nutritional antioxidants: Their role in disease prevention", *The New Zealand Medical Journal*, **108(1011)**, pp.447-449.

[4] C. Sunil, S. Ignacimuthu (2011), "*In vitro* and *in vivo* antioxidant activity of *Symplocos cochinchinensis* S. Moore leaves containing phenolic compounds", *Food and Chemical Toxicology*, **49(7)**, pp.1604-1609, DOI: 10.1016/j.fct.2011.04.010.

[5] D. Tungmunnithum, A. Thongboonyou, A. Pholboon, et al. (2018), "Flavonoids and other phenolic compounds from medicinal plants for pharmaceutical and medical aspects: An overview", *Medicines (Basel)*, **5(3)**, DOI: 10.3390/medicines5030093.

[6] D.M. Kasote, S.S. Katyare, M.V. Hegde, et al. (2015), "Significance of antioxidant potential of plants and its relevance to therapeutic applications", *Int. J. Biol. Sci.*, **11(8)**, pp.982-991, DOI: 10.7150/ijbs.12096.

[7] H. Cory, S. Passarelli, J. Szeto, et al. (2018), "The role of polyphenols in human health and food systems: A mini-review", *Front. Nutr.*, **5**, DOI: 10.3389/fnut.2018.00087.

[8] K.B. Pandey, S.I. Rizvi (2009), "Plant polyphenols as dietary antioxidants in human health and disease", *Oxid. Med. Cell. Longev.*, **2(5)**, pp.270-27, DOI: 10.4161/oxim.2.5.9498.

[9] M. Ali, K.K. Bhutani, T.N. Srivastava (1990), "Triterpenoids from *Symplocos* racemosa bark", *Phytochemistry*, **29(11)**, pp.3601-3604, DOI: 10.1016/0031-9422(90)85284-M.

[10] I. Ciulei (1982), *Practical Manuals on the Industrial Utilization of Chemical and Aromatic Plants I. Methodology for Analysis of Vegetable Drugs*, Bucharest, 67pp.

[11] P. Chumark, K. Panya, S. Yupin, et al. (2008), "The *in vitro* and *ex vivo* antioxidant properties, hypolipidaemic and antitherosclerotic activities of water extract of *Moringa oleifera* Lam. leave", *Journal of Ethnopharmacology*, **116(3)**, pp.439-446, DOI: 10.1016/j.jep.2007.12.010.

[12] F. Alhakmani, S. Kumar, S.A. Khan (2013), "Estimation of total phenolic content, *in-vitro* antioxidant and anti-inflammatory activity of flowers of *Moringa oleifera*", *Asian Pac. J. Trop. Biomed.*, **3(8)**, pp.623-627, DOI: 10.1016/S2221-1691(13)60126-4.

[13] N. Pellegrini, M. Serafini, B. Colombi, et al. (2003), "Total antioxidant capacity of plant foods, beverages and oils consumed in Italy assessed by three different *in vitro* assays", *J. Nutri.*, **133(9)**, pp.2812-281, DOI: 10.1093/jn/133.9.2812.

[14] M. Oyaizu (1986), "Studies on product of browning reaction prepared from glucose amine", *Japan Journal of Nutrition*, **44(6)**, pp.307-315, DOI: 10.5264/eiyogakuzashi.44.307.

[15] X. Pereira, F. Souza, J.R.K. da S. Almeida, et al. (2012), "Biological oxidations and antioxidant activity of natural products", *Phytochemicals as Nutraceuticals - Global Approaches to Their Role in Nutrition and Health*, DOI: 10.5772/26956.

[16] Y.Z Cai, Q. Luo, M. Sun, et al. (2004), "Antioxidant activity and phenolic compounds of 112 Chinese medicinal plants associated with anticancer", *Life Sci.*, **74(17)**, pp.2157-2184, DOI: 10.1016/j.lfs.2003.09.047.

[17] A. Djeridane, M. Yousfi, B. Nadjemi, et al. (2007), "Screening of some Algerian medicinal plants for the phenolic compounds and their antioxidant activity", *Eur. Food Res. Technol.*, **224**, pp.801- 809, DOI: 10.1007/s00217-006-0361-6.

DOI: 10.31276/VJSTE.64(1).49-52

Aristolochia versicolor S.M. Hwang (Aristolochiaceae), a new record for the flora of Vietnam

Van Truong Do[1*], Thi Thao Hoang[2]

[1]*Vietnam National Museum of Nature, Vietnam Academy of Science and Technology, 18 Hoang Quoc Viet Street, Nghia Do Ward, Cau Giay District, Hanoi, Vietnam*
[2]*Bac Giang Agriculture and Forestry University, Bich Dong Town, Viet Yen District, Bac Giang Province, Vietnam*

Received 6 May 2021; revised 19 July 2021; accepted 2 August 2021

Abstract:

With over 600 species, the genus *Aristolochia* L. (Aristolochiaceae) is extensively spread in temperate, subtropical, and tropical climates. Numerous *Aristolochia* species are significant host plants for the Papilionidae family of butterflies and are regarded as a key group to research the relationship between plants and butterflies. Moreover, traditional Chinese and Vietnamese medicine frequently use a few Aristolochia species. *Aristolochia* biodiversity hotspots are found in southern China and northern Vietnam. There are currently 25 *Aristolochia* species recognized from Vietnam. We just gathered some intriguing *Aristolochia* specimens in northern Vietnam's protected forests while updating the taxonomy of the species. After a thorough analysis of the specimens and comparisons with the protologue and type specimens of previously identified Siphisia species, it was determined that the specimens perfectly matched *A. versicolor* S.M. Hwang, a medicinal plant that was previously identified. As a result, *A. versicolor* is now listed as a new record for Vietnam's flora. The description of the morphology, color images, iconography, distribution, phenology and habitat, state of conservation, and comparison with other morphologically are provided.

Keywords: ***Aristolochia westlandii,*** **biodiversity hotspot, *Siphisia*, Vietnam.**

Classification number: **3.4**

1. Introduction

The genus *Aristolochia* L. (Aristolochiaceae) comprises around 600 species and is widely distributed throughout the tropics, subtropics, and temperate regions [1]. Many *Aristolochia* species are important host plants for the butterfly family Papilionidae, and considered as a major group for studying plant-butterfly interaction [2]. Furthermore, some *Aristolochia* species are commonly used in Chinese and Vietnamese traditional medicine [3]. Southern China and northern Vietnam are considered biodiversity hotspots of the genus *Aristolochia* [4]. Additionally, some *Aristolochia* species that are known endemically to southern China (Guangxi, Guangdong, and Yunnan provinces) [3], were also newly recorded for the country by recent investigations in northern Vietnam [5-8] due to similarities of topology and habitats. Currently, 25 *Aristolochia* species belonging to two subgenera are known from Vietnam, of which 18 are in subgenus *Siphisia* and seven are in subgenus *Aristolochia* [9-12].

While revising taxonomy of *Aristolochia* from Vietnam, we recently collected some interesting *Aristolochia* specimens in protected forest areas in northern Vietnam. These specimens have the morphological characters such as a U-shaped perianth, a 3-lobed limb, and a 3-lobed gynostemium, which are specific for the subgenus *Siphisia* [4]. Detailed examination of these specimens and studies on the protologue and type specimens of previously known *Siphisia* species revealed that these specimens completely matched with *A. versicolor* S.M. Hwang, which was a medicinal plant and previously known to southern China [13] and northern Thailand [14]. Thus, we herein report *A. versicolor* as a new record for the flora of Vietnam. The morphological description, colour illustrations, iconography, habitat and phenology, distribution, conservation status, and comparison with the morphologically similar species are provided.

2. Materials and methods

Materials were gathered from numerous field works conducted in protected forest areas of the Lao Cai and Lang Son provinces in northern Vietnam. The morphological characters of productive organizations (e.g., the morphology and the colouration of perianth, utricle, tube, and limb) were observed and taken by a Pentax Optio W80 digital camera (Indonesia), which are probably not indicated in dried specimens.

Herbarium specimens available from the following major herbaria: BKF, HITBC, HN, HNU, IBK, IBSC, KUN, NIMM, and VNMN (herbarium code according

*Corresponding author: Email: dovantruong_bttn@yahoo.com

to http://sweetgum.nybg.org/science/ih/) were examined. The protologue, taxonomic treatments, and type specimens of previously described *Siphisia* species from Vietnam [4, 10] and adjacent areas such as the flora of China [3], the flora of Thailand [14], and the flora Malesianae [15] were also consulted.

The terminology of species description followed the works of J.G. Harris, et al. (2001) [16], S.M. Hwang, et al. (2003) [3], and T.V. Do, et al. (2015) [4].

Assessment of the conservation status has been performed in accordance with the categories and criteria of IUCN (2019) [17].

3. Taxonomic treatment

A. versicolor S.M. Hwang, Acta Phytotax. Sin. 19(2): 224. 1981. (Figs. 1, 2).

Type: China. Yunnan: Xishuangbanna, alt. 1050m, 6 December 1961, *Y.H. Li 3694* (holotype: KUN, isotype: IBK!, IBSC!).

Description: Perennial woody lianas, with cylindrical underground organs. Stem terete, internode 1-1.5 cm long, glabrescent to pubescent, corky when older. Petiole 1-1.2 cm long, straight, glabrescent. Leaf blade lanceolate, oblanceolate to obovate, 12-20 cm long, 4-8 cm wide, subcoriaceous, base cordate, sinus 3-4 mm deep, apex acute to acuminate, sometime cuspidate, adaxially glabrescent, abaxially pubescent, glaucous, venation pinnate, 8-10 pairs, slightly sunken on the adaxial surface, prominent on the abaxial surface, margin entire. Inflorescence cymose, 1-2-flowered cymes, solitary or in pairs on young branches and old woody stems, flowers clearly separated from each other. Inflorescence axis 2-2.2 cm long, straight, dark-purple, pubescent. Bracteole oblong, clasping the axis, conspicuous, 3-3.5 mm long, 1.2-1.5 mm wide, both surfaces densely brown villous, sessile, persistent. Pedicel 3.5-4 cm long, pendulous, sparsely villous. Ovary linear-oblong, 1.8-2 cm long, 0.3-0.4 cm in diam., yellowish-green, densely brown villous. Perianth narrowly U-shaped, 7-9 cm in height, outside densely brown villous, purple with visibly parallel ridges. Utricle oblong-cylindrical, 4-4.2 cm high, 0.8-1 cm in diam., inside dark purple, lower a half densely covered by glandular trichomes. Tube geniculately curved, lower part horseshoe-shaped, 1.1-1.2 cm high, 0.8-0.9 cm in diam., inflated, inside dark-purple, smooth, upper part bent upwards and attached to the utricle, funnel-shaped, 1.5-1.8 cm high, 0.6-1.2 cm in diam., inside cream, with or without purple blotches, smooth. Limb sub-equally deltoid 3-lobed, valvate in pre-anthesis, the two lateral lobes 3.7-4 cm wide, 1.7-2 cm high, the median lobe 3-3.2 cm wide, 1.1-1.3 cm high, outside greenish-yellow, densely brown villous, with visibly purple blotches and veins, during anthesis forming a discoid-subrotund-shaped limb, 5-7(-8) cm in diam., broadly rounded 3-lobed, inside exclusively reddish to dark-purple with sunken veins, smooth, the two lateral lobes curved backward. Annulus present, ring-like. Mouth 5-6 mm in diam. with cream throat. Gynostemium 3-lobed, 6 mm high, 4 mm in diam., yellowish-white, the lobes with obtuse apices. Anthers 6 in 3 pairs, oblong, 3.5-4 mm long, yellow. Young capsule cylindrical, 6-angled, 3-4 cm long, 6-8 cm in diam., yellowish-green, densely brown villous (Figs. 1, 2).

Iconography citation: See Fig 4: *Aristolochia versicolora* in [13], S.M. Hwang (1981:225).

Habitat and phenology: This species grows in evergreen forests, thickets, moist shady valleys, and one sandstone in mixed deciduous forests, alt. 500-1500 m. Flowering from April to June and fruiting from June to October.

Distribution: Southern China (Yunnan, Guangxi, Guangdong provinces), north-eastern Thailand (Loei province), and new to northern Vietnam (Lang Son province).

Conservation status: A. versicolor is known from more than 30 collections in a wide range of protected forest areas in the Indo-Chinese floristic region (including southern China, north-eastern Thailand, and northern Vietnam) where the habitats are still protected very well. Furthermore, the large-sized populations occurring together with well-generated saplings are also recorded from these areas. Therefore, this species has been assessed as being of Least Concern (LC) according to IUCN (2019).

Taxonomic notes: A. versicolor is greatly varying in shape and size of leaves and perianth limb. The specimens were collected in northern Vietnam having a larger leaf blade and limb in comparison with the type specimens from China. Morphologically, *A. versicolor* is most similar to *A. westlandii*, a *Siphisia* species occurring in China [3, 11] and Thailand [12]. It is also quite similar to *A. quangbinhensis*, another *Siphisia* species endemic to central Vietnam [18]. However, it is distinguished from these two species by the size of perianth, lower part of tube, the shape, size, inside of limb lobes, and the colour of throat. A detailed morphological comparison of *A. versicolor* with *A. westlandii* and *A. quangbinhensis* is given in Table 1 and Fig. 2.

Table 1. Morphological comparison of *A. versicolor* with *A. westlandii* [3, 12] **and *A. quangbinhensis*** [18].

Characteristics	*A. versicolor*	*A. westlandii*	*A. quangbinhensis*
Perianth	7-9 cm in high	10-15 cm in high	3.2-3.5 cm in high
Tube			
lower part	1.1-1.2 cm in diam.	5-6 cm in diam.	0.6-0.8 cm in diam.
upper part	funnel-shaped, inside cream with or without purple blotches	cylindrical-shaped, inside dark-purple	cylindrical-shaped, inside cream without purple blotches
Limb shape	discoid-subrotund	discoid-subrotund	campanulate
Limb lobes			
shape	Sub-equally 3-lobed	unequally 3-lobed	unequally 3-lobed
size	5-7 cm	8-13 cm	2-2.5 cm
inner surface	exclusively reddish to dark purple without dots or blotches	purple with visibly white veins or blotches	exclusively purplish-pink without dots or blotches
Throat	cream	dark purple	dark purple

Additional specimens examined: Vietnam. Lang Son: Loc Binh, Loi Bac, Con Sung, 30 March 2021, *DVT404* (VNMN).

Fig. 1. *A. versicolor*, a new record for the flora of Vietnam.

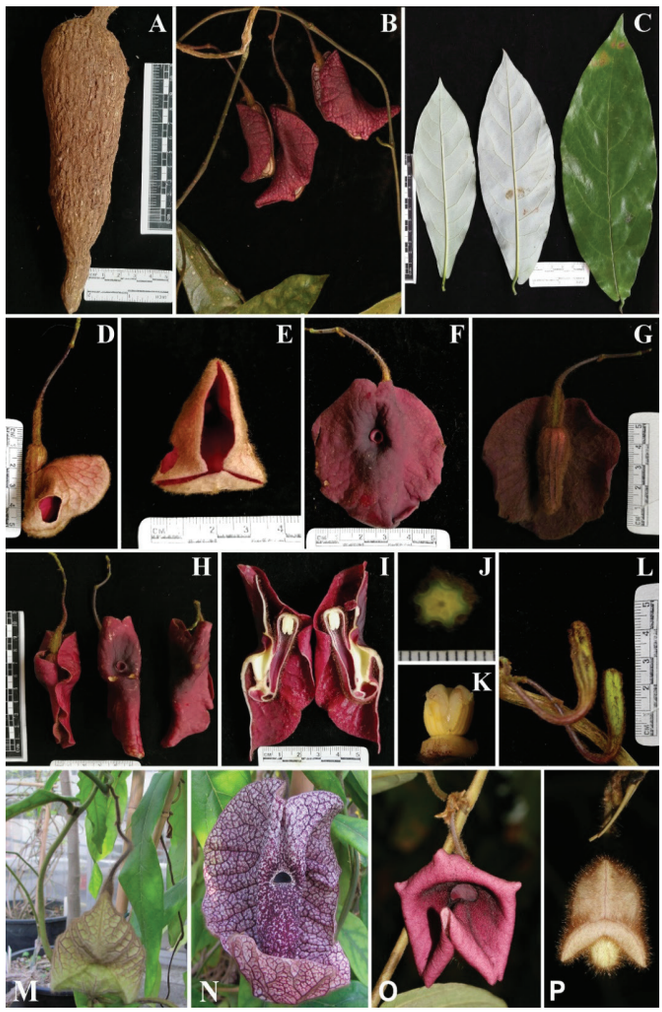

Fig. 2. Detailed illustrations of *A. versicolor* (A-L). (A) Underground organ; **(B)** A branch; **(C)** Leaf shape; **(D-E)** Lateral and frontal views of flower in pre-anthesis; **(F-G)** Frontal and dorsal views of opened flower; **(H)** Different views of two lateral lobes curved backward; **(I)** General view of a longitudinally dissected perianth; **(J)** Crossed section of ovary; **(K)** Close up of 3-lobed gynostemium; **(L)** Young capsule; and comparison with *A. westlandii* (M-P). **(M)** Frontal views of flower in pre-anthesis; **(N)** Frontal views of opened flower; *A. quangbinhensis* (O-P). **(O)** Dorsal views of opened flower and longitudinally dissected perianth; **(P)** Close up of 3-lobed gynostemium.

CRediT author statement

Van Truong Do: Conceptualisation, Methodology, Writing, Reviewing and Editing; Thi Thao Hoang: Conceptualisation, Writing and Editing.

ACKNOWLEDGEMENTS

We are grateful to the curators of the following herbaria: BKF, HITBC, HN, HNU, IBK, IBSC, KUN, NIMM, and VNMN for providing online access to specimens. Furthermore, we would like to thank Hoang

Van Quoc for field assistance in Lang Son province, Vietnam, and Christoph Neinhuis from Dresden Botanic Garden, Germany, for sharing the photos of *A. westlandii*. The Vietnam Academy of Science and Technology financially supported this research work under the project code DLTE 00.09/21-22.

COMPETING INTERESTS

The authors declare that there is no conflict of interest regarding the publication of this article.

REFERENCES

[1] C. Neinhuis, S. Wanke, K.W. Hilu, et al. (2005), "Phylogeny of Aristolochiaceae base on parsimony, likelihood, and Bayesian analyses of *trn*L-*trn*F sequences", *Plant Syst. Evol.*, **250(1)**, pp.7-26, DOI: 10.1007/s00606-004-0217-0.

[2] F.L. Condamine, F.A.H. Sperling, N. Wahlberg, et al. (2012), "What causes latitudinal gradients in species diversity? Evolutionary processes and ecological constraints on swallowtail biodiversity", *Ecol. Lett.*, **15(3)**, pp.267-277, DOI: 10.1111/j.1461-0248.2011.01737.x.

[3] S.M. Hwang, L.M. Kelly, M.G. Gilbert (2003), *Flora of China*, **5**, Beijing: Science Press, St. Louis: Missouri Botanical Garden Press, 423pp.

[4] T.V. Do, H.T. Luu, S. Wanke, et al. (2015), "Three new species and three new records of *Aristolochia* subgenus *Siphisia* from Vietnam including a key to the Asian species", *Syst. Bot.*, **40(3)**, pp.671-691.

[5] T.V. Do (2016), "Notes on taxonomy of *Aristolochia impressinervis* C.F. Liang (Aristolochiaceae) from Vietnam", *Guihaia*, **36(4)**, pp.503-506.

[6] Y.G. Wei (2018), *The Distribution and Conservation Status of Native Plants in Guangxi, China*, China Forestry Publishing House, 876pp.

[7] O.T. Pham, H.V. Lai, T.T. Nguyen, et al. (2018), "*Aristolochia chlamydophylla* (Aristolochiaceae), a new record for the flora of Vietnam", *VNU Journal of Science: Natural Sciences and Technology*, **34(2)**, pp.69-73, DOI: 10.25073/2588-1140/vnunst.4745.

[8] H.V. Lai, T.T. Nguyen, T.V. Do (2019), "*Aristolochia mulunensis* (Aristolochiaceae), a new record and notes on taxonomy, distribution of some *Aristolochia* species for the flora of Vietnam", *VNU Journal of Science: Natural Sciences and Technology*, **35(2)**, pp.58-6, DOI: 10.25073/2588-1140/vnunst.4867.

[9] T.V. Do, T.D. Nghiem (2017), "Taxonomic notes on some *Aristolochia* species in Vietnam", *Taiwania*, **62(2)**, pp.216-218, DOI: 10.6165/tai.2017.62.216.

[10] T.V. Do, H.T.T. Vu, T.H. Luu, et al. (2019), "*Aristolochia nuichuaensis* (subg. *Siphisia*, Aristolochiaceae), a new species, an updated key and a checklist to the species of *Siphisia* in Vietnam", *Ann. Bot. Fenn.*, **56(1-3)**, pp.107-113, DOI: 10.5735/085.056.0116.

[11] H.V. Lai, T.T. Nguyen, D.V. Phan, et al. (2019), "*Aristolochia binhthuanensis*, a new species and a key to the species of *A.* subgen. *Aristolochia* in Vietnam", *Ann. Bot. Fenn.*, **56(4-6)**, pp.241-246, DOI: 10.5735/085.056.040.

[12] T.V. Do, H.V. Nguyen, K.D. Le (2021), "*Aristolochia vuquangensis* (Aristolochiaceae), a new species from Central Vietnam", *Phytotaxa*, **500(1)**, pp.107-113, DOI: 10.11646/phytotaxa.500.1.5.

[13] S.M. Hwang (1981), "Materials for Chinese *Aristolochia*", *J. Syst. Evol.*, **19(2)**, pp.222-231.

[14] L. Phuphathanaphong (1987), *Flora of Thailand*, **1**, The Chutima Press, 164pp.

[15] D. Hou (1984), *Flora Malesiana*, **10**, Martinus Nijhoff Publishers, 164pp.

[16] J.G. Harris, M.W. Harris (2001), *Plant Identification Terminology: An Illustrated Glossary*, Spring Lake Publishing House 216pp.

[17] IUCN Standards and Petitions Subcommittee (2019), "Guidelines for using the IUCN red list categories and criteria, version 14", https://cmsdocs.s3.amazonaws.com/RedListGuidelines.pdf, accessed 20 March 2021.

[18] T.V. Do, T.D. Nghiem, S. Wanke, et al. (2014), "*Aristolochia quangbinhensis* (Aristolochiaceae), a new species from Central Vietnam", *PhytoKeys*, **33**, pp.51-59, DOI: 10.3897/phytokeys.33.6094.

A review on injectable hydrogels from xanthan gum for biomedical applications

Thai Phuong Thao Nguyen[1, 2], Phuong Hien Le[1, 2], Thi-Hiep Nguyen[1, 2*]

[1]*School of Biomedical Engineering, International University, Quarter 6, Linh Trung Ward, Thu Duc City, Ho Chi Minh City, Vietnam*
[2]*Vietnam National University - Ho Chi Minh City, Quarter 6, Linh Trung Ward, Thu Duc City, Ho Chi Minh City, Vietnam*

Received 8 February 2022; revised 25 February 2022; accepted 11 March 2022

Abstract:

Biomaterials are a broad category of materials that include polymeric constructs and metallic orthopaedic implants. Their purpose is to replace, regenerate, or repair tissue structure and/or function that has been lost. Hydrogels are frequently made using both synthetic and natural polymers. Demand for less expensive biodegradable, biocompatible, and non-toxic products has increased recently, with natural polymers outpacing synthetic polymers in this regard. Xanthan gum (XG) is recognised as one of the most popular natural polymers extensively used today due to its biodegradable and biocompatible properties, and, therefore, XG can be used to produce hydrogels with other polymers to expand its uses. However, at present, there has not been much research on preparing injectable hydrogels from XG. Moreover, up to now, there are only a limited number of review articles related to this topic. This review will provide a well-organised and somewhat extensive presentation of previous studies that have been executed on injectable hydrogels from XG. Also, applications have been using XG to fabricate injectable hydrogels such as cartilage tissue engineering, bone tissue engineering, delivery system, and bioink will be reviewed.

Keywords: **biomedical application, injectable hydrogel, xanthan gum.**

Classification number: **3.6**

1. Introduction

Biomaterials cover a wide spectrum of materials from metallic orthopaedic implants to polymeric constructs-all of which are used to replace, restore, or regenerate missing tissue structure and/or function. Polymeric hydrogels, traditionally understood as three-dimensional (3D), are water-swollen polymer networks generated via physical or chemical crosslinking is an ever-increasing class of biomaterials. They have been extensively explored for countless biomedical applications due to advantages such as oxygen and nutrient permeability, biocompatibility, physical characteristics like those of the native ECM, and adjustable physical and mechanical characteristics [1].

Nevertheless, the use of pre-formed hydrogels at a desired spot in the body necessitates an intrusive surgical process that can bring discomfort and pain, heavy bleeding, infection, nerve damage, as well as a prolonged recovery time of the patient. As a result, their clinical utility is restricted. Hence, to overcome these drawbacks of pre-formed hydrogels, recent hydrogel research has focused on injectable hydrogels defined as hydrogels undergoing the transition from sol to gel under environmental conditions at the injection site. Injectable hydrogels not only possess the benefits of traditional hydrogels, but they also have superior properties such as the ability to be injected into target sites with little invasiveness and the capability of filling oddly shaped defect sites. As a result, they have emerged as a potential and effective material system for a variety of biomedical applications including the delivery systems for therapeutic agents delivery like cells, drugs, and bioactive molecules to cure infectious and inflammatory diseases as well as cancers, and even the repair and restoration of tissues like muscle, bone, skin, and cartilage [2].

Natural and synthetic polymers are commonly used to fabricate hydrogels. Recently, there has been an upsurge of demand for cheaper biodegradable and biocompatible non-toxic products with natural polymers taking precedence over synthetic polymers. XG is recognized as a natural polymer that is extensively used today due to excellent biodegradability and biocompatibility; therefore, XG can be used to produce hydrogels with other polymers to expand its uses [3, 4]. However, at present, there has not been much research on preparing injectable hydrogels from XG. Therefore, in this review, studies of injectable hydrogels from XG will be presented in a well-organised and extensive manner. Also, the applications of XG-based injectable hydrogels such as cartilage tissue engineering, bone tissue engineering, delivery system, and bioink will be reviewed.

2. Structure and properties of XG

2.1. Structure

XG is an anionic exocellular polysaccharide mainly produced from the Gram-negative bacteria *Xanthomonas campestris*. The structure of XG is primarily made up of repeating pentasaccharide units including two D-glucose units, two D-mannose units, and one D-glucuronic acid unit [5] (Fig. 1). A pendant trisaccharide side chain including a D-glucuronic acid unit between two D-mannose units is attached to the O-3 position of D-glucose units by α-1,3 linkages. The terminal β-D-mannose is linked to

*Corresponding author: Email: nthiep@hcmiu.edu.vn

the O-4 position of the β-D-glucuronic acid, which is successively linked to the O-2 position of an α-D-mannose. There are groups of acetates and pyruvates of varying amounts attached at the two D-mannose units, which depend on the bacterial strain, the conditions of fermentation, and chemical modifications [6].

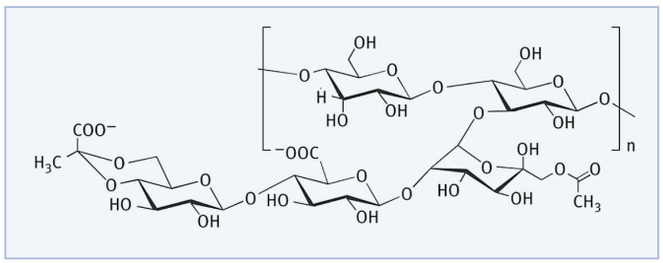

Fig. 1. Structure of XG.

XG has two molecular conformations including helical/ordered conformation and random coil/disordered conformation. Right-handed five-fold helix conformations are stabilised by non-covalent interactions between the side chains of the trisaccharide and the backbone of the chain and are destabilised by electrostatic attraction between carboxylate groups. Consequently, XG can undergo order-disorder conformation transitions (Fig. 2) if the temperature or ionic strength is changed. Random coils can be formed under high temperature or low ionic strength whereas high ionic strength or low temperature can stabilise the order conformation resulting in an extraordinarily stable XG, which commonly manifests as a dimeric or double-stranded chain. As a result of this behaviour, XG alone can form a weak gel when prepared at a concentration higher than the critical concentration of approximately 0.3% w/v [7].

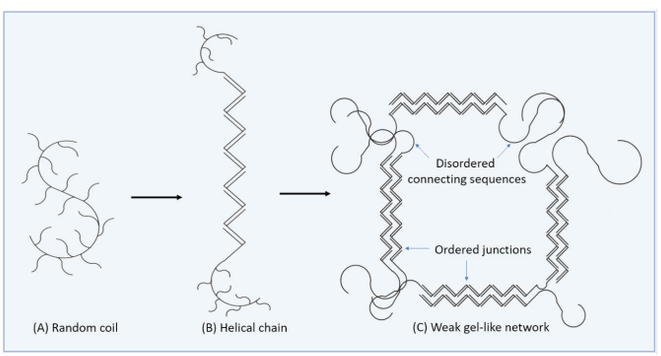

Fig. 2. (A) The disordered conformation of XG, (B) the ordered conformation of XG, and (C) the lateral association of ordered chains to form a weak gel-like network.

2.2. Properties

Viscosity and rheological properties: XG shows a high solubility in both cold and hot water, which is due to the polyelectrolyte structure of XG molecules. XG solutions are highly viscous even at low polymer concentrations, which contribute to its excellent suspension and thickening properties [8]. XG solutions exhibit the behaviour of non-Newtonian fluids and a highly pseudoplastic property of which its viscosity declines speedily as the shear rate increases. Fig. 3 presents how the XG polymer network is influenced by mechanical shear being applied and removed. When the yield stress is surpassed, XG solutions become pseudoplastic. The network then disassembles with individual polymer molecules positioning themselves in a straight line along the shear force direction. The level of the disassembly is commensurate with the shear rate. Once shear is no longer applied, the network will promptly reorganise. At adequate concentrations of XG, it looks almost gel-like at rest, yet, they can easily be pumped or mixed [9].

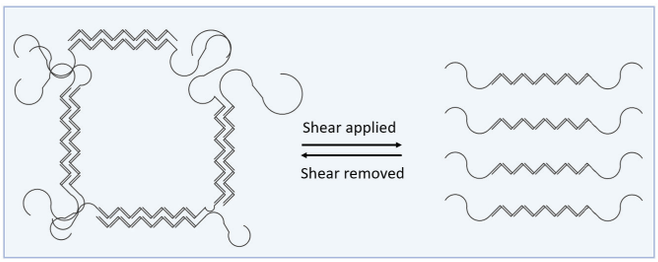

Fig. 3. Effect of shear on the polymer network of XG.

Influence of pH on the viscosity of XG: The viscosity of an XG solution is practically constant as pH changes between 1 and 13. XG is steadily deacetylated at pH>9 [10], while at pH<3 it loses the pyruvic acid acetal groups [11]. Neither deacetylation nor depyruvylation significantly affect XG solution viscosity since the rheological properties of deacetylated or depyruvylated XG are similar to those of native XG [8]. However, pH variations will affect changes in the reduced viscosity of XG solution. At pH values of 2.5 and 3.5, XG solutions exhibit straight decreasing lines of the reduced viscosity with dilution, which represents the behaviours of neutral polymers. This can be clarified based on the protonation of carboxylic groups in an acid medium, where XG chains carry no charge and are partially flexible. The carboxylic groups within a weak acid medium are incompletely protonated (pH=4) or entirely deprotonated (pH=6) [12]. At pH=5, carboxylic groups on the side chain of XG create electrostatic repulsive forces that cause the chain to enlarge and make the reduced viscosity amplify constantly alongside the dilution of the polymer. When an XG solution is at a high dilution in water, a polyelectrolyte effect can be implied from the upward curvature [13].

Effect of electrolytes on the viscosity of XG: Fluid in the human body contains an enormous amount of electrolytes that are supposed to change the solvation sphere around biodegradable materials. If the environment is negatively affected by the electrolytes and becomes disadvantageous for the diffusion of water molecules into biodegradable polymers, then its properties of degradability should reflect this. The viscosity of an XG solution is mainly dependent on gum concentration. The effects of electrolytes have little impact on XG. Under 0.15% w/v gum concentration, a small amount of an added electrolyte like sodium chloride can slightly reduce the viscosity. This is because the addition of electrolyte reduces the electrostatic forces between XG molecules resulting in less availability in the XG molecular network [14]. In other

words, the helical conformation of XG seems to be stabilised by the low level of electrolyte concentration, which also downgrades the carboxylate anions' electrostatic repulsion (Fig. 4). However, the addition of electrolytes acts in the opposite manner at higher concentrations of gum. Electrolyte addition marginally increases the solution viscosity until reaching a peak at 0.02-0.07% w/v concentration of sodium chloride; however, additional salt has little or no impact on viscosity above this level, which is due to the enhanced interactions between salt molecules and XG molecules. Thus, the viscosity of an XG solution will be independent of the salt if the salt amount exceeds 0.1% w/v [15].

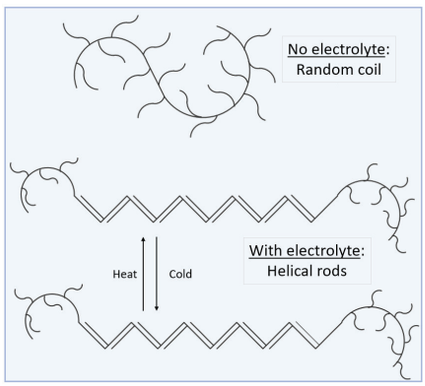

Fig. 4. Effect of electrolyte on XG molecular conformation.

Influence of temperature on the viscosity of XG: XG solutions are affected by two characteristic temperatures including the measurement temperature (T_M, the temperature when the viscosity is measured) and the dissolution temperature (T_D, the temperature when XG is dissolved). The viscosity of XG solutions decrease when T_M increases. Alternatively, there is a decrease in XG viscosity when T_D is raised up to 40°C. From T_D=40 to 60°C, XG viscosity increases with an increase in temperature. XG solutions exhibit this behaviour because the XG conformation will go through an ordered-disordered state change as T_D shifts from low to high (Fig. 2). This results in an increase in XG molecule hydrodynamic volume and, thus, gives rise to the viscosity. For T_D above 60°C, the viscosity decreases with an increase in temperature [8].

Effect of enzymes and oxidants on the stability of XG: XG cannot easily be affected by most degradation by microorganisms; however, it can somewhat be vulnerable to cellulase in the disordered conformation. On the other hand, XG can be completely biodegradable, which means it can be depolymerised by enzymes produced by certain microorganisms when certain environmental conditions are met. Additionally, like other gums, XG is susceptible to degradation by strong oxidising agents such as persulfates and peroxides [15].

Biocompatibility of XG: A well-known attribute of XG is its excellent biocompatibility, non-toxicity, and intrinsic ability as an immunological agent since XG alone does not adversely affect the viability of rabbit chondrocyte cells [16]. Moreover, in vitro and in vivo studies with the fibroblast cell line L-929 showed good biocompatibility for hydrogels prepared by a combination of XG with other polysaccharides as chitosan (CHT) [17].

3. Fabrication of XG-based injectable hydrogels

There have been several studies on fabricating injectable hydrogels from XG. It can be seen from those studies that there are three approaches typically applied. The first approach is to purify and use XG alone to inject directly into the injection site due to its shear-thinning properties. In addition, thanks to its large number of functional groups, XG can be combined with other polymers through the second approach - via physical crosslink, and the third approach - via chemical crosslinking to fabricate injectable hydrogels.

3.1. Purified XG for direct injection

Due to the shear-thinning property, XG alone can be directly injected through a needle to the target site of the body. For example, G. Han, et al. (2012) [18] investigated the ability of intra-articular (IA) injection of XG into rabbits' knee joint. In this case, using conventional XG types (with unguaranteed purity and unknown protein and endotoxin content) would affect the accuracy of the XG injection's evaluation. So, to accurately evaluate XG for IA injections, the test sample XG needs to have high purity, high viscosity, low protein-content, and be endotoxin free. The procedure of making purified XG is illustrated in Fig. 5. He began with XG fermented broth, brought it through a precipitation step, and then through a purification process including the combination of cake filtration, enzymatic treatment, active carbon absorption, and repeated isopropanol precipitation methods in order to obtain good quality XG. This purification process, especially the enzyme treatment, helps eliminate undissolved matter and impurities such as proteins, fats, or bacterial cell residues contained in the XG fermented broth [18].

The process of enzyme treatment is preferably at a temperature of 50 to 60°C, at a pH range from 6.5 to 7.5, for about 30 min to 2 h. In terms of productivity, a temperature below 40°C is not recommended since a resulting lowered enzymatic activity would involve more than 6 h of treatment time. Enzyme deactivity can also be triggered by high temperature, causing the treatment to become ineffectual. Acidity lower than pH 6.0 would disable alkaline protease, while pH above this range is also unwanted as it can devolve the product's physical properties. If the protease concentration is too low, a satisfactory effect would not be achieved even when the treatment time is extended. Conversely, it is not advisable for the protease concentration to exceed 500 ppm by reason of creating higher costs in production without producing any further improvements. So, the process is preferred to be conducted at relatively neutral pH and at a mild temperature such that protease will exhibit an acceptable activity level to purify the XG solution [19].

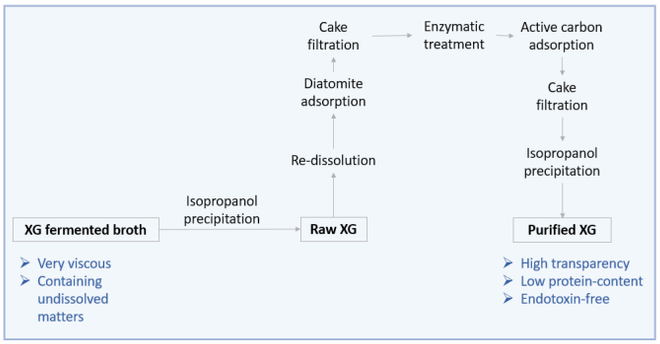

Fig. 5. Schematic procedure of making purified XG.

The final product contained 99.6% of XG, which indicated that it met the initial requirement of high purity. Moreover, the purified XG contained no proteins and no endotoxins. Finally, the acquired IA injection of XG was observed to be transparent, highly viscous (1597±32 mPas), and heat stable (could be sterilized at 121°C for 15 min) [18].

3.2. Polymers combined with XG via physical crosslinks to fabricate injectable hydrogels

Hydrogels that are physically crosslinked undergo the gel state by altering intermolecular forces like electrostatic ionic repulsion, hydrophobic interaction, hydrogen boding, or intermolecular assemblies like complementary binding, stereo-complexation, and guest-host inclusion. These changes can be caused by the internal organization of the polymers or stimulated by external stimuli such as pH, heat, or the presence of certain molecules [20]. Physical crosslinking methods are easy and safe ways to prepare injectable hydrogels since they do not require the use of potentially harmful crosslinkers or catalysts.

Having prepared injectable hydrogels based on XG and methylcellulose (MC) via thermo-induced interaction, Z. Liu, et al. (2015) [21] later described that a blended solution of the two polymers instantly retrieved its high viscosity and promptly created a hydrogel at body temperature. MC is a water-soluble cellulose derivative that can induce a sol-gel transition guided by hydrophobic interactions that depend on temperature changes. At 23°C, the XG/MC blend carries only the XG network interfered with MC molecules, which is the reason why the combination at 23°C has the behaviour of shear-thinning, but the viscosity is not as high as that of solution containing only XG. When the temperature is raised to 37°C, intermolecular hydrophobic interactions trigger the XG/MC blend solution to form gels so it possesses the double networks of XG and MC at the same time (Fig. 6). With the rat's body being analysed in terms of biocompatibility, elimination, and gelation, the proportion of hydrogel grew in the first week of post-injection because of swelling, which then slowly decreased until the 36th day after injection when it finally disappeared. The inflammatory cells in the tissues were monitored around the implanted XG/MC hydrogel and the signs of inflammation decreased as the duration of implantation increased In addition, on the 27th day after injection, inflammation of the cells practically disappeared and the histology of the tissues around the site was entirely recovered 37th days post-injection [21].

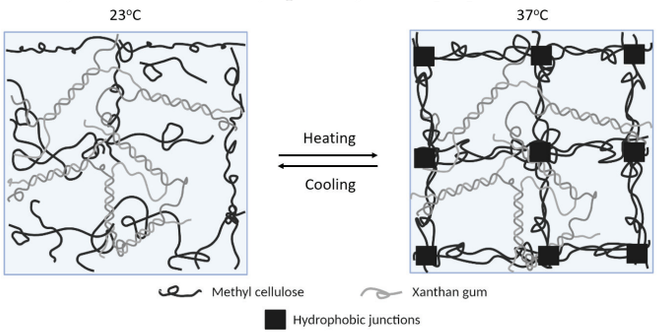

Fig. 6. Gelation mechanism of XG/MC hydrogels.

Additionally, XG can also be combined with pluronic F127 (PF127) to fabricate injectable hydrogels through hydrophobic interaction and hydrogen bonding. PF127, a triblock copolymer comprised of poly (ethylene oxide-b-propylene oxide-b-ethylene oxide or PEO-b-PPO-b-PEO), can undergo a sol-gel transition at around 20-25°C depending on the concentration of the copolymer [22]. The gelation of PF127 occurs owing to its dehydration, which forces this substance to be constructed with micelle subunits where the core of which is made up of hydrophobic PPO blocks and the shell is made up of hydrophilic PEO chains (Fig. 7A). However, the low sol-gel temperature and thermo-reversible property of PF127 make this substance inconvenient and difficult to fabricate stable hydrogels. Therefore, different PF127-based formulations combined with XG were modulated to create a stable *in-situ* gel and ensure gelation at around 37°C. In the viscosity studies, XG/PF127 *in-situ* gel revealed a rise in temperature and concentration that was dependent on viscosity. The viscosity of the *in-situ* gel rose as the micelle concentration rose because of the intermicellar distance being shortened. Furthermore, the increase of XG concentrations from 0.2 to 0.6% also made the viscosity of *in situ* gels decrease. This is a consequence of the electrostatic repulsion of the charged groups where XG chains are substantially stretched at room temperature and create helical structures through hydrogen bonding. As the temperature rises, the lengthy chains of XG form a coil-like conformation (Fig. 7B). In the situation of *in-situ* gels, the lengthy XG chains infiltrate across distinct copolymer micelles and interact with PEO corona, which ensures a higher degree of elasticity and high viscosity to the resultant gel (Fig. 7C) [23].

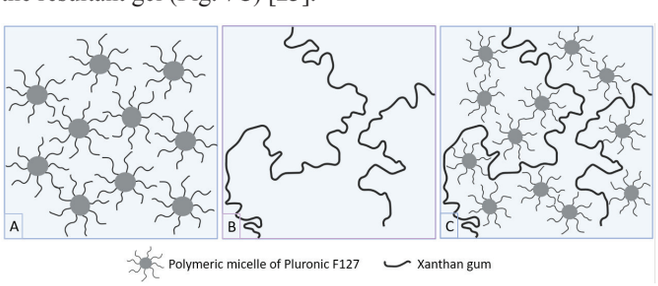

Fig. 7. (A) PF127 hydrogel, (B) XG solution, and (C) XG/PF127 hydrogel at 37°C.

In another research works, XG was combined with gellan gum (GG) to create an *in situ* gelling system via temperature and ionic gelation mechanism with Ca^{2+} ions or DMEM supplemented as the supply of cations for gelation [24, 25]. GG, an anionic extracellular polysaccharide, appears in a random coil shape when dissolved in water at temperatures over 80°C, which transforms to a double-helix structure when cooled, followed by self-assembling and the production of oriented bundles [26]. Cations aid in the creation of a stable gel by assisting in the linking of the bundles. The creation of double helical junction zones and the later aggregation of the double-helical segments lead to a 3D network via cation complexation and hydrogen bonding with water [27] (Fig. 8). The combination of XG and GG demonstrated a shear-thinning effect at various shear stresses for all of the tested concentrations, indicating that the hydrogel was easy to inject. This was due to the shear force at the interface of the needle and tissue, which allows the gels to shear-thin and then flow into the defect site. The polymer solution returns to its gel state after the shear stress is removed, suggesting that the hydrogel could be provided through injection. Measurements of viscosity versus temperature validated the gelation temperature being between 37 and 40°C for all tested concentrations, with the onset of gelation at roughly 42°C.

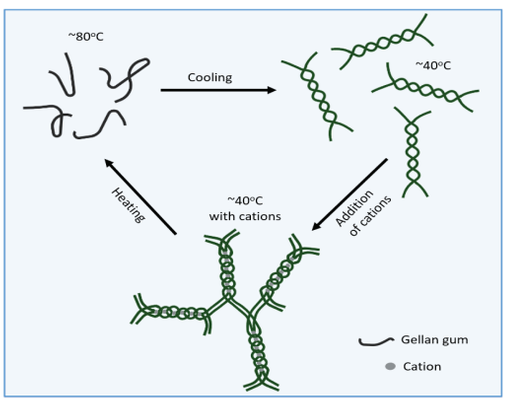

Fig. 8. Gelation mechanism of GG.

Another polymeric combination belongs to XG and konjac gum (KG), which was investigated to study its printing properties [28]. In XG/KG hydrogels, A. Abbaszadeh, et al. (2016) [29] hypothesised two forms of interaction (type A and type B) (Fig. 9). As for type A, XG maintains helical conformations and the produced hydrogel melts at a lower temperature range (from 30 to 45°C). In a type B interaction, the 2-fold structure of disordered XG is accountable for the synergistic binding with KG. Backbone-to-backbone development of junction zones causes the contact and the resulting gel melts at a higher temperature of around 60°C. Changes in ambient parameters such as functional group content, pH, and ionic concentration can affect the XG transition temperature, which is a critical parameter in defining the type of contact [29]. The XG/KG mixture with the addition of syrup investigated in work of [28] had an interaction type A with a melting temperature of around 45°C. The printing temperatures investigated had a significant impact on the rheological features of the hydrogels, which imply a distinct type of interaction. In terms of temperature, changes in elastic modulus (G′) were more connected than those of viscous modulus (G″). Printed samples at 50°C had lower G' values than those at 25°C, which indicates less elasticity at 50°C. In terms of the effect of composition on rheological characteristics, mixtures with lower syrup concentrations but higher XG and KG values had higher G′, G″, and η* values [28].

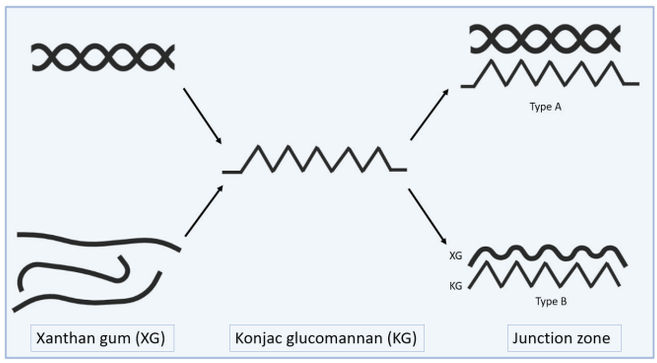

Fig. 9. Mechanisms for the interaction between XG and KG.

CHT, a linear cationic polysaccharide, can be combined with XG to generate injectable hydrogels via electrostatic attraction or ionic interaction between the amino groups of CHT and carboxyl groups of XG [30] (Fig. 10). CHT molecules contain positive charges at low pH, which combine with negatively charged polyions of XG to create polyelectrolyte complexes [31]. J. Kim, et al. (2017) [32] prepared XG/CHT-based polyelectrolyte hydrogels having a viscoplastic behaviour that satisfies all the rheological models like the Bingham, Herschel-Bulkley, Power law, modified-Bingham, and modified Herschel-Bulkley, as well as Casson models as a non-Newtonian material.

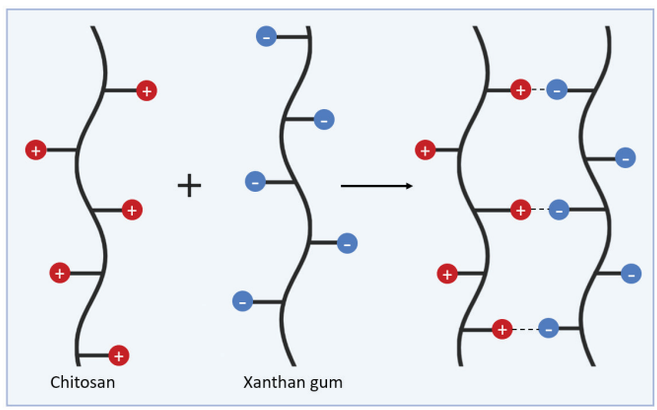

Fig. 10. Illustration of ionic interaction of CHT and XG.

3.3. Polymers combined with XG via chemical crosslinks to fabricate injectable hydrogels

Chemically crosslinked hydrogels are a type of hydrogel that can transition from liquid to gel state by chemically creating new covalent bonds in the polymer network. Reactions can

be triggered by a variety of processes such as click chemistry, Schiff base reactions, Michael reactions, enzymatic reactions, photo-polymerization, disulphide-forming reactions, or redox reactions. From these reactions, newly created covalent bonds build a polymeric 3D network structure that can trap water and encapsulate living cells or therapeutic agents.

In the preparation of an injectable hydrogel combining CHT and oxidized XG (OXG) via Schiff base reaction between free amine groups on CHT and aldehyde groups on OXG (Fig. 11), the observed swelling capacity was not much different among the three ratios used in the preparation of CHT/OXG hydrogels (CHT/OXG=80/20; 70/30; 75/25). This was believed to be due to the small crosslinks of the structure and tighter intramolecularly, and thus lower swelling ratios [33]. Critical strain for 80/20 and 75/25 CHT/OXG hydrogels was around 10%. However, when the OXG concentration was increased in the 70/30 CHT/OXG hydrogel, the critical strain was found to be roughly 2.52%, indicating that the linear viscoelastic zone was at a lower strain at this ratio. In the tests of gelling time and gel fraction, it was proved that when the volume ratio of OXG was raised, the gelling time lowered, and the gel formed was comparatively more stable. The 70/30 ratio hydrogel had the fastest gelation time of about 18 s suggesting that the crosslinking was higher and the gels were becoming stronger and more stable over time. In another study about the preparation of an injectable hydrogel from OXG and carboxymethyl chitosan (NOCC) via Schiff base reaction, the hydrogel with a mass ratio of 1/0.33 (OXG/NOCC) had the fastest gelation time of 10±5 s. Moreover, the 1/0.33 ratio hydrogel also had the highest swelling ratio compared to all the samples, was stable, and had a viscoelastic solid-like behaviour [34].

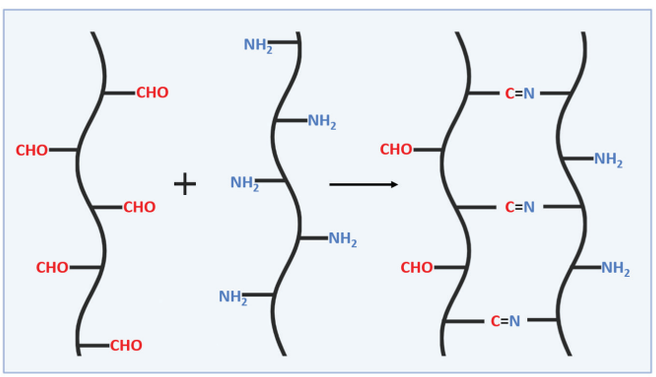

Fig. 11. Schiff base reaction between aldehyde groups and amine groups [35].

An injectable hydrogel from XG, silk fibroin (SF), and sodium trimetaphosphate (STMP) with ion conductivity was prepared in previous research [36]. SF, a high molecular weight disulphide-linked block copolymer, has been used to create hydrogels with great mechanical strength and biocompatibility [37]. STMP, a water-soluble and non-toxic crosslinker, is used in food and medicine, for example, as a chemical crosslinking agent to make polysaccharide hydrogels or to induce phosphorylation, which improve the functional characteristics of proteins and sugars. The blending of XG, SF, and STMP produces hydrogels with the characteristics of swelling but water insoluble. The viscosity of a XG/SF/STMP hydrogel is mostly determined by XG since XG/STMP and XG/SF/STMP gels both contain 3 wt% XG and had very identical viscosity-shear rate curves. All XG/SF/STMP hydrogels have a viscosity that decreases significantly with the rise of shear rate, which indicates a shear-thinning property. Additionally, with 3 wt% XG, the addition of SF particles to withstand deformation against compressive stress improved the stiffness of XG/SF/STMP hydrogels compared to XG/STMP hydrogels. Moreover, the hydrogels regained their initial values of storage moduli after being relieved of excessive strain in rheological investigations, which suggests a self-healing property in the XG/SF/STMP hydrogels. The XG/STMP and XG/SF/STMP hydrogels' ionic conductivity was equal to that of PBS [36]. In another study, R. Zhang, et al. (2018) [38] created novel injectable hydrogels with self-healing properties from XG, TM3a, and STMP. TM3a, a coded hyperbranched polysaccharide, was chemically crosslinked with XG using STMP as crosslinkers via an esterification reaction between the -OH groups of XG, TM3a, and STMP (Fig. 12). According to oscillatory rheological tests, chemical crosslinking occurred quickly after mixing STMP solutions into XG-TM3a solutions, and the crosslinked network developed gradually over time. From the beginning of the rheological tests, the storage modulus was far ahead of the loss modulus, and these moduli increased slowly during the experimental period. Moreover, XG/TM3a/STMP hydrogels shown a self-healing property when a large and small amplitude oscillation was applied one at a time. Furthermore, XG/TM3a/STMP hydrogels also show a shear-thinning behaviour, which make XG/TM3a/STMP hydrogels an ideal candidate for forming injectable hydrogels or for 3D printing.

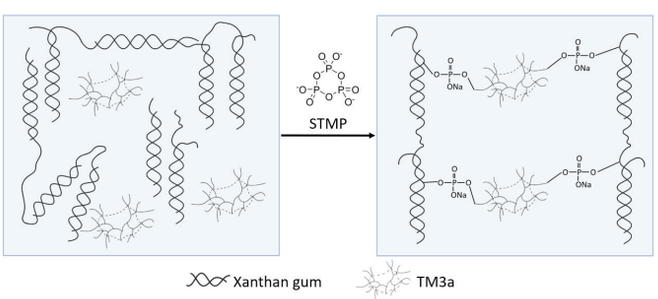

Fig. 12. Illustration of XG/TM3a/STMP hydrogels' synthesis.

Another study used intermolecular crosslinking between OXG and 8-arm poly (ethylene glycol) (PEG) hydrazine via hydrazone links to create an injectable hydrogel with self-healing property (Fig. 13). According to recorded data, a greater PEG hydrazine concentration prompted greater elasticity, which means these hydrogels were more likely to endure the formulation and delivery strains as an injectable formulation. The findings from the thixotropic test revealed that even though hydrogels developed quickly, they were effortlessly extrudable

when passing through the needle and instantly regained their viscoelastic gel properties. To comprehend the self-healing properties of hydrogels, their tendencies to seamlessly heal themselves into union when violently cut into two separate pieces were explored via rheological studies and a visual method. It was found that hydrogels recovered instantly after being relieved of excessive strain in rheological investigations. This is due to the use of dynamic hydrazone linkages to generate hydrogels. In the visual method, there were no obvious seams observed indicating that the two pieces had healed properly. Research on self-healing ability were also performed on hydrogels fabricated at different pH values. The results showed that gels fabricated at a mildly acidic pH had more efficient drug/dye distributions than gels tested at neutral pH [39].

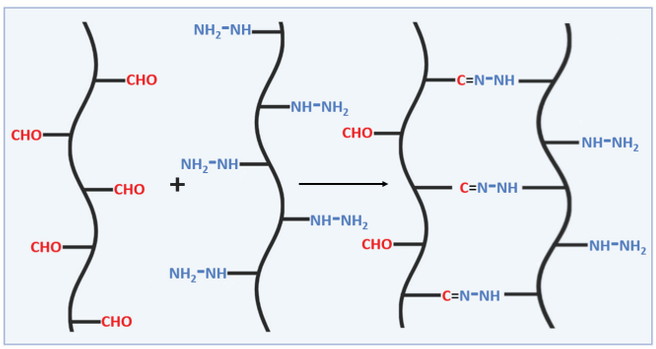

Fig. 13. Hydrazone linkage between aldehyde groups and hydrazide groups [35].

4. Applications of XG-based injectable hydrogels

4.1. Cartilage tissue engineering

OA occurs because of chondrocyte apoptosis. The excessive expression of mediators causing inflammation like nitric oxide (NO), tumour necrosis factor-α (TNF-α), interleukin-1 (IL-1), and prostaglandin E2 (PGE2) in serum or in synovial fluid causes chondrocyte apoptosis. The poor proliferative potential of chondrocytes after injury or during the healing process complicates cartilage regeneration. In cases of osteoarthritis, cartilage tissue engineering plays the most important role in overcoming these obstacles [40].

IA injection of XG is proven to treat OA better than hyaluronic acid (HA) since no statistically significant differences on OA were observed for the effects of chondro-protection by IA injection of XG and HA [18]. Also, the preliminary cytotoxicity effects of XG on rabbit chondrocytes regarding proliferation and protein expression of matrix metalloproteinases (MMPs) and tissue inhibitors of metalloproteinase-1 (TIMP-1) in chondrocytes induced by IL-1β were assessed. Down-regulating MMPs and up-regulating of TIMPs (or MMPs inhibitors) are rational targets for treating OA since the imbalance between MMPs and TIMPs play an important role in the development of OA. In experiments using various doses of XG with and without IL-1β, the results showed that XG alone did not cause adverse effects on the viability of chondrocyte cells, and also significantly reversed the IL-1β-induced reduction of the proliferation of chondrocyte cells. Additionally, XG increased TIMP-1 expression in a dose-dependent manner while inhibiting MMP release produced by IL-1β [16] (Fig. 14). XG does not exhibit any cytotoxicity on the chondrocyte cells of rats and has effects on the ATDC5 cells' Wnt3a/β-catenin signalling [41]. In addition, an injection of low molecular weight XG (from 1×10^6 to 1.5×10^6 Da) could protect cartilage tissue from damage, reduce the concentration of NO in the synovial fluid, and was able to reverse the amplification of knee joint width similar to high molecular weight (HMXG) [42]. LWXG promotes chondrocyte proliferation while decreasing apoptosis at the cellular level. These effects are evoked via down-regulation of the protein levels of caspases-3 and bax (an apoptosis inducer) and via up-regulation of protein levels of bcl-2 (apoptosis inhibitor) in cartilage both *in vitro* and *in vivo* [43]. Furthermore, the combination of XG with CHT to form an injectable hydrogel is an excellent scaffold for cartilage regeneration. The hydrogel has been proven to provide a static environment that enables cells to maintain their chondrogenic phenotype while allowing unimpeded diffusion of nutrients and waste materials for every cell during the culture periods [33].

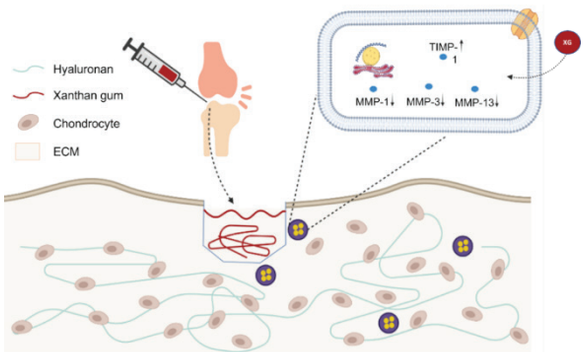

Fig. 14. IA injection of XG could increase the expression of TIMP-1 and down-regulate the expression of MMP-1, MMP-3, and MMP-13.

4.2. Bone tissue engineering

Bone defects have risen to the top of the list of causes of illness and disability among the elderly around the world. Even when autografting is seen as the benchmark repair method of bone defects, it is constrained by donor-site illness and unknown side effects. As a result, bone tissue engineering has piqued researchers' interest as a viable technique for fixing bone defects without the drawbacks and restrictions of bone allografts, xenografts, or autografts [44]. Injectable hydrogels are at an advantage over other materials since they can adjust to the defect's edges and can be inserted into deep defect sites with little invasiveness. As a result, injectable hydrogels can significantly minimize surgery duration, scar creation, post-operative discomfort (due to the fact that fewer muscles are affected during surgery), and recovery time [45]. Additionally, most hydrogels can imitate the native ECM, which allow cells to multiply and develop in a favourable

environment [46]. By incorporating growth factors, along with different osteoinductive components, can further help to improve the treatment's outcome [47].

D. Dyondi, et al. (2013) [25] used a dual growth-factor system to enhance the development of foetal osteoblast cells in the human body using injectable XG/GG hydrogels with CHT nanoparticles, basic fibroblast growth factor (bFGF), and bone morphogenetic protein 7 (BMP7). Due to the prolonged release of growth factors, XG/GG hydrogels combined with nanoparticles demonstrated a considerable improvement in cell proliferation and differentiation. When compared to hydrogels consisting of a single growth factor, dual growth factor hydrogels had more calcium deposition and alkaline phosphatase. In this experiment, the viability of L929 mouse fibroblast cells was higher than 95%, while the viability of human foetal osteoblast cells was reported to be 80% with XG/GG hydrogels as measured by the MTT assay for 48 h. Furthermore, in implant failure, XG/GG hydrogels shows antibacterial activity against common infections such as Pseudomonas aeruginosa, Staphylococcus epidermidis, and Staphylococcus aureus. In addition, D. Dyondi, et al. (2011) [24] had previously investigated the synergistic effect of platelet-derived growth factor BB (PDGF-BB) and basic fibroblast growth factor (bFGF) encapsulated inside an injectable porous hydrogel derived from XG and GG. The results show that there was an increase in the amount of total protein synthesis from osteoblasts and the amount of collagen in hydrogels that contained bFGF and PDGF by the 21st day.

4.3. Delivery system

The use of injectable hydrogels as a system or a carrier in the process of delivering cells, bioactive molecules, drugs, and other therapeutic agents is another common application. In addition to possessing properties that make hydrogels widely used for the delivery purposes (such as possessing a water-swollen porous structure that offers a suitable environment for cells, bioactive molecules, and also permitting for their controlled release), injectable hydrogels have several other benefits within the range of this application such as minimal invasive administration and better homogeneous encapsulation [35].

A previous study demonstrated that an injectable hydrogel containing an XG/MC combination could be a suitable long-term medication delivery strategy since it showed sustained release behaviour when loading with an anthracycline anticancer drug named doxorubicin (DOX). Longer release occurs with higher DOX concentration. Moreover, the loaded DOX would be released faster *in vivo* via hydrogel degradation [21]. Additionally, J. Huang, et al. (2018) [34] created an *in situ*-forming hydrogel for local drug delivery based on OXG and NOCC. According to the releasing assay of bovine serum albumin-fluorescein isothiocyanate (BSA-FITC, a model drug), the OXG/NOCC hydrogel could provide a stable and uninterrupted drug release for 10 h. After 20 h, the BSA-FITC releasing ratio was over 80%. Moreover, in comparison to conventional injectable fibrin gel, the OXG/NOCC hydrogel had the advantage of avoiding drug eruption in liquids, which was beneficial for wet wounds. Besides, the controlled release properties of hydrogels derived from XG, TM3a, and STMP were also investigated. The diffusion kinetic profiles of BSA and 5-Fu (model drugs) from the hydrogels revealed that the BSA-loaded and 5-Fu-loaded XG/TM3a/STMP hydrogels displayed a controlled release behaviour at a slower rate and reaching a maximum after being placed on a platform, which indicated that the BSA and 5-Fu diffused moderately and in a prolonged manner into the PBS medium [38]. Furthermore, several other XG-based injectable hydrogels have also been evaluated for delivery applications. The XG/CHT-based polyelectrolyte hydrogels for the delivery of Chlorhexidine (CHX), an antiseptic agent that has been used in dental therapies for gingival inflammation and plaque control, may be useful for acute or chronic periodontitis [32]. The XG/SF/STMP hydrogels containing BSA as a drug model could be used as drug carriers with the property of controlled release while having 59.1% of BSA cumulative release ratios into PBS medium [36]. A prepared XG/PF127 *in situ* gels containing methotrexate (MTX), the most used disease-modifying anti-rheumatic drug, shows to be a promising drug delivery system that could minimise the dose and dosing frequency, and was also predicted to be an effective IA drug delivery that could treat rheumatoid arthritis [48].

4.4. Bioink

Bioink, or 3D printing, enables the production of personalised tissue-engineered products with high tunability and complexity. Printable and biocompatible hydrogels are attractive materials for 3D printing applications because they offer favourable biomimetic environments for live cells such as high water content, porous structure, bioactive molecule incorporation, and tuneable mechanical properties and degradation rates. An ideal 3D printing gel would have a well-defined network, sufficient gel strength, appropriate viscosity, ability to fuse with previously printed layers, and ability to maintain its print shape [49].

In the work of synthesising 3D printing hydrogels based on XG and KG, the printing quality of 3D structures has shown to be significantly affected by the printing temperature. For the printing of a five-point star, models printed at 50^{o}C were more delicate yet well-defined than models printed at 25^{o}C. In this research, P.G. Segovia, et al. (2020) [28] did the optimisation with the goal of increasing the figure's height after 5 min and 1 h while keeping the figure's area approximately 12.3 cm^2. The optimal composition obtained from the process variables for the printing of a five-points star at a printing temperature of 50^{o}C was 0.9773/0.0062/0.016 (syrup/XG/KGM). In another study, R. Zhao, et al. (2020) [36] fabricated a printable and self-healing hydrogel ink based on SF and XG chemically crosslinked with

STMP. Rheological data demonstrated that incorporation of the SF microparticles into the STMP-crosslinked XG hydrogel could be attributed to the improvement of storage modulus and viscosity. With the same concentration of XG and STMP, the hydrogel containing SF in the composition had its 3D print possess a smaller width value than the one only containing XG and STMP. This indicates that the XG/SF/STMP hydrogels were more suitable to apply as an injectable material for fibre forming or 3D bioprinting with better shape fidelity of the printed structures than the XG/STMP hydrogel.

5. Conclusions

To sum up, XG is an outstanding natural polymer in terms of good water solubility, excellent biodegradability, and biocompatibility that can be applied for injection purposes following purification due to shear-thinning properties. Additionally, XG has been shown to be able to crosslink with other polymers by physical or chemical crosslinking mechanisms. The physical crosslinking mechanism allows XG to combine with other polymers via ionic interactions, hydrophobic interactions, hydrogen bonding, or heat-induced effects. Chemical crosslinking allows XG to bind to polymers through covalent bonds created by the Schiff base reaction, esterification reaction, and via hydrazone linkages. As described in this review, XG-based injectable hydrogels have been successfully applied in areas such as bone and cartilage tissue engineering, delivery systems for biomolecules, and bioink; however, the amount of research on these applications or other areas of biomedicine is still limited. As a result, current trends in the usage of XG-based injectable hydrogels in several biomedical applications are thoroughly examined in order to gain a better knowledge of this polymer in this field. From this review, it proves to have a promising future with the role of a biopolymer in accentuating the excellent features of tissue engineering products. Furthermore, the properties of gelling and shear-thinning possessed by XG may be more advantageous in 3D bioprinting of tissue scaffolds, and this shall set a firm ground for practical uses of tissue engineering in the future.

CRediT author statement

Thai Phuong Thao Nguyen: Conceptualisation, Methodology, Software, Writing and Editing; Phuong Hien Le: Data curation, Writing - Original draft preparation; Thi-Hiep Nguyen: Conceptualisation, Methodology and Writing, Editing and Reviewing.

ACKNOWLEDGEMENTS

The authors would like to thank the authors whose works have been cited in this article. This work was funded by Ministry of Science and Technology of Vietnam under grant number: DTDL.CN-54/21.

COMPETING INTERESTS

The authors declare that there is no conflict of interest regarding the publication of this article.

REFERENCES

[1] J.H. Lee (2018), "Injectable hydrogels delivering therapeutic agents for disease treatment and tissue engineering", *Biomaterials Research*, **22(1)**, pp.1-14, DOI: 10.1186/s40824-018-0138-6.

[2] M.D. Baumann, CE. Kang, J.C. Stanwick, et al. (2009), "An injectable drug delivery platform for sustained combination therapy", *Journal of Controlled Release*, **138(3)**, pp.205-213, DOI: 10.1016/j.jconrel.2009.05.009.

[3] N. Kayra, A.O. Aytekin (2009), "Synthesis of cellulose-based hydrogels: Preparation, formation, mixture, and modification", *Cellulose-Based Superabsorbent Hydrogels*, DOI: 10.1007/978-3-319-76573-0_16-1.

[4] F. Ullah, M.B.H. Othman, F. Javed, et al. (2015), "Classification, processing and application of hydrogels: A review", *Materials Science and Engineering: C*, **57**, pp.414-43, DOI: 10.1016/j.msec.2015.07.053.

[5] P.E. Jansson, L. Kenne, B. Lindberg (1975), "Structure of the extracellular polysaccharide from Xanthomonas campestris", *Carbohydrate Research*, **45(1)**, pp.275-282, DOI: 10.1016/S0008-6215(00)85885-1.

[6] A. Abbaszadeh, M. Lad, M. Janin, et al. (2015), "A novel approach to the determination of the pyruvate and acetate distribution in xanthan", *Food Hydrocolloids*, **44**, pp.162-171, DOI: 10.1016/j.foodhyd.2014.08.014.

[7] H. Acar, A. Kurt (2020), "Purified salep glucomannan synergistically interacted with xanthan gum: Rheological and textural studies on a novel pH-/thermo-sensitive hydrogel", *Food Hydrocolloids*, **101**, DOI: 10.1016/j.foodhyd.2019.105463.

[8] F.G. Ochoa, V.E. Santos, J.A. Casas, et al. (2000), "Xanthan gum: Production, recovery, and properties. Biotechnology advances", *Biotechnology Advances*, **18(7)**, pp.549-579, DOI: 10.1016/S0734-9750(00)00050-1.

[9] A. Kumar, K.M. Rao, S.S. Han (2018), "Application of xanthan gum as polysaccharide in tissue engineering: A review", *Carbohydrate Polymers*, **180**, pp.128-144, DOI: 10.1016/j.carbpol.2017.10.009.

[10] M. Tako, S. Nakamura (1984), "Rheological properties of deacetylated xanthan in aqueous media", *Agricultural and Biological Chemistry*, **48(12)**, pp.2987-2993, DOI: 10.1080/00021369.1984.10866637.

[11] I. Bradshaw, B.A. Nisbet, M.H. Kerr, et al. (1983), "Modified xanthan - its preparation and viscosity", *Carbohydrate Polymers*, **3(1)**, pp.23-38, DOI: 10.1016/0144-8617(83)90010-3.

[12] V.B. Bueno, R. Bentini, L.H. Catalani, et al. (2013), "Synthesis and swelling behaviour of xanthan-based hydrogels", *Carbohydrate Polymers*, **92(2)**, pp.1091-1099, DOI: 10.1016/j.carbpol.2012.10.062.

[13] C.E. Brunchi, M. Bercea, S. Morariu, et al. (2016), "Some properties of xanthan gum in aqueous solutions: Effect of temperature and pH", *Journal of Polymer Research*, **23(7)**, pp.1-8, DOI: 10.1007/s10965-016-1015-4.

[14] R. Lochhead (2017), "The use of polymers in cosmetic products", *Cosmetic Science and Technology*, **13**, pp.171-221, DOI: 10.1016/B978-0-12-802005-0.00013-6.

[15] K. Kang, D. Pettitt (1993), "Xanthan, gellan, welan, and rhamsan", *Industrial Gums*, **13**, pp.341-397, DOI: 10.1016/B978-0-08-092654-4.50017-6.

[16] G. Han, H. Shao, X. Zhu, et al. (2012a), "The protective effect of xanthan gum on interleukin-1beta induced rabbit chondrocytes", *Carbohydrate Polymers*, **89(3)**, pp.870-875, DOI: 10.1016/j.carbpol.2012.04.023.

[17] F. Chellat, M. Tabrizian, S. Dumitriu, et al. (2000), "*In vitro* and *in vivo* biocompatibility of chitosan-xanthan polyionic complex", *Journal of Biomedical Materials Research*, **51(1)**, pp.107-116, DOI: 10.1002/(sici)1097-4636(200007)51:1<107::aid-jbm14>3.0.co;2-f.

[18] G. Han, G. Wang, X. Zhu, et al. (2012b), "Preparation of xanthan gum injection and its protective effect on articular cartilage in the development of osteoarthritis", *Carbohydrate Polymers*, **87(2)**, pp.1837-1842, DOI: 10.1016/j.carbpol.2011.10.016.

[19] J.M. Kobzeff, D.E. Mead, T.A. Talashek, et al. (2003b), *Process for Clarification of Xanthan Solutions and Xanthan Gum Produced Thereby*, Official Gazette of the United States Patent and Trademark Office Patents 1272(1).

[20] Y. Qiu, K. Park (2001), "Environment-sensitive hydrogels for drug delivery", *Advanced Drug Delivery Reviews*, **53(3)**, pp.321-339, DOI: 10.1016/S0169-409X(01)00203-4.

[21] Z. Liu, P. Yao (2015), "Injectable thermo-responsive hydrogel composed of xanthan gum and methylcellulose double networks with shearthinning property", *Carbohydrate Polymers*, **132**, pp.490-498, DOI: 10.1016/j.carbpol.2015.06.013.

[22] M. Bercea, R.N. Darie, L.E. Nita, et al. (2011), "Temperature responsive gels based on Pluronic F127 and poly (vinyl alcohol)", *Ind. Eng. Chem. Res.*, **50(7)**, pp.4199-4206, DOI: 10.1021/ie1024408.

[23] M. Bercea, R.N. Darie-Nita, S. Morariu (2013), "Rheological investigation of xanthan/ Pluronic F127 hydrogels", *Rev. Roum. Chim*., **58(2-3)**, pp.189-196.

[24] D. Dyondi, T.J. Webster, R. Banerjee (2011), "Development of a dual growth factor loaded biodegradable hydrogel and its evaluation on osteoblast differentiation *in vitro*", *MRS Proceedings*, **1312**, DOI: 10.1557/opl.2011.916.

[25] D. Dyondi, T.J. Webster, R. Banerjee (2013), "A nanoparticulate injectable hydrogel as a tissue engineering scaffold for multiple growth factor delivery for bone regeneration", *International Journal of Nanomedicine*, **8**, pp.47-59, DOI: 10.2147/IJN.S37953.

[26] R. Chandrasekaran, R.P. Millane, S. Arnott, et al. (1988), "The crystal structure of gellan", *Carbohydrate Research*, **175(1)**, pp.1-15, DOI: 10.1016/0008-6215(88)80151-4.

[27] S. Matsukawa, Z. Tang, T. Watanabe (1999), "Hydrogen-bonding behaviour of gellan in solution during structural change observed by 1H NMR and circular dichroism methods", *Physical Chemistry and Industrial Application of Gellan Gum*, **114**, pp.15-24, DOI: 10.1007/3-540-48349-7_3.

[28] P.G. Segovia, V. Garcia-Alcaraz, S. Balasch-Parisi, et al. (2020), "3D printing of gels based on xanthan/ konjac gums", *Innovative Food Science & Emerging Technologies*, **64**, DOI: 10.1016/j.ifset.2020.102343.

[29] A. Abbaszadeh, W. MacNaughtan, G. Sworn, et al. (2016), "New insights into xanthan synergistic interactions with konjac glucomannan: A novel interaction mechanism proposal", *Carbohydrate Polymers*, **144**, pp.168-177, DOI: 10.1016/j.carbpol.2016.02.026.

[30] F. Chellat, M. Tabrizian, S. Dumitriu, et al. (2000), "Study of biodegradation behaviour of chitosan-xanthan microspheres in simulated physiological media", *J. Biomed. Mater. Res.*, **53(5)**, pp.592-599, DOI: 10.1002/1097-4636(200009)53:5<592::aid-jbm20>3.0.co;2-p.

[31] J.H. Hamman (2010), "Chitosan based polyelectrolyte complexes as potential carrier materials in drug delivery systems", *Mar. Drugs*, **8(4)**, pp.1305-1322, DOI: 10.3390/md8041305.

[32] J. Kim, J. Hwang, Y. Seo, et al. (2017), "Engineered chitosan-xanthan gum biopolymers effectively adhere to cells and readily release incorporated antiseptic molecules in a sustained manner", *Journal of Industrial and Engineering Chemistry*, **46**, pp.68-79, DOI: 10.1016/j.jiec.2016.10.017.

[33] K. Chinchu (2019), *A Novel Chitosan Based Injectable Hydrogel for Cartilage Tissue Engineering*, Master of Philosophy Thesis, 68pp.

[34] J. Huang, Y. Deng, J. Ren, et al. (2018), "Novel *in situ* forming hydrogel based on xanthan and chitosan re-gelifying in liquids for local drug delivery", *Carbohydrate Polymers*, **186**, pp.54-63, DOI: 10.1016/j.carbpol.2018.01.025.

[35] Q.V. Nguyen, D.P. Huynh, J.H. Park, et al. (2015), "Injectable polymeric hydrogels for the delivery of therapeutic agents: A review", *European Polymer Journal*, **72**, pp.602-619, DOI: 10.1016/j.eurpolymj.2015.03.016.

[36] L. Zhao, F. Pan, A. Mehmood, et al. (2020), "Protective effect and mechanism of action of xanthan gum on the color stability of black rice anthocyanins in model beverage systems", *Int. J. Biol. Macromol.*, **164**, pp.3800-380, DOI: 10.1016/j.ijbiomac.2020.09.027.

[37] N.R. Raia, B.P. Partlow, M. McGill, et al. (2017), "Enzymatically crosslinked silk-hyaluronic acid hydrogels", *Biomaterials*, **131**, pp.58-67, DOI: 10.1016/j.biomaterials.2017.03.046.

[38] R. Zhang, Y. Tao, W. Xu, et al. (2018), "Rheological and controlled release properties of hydrogels based on mushroom hyperbranched polysaccharide and xanthan gum", *Int. J. Biol. Macromol.*, **120(B)**, pp.2399-2409, DOI: 10.1016/j.ijbiomac.2018.09.008.

[39] P.K. Sharma, S. Taneja, Y. Singh (2018), "Hydrazone-linkage-based self-healing and injectable xanthan-poly(ethylene glycol) hydrogels for controlled drug release and 3D cell culture", *ACS Appl. Mater. Interfaces*, **10(37)**, pp.30936- 30945, DOI: 10.1021/acsami.8b07310.

[40] M. Kapoor, J. Martel-Pelletier, D. Lajeunesse, et al. (2011), "Role of proinflammatory cytokines in the pathophysiology of osteoarthritis", *Nat. Rev. Rheumatol*., **7(1)**, pp.33-42, DOI: 10.1038/nrrheum.2010.196.

[41] J. Li, G. Han, M. Ma, et al. (2019), "Xanthan gum Ameliorates Osteoarthritis and Mitigates Cartilage degradation via regulation of the Wnt3a/β-Catenin signaling pathway", *Med. Sci. Monit.*, **25**, pp.7488-7498, DOI: 10.12659/MSM.916092.

[42] G.Y. Han, X.F. Mei, T.M. Zhang, et al. (2014), "Xanthan gum inhibits cartilage degradation by down-regulating matrix metalloproteinase-1 and -3 expressions in experimental osteoarthritis", *Journal of Bioactive and Compatible Polymers*, **29(2)**, pp.180-189, DOI: 10.1177/0883911514521916.

[43] G. Han, Q. Chen, F. Liu, et al. (2017), "Low molecular weight xanthan gum for treating osteoarthritis", *Carbohydrate Polymers*, **164**, pp.386-395, DOI: 10.1016/j.carbpol.2017.01.101.

[44] A. Khojasteh, F. Fahimipour, M.B. Eslaminejad, et al. (2016), "Development of PLGA-coated β-TCP scaffolds containing VEGF for bone tissue engineering", *Mater. Sci. Eng. C. Mater. Biol. Appl.*, **69**, pp.780-788, DOI: 10.1016/j.msec.2016.07.011.

[45] L. Zhao, M.D. Weir, H.H.K. Xu, et al. (2010), "An injectable calcium phosphate-alginate hydrogel-umbilical cord mesenchymal stem cell paste for bone tissue engineering", *Biomaterials*, **31(25)**, pp.6502-6510, DOI: 10.1016/j.biomaterials.2010.05.017.

[46] M.W. Tibbitt, K.S. Anseth (2009), "Hydrogels as extracellular matrix mimics for 3D cell culture", *Biotechnology and Bioengineering*, **103(4)**, pp.655-663, DOI: 10.1002/bit.22361.

[47] Y. Tabata, K. Yamada, S. Miyamoto, et al. (1998), "Bone regeneration by basic fibroblast growth factor complexed with biodegradable hydrogels", *Biomaterials*, **19(7- 9)**, pp.807-81, DOI: 10.1016/s0142-9612(98)00233-6.

[48] T. Das, V.M. Prakash, P.K.T. Math (2019), "Injectable *in situ* gel of methotrexate for rheumatoid arthritis: development, *in vitro* and *in vivo* evaluation", *J. App. Pharm. Sci.*, **9(5)**, pp.40-48, DOI: 10.7324/JAPS.2019.90505.

[49] F.C. Godoi, S. Prakash, B.R. Bhandari (2016), "3D printing technologies applied for food design: Status and prospects", *Journal of Food Engineering*, **179**, pp.44-54, DOI: 10.1016/j.jfoodeng.2016.01.025.

DOI: 10.31276/VJSTE.64(1).63-71

A deep learning approach in detection of malaria and acute lymphoblastic leukemia diseases utilising blood smear microscopic images

Quyen Hoang Vo[1, 2], Xuan-Hieu Le[1, 2], Thanh-Hai Le[2, 3], Thi-Thu-Hien Pham[1, 2*]

[1]*School of Biomedical Engineering, International University, Quarter 6, Linh Trung Ward, Thu Duc City, Ho Chi Minh City, Vietnam*
[2]*Vietnam National University - Ho Chi Minh City, Quarter 6, Linh Trung Ward, Thu Duc City, Ho Chi Minh City, Vietnam*
[3]*Faculty of Mechanical Engineering, Ho Chi Minh City University of Technology, 268 Ly Thuong Kiet Street, Ward 14, District 10, Ho Chi Minh City, Vietnam*

Received 30 December 2021; revised 14 February 2022; accepted 23 February 2022

Abstract:

The numerous rising infections and deaths of malaria and acute lymphoblastic leukaemia (ALL) highlights the urgent need for early, useful, and efficient diagnosis methods. Recently, the framework of artificial intelligence has been applied to minimize time-consuming tasks, to increase the accuracy and flexibility of clinical diagnoses, and to reduce the pressure on physicians, diagnosticians, and clinical experts. In this study, a detection system for malaria and ALL is proposed that utilizes blood smear microscopic images with the aid of deep learning algorithms to identify and classify these two diseases automatically. The blood smear microscopic images consist of 1503 ALL images, 891 malaria images, and 1503 normal images that were divided into a training, validation, and testing sets in ratios of 50, 25, and 25%, respectively. The proposed model was built into three stages including the first stage for segmentation-applied modified UNet pre-trained model, the second stage for classification based on the convolution neural network model, and the final stage for classification utilizing perceptron as the combining model. As a result, the proposed system provides an alternative and interpretable method to detect abnormal leukocytes for ALL and malaria-infected blood cells with a 93% overall accuracy including the detection rate for ALL of 95% and the detection rate for malaria of 92%.

Keywords: **acute lymphoblastic leukaemia, blood smear microscopic image, deep learning, malaria.**

Classification number: **3.6**

1. Introduction

Malaria and ALL are two of the most dangerous blood diseases known today. According to the published data of the World Health Organization (WHO), there were an anticipated 241 million cases of malaria worldwide in 2020, with 627,000 deaths from this disease [1]. Whereas, ALL is a leading type of blood cancer that could grow rapidly to a deadly condition within weeks. Consequently, ALL contributed to the cause of 111,000 deaths globally and seriously impacted the lives of at least 876,000 patients in 2015 [2].

Malaria is a life-threatening disease that occurs due to the invasion of red blood cells (RBCs) caused by plasmodium parasites through the bites of infected mosquitoes. Consequently, the disease can be widely spread and affect the lives of millions of people in the world. Once bitten, the infection initially occurs in the liver before the parasites re-enter the bloodstream and target RBCs. At this moment, RBCs be infected with plasmodium become easily "sticky", and when they go through the small blood vessels inside the organs, they get stuck. Since the number of stuck RBCs enlarges, blood volume flows to the organ is reduced, which causes further complications such as kidney failure, coma, etc. If the sequential process happens inside the blood vessels in the brain, the result is clinically recognized as malaria disease - complications can emerge including impaired consciousness, coma, and even death [3].

Leukaemia is a term to describe a group of blood cancers that begin in the bone marrow, resulting in an excessive amount of abnormal white blood cells (WBCs). Four types of leukaemia cancer are ALL, acute myeloid leukaemia (AML), chronic myeloid leukaemia (CML), and chronic lymphocytic leukaemia (CLL). Among them, ALL occurs most frequently and it is a dangerous

*Corresponding author: Email: ptthien@hcmiu.edu.vn

disease that occurs when there is an uncontrollable proliferation of lymphoid precursors (i.e., lymphoblasts) in the bone marrow with restrained maturation. These overproduced leukemic cells cannot function properly and even suppress other normal WBCs from forming. These abnormal cells are the cause of fatigue, anaemia, fever, and bone pain because of the spread of these cells into the bone and joint surfaces, which further causes recurrent infections. The leukemic cells can then diffuse out of the bone marrow moving in the bloodstream and accumulate in various organs such as the lymph nodes (or lymph glands), spleen, liver, and central nervous system (brain and spinal cord) [4]. Consequently, patients diagnosed with ALL could die from various threats such as infection of bacteria, fungus, or even excessive bleeding in organs [3]. If left untreated, ALL disease can be fatal within weeks.

Among the current methods of examination and diagnosis, visual microscopical examination of Giemsa-stained blood smears is the most extensively used approach for assessing the development stage of malaria and leukaemia diseases [5]. However, the quality of the reagents, the image resolution of microscopes, and the experience of laboratory physicians/specialists all play a role in diagnosis. Another method is a polymerase chain reaction (PCR), which is also used to detect parasite nucleic acids of malaria or leukaemia. Although the PCR method is slightly more sensitive than smear microscopy, it has some limitations in the diagnosis of patients under restricted health care conditions [6]. Besides, a complete blood count (CBC) test is also commonly used to diagnose ALL. However, the sensitivity of this method is quite low because it depends on the number of white blood cells, for example, when the white blood cell count is not large enough and the symptoms may not be sufficiently obvious for the clinician to be able to confirm whether the patient has leukaemia [7]. In summary, these manual approaches may sometimes be time-consuming and expensive because all of the methods of detecting malaria and leukaemia are manual and completely rely on the expertise and knowledge of trained medical doctors [8].

Recently, blood smear microscopic image analysis has allowed pathologists to examine thin blood smear samples under optical microscopes to identify the presence of infected red blood cells for malaria cases or cancerous lymphocytes, which indicate the existence of malaria or ALL [9, 10]. It must be said that the analysis of smear films remains a challenge for pathologists not only due to the time-consuming assessment but also because of the requirement for specialized knowledge of image evaluation and for the massive workload that they must go through every day [10]. Obviously, improvements in image analysis, especially the applications of artificial intelligence (AI), are becoming increasingly popular and studied more widely. These advanced methods have the potential of automatic detecting processes that encourage faster and more precise diagnosis in the clinical microbiology field for infectious diseases [11]. Computer-aided diagnosis becomes more powerful and reliable when machine learning/deep learning approaches are combined with image processing techniques. The benefit of the machine learning/deep learning methods is to reduce human interaction while also improving the quality of the diagnostic results. Deep learning, a subset of machine learning, provides a better end-to-end approach by automatically extracting relevant features and learning how to employ those features in performing given tasks on their own in an incremental manner. Deep learning deals with studies that require more precision, more mathematics, and more computation, which are being used in various fields to improve the reliability of automated systems. Thus, biomedical image analysis with deep learning techniques has become a popular area in recent years as it eliminates the need for specialized expertise and complicated manual feature extraction [12].

Among the available studies on leukaemia detection, one of the most impressive is the work of T.T.P. Thanh, et al. (2018) [13]. Thanh's group investigated the use of CNN-based models to detect leukaemia. Although having an impressive accuracy of 96.6%, the stability of the model and the results of this work should take into account the training set contained only 108 original images. However, the authors suggested data augmentation methods such as rotation and flip/flop could overcome the fact of insufficiency of the training set data in [13]. In other studies, P. Jagadev, et al. (2017) [14] and L. Putzu, et al. (2014) [15] used traditional computer vision techniques combined with deep learning algorithms to detect leukaemia. P. Jagadev, et al. (2017) [14] enhanced the image content by applying different traditional methods including Otsu's algorithm and Kmeans clustering to segment the potential WBCs. However, the best performance of the ensembled model achieved only 90% precision and 89% recall. L. Putzu, et al. (2014) [15] proposed a mathematical morphology approach of mathematical expressions of sample features

such as shape, bending, and roundness ratio. Then, chain codes are extracted and fed to a support vector machine (SVM) classifier. As a result, their work reached a recall of 93%, which is promising.

For malaria detection, J. Hung, et al. (2017) [16] presented the Faster R-CNN model and pre-trained AlexNet model to detect each RBC in the microscopic blood smear images. Utilizing both transfer learning and object detection methods, their research reached an accuracy of 96% compared to the one-stage classifier. Another work, by N.E. Ross, et al. (2006) [17], proposed the identification of infected malaria cells by segmentation of RBCs utilizing thresholding techniques. They extracted the sample features by feeding images to an SVM classifier. The results achieved an accuracy of 81-85%. Later, M. Poostchi, et al. (2018) [18] presented a method that blended a multiscale Laplacian of Gaussian filter and an approximate centroid for the marker-controlled watershed to detect and segment RBCs individually. They applied a voting-based detection system that reached a precision of 88%. Whereas, based only on manual extraction features, M. Sheikhhosseini, et al. (2013) [19] applied a rule-based system that reached a considerable sensitivity (recall of disease class) of 82.88%.

In the proposed study, a deep learning model is applied to analyse microscopic images of blood smear to determine the existence of ALL and malaria with the aid of deep learning. Firstly, a convolutional neural network (CNN) is trained to segment the components of blood smear images, which are WBCs and RBCs. The dataset of blood smear microscopic images were collected from several different sources that are validated by scientific research community. Then, for malaria detection, each segmented RBC component is fed to another trained network to determine whether the RBC is healthy or has a high-risk of being infected with malaria. Whereas for ALL detection, the same process is applied to WBCs to examine if they are normal or leukemic. As a result, the evaluation metrics of the achieved results show that this proposed study is promising, highly accurate, and can be extended further into practical application.

2. Materials and methods

Three major tasks of a deep learning model are detection, classification, and segmentation. Detection is concentrated on detecting objects in an image and marking them with a rectangle around the object, for example, a person or an animal. On the other hand, classification is defined by categorizing the whole image into a predefined class such as "people", "animals", or "furniture". Meanwhile, segmentation deals with the association of each pixel in an image with a class label, such as WBC, RBC, background, etc. It should be noted that segmentation models provide an exact contour of the classified object in the image meanwhile classification models identify what is in the image, and the detection models place a bounding box around a specific object. To improve the accuracy and usefulness of this study, both segmentation and classification models were applied in this approach.

2.1. Loss functions

Loss function is an important part of artificial neural networks, which is used to measure the inconsistency between the predicted value and actual value. The loss function has a non-negative value, which means that the robustness of the model increases along with a decrease of the value of the loss function. Besides accuracy, the loss function can also be used to evaluate whether a model is overfitting or underfitting. Even though there are several available loss functions, each function is only suitable for a particular task. In the scope of the proposed study, 2 loss functions are explained, which are soft Dice and categorical cross-entropy [20].

Categorical cross entropy (CCE) is the most fundamental loss function and it is commonly used in classification tasks. The cross entropy can be formulated as follows [20]: $CE = -\sum_{i}^{C} t_i \log(s_i)$ (1)

where t_i and s_i are the ground truth and the CNN score from class i to class C, respectively. For example, given $C=2$ (where a classification only has two classes, i.e., positive and negative), Eq. (1) becomes [20]:

$$CE = -\sum_{i=1}^{C=2} t_i \log(s_i) = -t_1 \log(s_1) - (1-t_1)\log(1-s_1) \quad (2)$$

where $t_2=1-t_1$ and $s_2=1-s_1$ are the ground truth and the score for C_2. Equation (2) is often called binary cross entropy (BCE). Similarly, CCE only differs in the way of defining scores. The CCE requires the scores to be probabilities of one class on C classes, that is then scaled by a softmax function. Specifically [20],

$$f(s)_i = \frac{e^{s_i}}{\sum_j^C e^{s_j}} \quad (3)$$

$$CE = -\sum_{i=1}^{C=2} t_i \log(f(s)_i) \quad (4)$$

where t is a one-hot vector and p is the correct label. If there is only one element in t, where $t=tp$, that forms the CE non-zero. Then, Eq. (4) becomes [20]:

$$CE = -\log\left(\frac{e^{s_p}}{\sum_j^C e^{s_j}}\right) \tag{5}$$

where p represents the true class (i.e., positive class). It is noted that the CCE will go down as the prediction (i.e., the predicted score for the true class) becomes more accurate. CCE equals zero if the prediction is perfect. Therefore, cross-entropy can be a loss function for training a classification model.

In semantic segmentation tasks, soft Dice loss is a commonly used object function. It was inspired by the Dice coefficient formula suggested by T.J. Sørensen (1948) [21]. The Dice coefficient measures the similarity of 2 samples. In the context of semantic segmentation, it measures the overlapped region between the predicted mask and the ground truth. Simply, the larger the coefficient, the better the performance of the prediction model. The Dice coefficient is given by:

$$Dice = \frac{2\times|mask \cap prediction|}{|mask|+|prediction|} \tag{6}$$

In contrast, soft Dice loss is defined as the subtraction of the Dice coefficient from 1. The larger the loss values, the worse the performance of the model. Given the fact that any image could be treated as a 2-dimensional matrix, where each element is equivalent to a pixel of that image, $|A \cap B|$ can be approximated as the element-wise multiplication between the prediction and mask. Then, sum the resulting matrix.

To quantify $|A|$ and $|B|$, one can apply the squared sum of each matrix. Therefore, the mathematical expression of soft Dice loss is defined as follows:

$$Soft\text{-}dice = 1 - \frac{2\sum_{pixels} y_{true} y_{predicted}}{\sum_{pixels}(y_{true}^2 + y_{predicted}^2)} \tag{7}$$

Metrics

To evaluate the model on a dataset, different metrics are applied. Some commonly used metrics for classification tasks are the confusion matrix, sensitivity, precision, and accuracy. The confusion matrix illustrates the performance of a model with two or more classes. A confusion matrix contains 4 components including True Positive (TP), True Negative (TN), False Positive (FP), and False Negative (FN) where TP is defined as a total number of accurate predictions that are "positive", FP is defined as the total number of inaccurate predictions that are "positive", TN is defined as the total number of accurate predictions that are "negative" and FN is defined by the total number of inaccurate predictions that are "negative".

Precision (also called positive predictive value) is the probability that subjects having a positive test precisely have the disease. Meanwhile, the recall of a test (also called the true positive rate) is defined as the proportion of subjects having the disease that have a positive result. In other words, the recall is a high value when a model is highly sensitive. The precision and recall can be defined as follows:

$$\text{Precision} = \frac{TP}{(TP+FP)} \tag{8}$$

$$\text{Recall} = \frac{TP}{(TP+FN)} \tag{9}$$

Classification accuracy is the number of correct predictions made as a ratio of all predictions made. This is the most common evaluation metric for classification problems. However, it is only suitable when there are an equal number of observations in each class (which is rarely the case), while most of the models often face an imbalanced dataset. When a dataset is imbalanced, the dominance in a proportion of the majority class can make classification accuracy a misleading evaluation.

Semantic segmentation uses different metrics for evaluation compared to classification tasks. The most widely used metrics for segmentation models are the Dice coefficient and intersection over union (IoU). IoU is a metric that allows the evaluation of how much overlap a predicted bounding box has on the ground truth bounding box. The IoU compares the ratio of the area where the two boxes overlap to the total combined area of the two boxes.

Assuming the predicted mask is bounded by a rectangle and the ground truth is also placed within another rectangle, the coordinates of these two rectangles are used to simplify the calculation and implementation of the IoU algorithm as described in Fig. 1.

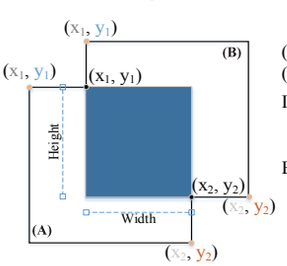

Fig. 1. Implementation of IoU calculation.

2.3. Transfer learning with VGG16 & UNET

The transfer learning technique allows pre-trained models to achieve the expected accuracy with fewer training epochs on a new dataset. Especially when the dataset is small, reusing knowledge from pre-trained models will help the trained models make better predictions because the models are learning from both knowledge sources, that is, new data and old data. Due to the advantages of using pre-trained models and the goals of this study, two popular models were selected including VGG16 [22] for the classification task and UNet [23] for the segmentation task. VGG16 is a CNN model that took first and second place in the localization and classification tasks respectively in the 2014 ImageNet challenge. The pretrained VGG16 has the ability of learning and extracting sufficient features for the classification task. UNet was presented by O. Ronneberger, et al. (2015) [23] to segment neural structures in human brain in 2012. The UNet architecture consists of two U-shaped symmetrical paths: the contraction (also called the encoder) is on the left and the extension (also called the decoder) is on the right. The contraction path is used to do the feature extraction task of capturing the context of the image. This path is called contraction because the size of the layers are decreasing. Simultaneously, the depth of layers increases gradually from 3 to 512. The extension path contains symmetrical layers corresponding to the layers of the contraction path. The decoder process is applied to help increase the layer size gradually. Finally, a segmented mask is obtained to show the prediction label of each pixel. The unique feature of UNet architecture is that it applies a symmetric skip connection between the encoder and decoder path.

2.4. Data collection

Table 1 presents two segmentation datasets that were collected and utilized to train RBC and WBC segmentation models. The combined datasets are called the WBC Image Dataset, which was published by X. Zheng (2018) [24] and "erythrocytesIDB" proposed by Universidad de Oriente of Cuba [25], respectively, for WBCs and RBCs. For WBCs, the dataset contains three hundred 120×120 px sub-images of a single WBC and one hundred 300×300 px colour images (including neutrophils, eosinophils, basophils, monocytes, and lymphocytes). These samples were taken by a motorized auto-focus microscope, then were processed with a developed haematology reagent for rapid WBC staining. For RBCs, the erythrocytesIDB dataset contains images of peripheral blood smear samples taken from patients with sickle cell disease that contain full-field images and individual cells classified as circular, elongated, or other. These samples were fixed with absolute alcohol and stained with Giemsa in a proportion of 2% of reagent to 1 ml of distilled water. The RBC segmentation model treated each sample as a full-sized blood smear microscopic image with a binary mask including red blood cell pixels that were coloured white. After segmentation, the number of samples in the datasets changed in size, as shown in Table 2.

Table 1. Segmentation database.

Dataset name	Number of images/Cell type	Release year
ErythrocytesIDB	320/RBCs	2017
WBC image dataset	400/WBCs	2018

Table 2. Distribution of samples for classification.

Class name	Sample size
Normal	1503
ALL	1503
Malaria	891

Table 3 shows the sample size for the training, validation, and testing subsets. The percentages for training, validation, and testing were chosen as 50%, 25%, and 25%, respectively. The dataset, in fact, is made up of blood smear microscopic pictures gathered from different sources. Table 4 shows the distribution of samples organized by database name.

Table 3. Sample size of each data subset.

Data set	Sample size
Training set	1948 (50%)
Validation set	974 (25%)
Testing set	975 (25%)

Table 4. Distribution of dataset by sources.

Database name	Disease	Number of images
ALL-IDB	Leukaemia	1503
MLSRC	Malaria	668
MP-IDP	Malaria	223
ALL-IDB	Normal	1503

3. Implementation of model

3.1. System overview

Figure 2 illustrates the three-stage classifier system that was created to detect ALL or malaria on blood smear microscopic images. The system took each fed-in block to predict the mask for each block, and then combined all masks to generate the binary mask for the entire image in the first step. Then, the system segregated each blood cell (i.e., RBC and WBC) into every single image using contour finding and the watershed method.

In the second stage, each WBC was isolated and sent into a CNN classifier, which verifies whether the WBC is leukemic or malignant. Meanwhile, each RBC was loaded

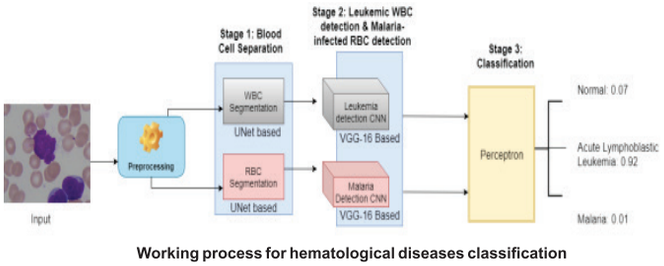

Fig. 2. The process of classifier.

into a second CNN model to determine the probability of an RBC becoming infected with malaria parasites. Only the maximum predicted probability for each type of RBC/WBC was reserved because an image might contain both numerous RBCs and WBCs. The two probabilities were concatenated and given to a perceptron network in the last stage of the system, which determines whether the studied image was a normal cell, infected with malaria, or ALL.

3.2. Implementation

Stage 1: Blood cell separation: two segmentation models were developed, which were the WBC segmentation model for WBCs and the RBC segmentation model for RBCs. Every image was divided into numerous 128x128 px images to save time and prevent system crash owing to the large size of the images. Each sub-image was then supplied to one of the two segmentation models based on the UNet pre-trained model. The predicted binary masks of all sub-images were then concatenated together for each segmentation model to generate the total binary masking for the original image. The whole process for the first stage is visualized in Fig. 3.

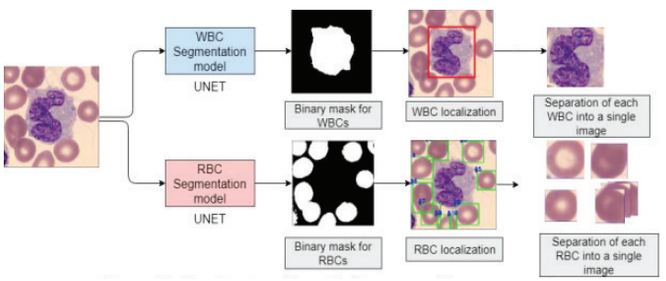

Fig. 3. Visualization the first stage of the system.

The results of the UNet training process were the RBC mask, in which positive pixels (i.e., white pixels) correspond to RBCs, and the WBC mask, in which each white pixel corresponded to WBCs. These masks are commonly used in fully convolutional networks for segmenting biological molecules. After that, each binary mask was subjected to contour finding and minimum enclosing rectangle to produce rectangle images with only one cell of interest in the centre. The models were trained using the soft Dice loss function and the customized IoU measure, which was adapted from the original UNet.

Stage 2: Blood cell type classification: following Stage 1, each isolated cell was fed into one of two models in Stage 2 as shown in Fig. 4. The first classifier determines the likelihood of a malaria-infected RBC. The second model identified the likelihood that a WBC is leukemic. Both models were trained in 30 epochs on the same training dataset and then validated on the same validation dataset using the same VGG16 structures with the same modifications. The last layer was removed and replaced with a sigmoid-activated layer of 2 units. Stage 2 generates a list of probabilities for RBCs being infected with malaria and a list of probabilities for WBCs being leukemic lymphoblasts from an image containing numerous RBCs and WBCs. Nonetheless, only the highest probability of each vector was preserved for processing in the next stage.

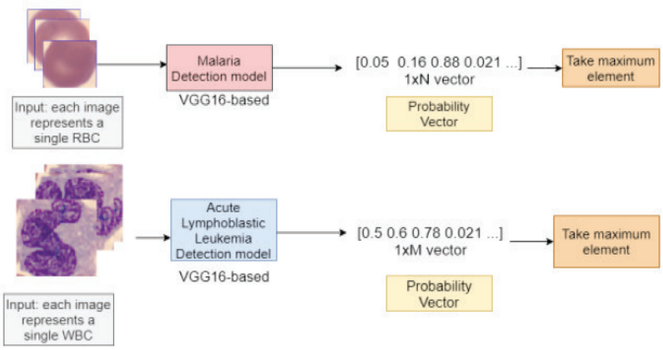

Fig. 4. Visualization of Stage 2 of the proposed model.

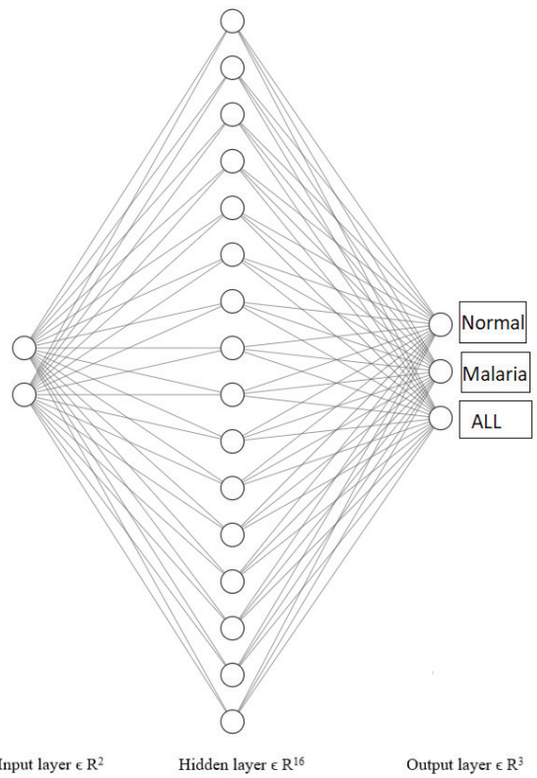

Fig. 5. Visualization of the perceptron architecture.

Stage 3: Classification utilizing perceptron as the combining model: the two maximum probabilities from Stage 2 were used as the two input neurons for a perceptron model in the third stage of this technique. The perceptron model was made up of three layers as illustrated in Fig. 5. The first layer is the input layer, which has two neurons that correspond to the two maximum probabilities mentioned. The middle layer is a hidden layer of neurons. The last layer is the output of 16 nodes, which have a softmax activation function and indicate the probabilities of the original input classified as "malaria", "ALL", or "normal". As a combined classifier, the perceptron model is used. On the training set, the perceptron was trained for 20 epochs.

4. Results and discussion

Figures 6 and 7 show the results of the two WBC and RBC segmentation models, respectively. The training loss and validation loss for the WBC segmentation model significantly reduced throughout epochs indicating that the model is accurately and effectively trained. After 85 epochs, the model learns and begins to converge at a mean IoU of 0.91. A 0.91 mean IoU score simply means that the projected segmentation region overlaps the ground truth by 91%, which is a good and promising precision for the segmentation challenge. With a mean IoU of 0.94, the RBC segmentation model's training and validation losses saturate after 90 epochs.

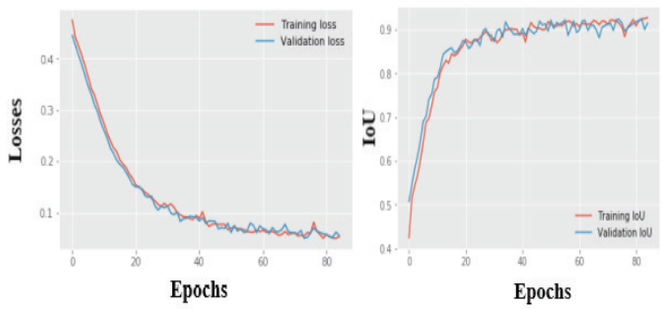

Fig. 6. Training and validation losses / IoUs of WBC segmentation model.

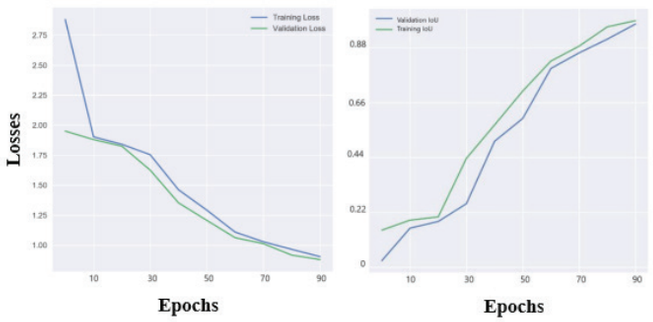

Fig. 7. Training and validation losses/IoUs of RBC segmentation model.

In the second stage, two CNN classification models are built. Fig. 8 shows the loss and accuracy values of the malaria detection model over epochs. Fig. 9 illustrates the same parameters for ALL. Both models achieved a high accuracy of validation when training.

A confusion matrix is developed to infer the meaning of precision, recall, and accuracy to evaluate the performance of an entire system on the testing dataset. Fig. 10 and Table 5 provide more information on these metrics. Fig. 10 depicts the confusion matrix's insight, which provides readers with a numerical expression of the model's performance. Table 5 summarizes the overall performance of the system on the testing dataset.

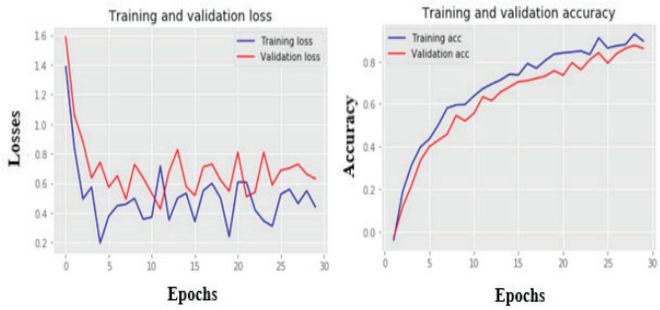

Fig. 8. Training and validation losses/accuracies of the malaria detection model.

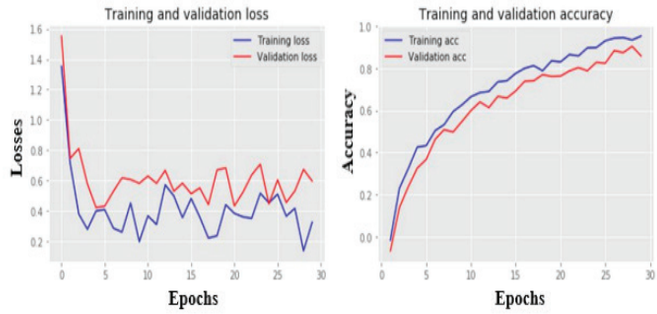

Fig. 9. Training and validation losses/accuracies for the ALL detection model.

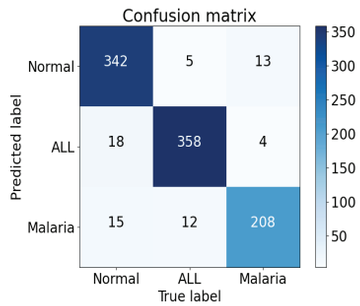

Fig. 10. Confusion matrix for evaluation of whole system on testing set.

Table 5. The results of precision, recall for each class and whole accuracy of the system.

Class name / Metrics (%)	Normal	ALL	Malaria
Precision	95	94	88
Recall	91	95	92
Whole accuracy of the system		**93**	

With the help of ensemble learning, the overall performance of the classification system reaches an accuracy of 93%. Individually, each sub-performance model is rather good and acceptable. For the segmentation task, the average IoU is over 0.9 indicating that the system can forecast masks with over 90% overlapped area with true ground truths. Both CNN detection models were found to have an accuracy of more than 90%. The accuracy of the malaria detection model is less than that of the model for detecting acute lymphoblastic leukaemia (89 vs 92%). Furthermore, the loss plots of all the models show that the models are correctly trained without overfitting or underfitting. Tables 6 and 7 compare the precision and recall of classification among the proposed system and other publications.

Table 6. Comparison of the proposed method in malaria detection with other studies by precision and recall.

Study	Malaria detection precision (%)	Malaria detection recall (%)
Our method	**88**	**92**
J. Hung, et al. (2017) [16]	98	97
N.E. Ross, et al. (2006) [17]	81	85
M. Poostchi, et al. (2018) [18]	88	91
M. Sheikhhosseini, et al. (2013) [19]	Not mentioned	82.28

Table 7. Comparison of the proposed method in ALL detection with other studies by precision and recall.

Study	ALL detection precision (%)	ALL detection recall (%)
Our method	**94**	**95**
H. Chowdhury, et al. (2018) [9]	90	89
T.T.P. Thanh, et al. (2018) [13]	97	97
L. Putzu, et al. (2014) [15]	Not mentioned	93

Compared to other studies, the proposed study outperforms H. Chowdhury, et al. (2018) [9] and L. Putzu, et al. (2014) [15], but lags behind T.T.P. Thanh, et al. (2018) [13] in detecting ALL in a blood smear microscopic image. The algorithm of Thanh, et al., on the other hand, appears to be overfitted, as their study used only 108 unique images for the dataset. Even though augmentation can expand datasets, it is not recommended to use augmented images on testing, as group of Thanh did, because this might lead to overfitting issues. In terms of malaria detection, the proposed study outperforms M. Poostchi, et al. (2018) [18], M. Sheikhhosseini, et al. (2013) [19], and N.E. Ross, et al. (2006) [17], but falls short of J. Hung, et al. (2017) [16]. J. Hung's group built a two-stage detection approach with Faster-RCNN, which is comparable to our proposed solution, however, their method requires hard-core training and does not directly flag up problematic cells.

Although the proposed study is not among the top performances, the suggested method still has several advantages than other studies in some respects. Firstly, the proposed method can perform both abnormal leukocytes for ALL and malaria-infected blood cells identification while other studies only detected one type of disease. Secondly, compared to related works that suggested only one CNN classifier, the proposed system is more interpretable as it can indicate the locations of not only ALL in white blood cells but also malaria-infected blood cells. Obviously, the detecting result of multiple diseases from blood smear microscopic images will provide more information for the histopathologist to evaluate the sample. Due to the proposed study indicating the potential subjects for detection, haematologists can have a quick look through those potential objects to verify the results faster and more precisely. In addition, if diagnosed with a disease, haematologists can also see why the proposed system classified the disease and in which cell(s) the model recognized the disease(s).

The system, in fact, has a number of challenges. The method takes longer to process an image than other alternatives, which is the most evident shortcoming. This is owing to the time-consuming nature of merging multiple models and processes at once. However, if parallel-computation techniques are used, this problem can be solved. Another issue that has been brought up is a lack of training data. Ideally, one would want hundreds of thousands of images to train a deep learning system. This difficulty can be solved by collecting more data or using the synthetic minority over-sampling technique (SMOTE).

5. Conclusions

This study has proposed a learning-based method that consists of three stages to segment white blood cells and red blood cells in blood smear microscopic images by the UNet model. The probability of acute lymphoblastic leukaemia and malaria is calculated by the VGG16 model and then those diseases are classified by the perceptron model. The performance of the proposed study achieves an average IoU of 90% for the segmentation task and an overall classification accuracy of 93% for the three types of conditions (malaria, acute lymphoblastic leukaemia, and normal). Overall, the achieved results indicate that the proposed system has promising potential for

the development of learning-based approaches for automated diagnosis of blood diseases utilizing blood smear microscopic images.

CRediT author statement

Quyen Hoang Vo, Xuan-Hieu Le, Thanh-Hai Le: Data curation, Software, Visualisation, Investigation, Writing original draft preparation; Thi-Thu-Hien Pham: Conceptualisation, Methodology, Supervision.

ACKNOWLEDGEMENTS

The authors gratefully acknowledge the financial support provided to this study by Vietnam National University, Ho Chi Minh city under Grant No. DS2020-28-02.

COMPETING INTERESTS

The authors declare that there is no conflict of interest regarding the publication of this article.

REFERENCES

[1] World Health Organization (2020), *World Malaria Report 2020*, https://www.who.int/publications/i/item/9789240015791, accessed 27 March 2021.

[2] Global Burden of Disease 2015 Disease and Injury Incidence and Prevalence Collaborators (2016), "Global, regional, and national incidence, prevalence, and years lived with disability for 310 diseases and injuries, 1990-2015: A systematic analysis for the global burden of disease study 2015", *Lancet*, **388**, pp.1545-1602, DOI: 10.1016/S0140-6736(16)31678-6.

[3] K.N. Suh, K.C. Kain, J.S. Keystone (2004), "Malaria", *CMAJ*, **170(11)**, pp.1693-1702, DOI: 10.1503/cmaj.1030418.

[4] P. Anderlini, M. Luna, H.M. Kantarjian, et al. (1996), "Causes of initial remission induction failure in patients with acute myeloid leukaemia and myelodysplastic syndromes", *Leukemia*, **10(4)**, pp.600-608.

[5] M.T. Makler, C.J. Palmer, A.L. Alger (1998), "A review of practical techniques for the diagnosis of malaria", *Annals of Tropical Medicine and Parasitology*, **92(4)**, pp.419-433, DOI: 10.1080/00034989859401.

[6] Division of Parasitic Diseases and Malaria (2020), *Malaria Diagnostic Tests*, https://www.cdc.gov/malaria/diagnosis_treatment/ diagnostic_tools.html#tabs-1-1, accessed 27 March 2021.

[7] American Cancer Society, *Tests for Acute Myeloid Leukemia (AML)*, https://www.cancer.org/cancer/acute-myeloid-leukemia/detection-diagnosis-staging/how-diagnosed.html, accessed 27 March 2021.

[8] S. Shafique, S. Tehsin (2018), "Acute lymphoblastic leukaemia detection and classification of its subtypes using pretrained deep convolutional neural networks", *Technology in Cancer Research and Treatment*, **17**, DOI: 10.1177/1533033818802789.

[9] H. Chowdhury, S. Banik, A. Hossain, et al. (2018), *Detection of Acute Lymphocytic Leukaemia (ALL) and Its Type by Image Processing and Machine Learning*, Thesis, BRAC University, 80pp.

[10] M. Poostchi, I. Ersoy, K. McMenamin, et al. (2018), "Malaria parasite detection and cell counting for human and mouse using thin blood smear microscopy", *Journal of Medical Imaging*, **5(4)**, DOI: 10.1117/1.JMI.5.4.044506.

[11] K.P. Smith, J.E. Kirby (2020), "Image analysis and artificial intelligence in infectious disease diagnostics", *Clinical Microbiology and Infection*, **26(10)**, pp.1318-1323, DOI: 10.1016/j.cmi.2020.03.012.

[12] S. Chakraborty, K. Mali (2020), "An overview of biomedical image analysis from the deep learning perspective", *Applications of Advanced Machine Intelligence in Computer Vision and Object Recognition: Emerging Research and Opportunities*, pp.197-218, DOI: 10.4018/978-1-7998-2736-8.ch008.

[13] T.T.P. Thanh, C. Vununu, S. Atoev, et al. (2018), "Leukemia blood cell image classification using convolutional neural network", *International Journal of Computer Theory and Engineering*, **10(2)**, pp.54-58, DOI: 10.7763/IJCTE.2018.V10.1198.

[14] P. Jagadev, H. Virani (2017), "Detection of leukaemia and its types using image processing and machine learning", *2017 International Conference on Trends in Electronics and Informatics (ICEI)*, pp.522-526, DOI: 10.1109/ICOEI.2017.8300983.

[15] L. Putzu, G. Caocci, C.D. Ruberto (2014), "Leucocyte classification for leukaemia detection using image processing techniques", *Artificial Intelligence in Medicine*, **62(3)**, pp.179-191, DOI: 10.1016/j.artmed.2014.09.002.

[16] J. Hung, S.C.P. Lopes, O.A. Nery, et al. (2017), "Applying faster R-CNN for object detection on malaria images", *2017 IEEE Conference on Computer Vision and Pattern Recognition Workshops*, pp.808-813, DOI: 10.1109/cvprw.2017.112.

[17] N.E. Ross, C.J. Pritchard, D.M. Rubin, et al. (2006), "Automated image processing method for the diagnosis and classification of malaria on thin blood smears", *Medical and Biological Engineering and Computing*, **44(5)**, pp.427-436, DOI: 10.1007/s11517-006-0044-2.

[18] M. Poostchi, K Silamut, R.J. Maude, et al. (2018), "Image analysis and machine learning for detecting malaria", *Translational Research*, **194**, pp.36-55, DOI: 10.1016/j.trsl.2017.12.004.

[19] M. Sheikhhosseini, H. Rabbani, M. Zekri, et al. (2013), "Automatic diagnosis of malaria based on complete circle-ellipse fitting search algorithm", *Journal of Microscopy*, **252(3)**, pp.189-203, DOI: 10.1111/jmi.12081.

[20] D.R. Cox (1958), "The regression analysis of binary sequences", *Journal of The Royal Statistical Society, Series B (Methodological)*, **20(2)**, pp.215-242.

[21] T.J. Sørensen (1948), "A method of establishing groups of equal amplitude in plant sociology based on similarity of species content and its application to analyses of the vegetation on Danish commons", *København I Kommission hos E. Munksgaard*, 34pp.

[22] K. Simonyan, A. Zisserman (2015), "Very deep convolutional networks for large-scale image recognition", *International Conference on Learning Representations (ICLR) 2015*, DOI: 10.48550/arXiv.1409.1556.

[23] O. Ronneberger, P. Fischer, T. Brox (2015), "U-net: Convolutional networks for biomedical image segmentation", *Medical Image Computing and Computer-Assisted Intervention - MICCAI 2015*, Springer, **9351**, DOI: 10.1007/978-3-319-24574-4_28

[24] X. Zheng (2018), "Data for: Tast and robust segmentation of cell images by self-supervised learning", *Mendeley Data*, DOI: 10.17632/w7cvnmn4c5.1.

[25] J.B.Z. Alfonso (2017), "ErythrocytesIDB", *Special Hematology Department of The General Hospital*, http://erythrocytesidb.uib.es/, accessed 27 March, 2021.

DOI: 10.31276/VJSTE.64(1).72-77

The impairment of osteogenic differentiation of human adipose tissue-derived mesenchymal stem cells under high D-glucose concentrations

Yen-Nhi Ha Nguyen[1, 2], Long Binh Vong[1, 2], Hong-Anh Pham[1, 2], Dang-Quan Nguyen[3], Phan Ngoc Uyen Phuong[3], Huu-Phuong Mai[2, 4], Nhu-Thuy Trinh[1, 2*]

[1]School of Biomedical Engineering, International University, Quarter 6, Linh Trung Ward, Thu Duc City, Ho Chi Minh City, Vietnam
[2]Vietnam National University, Ho Chi Minh City, Quarter 6, Linh Trung Ward, Thu Duc City, Ho Chi Minh City, Vietnam
[3]Biotechnology Center of Ho Chi Minh City, 2374, Highway 1, Quarter 2, Trung My Tay Ward, District 12, Ho Chi Minh City, Vietnam
[4]University of Science, Ho Chi Minh City, 227 Nguyen Van Cu Street, Ward 4, District 5, Ho Chi Minh City, Vietnam

Received 13 January 2022; revised 10 February 2022; accepted 27 February 2022

Abstract:

Type 2 diabetic patients have an increased risk of developing serious long-term complications such as cardiovascular disease, retinopathy, nephropathy, neuropathy, diabetic foot, and osteoporosis. However, the correlation between hyperglycaemia and osteoporosis has not yet been fully clarified. In this research, we investigated the effect of different high D-glucose concentrations (25, 50, and 100 mM) on osteogenic differentiation of human non-diabetic and diabetic adipose tissue-derived mesenchymal stem cells (nAT-MSCs and dAT-MSCs). The differentiated cells were qualified by Alizarin Red S staining and quantified by measuring the absorbance at 482 nm. The expressions of osteogenic master genes were examined by quantitative reverse transcription polymerase chain reaction (qRT-PCR) methods. Interestingly, the osteogenic differentiation and the expression of osteogenic-specific genes (Runx-2 and ALP) decreased with an increase of D-glucose concentration. Our work contributes to the understanding of the relationship between hyperglycaemia and osteoporosis and support the role of stem cells in developing new medicine or therapeutic treatment for preventing diabetic complications.

Keywords: **AT-MSCs, diabetes, differentiation potential, high D-glucose concentrations, osteoporosis.**

Classification number: **3.6**

1. Introduction

Diabetes mellitus (DM) brings a significant national and global disease burden that, according to the WHO (World Health Organization), is expected to affect the lives of 380 million people by the year 2025. Type 2 DM is found in up to 95% of people with DM [1]. According to previous research, chronic hyperglycaemia not only damages the organs but also had a deleterious effect on the skeletal system, degeneration of bone quality, loss of bone strength, increased fracture risk, and delayed bone healing [2]. Osteoporosis is a condition in which the density of osteocytes in the bones fall over time causing the bones to become increasingly brittle and prone to injury or fracture even under minor force. Despite the fact that DM and osteoporosis are two different diseases, there is a lot of evidence and speculation that the two diseases are genetically linked [3]. With an increasing proportion of patients with DM having a risk of bone fractures, the exact impact on bone structure is complex and has been poorly investigated [4, 5]. Mesenchymal stem cells, which have been widely known for their self-renewable, differentiation potential, and immunosuppressive properties, has demonstrated therapeutic effects in the treatment of osteoporosis in preclinical animal models [6, 7]. Adipose tissue-derived mesenchymal stem cells (AT-MSCs) have been shown to be abundant sources that have many outstanding properties for stem cell therapy compared to other source-derived stem cells.

According to Y.M. Li, et al. (2007) [8], AT-MSCs have shown the ability to differentiate into osteocytes under 25 mM D-glucose. Consistent with previous research, high D-glucose (25 mM) was proven to promote

*Corresponding author: Email: tnthuy@hcmiu.edu.vn

osteogenic differentiation in periodontal ligament stem cells (HDLSCs) [9]. However, persistent high glucose concentrations and AT-MSCs from diabetic donors with T2DM altered the osteogenic differentiation potential of AT-MSCs, which was demonstrated by ALP gene expression under 5.5, 13.5, and 55.5 mM D-glucose [10]. Moreover, high D-glucose concentration has been shown to suppress the expression of ALP and osteogenic gene Runx-2 [11-13]. ALP is an early marker of osteoblast differentiation, and its increased expression is associated with the progressive differentiation of osteoblasts [14]. Besides, Runx-2 is a critical regulator during osteogenic development, and the loss of Runx-2 expression at this early stage impairs osteogenic differentiation in bone development [15]. According to W. Xia, et al. (2022) [16], Runx-2 expression was decreased under the treated of 25 mM D-glucose in MC3T3-E1 cells. On the other hand, we recently identified that the AT-MSCs under high D-glucose concentrations (25, 50, and 100 mM) induced the expression of EGR-1, PTEN, and GGPS-1, which are involved in insulin resistance [17]. All of these findings contributed to the clarification of the relationship between T2DM and osteoporosis, as well as the improvement of stem cell therapy for the diseases. However, there are very few studies and a lot of controversy over the effect of the high D-glucose on osteogenic differentiation. Therefore, the aim of this study is to demonstrate the quantification and qualification of osteogenic differentiation of AT-MSCs from type 2 diabetic donors and non-diabetic donors under high D-glucose concentrations.

2. Materials and methods

2.1. Stem cell culture

Non-diabetic AT-MSCs (nAT-MSCs) and diabetic AT-MSCs (dAT-MSCs) were provided by the Laboratory of Regenerative Medicine and Stem Cell Biology, University of Tsukuba, Japan. These cells were characterized in previous reports [18, 19]. nAT-MSCs and dAT-MSCs were cultured in Iscove's modified Dulbecco's medium (Thermo, USA), supplemented with 10% foetal bovine serum (Thermo, USA), 1% antibiotics (Sigma, USA), and 5 ng/ml basic fibroblast growth factor (bFGF, Sigma, USA) at 37°C and 5% CO_2. The medium was renewed every 3 days until reaching 70-80% confluence, then cell passages were performed. nAT-MSCs and dAT-MSCs were cryopreserved in cell banker solution (Sigma, USA) and stored in liquid nitrogen for further experiments. All AT-MSCs used for this study were at passage 5-8.

2.2. Cell proliferation assay

nAT-MSCs and dAT-MSCs were seeded in a 24-well plate at density of $1.5x10^4$ cells/well and supplemented with high D-glucose concentrations (25, 50, and 100 mM). The cell culture medium was replaced every 3 days. The proliferation rate of AT-MSCs was investigated for 11 days after supplement with D-glucose. Trypan blue exclusion method was used to determine cell proliferation for every 48 hours until 11 days.

2.3. In vitro osteogenic differentiation of AT-MSCs

nAT-MSCs and dAT-MSCs were cultured in culture medium until reaching 100% confluence, then the cells were changed into a new medium with or without the induced osteogenic differentiation medium (including dexamethasone, β-glycerol-2-phosphate, ascorbic acid, human epidermal growth factor) [20]. The nAT-MSCs and dAT-MSCs, which were used as negative controls in the experiment, were cultured in normal medium.

2.4. Osteogenic differentiation qualification and quantification

After 21 days of the induction of osteogenic differentiation, the cells were fixed by 10% formalin (Merck, Germany) and the differentiation cells were qualified by Alizarin red S (Sigma, USA) staining to examine calcification in osteoblasts. The osteoblasts were visualized in red under an inverted microscope at 10x magnification. After that, osteoblasts were qualified and measured at 482 nm using a 96-well-plate microplate reader.

2.5. Quantitative reverse transcription polymerase chain reaction

To examine the expression of genes related to osteogenic differentiation, nAT-MSCs and dAT-MSCs were assessed at day 7 after differentiation induction. RNA was extracted using Sepasol-RNA I Super G (Nacalai Tesque, Japan). Total RNA (300 ng) was reverse-transcribed using reverse transcription polymerase chain reaction (RT-PCR) Kit (TOYOBO, Japan) to create a cDNA library. cDNA was analysed using a LightCycler 96 System (Roche, Switzerland) using Maxima SYBR Green/ROX qPCR Master Mix (2X) Kit (Thermo, USA). The expression levels of the target genes were analysed using the method. The β-actin gene was used as an internal control for the experiments. The sequences of the primer sets used for the PCR reactions are shown in Table 1.

Table 1. Primers used for quantitative polymerase chain reaction.

Function	Gene	Primer	Sequence
Internal control	β-actin	5'-primer	GTGCGTGACATTAAGGAGAA GCTGTGC
		3'-primer	GTACTTGCGCTCAGGAGGAG CAATGAT
Osteogenic markers	Runx-2	3'-primer	CAGATGGGACTGTGGTTACT GTCATGG
		5'-primer	CCTAAATCACTGAGGCGGTC AGAGAAC
	ALP	3'-primer	ACGTGGCTAAGAATGTCATC
		5'-primer	CTGGTAGGCGATGTCCTTA

2.6. Statistical analysis

Significant differences among various groups were performed using student's t-test and one-way analysis of variance (ANOVA) (Tukey post-hoc test; SPSS 20 software, IBM Corp.). The experiments in the research were repeated at least 3 times, and the $p<0.05$ value was considered as a statistically significant difference. Data was presented as the mean ±standard deviation (SD).

3. Results

3.1. The impairment of nAT-MSCs under high D-glucose concentrations

Glucose is considered the energy source of cells. However, high D-glucose concentrations can induce the senescence of cells via promoting ROS production [21, 22]. Thus, we evaluated the effect of different D-glucose concentrations (25, 50 and 100 mM) on the proliferation of nAT-MSCs for 11 days and compared them with the dAT-MSCs. The doubling time result indicated that there was no significant difference in the growth rate between nAT-MSCs (35.67±0.49 h) and dAT-MSCs (34.9±1.26 h). On the other hand, the high D-glucose supplemented groups showed a lower proliferation rate than the control group and dAT-MSCs (Fig. 1). Significantly, we found that the doubling time of the highest D-glucose treated group was 1.70-fold decreased (60.95±4.18 h, $p<0.01$, n=3), compared to the control group. This result proves that high D-glucose concentrations decelerated the growth of nAT-MSCs. However, the high D-glucose treated cells continued to proliferate, which is considered to be suitable for further experiments.

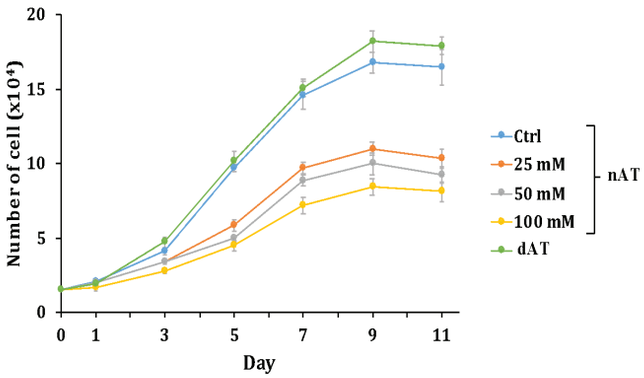

Fig. 1. The proliferation curve of nAT-MSCs under the effect of high D-glucose concentrations, compared with dAT-MSCs. The number of cells were determined every 48 hours by using trypan blue exclusion method for 11 days after D-glucose supplementation. High D-glucose concentrations inhibit the proliferation of nAT-MSCs. The data indicated the average values of three independent experiments (mean ± SD); Ctrl: control group is the non-treated group.

3.2. Qualification of the osteogenic differentiation in nAT-MSCs under high D-glucose concentrations

We hypothesized that the high D-glucose treated nAT-MSCs had decreased osteogenic differentiation according to the concentrations. To test this hypothesis, the osteogenic potential of nAT-MSCs was examined under high D-glucose concentrations (25, 50, and 100 mM). After 21 days, the osteoblasts were stained with Alizarin Red S, which is identified by the colour red (Fig. 2).

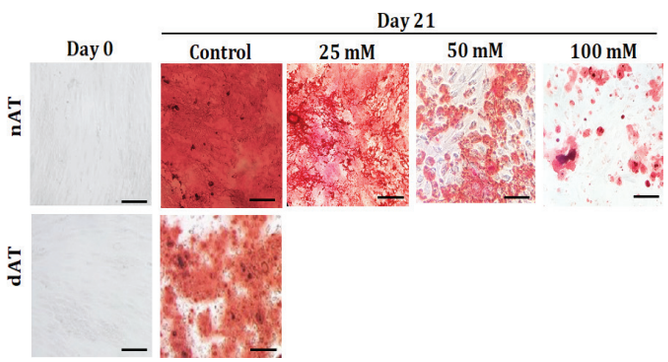

Fig. 2. The qualitative result of osteogenic differentiation of adipose tissue-derived mesenchymal stem cells (AT-MSCs) under the effect of high D-glucose concentrations. Osteoblasts were determined at day 21 using Alizarin red S staining, which indicated the calcification of the surface of osteoblasts (red). Scale bar: 50 μm.

The result demonstrated that osteoblasts differentiated from nAT-MSCs were greater than those from nAT-MSCs. On the other hand, osteoblasts differentiated from the high D-glucose-treated groups were worse than those

from the non-treated groups and dAT-MSCs (Fig. 2). The high D-glucose concentrations reduced the ability to differentiate into osteocytes of nAT-MSCs. This staining result suggested that high glucose conditions have a negative effect on osteogenic differentiation of mesenchymal stem cells.

3.3. Quantification of the osteogenic differentiation in nAT-MSCs under high D-glucose concentrations

To compare the significant difference in osteogenic differentiation of dAT-MSCs and nAT-MSCs under high D-glucose concentration, we quantified the osteoblasts that were differentiated from nAT-MSCs and dAT-MSCs by cell lysis and measured at 482 nm.

The result showed that the osteogenic differentiation ability of dAT-MSCs was significantly lower than that of non-treated nAT-MSCs ($p<0.05$, n=3 in each). The quantitative result showed that the calcification of nAT-MSCs in the high D-glucose-treated groups was significantly reduced as compared to the control group (25 mM, 1.16-fold ±0.04 decrease, $p<0.05$, n=3 in each; 50 mM, 1.77-fold ±0.05 decrease, $p<0.01$, n=3 in each; 100 mM, 7.4-fold ±0.08 decrease, $p<0.01$, n=3 in each) (Fig. 3). Interestingly, the level of osteogenic differentiation in dAT-MSCs was not significantly different between nAT-MSCs and dAT-MSCs. However, the increase in D-glucose concentration at 50 and 100 mM caused a remarkable decrease in osteogenic differentiation of nAT-MSCs compared to dAT-MSCs ($p<0.01$) (Fig. 3). Collectively, the higher D-glucose concentration the lower osteogenic differentiation.

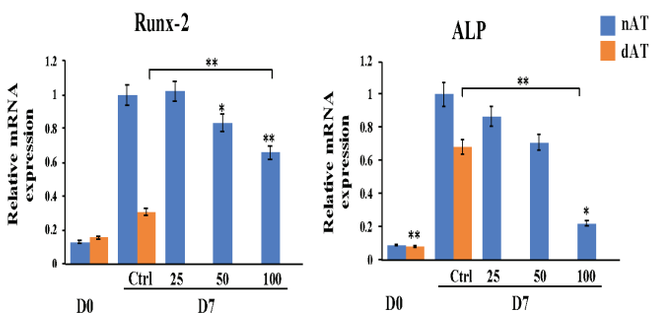

Fig. 3. The quantitative result of calcification of adipose tissue-derived mesenchymal stem cells (AT-MSCs) under different D-glucose concentrations. Absorbance was measured using microplate reader at 482 nm for Alizarin red S staining. The higher D-glucose concentrations were added, the lower absorbance ratio of Alizarin red S was determined. Data indicated average values of three independent experiments (mean ± SD); $p<0.05$ (*); $p<0.01$ (**); D0: day 0; D21: day 21.

3.4. High D-glucose concentrations decreased osteogenic gene expression

In agreement with the staining result, the expression of osteogenic-specific genes (Runx-2 and ALP) in AT-MSCs gradually decreased with high D-glucose concentrations compared with control groups (Fig. 4).

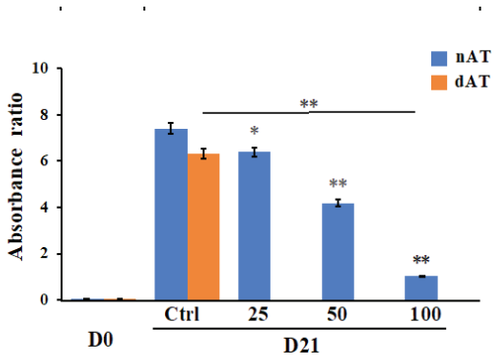

Fig. 4. The influence of high D-glucose concentrations on the expression of osteocyte-specific genes.

Runx-2 and ALP expression in the 25-mM D-glucose-treated group was not statistically different compared to nAT-MSCs in the control group. However, in the 50-mM D-glucose-treated group, Runx-2 expression decreased 1.20-fold ±0.06 ($p<0.05$, n=3 in each) and ALP expression decreased 1.41-fold ± 0.01 ($p<0.01$, n=3 in each) compared with nAT-MSCs in the control group. Besides, it was important to notice that the expression of Runx-2 in the 100-mM D-glucose-treated group was 2.13-fold±0.13 higher than in dAT-MSCs ($p<0.01$, n=3 in each), while the ALP expression was 3.1-fold ±0.47 lower than that in dAT-MSCs (Fig. 4). Therefore, these genes may play an important role in inhibiting the nAT-MSCs function under high D-glucose conditions in osteogenic differentiation, leading to impairing osteoblast production in diabetic conditions.

4. Discussion

AT-MSCs have been shown to have a great potential for therapeutic treatment [6]. However, AT-MSCs under diabetic condition (dAT-MSCs) had impaired functions of cell survival, migration, inflammation, and angiogenesis [19]. According to our previous report, nAT-MSCs have increased insulin resistance genes under high D-glucose concentrations (25, 50, and 100 mM) compared to dAT-MSCs [17]. In agreement with our previous study, these glucose concentrations inhibited cell proliferation and osteogenic differentiation of nAT-MSCs in comparison of dAT-MSCs.

Persistent high D-glucose concentrations have decreased the growth rate of AT-MSCs at day 5 (Fig. 1). These findings were consistent with previous research that found high D-glucose concentration induced the senescence via an extrinsic caspase pathway [10, 23, 24]. However, we observed that at the concentration of 100 mM, nAT-MSCs were not completely gone in the apoptosis process. This indicated that 100 mM of D-glucose was considered as acceptable for further experiment, yet the threshold for nAT-MSCs.

In addition to the inhibition of the proliferation, we found that high D-glucose concentrations decreased the osteogenic differentiation of nAT-MSCs (Figs. 2-4). The results of qualification, quantification in osteogenic differentiation of nAT-MSCs under high D-glucose concentrations, and dAT-MSCs in cooperation with the expression of osteogenic-specific genes (Runx-2 and ALP). Runx-2 (Runt-related transcription factor 2) is the key factor that plays an essential role upstream of osteoblastic differentiation, which induces the expression of osteogenic extracellular matrix genes during osteoblast maturation such as collagen-I, alkaline phosphatase (ALP), and osteocalcin [15]. Besides, ALP (alkaline phosphatase) is an enzyme that is involved in the mineralization of bone. ALP is expressed early in development in both bone and calcifying cartilage tissues, and can be found on the cell surface and in matrix vesicles [14]. According to W. Hankamolsiri, et al. (2016) [24], despite the fact that they only investigated the effect of high D-glucose at 25 mM, they concluded that high D-glucose concentration did not affect osteogenic differentiation of both BM-MSCs and gestational tissue-derived MSCs. Another research has shown that high D-glucose at 44 mM decreased ALP activity and calcium deposition via increasing collagenase [25]. In this study, D-glucose at concentrations of 50 and 100 mM have shown remarkable inhibition in osteogenesis of nAT-MSCs based on the results of calcification and gene expression. These findings are consistent with clinical findings of the circumstance of diabetic patients having a higher chance of suffering from aplastic bone disease [26-28]. Although we found a negative effect of high glucose concentrations in nAT-MSCs in proliferation and osteogenic differentiation, further studies are necessary to determine a medication that can rescue the impaired osteogenic differentiation ability and its mechanism by manipulating gene expression in nAT-MSCs compared to dAT-MSCs.

5. Conclusions

This study demonstrated that high D-glucose concentrations not only inhibited the proliferation but also impaired the osteogenic differentiation of AT-MSCs by suppressing the expression of osteogenic-specific genes Runx-2 and ALP. The knowledge gained from this study contribute to the understanding of the relationship between T2DM and osteoporosis, suggesting the role of stem cells in developing new medicine or therapeutic treatment for preventing diabetic complications.

CRediT author statement

Yen-Nhi Ha Nguyen, Long Binh Vong, Hong-Anh Pham, Dang-Quan Nguyen, Phan Ngoc Uyen Phuong, Huu-Phuong Mai: Data curation, Software, Visualisation, Investigation, Writing original draft preparation; Nhu-Thuy Trinh: Conceptualization, Methodology, Supervision.

ACKNOWLEDGEMENTS

This research is funded by Vietnam National University Ho Chi Minh city (VNU-HCM) under grant number C2021-28-02. The authors thank professor Osamu Ohneda for providing stem cells and the Biotechnology Center for supporting some research materials and equipment.

COMPETING INTERESTS

The authors declare that there is no conflict of interest regarding the publication of this article.

REFERENCES

[1] M.D. McCall, C. Toso, E.E. Baetge, et al. (2009), "Are stem cells a cure for diabetes?", *Clin. Sci. (Lond)*, **118(2)**, pp.87-97, DOI: 10.1042/CS20090072.

[2] C. Marin, F.P. Luyten, B.V.D. Schueren, et al. (2018), "The impact of type 2 diabetes on bone fracture healing", *Front. Endocrinol. (Lausanne)*, **9**, DOI: 10.3389/ fendo.2018.00006.

[3] L.K. Billings, Y.H. Hsu, R.J. Ackerman, et al. (2012), "Impact of common variation in bone-related genes on type 2 diabetes and related traits", *Diabetes*, **61(8)**, pp.2176-2186, DOI: 10.2337/db11-1515.

[4] V. Carnevale, E. Romagnoli, E. D'Erasmo (2004), "Skeletal involvement in patients with diabetes mellitus", *Diabetes Metab. Res. Rev.*, **20(3)**, pp.196-204.

[5] D. Merlotti, L. Gennari, F. Dotta, et al. (2010), "Mechanisms of impaired bone strength in type 1 and 2 diabetes", *Nutr. Metab. Cardiovasc. Dis.*, **20(9)**, pp.683-690, DOI: 10.1002/dmrr.449.

[6] Y. Qi, J. Ma, S. Li, et al. (2019), "Applicability of adipose-derived mesenchymal stem cells in treatment of patients with type 2 diabetes", *Stem. Cell. Res. Ther.*, **10(1)**, DOI: 10.1186/s13287-019-1362-2.

[7] L. Hu, C. Yin, F. Zhao, et al. (2018), "Mesenchymal stem cells: Cell fate decision to Osteoblast or Adipocyte and application in Osteoporosis treatment", *Int. J. Mol. Sci.*, **19(2)**, DOI: 10.3390/ijms19020360.

[8] Y.M. Li, T. Schilling, P. Benisch, et al. (2007), "Effects of high glucose on mesenchymal stem cell proliferation and differentiation", *Biochem. Biophys. Res. Commun.*, **363(1)**, pp.209-215, DOI: 10.1016/j.bbrc.2007.08.161.

[9] S. Seubbuk, H. Sritanaudomchai, J. Kasetsuwan, et al. (2017), "High glucose promotes the osteogenic differentiation capability of human periodontal ligament fibroblasts", *Molecular Medicine Reports*, **15**, pp.2788-2794, DOI: 10.3892/mmr.2017.6333.

[10] C. Cramer, E. Freisinger, R.K. Jones, et al. (2010), "Persistent high glucose concentrations alter the regenerative potential of mesenchymal stem cells", *Stem Cells and Development*, **19(2)**, pp.1875-1884, DOI: 10.1089/scd.2010.0009.

[11] D.H. Zheng, Z.Q. Han, X.X. Wang, et al. (2019), "Erythropoietin attenuates high glucose-induced oxidative stress and inhibition of osteogenic differentiation in periodontal ligament stem cell (PDLSCs)", *Chemico-biological Interactions*, **305**, pp.40-47, DOI: 10.1016/j.cbi.2019.03.007.

[12] X. Dong, X. Wang, M. Xing, et al. (2020), "Inhibition of the negative effect of high glucose on osteogenic differentiation of bone marrow stromal cells by silicon ions from calcium silicate bioceramics", *Regenerative Biomaterials*, **7(1)**, pp.9-17, DOI: 10.1093/rb/rbz030.

[13] I. Soundharrajan, D.H. Kim, S. Srisesharam, et al. (2018), "Limonene promotes osteoblast differentiation and 2-deoxy-d-glucose uptake through p38MAPK and Akt signaling pathways in C2C12 skeletal muscle cells", *Phytomedicine: International Journal of Phytotherapy and Phytopharmacology*, **45**, pp.41-48, DOI: 10.1016/j.phymed.2018.03.019.

[14] R.S. Siffert (1951), "The role of alkaline phosphatase in osteogenesis", *The Journal of Experimental Medicine*, **93(5)**, pp.415-426.

[15] T.M. Liu, E.H. Lee (2013), "Transcriptional regulatory cascades in Runx2-dependent bone development", *Tissue Engineering Part B: Reviews*, **19(3)**, pp.254-263, DOI: 10.1089/ten.TEB.2012.0527.

[16] W. Xia, X. Han, L. Wang (2022), "E26 transformation-specific 1 is implicated in the inhibition of osteogenic differentiation induced by chronic high glucose by directly regulating runx2 expression", *Journal of Biomedical Research*, **36(1)**, pp.39-47, DOI: 10.7555/JBR.35.20210123.

[17] H.P. Mai, N.T. Trinh, V.B. Long, et al. (2020), "The high D-glucose concentration reduces the ability of wound healing *in vitro* of human adipose tissue- derived mesenchymal stem cells", *International Conference on The Development of Biomedical Engineering in Vietnam*, Springer, DOI: 10.1007/978-3-030-75506-5_49.

[18] N.T. Trinh, T. Yamashita, K. Ohneda, et al. (2016), "Increased expression of EGR-1 in diabetic human adipose tissue-derived mesenchymal stem cells reduces their wound healing capacity", *Stem Cells and Development*, **25(10)**, pp.760-773, DOI: 10.1089/scd.2015.0335.

[19] N.T. Trinh, T. Yamashita, T.C. Tu, et al. (2016), "Microvesicles enhance the mobility of human diabetic adipose tissue-derived mesenchymal stem cells *in vitro* and improve wound healing *in vivo*", *Biochemical and Biophysical Research Communications*, **473(4)**, pp.1111-1118, DOI: 10.1016/j.bbrc.2016.04.025.

[20] M. Nagano, K. Kimura, T. Yamashita, et al. (2010), "Hypoxia responsive mesenchymal stem cells derived from human umbilical cord blood are effective for bone repair", *Stem Cells and Development*, **19(8)**, pp.1195-1210, DOI: 10.1089/scd.2009.0447.

[21] N. Abuarab, T.S. Munsey, L.H. Jiang, et al. (2017), "High glucose-induced ROS activates TRPM2 to trigger lysosomal membrane permeabilization and Zn^{2+}- mediated mitochondrial fission", *Science Signaling*, **10**, DOI: 10.1126/scisignal.aal4161.

[22] W. Wagner, P. Horn, M. Castoldi, et al. (2008), "Replicative senescence of mesenchymal stem cells: A continuous and organized process", *PLOS ONE*, **3(5)**, DOI: 10.1371/journal.pone.0002213.

[23] A. Stolzing, N. Coleman, A. Scutt (2006), "Glucose-induced replicative senescence in mesenchymal stem cells", *Rejuvenation Research*, **9(1)**, pp.31-35, DOI: 10.1089/rej.2006.9.31.

[24] W. Hankamolsiri, S. Manochantr, C. Tantrawatpan, et al. (2016), "The effects of high glucose on adipogenic and osteogenic differentiation of gestational tissue-derived MSCs", *Stem Cells International*, DOI: 10.1155/2016/9674614.

[25] D. Zhen, Y. Chen, X. Tang (2010), "Metformin reverses the deleterious effects of high glucose on osteoblast function", *Journal of Diabetes and Its Complications*, **24(5)**, pp.334-344, DOI: 10.1016/j.jdiacomp.2009.05.002.

[26] M. Rosato, S. Schneider, S. Shapses (1998), "Bone turnover and insulin-like growth factor I levels increase after improved glycemic control in noninsulin-dependent diabetes mellitus", *Calcified Tissue International*, **63(2)**, pp.107-111, DOI: 10.1007/s002239900498.

[27] I. Yamawaki, Y. Taguchi, K. Shiomi, et al. (2021), "Osteogenic differentiation of bone marrow mesenchymal cells on alkali treated titanium surfaces in a diabetes mellitus model", *Journal of Osaka Dental University*, **55(2)**, pp.255-261, DOI: 10.18905/jodu.55.2_255.

[28] M. Chen, D. Jing, R. Ye, et al. (2021), "PPARβ/δ accelerates bone regeneration in diabetic mellitus by enhancing AMPK/mTOR pathway-mediated autophagy", *Stem Cell Research & Therapy*, **12(1)**, DOI: 10.1186/s13287-021-02628-8.

 DOI: 10.31276/VJSTE.64(1).78-84

Radon concentrations and forecasting exposure risks to residents and workers in rare earth and copper mines containing radioactivity in northwest Vietnam

Van Dung Nguyen[1]*, Thi Lan Anh Vu[1, 2], Dinh Huan Trinh[3], Thi Cuc Nguyen[1]

[1]Faculty of Environment, Hanoi University of Mining and Geology, 18 Vien Street, Duc Thang Ward, Bac Tu Liem District, Hanoi, Vietnam
[2]Faculty of Environment, University of Science, Vietnam National University - Hanoi, 334 Nguyen Trai Street, Ha Dinh Ward, Thanh Xuan District, Hanoi, Vietnam
[3]Geological Division for Radioactive and Rare Elements, General Department of Geology and Minerals of Vietnam, 6 Pham Ngu Lao Street, Phan Chu Trinh Ward, Hoan Kiem District, Hanoi, Vietnam

Received 11 December 2020; revised 27 February 2021; accepted 8 March 2021

Abstract:

Radon and its isotopes are inert gases as they do not interact with any chemical compounds. Compared with thoron (^{220}Rn) and radon-219 (^{219}Rn), the risk of radioactive exposure of radon-222 (^{222}Rn) is very high due to its long half-life of 3.8 d, while the half-life of ^{220}Rn is 55 sec and of ^{219}Rn is 4 sec. As a gas, radon can escape from the surfaces of ore, minerals, and rocks, then dissolve into groundwater and move very far from the formation site. While all these radioisotopes emit alpha radiation, Rn-222 is the most important as it is the main factor behind dangerous doses to the respiratory tract that are harmful to human health. Survey results of radon concentration in the air and retrospective data (from 2017 to 2019) on the health of residents and workers near and in the rare earth mines Dong Pao and Muong Hum, as well as the Sin Quyen copper mine, illustrated the health characteristics of the people involved in the northwestern mineral mines (Lao Cai - Lai Chau) that are exposed to radon. At the Dong Pao and Muong Hum rare earth mines, as well as the Sin Quyen copper mine, residents and workers were exposed to high concentrations of radon gas and thus developed some related illnesses such as respiratory, urological, digestive, genetic, and neurological diseases. Assessing the risk of pulmonary tuberculosis and estimating the average death rate from lung cancer with radon exposure shows that, in the surveyed area, the risk value is high (0.046) compared to other regions of Vietnam. However, it is within the limits allowed by the United States Environmental Protection Agency (EPA).

Keywords: **lung cancer, radioactive, radon, radon exposure, risk level.**

Classification numbers: **4.2, 5.3**

1. Introduction

Radon gas is present in almost every part of the earth's crust as it escapes from the soil, finding its way through cracks, holes, faults, and groundwater, then enters the air by diffusion and convection. Radon exists in high concentrations in radioactive mineral mines, in houses, especially in closed rooms such as a bedroom or office; and in construction materials. This type of gas is classified by international organisations such as the Centers for Disease Control, the American Lung Association, and the United States Environmental Protection Agency (EPA), which all have radon gas listed as a carcinogen along with an information on its effects on human health.

The main danger of radon to health is from the exposure of alpha radiation during breathing and eating. Radon has also been associated with many deaths from lung cancer and is suspected to be associated with several other types of cancer such as leukemia, melanoma, kidney cancer, and some cancers of children. Epidemiological investigations have shown that radon can enter the body and mix with fat and blood cells in the same way that oxygen enters the blood [1-5]. One result is the accumulation of fat cells in bone marrow. In essence, radon can enter the human body and leave behind unpredictable consequences [6, 7]. Among the types of cancer caused by radon, lung cancer is considered to be the most dangerous because it holds the highest number of deaths [6].

Among these lethal risks, radon is estimated to cause about 21,000 (13.4%) deaths from lung cancer each year across the United States, more than all other risks posed to humans. This shows that the danger from radon in the home is very large [6].

Radon exposure does not cause acute illness, nor irritation, nor any early warning signs compared to other common environmental risks. Nonetheless, concentrated radon exposure increases the risk of lung cancer, especially

*Corresponding author: Email: nguyenvandung@humg.edu.vn

in smokers. This risk increases with a person's radon level, length of exposure, and the amount of cigarettes smoked [6, 7].

Some studies show that radon is a related cause of leukemia, skin cancer, melanoma, kidney cancer in children, and some other cancers. Studies are based on statistical analysis of indoor radon and the extent of cancer effects [7]. The main damages caused by chronic exposure to radon are lung cancers (usually arising from bronchi), lung fibrosis, chronic obstructive pulmonary disease, pneumoconiosis, and overall respiratory damage.

Therefore, the determination of radioactive aerosol content caused by radon is very important for the purpose of monitoring and warning of the risk of lung cancer to communities near mineral mines, in mining areas, in houses and especially in bedrooms and offices. According to the United States Environmental Law, the permissible level of radon in homes is <4 $pCi.l^{-1}.year^{-1}$, which is equivalent to 148 $Bq.m^{-3}.year^{-1}$. According to the radiation safety standards of the International Atomic Energy Agency (IAEA), the annual radiation dose limit for workers is recommended not to exceed 20 $mSv.year^{-1}$ [8].

The content of this paper presents the results of radon gas concentration surveys and risk assessments of radon exposure from residents and workers near and in the Dong Pao and Muong Hum rare earth mines and the Sin Quyen copper mines.

2. Research subjects

2.1. Mineral geological characteristics of the study area

The northwest region of Vietnam is concentrated with many radioactive minerals with large reserves such as the Dong Pao, Muong Hum, and Nam Xe rare earth mines, and the Sin Quyen copper mine, etc. Currently, the abovementioned radioactive mines have been explored and exploited and the resulting minerals are processed there as well, thus, radioactive elements including radon (Rn-222) are perpetually being released into the environment [9].

The Dong Pao rare earth mine is bounded by the coordinates 103°33'E, 22°18'N, in the Tam Duong commune of the Tam Duong district, Lai Chau province. The Dong Pao rare earth mine houses a group of fluorcarbonites with the main mineral components being bastnaesite, parisite, baryt (or barite), and fluorite. The proportion of minerals can be divided into the following types of ore: rare earth TR_2O_3>5%; rare earth - baryt TR_2O_3 0.5-30%; rare earth - baryt - fluorite TR_2O_3 0.5-30%; and rare earth fluorite TR_2O_3 1-5%. Trusted resources of TR_2O_3 make up 645,000 tons, estimated resources are 7 million tons; CaF_2 is 9.4 million tons; and $BaSO_4$ is 288 million tons (Fig. 1). The content of the radioactive mineral ThO_2 ranges from 0.002-0.054% with an average of 0.013% and the content of radioactive U_3O_8 ranges from 0.002-0.014% with an average of 0.007% [9-11].

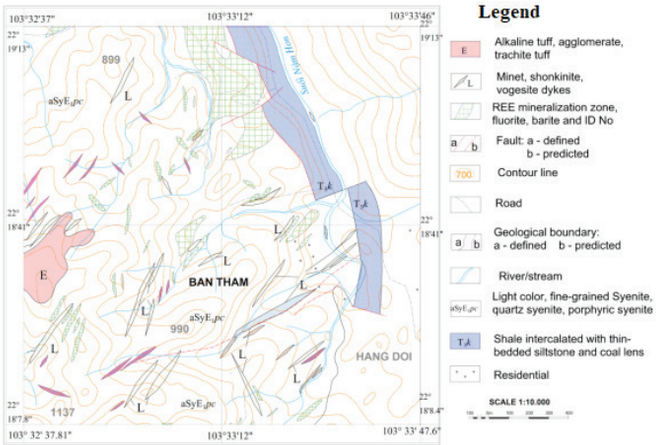

Fig. 1. Geological characteristics of Dong Pao rare earth mine [11].

The Muong Hum rare earth mine belongs to the Nam Pung and Muong Hum communes of the Bat Xat district, Lao Cai province, and is bounded by the coordinates of 22°51'-22°55'N and 103°68'-103°74'E. This is an area of complex terrain; the center along the northwest-to-southeast direction is a low mountainous terrain that is surrounded by two sharply separated high mountain ranges (Fig. 2). According to the survey results of the Geological Division for Radioactive and Rare Elements [9, 11], this is a rare earth mine with large reserves with 175,000 tons of rare earth resources of TR_2O_3 on the spot and 37,500 tons of heavy rare earth resources. In addition to rare earth minerals, these areas also contain the radioactive substances U and Th with high content. For example, the uranium content U_3O_8 ranges from 0.007-0.0264% with an average of 0.0175% and the thorium ThO_2 content ranges from 0.0039-0.279% with an average reaching 0.176%.

The Sin Quyen copper mine is located in the Bat Xat district, Lao Cai province, with geographical coordinates 22°37'20'N, 103°45'50'E. The ore area is located on the northeastern flank of the Hoang Lien Son mountain range in the Lao Cai province, on the right bank of the Red river, right next to the Vietnam - China border, about 1-3 km from the Red river and 25 km from southeast of Lao Cai. The mountainous terrain extends from the northwest to the southeast. The geological characteristics of the area include the Suoi Chieng formation (PP_{sc}), the Sin Quyen formation ($PP\text{-}MP_{sq}$), the Ban Nguan formation (D_1bn), the Cha Pa formation (NPcp), and the Ban Pap formation ($D_{1\text{-}2}bp$) (Fig. 2). The copper content of this ore form

varies from 0.1-4.7% and its rare earth content is <1%. In primary copper ores, radioactive elements such as uranium, thorium, etc. have been detected. The content of U_3O_8 ranges between 0.005-0.265% and the ThO_2 content ranges between 0.006-0.03% [12].

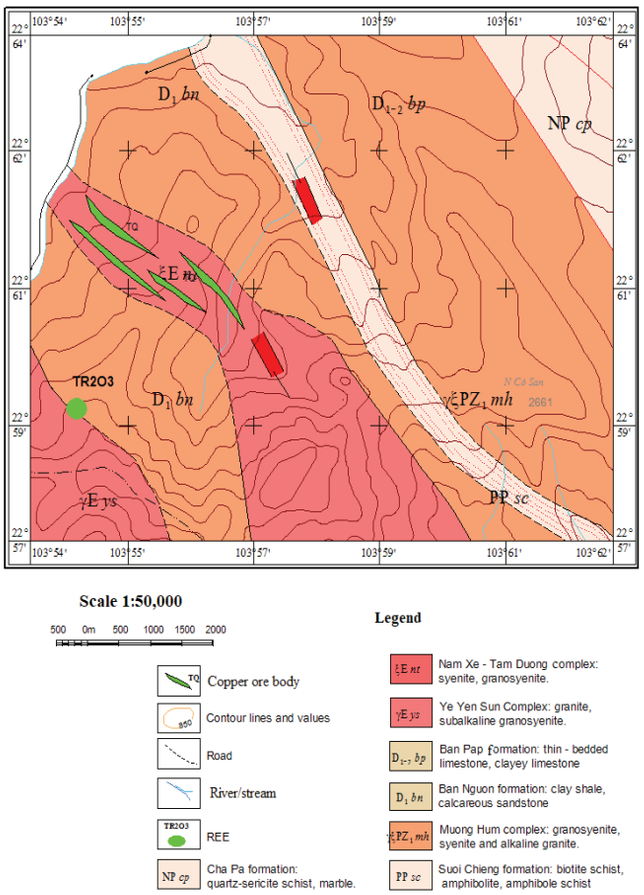

Fig. 2. Regional characteristics of Bat Xat district, Lao Cai province [12].

2.2. Research subjects

The surveyed subjects are residents and workers living and working near and in the rare earth mines of Dong Pao and Muong Hum and the Sin Quyen copper mines.

3. Research methods

- Collecting health data of people in mines and surrounding areas (outside the mines) over the last 3 years through retrospective methods at local health facilities.

- Reviewing periodic medical records of workers in the medical facilities of the mine with focus mainly on diseases related to the effects of radon. Diseases are statistically surveyed for research include respiratory diseases, digestive diseases, circulatory diseases, genetic diseases, and cancers.

- Surveying radon gas concentration in houses, workers' houses, workplaces, schools, sorting workshops, etc., to determine the internal radiation dose level caused by radon according to the following formula [13-15]:

$$H_t(mSv.year^{1})=0.047\times C_{Rn}(Bq.m^{-3}) \quad (1)$$

where H_t is the internal radiation dose caused by radon in the air and $C_{Rn}(Bq.m^{-3})$ is the concentration of radon in the air.

- Assessing the level of radon exposure from the work process, especially at places with high radon content could be experienced by residents and workers living and working in rare earth mines (Dong Pao, Muong Hum) and the copper mine Sin Quyen, as well as other humans affected by radon radioactivity [6, 7, 16, 17].

Calculation of cumulative exposure: accumulated exposures are defined as all activity levels (WL) multiplied by the exposure time. In the exposure assessments, this cumulative exposure is calculated by exposure for 1 month (or 170 working hours). Cumulative exposure is calculated using the following formula [6]:

$$WLM = \sum_{i=1}^{N}(WL)_i\left(\frac{t_i}{170}\right) \quad (2)$$

where WLM is cumulative exposure; $(WL)_i$ is the average concentration of radon and offspring during exposure; and t_i is the total exposure time with 1 $WL=C_{Rn}(Bq.m^{-3})\times 0.00027$.

The above formula is used for calculating cumulative exposures over time intervals with concentrations corresponding to those time periods. However, due to the limitations of research time and statistical data systems over a short time period, this article only intends to show the general method and calculation of the assessments for radon exposure in workers in different positions [6].

Average exposure rate value is estimated for one year:

$$EX = C\times\left[F\times 0.01WL\left(\frac{pCi}{l}\right)^{-1}\right]\times 12\ WLM(WLy)^{-1} \quad (3)$$

where EX is the average exposure rate estimated in a year $(WLy)^{-1}$; C is the average radon concentration $(pCi.l^{-1}$ or $Bq.m^{-3})$; F is the coefficient of balance between radon and its products, e.g., F=0.6 in the mine.

At a concentration of 1 $pCi.l^{-1}$, the exposure to offspring is calculated by:

$$EX=1pCil^{-1}[0.6\times 0.01WL\ (pCil^{-1})^{-1}]\times[12\ WLM(WLy)^{-1}]=0.072\ WLM/y \quad (4)$$

At a concentration of 1 $Bq.m^{-3}$, the exposure of descendants of radon is calculated by the formula:

$$EX=1Bq.m^{-3}[0.6\times 0.00027WL(Bq.m^{-3})^{-1}]\times[12WLM(WLy)^{-1}]=0.00194WML/y \quad (5)$$

4. Results and discussion

4.1. Concentration of radon radioactive gas in surveyed areas

The results of radon emission survey at the Dong Pao and Muong Hum rare earth mines and the Sin Quyen copper mine over 3 years from 2017 to 2019 are as follows:

In the Dong Pao rare earth mine area, the radon concentration ranges from 15 $Bq.m^{-3}$ to 648 $Bq.m^{-3}$ with an average of 67.8, which is 1.8 times higher than the world average for radon concentration in a house (40 $Bq.m^{-3}$) as measured by UNSCEAR 2000 [15]. The typical value of internal radiation dose at Muong Hum mine is 3.18 $mSv.year^{-1}$.

In the Muong Hum rare earth mine area, the radon concentration ranges from 35 to 856 $Bq.m^{-3}$ with an average of 88.4 $Bq.m^{-3}$, which is 2.4 times higher than the world average for radon concentration in a house (40 $Bq.m^{-3}$) as measured by UNSCEAR 2000 [15]. The typical value of internal radiation dose at Muong Hum mine is 4.15 $mSv.year^{-1}$.

At the Sin Quyen copper mine area, the radon concentrations in mining areas, sorting workshops, dump sites, and workplaces of officials and employees were valued from 15.7 to 476 $Bq.m^{-3}$ with an average of 48.1 $Bq.m^{-3}$, which is 1.3 times higher than the world average for indoor radon concentration (40 $Bq.m^{-3}$) as measured by UNSCEAR 2006 [15]. The typical dose measured in the Sin Quyen copper mine is 2.26 $mSv.year^{-1}$.

4.2. Health characteristics of residents and workers in the survey areas

Statistics of disease over three years from 2017 to 2019 in residents and workers near and in the rare earth mines Dong Pao and Muong Hum and the Sin Quyen copper mines (Fig. 3), where radon gas concentrations are high, demonstrate mainly respiratory, circulatory, and digestive system diseases.

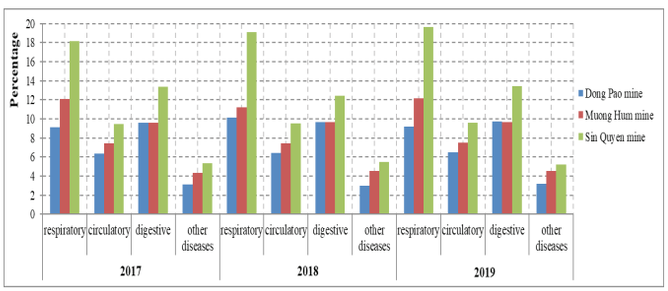

Fig. 3. Disease classification diagram of the Dong Pao and Muong Hum rare earth mines and the Sin Quyen copper mine.

The chart in Fig. 3 of disease classifications over the 3-year period of investigation shows diseases of the respiratory system, circulatory system, digestive system, and other diseases of residents living near the rare earth mines of Dong Pao and Muong Hum are not high. Residents living in this area mainly suffer from respiratory, circulatory, and digestive diseases. At the Dong Pao mine, the incidences of respiratory, circulatory, and digestive diseases by year are: 2017 (9.09; 3.37; 6.57%); 2018 (10.13; 3.45; 6.67%); and 2019 (9.13; 3.48; 6.75%) and at Muong Hum mine, they are: 2017 (12.12; 4.43; 6.61); 2018 (11.21; 4.46; 6.67%); and 2019 (12.17; 4.51; 6.63%). People classify circulatory weakness with major cardiovascular diseases such as limited hypertension and cardiac arrhythmia.

For the Sin Quyen copper mine, the proportion of workers suffering from respiratory, circulatory, and digestive diseases is higher than that of Dong Pao and Muong Hum mines over the 3-year investigation, which are, respectively, 2017 (17.18; 6.46; 10.37%); 2018 (18.08; 6.51; 11.42%); 2019 (18.67; 6.58; 11.41%), with circulatory diseases mainly presented as hypertension and arrhythmia.

Results of a 3-year disease situation survey at locations with high concentrations of radon gas such as field sites, transports, and screening plants are shown in Fig. 4.

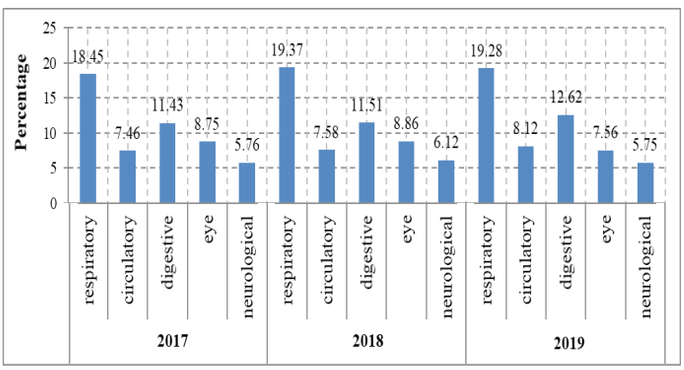

Fig. 4. Disease situation over 3 years (2017-2019) at training sites and sorting workshops.

In these locations, there have been many radon-related diseases such as respiratory, digestive, circulatory, eye, and neurological diseases. These diseases are most common in mining sites, ore transports, and sorting workshops. This may be due to the influence of many factors but the effect of exposure to relatively high radon content in the air is unavoidable.

Notably, in the results of the health examination of officials and workers of Sin Quyen Copper Company over the three years of survey, there were several workers with quite serious respiratory diseases: there were 12 cases of pneumonia, 28

cases of lung damage, 7 cases of tuberculosis, and 2 cases of collapsed lung(s). In 2017, the Company had 5 cases classified as poor respiratory health and 7 cases classified as poor health, which account for 2.15 and 1.8%, respectively. According to each working position in Table 1, it can be seen that the number of infected people is quite high at the mining, transporting, and recruitment sites. Among those working in the office, some people fell ill because they have had time to work in direct production positions. In 2018, the number of people with lung disease was the highest with 19 of the 42 people in the entire Company suffering from lung disease.

Table 1. Statistics of lung diseases by working positions at Sin Quyen copper mine.

No.	Partial	Total number of people infected	Total number of cases infected by year		
			2017	*2018*	*2019*
1	Office	10	3	4	3
2	Technical Department	3		2	1
3	Mining area	12	3	6	3
4	Shipping workshop	7	3	3	1
5	Electric workshop	2		2	
6	Recruitment Workshop	8	4	2	2
Total		**42**	**13**	**19**	**10**

4.3. Assess the exposure of radon to Sin Quyen copper mine workers

According to the results of the radon concentration survey in the Sin Quyen copper mine area, there no value exists that exceeds the permitted level by Vietnamese and world standards for workers. However, radon is a carcinogen with no harmful threshold, and, with long exposure time and other impact factors such as smoking, health care condition, etc., it can adversely affect worker health.

The radon concentration data at different working sites in the Sin Quyen copper mine will be used to calculate the exposure for workers with the theory that the workers of each location are exposed at this concentration during the working process until retirement. Calculation results are presented in Table 2.

Table 2. Assessment of exposure at work site.

Position	Exposure			
	Bq.m^{-3}	*pCi.l^{-1}*	*WL*	*WLM.y^{1}*
Mining pits	431	11.64	0.116	0.828
The bottom of the pan	376	10.16	0.102	0.711
Load the transport vehicle	328	8.86	0.089	0.651
Waste dump	87.4	2.36	0.024	0.181
Recruitment area	136	3.67	0.037	0.254
Mechanical house	123	3.32	0.033	0.217
Office	35.3	0.95	0.009	0.062

The results of the average annual exposure assessment of workers at the mine site indicate that exposure is within 0.062-0.828 WLM.y^{1}. This level of exposure is relatively safe for worker health, but considering long-term exposure and smoking status, there may be some effects that need to be considered and assessed.

4.4. Assessing health risks due to radon exposure for officials and workers working at Sin Quyen copper mine

To assess the risk of radon exposure for officials and workers at the Sin Quyen copper mine, the authors used the risk calculation model under the guidance of EPA (2009) to use a single model instead of 2 models like BEIR VI (NAS) [6] because the two previously proposed models almost all depend on the age and time of exposure. EPA uses a concentration model for risk calculations because a concentration model can assess the health effects of exposure at levels that change over time.

In BEIR VI, the risk/WLM is 6.52×10^{-4} for the concentration model and is 4.43×10^{-4} for the time period model. The EPA has calculated the concentration model so that the risk/WLM will be equal to the geometric significance of these two values, i.e., 5.38×10^{-4}. The risk factor according to the concentration model is $\beta=0.0768\times(4.43/6.52)^{0.5}=0.0634$, and the risk/WLM is $5.38\times10^{-4} \approx (6.52\times10^{-4})\times(4.43/6.52)^{0.5}$ [6].

The concentration model indicates that the relative risk of excess exposure depends on the time the exposure was initiated, the age reached, and the rate of exposure (concentration) as follows [6]:

$$ERR=\beta\times(w_{5-14}+\theta_{15-24}\times w_{15-24}+\theta_{25+}\times w_{25+})\times\varphi_{age}\times y_z \quad (6)$$

where ERR is an assessment of the level of risk; β is the risk factor; w_{5-14}, w_{15-24}, w_{25+} are exposure at ages 5-14; 15-24, and 25 years or more, respectively; θ_{5-14}; θ_{15-24}; θ_{25+} are the risk that is relatively dependent on the time the exposure is initiated; φ_{age} describes the dependence on the age achieved; for mine workers and for retired people at 55 years old, $\varphi_{age}=1.0$ and with retirement age of 60, $\varphi_{age}=0.57$; y_z is the classification from 1 for exposure <0.5WL to 0.11 for exposure >15WL, which describes the exposure speed dependence. For this calculation, since all WL values are <0.5, $y_z=1$.

Setting $\beta^*=\beta\varphi_{age}$ and using the parameters shown in Table 3, the authors estimate the parameters for the risk model [6] with the following equation for calculating the excess relative risk:

$$ERR=\beta^*\times(w_{5-14}+0.778w_{15-24}+0.51w_{25+})\times\varphi_{age} \quad (7)$$

where $\beta^*=0.0768$ for age x<55y; $\beta^*=0.0438$ for age 55 y≤x<65y; $\beta^*=0.0223$ for age 65 y≤x<75y; and $\beta^*=0.0069$ for age x≥75y.

Table 3. Estimated parameters for concentration model [6].

Concentration model (β×100=7.68)	
Time of exposure	$\theta_{15\text{-}24}$=0.78
	θ_{25+}=0.51
Where β*	0.0768 for x<55y
	0.0438 for 55 y≤x<65y
	0.0223 for 65 y≤x<75y
	0.0069 for x≥75y

In order to estimate the relative health risks for workers at different positions in the Sin Quyen copper mine, the authors make some assumptions:

- In direct labor positions, employees retired at the age of 55. For indirect working positions, employees retired at the age of 60.

- Workers maintain one position until retirement without changing.

- The average annual exposure to radon is applied for each position during the time the employee works until retirement.

- Age to being work and exposure to radon is 25.

The results of risk estimation for workers at the Sin Quyen copper mine are presented in Table 4.

Table 4. Estimation of risks at job locations at Sin Quyen copper mine.

Position	Relatively risk	
	EER (%)	*WLMy^{-1}*
Field workers	147	0.828
Classification worker	119	0.711
Workers loading and transporting vehicles	117	0.651
Workers in the disposal area	35.2	0.181
Workshop workers	42.6	0.254
Mechanic	38.5	0.217
Office staff	0.68	0.062

Comment: The above calculation model is applied for calculating the risks over a long time and the radon exposure phase of different periods are carefully observed as well as the concentration in each period. However, in this paper, due to the short time of execution and the short time measurement of exposure calculations, the authors only determine health risks for a select number of working positions under exposure conditions at a measured average concentration.

4.5. Estimated average risk of death from lung cancer due to radon exposure of workers at Sin Quyen copper mine

The estimated average risk of death from lung cancer with life-long exposure to average radon exposure using the EPA formula is calculated as follows [6]:

$$ER=w\times t\times \text{risk estimate} \quad (8)$$

where ER is the estimate of the average risk of death from radon exposure; w is the estimated average exposure value in a year (WLMy^{-1}); and t is the average life expectancy of a country.

Risk estimate =5.38×10^{-4}/WLM for the entire population

=9.68×10^{-4}/WLM who used to smoke

=1.67×10^{-4}/WLM for non-smokers

Table 5 shows the estimation of the risk/WLM by gender and smoking status.

Table 5. Estimating risk/WLM by gender and smoking status [6].

Gender	Smoking category	Risk per/ WLM (10^{-4})	Average life expectancy (year) EPA	Average life expectancy in Vietnam
Male	Smoking	10.6	71.5	69.4
	No smoking	1.74	72.8	70.7
	All men	6.40	72.1	70
Female	Smoking	8.51	78.0	74.2
	No smoking	1.61	79.4	75.6
	All women	4.39	78.8	75
General population	Smoking	9.68	74.2	70.8
	No smoking	1.67	76.4	73
	The whole population	5.38	75.4	72

To be able to estimate risks more accurately, it is assumed that, after retirement, workers will continue to live in this area for the rest of their lives. The average estimation of death risk is then written as [6]:

$$ER=(w_1\times t_1+w_2\times t_2)\times \text{risk estimate} \quad (9)$$

where w_1 is the estimated average exposure rate for a year corresponding to the concentration measured at the workplace; w_2 is the estimated average exposure rate for a year corresponding to background concentration in the area of the Bat Xat district; t_1 is the time the employee worked at a position in the mine (male worker directly 35 years; indirectly 30 years; female worker less than 5 years in both positions); t_2 is the average life expectancy minus t_1.

A representation of the average risk of death from lung cancer related to radon of 4 gender groups and smoking status at Sin Quyen copper mines is shown in Fig. 5. The results show that the risk of death in male smokers is 6 times higher than non-smokers, which is similar to a female smoker's risk that is 5 times higher than non-smokers.

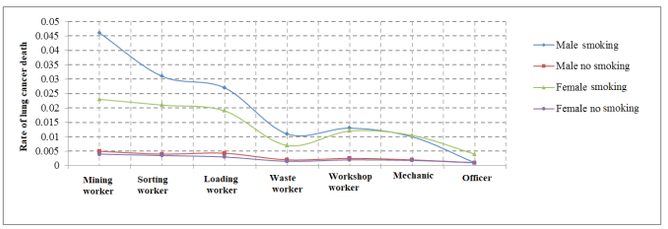

Fig. 5. Estimated average risk of death from lung cancer of several jobs at Sin Quyen copper mines.

Fig. 5 also shows that, in terms of exposure, mining workers, ore loaders, and sorting workers face the highest risk of death from lung cancer, especially smokers. Therefore, in the long term, the solution of transferring workers to different working positions can be helpful to reduce radon exposure for this group of workers.

5. Conclusions

Some health characteristics and diseases of residents and workers at the radioactive mineral mines in northwest Vietnam related to radon exposure are not really definitive.

At the Sin Quyen copper mine, where officials and workers are exposed to relatively high levels of radon (where the radon concentration in the air is up to 431 $Bq.m^{-3}$), there have been some related diseases such as respiratory, circulatory, digestive, eye, and neurological diseases. In particular, there were patients with lung damage.

The risk estimates for tuberculosis and the average estimate of lung cancer deaths with radon exposure in the survey area are quite high for smokers (0.046) compared to other regions of Vietnam.

CRediT author statement

Van Dung Nguyen: Conceptualization, Methodology, Supervision; Thi Lan Anh Vu, Dinh Huan Trinh, Thi Cuc Nguyen: Data curation, Software, Visualisation, Investigation, Writing original draft preparation.

COMPETING INTERESTS

The authors declare that there is no conflict of interest regarding the publication of this article.

REFERENCES

[1] M.T. Derin, P. Vijayagopal, B. Venkatraman, et al. (2012), "Radionuclides and radiation indices of high background radiation area in Chavara-Neendakara placer deposits (Kerala, India)", *PLOS ONE*, **7(11)**, DOI: 10.1371/journal. pone.0050468.

[2] International Atomic Energy Agency (2003), "Radiation protection against radon in workplaces other than mines", *Safety Reports Series*, **33**, 74pp.

[3] ICRP (2009), *International Commission on Radiological Protection Statement on Radon*, 2pp.

[4] WHO Regional Office for Europe (2009), "Radon levels in dwellings", *Fact Sheet 4.6*, 8pp.

[5] World Nuclear Association (2020), *Naturally-Occurring Radioactive Materials (NORM)*, https://www.world-nuclear.org/information-library/safety-and-security/radiation-and-health/naturally-occurring-radioactive-materials-norm.aspx, accessed 15 May 2020.

[6] United States Environmental Protection Agency (2003), *EPA Assessment of Risks from Radon in Homes*, 98pp.

[7] National Academy of Sciences (1994), *Health Effects of Exposure to Radon: Time for Reassessment*, The National Academies Press, Washington, 114pp.

[8] C.A. Papachristodoulou, D.L. Patiris, K.G. Ioannides (2010), "Exposure to indoor radon and natural gamma radiation in public workplaces in north-western Greece", *Radiation Measurements*, **45(7),** pp.865-871, DOI: 10.1016/j.radmeas.2010.02.018.

[9] Ministry of Trade and Industry (2011), *The Detailed Plan for Exploration, Mining, Processing and Use of Radioactive Ores for The Period to 2020, With a Vision to 2030* (in Vietnamese).

[10] N. Phuong, N.V. Dung, L.K. Phon, et al. (2013), "A study on the increase of natural radiation field due to the exploration of rare earth ores in the Dong Pao and Nam Xe areas - Lai Chau province", *J. Geol.*, **A(335)**, pp.56-62 (in Vietnamese).

[11] T.T. Binh, H.T. Dinh, N. Phuong (2007), "Investigating the current state of radioactive environment on the deposits of Dong Pao, Then Sin-Tam Duong (Lai Chau), Muong Hum (Lao Cai), Yen Phu (Yen Bai), Thanh Son (Phu Tho), An Diem, Ngoc Kinh - Suon Giua (Quang Nam)", *Journal of Geological*, **A(298)**, pp.41-47 (in Vietnamese).

[12] L.Q. Trung, B.K. Du, T.X. Ben, et al. (2008), *Exploration Proposal to Upgrade Reserves and Exploration in 2007 and 2008 During The Period Sin Quyen Copper Mine Production - Lao Cai month 04/2005*, Sin Quyen Copper Mining Company, 185pp (in Vietnamese).

[13] Ministry of Science and Technology (2012), *Circular No.19/2012/TT-BKHCN Provisions on Control and Ensure The Safety of Irradiated and Irradiated Career Public* (in Vietnamese).

[14] General Department of Geology and Minerals of Vietnam (2012), *Investigation and Evaluation of Geological Environment - Radioactive Air Method* (in Vietnamese).

[15] United Nations Scientific Committee on the Effects of Atomic Radiation (2006), *Annex E: Sources-to-Effects Assessment for Radon in Homes and Workplaces*, 112pp.

[16] United States Environmental Protection Agency (2009), *A Citizen's Guide to Radon: The Guide to Protecting Yourself and Your Family from Radon*, 16pp.

[17] National Research Council (1999), *Health Effects of Exposure to Radon: BEIR VI*, The National Academies Press, Washington, 592pp.

DOI: 10.31276/VJSTE.64(1).85-89

Tidal energy potential in coastal Vietnam

Huy Toan Do*, Thanh Binh Nguyen, Tuan Minh Ly

Center for Environmental Fluid Dynamics, University of Science, Vietnam National University - Hanoi, 334 Nguyen Trai Street, Thanh Xuan Trung Ward, Thanh Xuan District, Hanoi, Vietnam

Received 2 December 2020; revised 20 January 2021; accepted 29 January 2021

Abstract:

Tidal energy is a renewable energy source produced by the rise and fall of ocean tides. Tidal energy can be exploited using a special type of generator that converts tidal energy into electricity. Tidal power generation has the potential to open up many prospects for energy field and minimize carbon dioxide emissions that cause the greenhouse effect. To evaluate the possibility of tidal power, it is necessary to have documents and data on average annual tidal amplitude, tidal regime, and main tidal waves in the study area. To calculate the tidal power potential for the east coast of Vietnam, this article applies the calculation formula of tidal power energy by Russian scientist L.B. Bernstein. The annual mean tidal amplitude and the K1, O1, and M2 wave amplitude data at nearly 2000 calculation points along the coast of Vietnam were extracted from the TPOX8-Atlas harmonic constant set. Research results showed that Vietnam has great potential for tidal energy along the Hai Phong - Quang Ninh coastal area and the southeast region with a prospective 41.6 GWh/km^2/y.

Keywords: **tidal energy, tidal energy potential, TMD toolbox, TPOX8-Atlas.**

Classification number: **4.4**

1. Introduction

Energy is an important factor in the socio-economic development of a country. However, increasing energy demands have caused fossil energy reserves to quickly deplete. Environmental and politics issues have made energy security an urgent matter and a great concern for all nations. Nuclear power technology is unsafe and there is always a potential radiation hazard, such as Chernobyl (1986) and Fukushima (2011), leaving behind long-term damage to the global socio-economy and environment [1, 2]. Therefore, people are now looking for new sources of energy to replace fossil fuels and nuclear energy in effort to overcome their disadvantages.

With a global sustainable development strategy, especially during the period of "green economic development", the world is beginning to see new technologies for cleaner electricity generation. In the 21st century, humanity has witnessed the rapid development of new energy sources, especially from the ocean. Scientific and technological advances have allowed new resources to be exploited to produce electricity from marine renewable energy sources such as wind, ocean waves, tidal current, sea temperature gradient, and salt gradient, etc. Among these, some have already been commercialized on a large scale such as wind power stations (coastal and island), tidal energy stations, ocean wave power stations, and marine thermal gradient power stations [3].

Currently, research on tidal energy has particularly interested many countries with great potential for tidal energy such as the UK, France, Russia, India, China, Korea, and Canada. However, research on tidal energy in Vietnam is still limited. The few results have yielded mostly general assessments and sometimes used only tidal data from one location for simulations across a large region. This paper conducts research over a large area along the coast of Vietnam with the farthest data extraction point about 250 km from the coast (area 7). This is a new point compared to previous studies because research on tidal electric energy has been focused on coastal areas with a distance of 30-40 km [4].

This work evaluated the potential of tidal power for the coastal area of Vietnam by the Bernstein formula developed by the Russian scientist L.B. Bernstein

*Corresponding author: Email: dohuytoan@hus.edu.vn

[5]. Input data sources for the Bernstein formula were extracted using Tide model driver (TMD) tool with exploitation of the TPOX8-Atlas harmonic constant, which was researched and developed by Oregon State University, USA, with a resolution of 1/6°. The TMD TPOX8-Atlas tool uses new generation map data and satellite elevation data assimilation methods of L. Padman, et al. (2005) [6] and G.D. Egbert, et al. (1994) [7] into the global shallow water model. Research results are the basis for comparison with other evaluation methods and contribute to building a scientific basis for future related studies.

2. Materials and methods

2.1. Study area

The study area is the coastal area of Vietnam with a diverse and complex topography stretching from 7°N - 22°N, 103°E-111°E (Fig. 1). According to research by N.N. Thuy (1984) [8], Vietnamese tides are very diverse with all the tidal regimes of the world such as diurnal tide, mixed diurnal tide, semi-diurnal tide, and mixed semi-diurnal tidal all distributed alternately.

From north to south, the tidal regime changes its features, the study has divided the tidal regime into the following areas (Fig. 1):

- Area 1: North Sea to Thanh Hoa, diurnal tide.

- Area 2: Nghe An to Cua Gianh sea area, mixed diurnal tide, number of diurnal days accounts for more than half a month.

- Area 3: Southern sea area from Cua Gianh to Thuan An, mixed semi-diurnal tidal.

- Area 4: Thuan An and adjacent waters, semi-diurnal tidal.

- Area 5: Nam Thuan An to northern Quang Nam sea area, mixed semi-diurnal tide.

- Area 6: middle of Quang Nam to Binh Thuan sea area, mixed diurnal tide.

- Area 7: Ham Tan to Ca Mau cape sea area, mixed semi-diurnal tide.

- Area 8: Ca Mau cape to Ha Tien sea area, mixed diurnal tide.

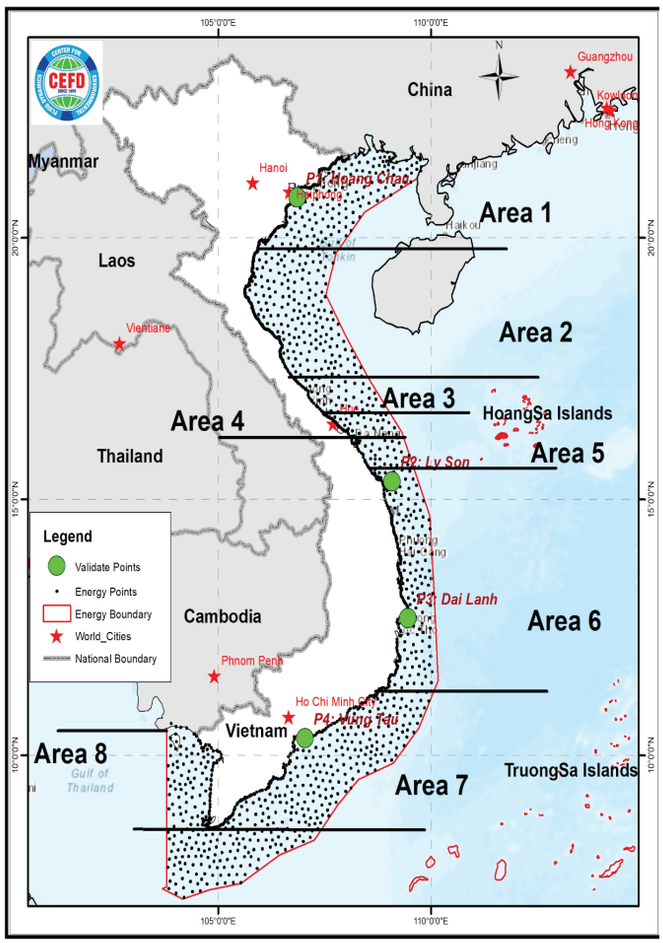

Fig. 1. Map of study area and calculation tool validation locations.

2.2. Data

The annual mean tidal amplitude and the K1, O1, and M2 wave amplitude data (calculated for year 2019) for nearly 2000 calculation points along the coast of Vietnam were extracted from the TPOX8-Atlas harmonic constant set.

Water level data used to validate the quality of TMD TPOX8-Atlas tool were observed water levels (10 min/obs) measured at Hoang Chau, Ly Son, Dai Lanh, and Vung Tau (Fig. 1).

2.3. Methods

The Bernstein formula has been widely applied when calculating coastal and estuary areas in the world.

According to Bernstein [5], the formula for evaluating the annual tidal energy potential for an area with a semi-diurnal tidal regime is as follows:

$$E_{tn} = 1.97 * 10^6 A_{tb}^2 S \quad (1)$$

For the area with the annual tidal regimes other than semi-diurnal tide, Bernstein applies the following formula:

$$E_{tn} = 1.97 * 0.5 * 10^6 A_{tb}^2 S(1 + \frac{4-D}{D}) \quad (2)$$

with E_{tn}: tidal energy potential/year; A_{tb}: annual average tidal amplitude; S: sea surface area (km^2); D: tidal feature value.

$D = \frac{H_{K1} + H_{O1}}{H_{M2}}$; H_{K1} moon-sun tidal waves amplitude K_1; H_{O1} diurnal tide wave amplitude O_1; H_{M2} semi-diurnal tide wave amplitude M_2.

In this study, Bernstein's formula (1) was applied to area 4 and formula (2) was applied to the remaining study areas along the coast of Vietnam.

3. Results and discussion

Simulated water level extracted from TMD TPXO8-Atlas tool for 4 locations (Hoang Chau, Ly Son, Dai Lanh, and Vung Tau) was compared with observed water level. Fig. 2 shows the evolution of water level in Hoang Chau (from 22nd August 2012 to 30th August 2012), Ly Son (from 14th June 2013 to 30th June 2013), Dai Lanh (from 9th August 2014 to 16th August 2014), and Vung Tau (from 31st August 2020 to 7th September 2020) showed that the TMD TPXO8-Atlas tool has well simulated the phase and magnitude of tides. The simulation results (Table 1) have high reliability with the Nash-Sutcliffe efficiency correlation coefficient (NSE) greater than 0.88. Therefore, the data set of annual average tidal amplitude and tidal wave amplitude K1, O1, and M2 extracted from the TMD TPOX8-Atlas tool is reliable enough to be included in Bernstein's formulae.

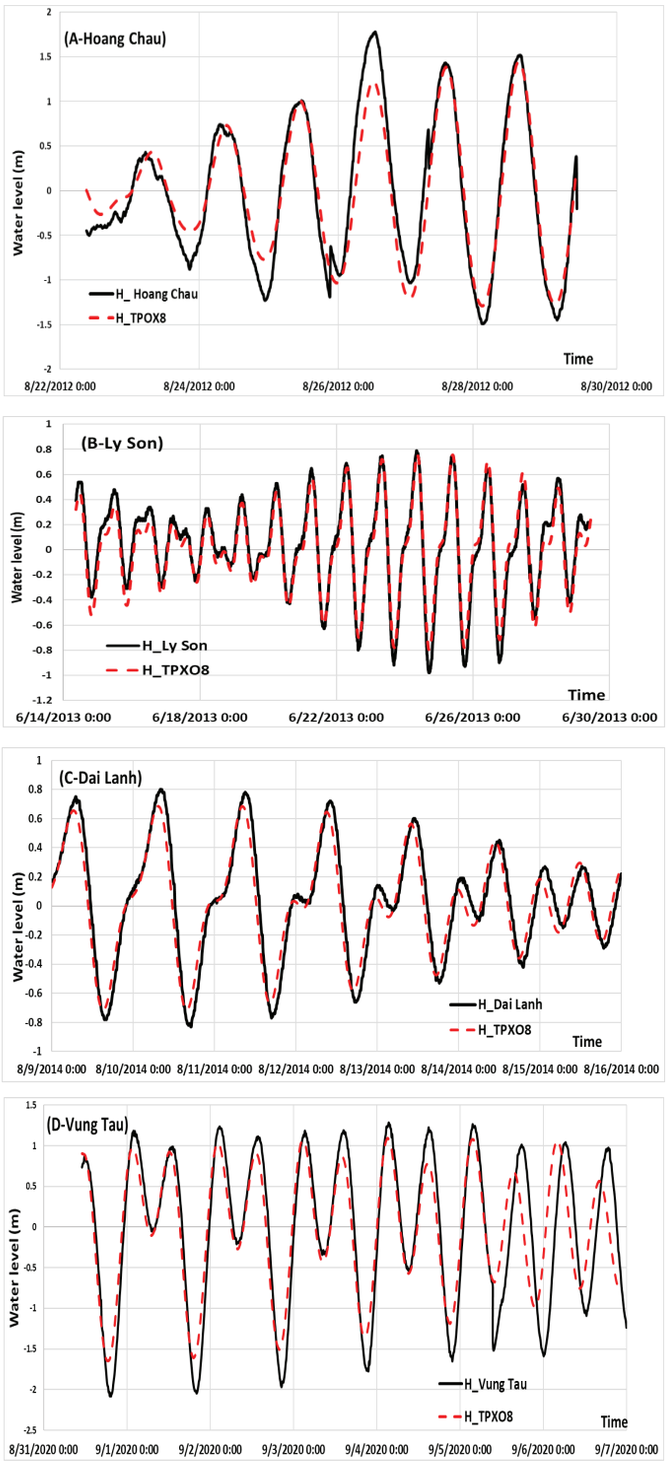

Fig. 2. Observed and simulated water level, TMD TPXO8-Atlas.

Table 1. Nash-Sutcliffe efficiency correlation coefficient (NSE).

Location	Hoang Chau	Ly Son	Dai Lanh	Vung Tau
NSE	0.91	0.94	0.97	0.88

The TMD TPOX8-Atlas tool was calculated for the simulation time of 2019. The obtained results were 1-year water level series and the amplitude of the tidal waves K1, O1, and M2 at nearly 2000 locations along the coast of Vietnam. From these series of water levels, the annual mean tidal amplitude for each location has been calculated.

Table 2 shows the annual mean tidal amplitude and tidal wave amplitude K1, O1, and M2 at some typical locations. Tidal amplitude decreases gradually from Quang Ninh to Thuan An and then gradually increases at the Ca Mau cape and decreases from Ca Mau cape to Ha Tien. Mong Cai, Ha Long, Vung Tau, and Dinh An has the largest tidal amplitude in Vietnam with results of 3.38, 2.95, 2.52, and 2.69 m, respectively. Thuan An and Ha Tien had the smallest tidal amplitude with results of 0.45 and 0.68 m, respectively. The study results have shown the correct distribution of the tidal range in the East Sea.

Table 2. Annual mean tidal amplitude and tidal wave amplitude K1, O1, M2 at some typical locations.

No	Location	A_{tb} (m)	H_{K1} (m)	H_{O1} (m)	H_{M2} (m)
1	Mong Cai	3.38	0.735	0.9439	0.2122
2	Ha Long	2.95	0.674	0.752	0.074
3	Hoang Chau	2.52	0.6797	0.7611	0.058
4	Sam Son	2.48	0.5985	0.6567	0.2584
5	Cua Gianh	1.48	0.2344	0.3181	0.2
6	Thuan An*	0.45	0.0383	0.048	0.1794
7	Ly Son	1.38	0.28	0.2242	0.1862
8	Dai Lanh	1.47	0.3331	0.2822	0.1724
9	Vung Tau	2.52	0.5819	0.3127	0.7408
10	Dinh An	2.69	0.5468	0.4189	0.7422
11	Ca Mau	1.66	0.4239	0.2354	0.2
12	Ha Tien	0.68	0.1935	0.1655	0.06

Formula (2) was not applied for Thuan An so K1, O1, M2 are not used.

The calculation results after applying Bernstein's formula are shown in Table 3 and Figs. 3 and 4. It can be concluded that area 7 has the greatest tidal power potential in the country, followed by areas 1 and 2. The largest, average, and smallest capacity in area 7 are 41.66, 10.39, and 0.91 GWh/km^2/y. The largest, average, and smallest capacity in area 1 are 17.33, 6.42, and 1.25 GWh/km^2/y, respectively. The largest, average, and smallest capacity in area 2 are 6.1, 3.02, and 0.27 GWh/km^2/y, respectively.

The above results show that tidal power energy in coastal Vietnam has a huge potential for exploitation.

Table 3. Tidal energy for each study area.

Area	E_{tn} medium (GWh/km^2/year)	E_{tn} max (GWh/km^2/year)	E_{tn} min (GWh/km^2/year)
Area 1	6.42	17.33	1.25
Area 2	3.02	6.1	0.27
Area 3	1.18	3.85	0.16
Area 4	0.8	2.75	0.16
Area 5	1.11	2.7	0.33
Area 6	1.74	4.29	0.62
Area 7	10.39	41.66	0.91
Area 8	0.74	4.01	0.05

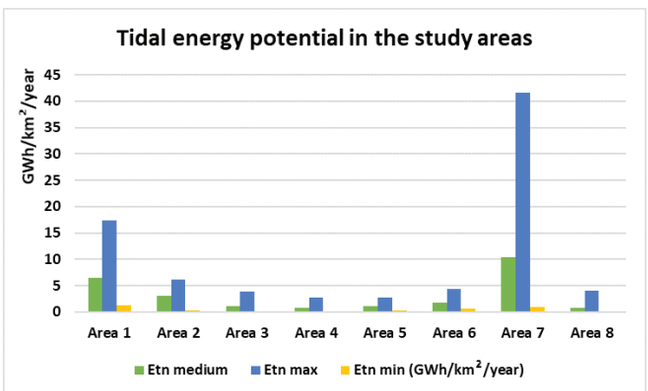

Fig. 3. Tidal energy potential in the study areas.

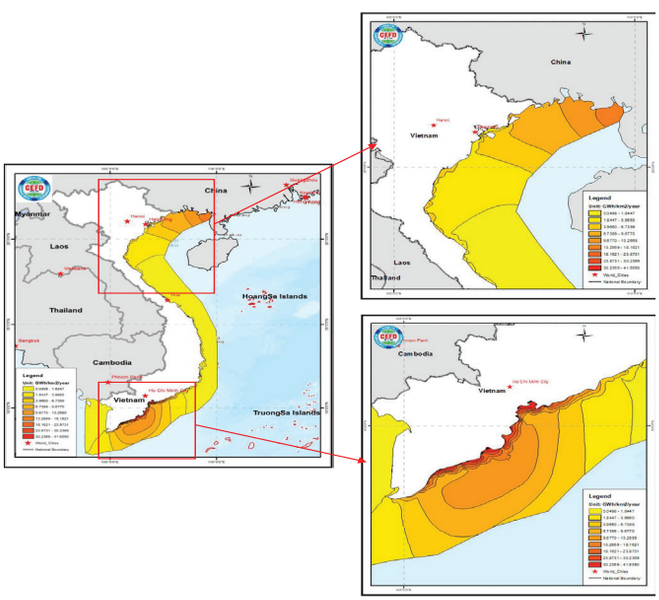

Fig. 4. Tidal energy potential in coastal Vietnam.

4. Conclusions

This article assessed the potential of tidal energy in coastal Vietnam using Bernstein formulae and the TMD TPOX8-Atlas tool. The annual mean tidal amplitude and the K1, O1, and M2 wave amplitude data at nearly 2000 calculation points along the coast of Vietnam were extracted from the TMD TPOX8-Atlas tool. The results showed that the three areas with the largest potential for coastal tidal energy in Vietnam, in descending order, are area 7, area 1, and area 2 with average potentials of 10.39, 6.42, and 3.02 GWh/km^2/y, respectively. The remaining potentials from the other areas ranged from 0.74 to 1.18 GWh/km^2/y. It can be concluded that tidal energy in areas 1, 2, and 7 have a high potential for tidal wave energy production.

Further studies need to have more complete and detailed input data on the annual average water level amplitude calculated from a tidal cycle of 18.6 years and detailed seabed topography for the coastal area and specific areas of the water bodies.

CRediT author statement

Huy Toan Do, Thanh Binh Nguyen, Tuan Minh Ly: Data curation, Software, Visualisation, Investigation, Writing original draft preparation, Conceptualization, Methodology, Supervision.

ACKNOWLEDGEMENTS

The authors would like to thank Center for Environmental Fluid Dynamics, University of Science, Vietnam National University, Hanoi for providing data and funding for this research.

COMPETING INTERESTS

The authors declare that there is no conflict of interest regarding the publication of this article.

REFERENCES

[1] Ministry of Industry and Trade of the Socialist Republic of Vietnam (2008), *Research the Overall National Energy Development Diagram of Vietnam*, https://openjicareport.jica.go.jp/pdf/11899812_01.pdf, accessed 6 June 2020 (in Vietnamese).

[2] D.T. Luong, V.D. Phan, T.T. Nguyen (2015), "Renewable energy in Vietnam: The main reasons for the development, resource potential and current status of exploitation", *Journal of Water Resources & Environmental Engineering*, **50(9/2015)**, pp.24-29 (in Vietnamese).

[3] D.V. Toan (2018), "The all Vietnam marine renewable energy", *The Project Green Offshore Wind Energy for Vietnam Sea*, https://www.researchgate.net/publication/328254137, accessed 6 June 2020.

[4] N.V. Dau (2020), "Tidal energy and ocean current energy - Potential and reality", Ho Chi Minh City Science, Technology and Economics Association, http://bientoancanh.org/nang-luong-thuy-trieu-va-nang-luong-hai-luu-tiem-nang-va-hien-thuc/, accessed 12 October 2020.

[5] D.V. Toan, N.Q. Trinh (2011) "Assessment of the potential for tidal power in the estuarine coastal area of southeast Vietnam", *Vietnam Journal of Hydrometeorology*, **9**, pp.47-51 (in Vietnamese).

[6] L. Padman, S. Erofeeva (2005), "Tide model driver manual", *Earth & Space Research*, 13pp.

[7] G.D. Egbert, A.F. Bennett, M.G.G. Foreman (1994), "TOPEX/POSEIDON tides estimated using a global inverse model", *Journal of Geophysical Research*, **99(C12)**, DOI: 10.1029/94JC01894.

[8] N.N. Thuy (1984), *Tides in Vietnam Ocean*, Science and Technics Publishing House, 262pp (in Vietnamese).

DOI: 10.31276/VJSTE.64(1).90-96

Applying the integrated model of GIS and AHP for evaluating ecological suitability of Ming aralia (*Polyscias fruticosa*): A case study of Hai Hau district, Nam Dinh province, Vietnam

Le Thuy Chau Ngoc, Truong Ngoc Kiem*

University of Science, Vietnam National University - Hanoi, 334 Nguyen Trai Street, Thanh Xuan Trung Ward, Thanh Xuan District, Hanoi, Vietnam

Received 20 September 2021; revised 22 November 2021; accepted 30 November 2021

Abstract:

The Hai Hau district, located in the southeast region of the Nam Dinh province, belongs to the Red river delta where residents mainly rely on agriculture, fisheries, and handicrafts as their livelihood. In recent years, many households have switched from growing rice to Ming aralia (*Polyscias fruticosa*), a tropical medicinal plant with high economic value. On the basis of analysing the influence of bioclimatological and soil conditions in Hai Hau district, Nam Dinh province on the growth and development of cloves through the integrated Analytic Hierarchy Process (AHP) - Geographic Information System (GIS) model, this study has divided the adaptive thresholds for each climate factor with corresponding weighted values to evaluate the ecological adaptability of Ming aralia to the criteria's in Hai Hau district. The research results show that the Hai Hau district has 25.3% of highly suitable area (S1), 33.8% of moderately suitable area (S2), 23.3% of marginally suitable area (S3), and 17.6% of not suitable area (N) for Ming aralia development. The suitable area for cultivation of Ming aralia with high economic efficiency is about 13,522.37 ha, or 59.1% of the total area, located in the northern communes of the district. This finding is a scientific basis for planning, planting, and exploitation of Ming aralia to improve sustainable livelihoods and promote local socioeconomics.

Keywords: **ecological adaptation, GIS - based AHP, Hai Hau, Ming aralia, *Polyscias fruticosa*.**

Classification number: **5.1**

1. Introduction

The assessment of ecological suitability determines the overall favourability level of geography such as landscape units, ecological units, land units, etc., for the object of development planning [1]. In Vietnam and around the world, depending on the units and subjects performing the ecological suitability assessment, many methods and models have been proposed. However, the model integrating AHP and GIS, which integrates a large amount of heterogeneous data to obtain the weights of enormous alternatives (criteria) with ease, is applied in this work due to its various advantages in a wide variety of decision-making problems [2]. The three principles of AHP, designed by T.L. Saaty (2001) [3], are analysis, comparative judgments, and combining priorities [4]. The process involves various options for decision making, and can analyse the sensitivity of the criteria and sub-criteria. A few important advantages of this technique are the detection of the compatibility and incompatibility of decision making, and identification and prioritization of the elements of decision making [5]. Therefore, the GIS technique and AHP methods have been applied to several studies to analyse the suitability of plants based on natural conditions and the ecological feature of the plant such as weather conditions, nutrients, physical conditions of soil, and economic and social factors. These techniques have been typically used for land suitability assessment in semi-arid regions for wheat and maize farming like in Neyshabur County, Iran, the spatial assessment of suitable areas for medicinal species of Astragalus in Bahar Mountain, Iran, assessing indigenous cinnamon species suitability in Tra Bong, Quang Ngai, and for land evaluation for coconut trees in Mo Cay Nam, Ben Tre… [6-9].

Ming aralia (*Polyscias fruticosa* (L.) Harms.) is widely grown in Vietnam and other countries in the Pacific region [10, 11]. Ming aralia is one of the most precious medicinal plants and it has been used for a long time as traditional medicine because it has the effect of replenishment, stimulating digestion, detoxifying, anti-bacterial and anti-inflammatory activity, and increasing endurance [10, 12]. In addition, Ming aralia is also known as "fish salad" and is used in culinary dishes in various ways [12].

Currently, in Nam Dinh, Ming aralia is grown mainly in the districts of Hai Hau, Nghia Hung, Giao Thuy, and Xuan Truong. Most of the cultivation areas are lands in gardens and ponds without any planning at larger

*Correspoding author: Email: kiemtn@gmail.com

scales. However, Ming aralia is easy to grow and easy to use, with typical medicinal properties of the ginseng family such as enhancing health, resistance, and improving adaptability [11]. Therefore, evaluating the ecological suitability of Ming aralia, with the application of GIS-based AHP for developing and planning Ming aralia in Hai Hau district, has a high scientific and practical significance. This article provides research results on the ecological suitability of Ming aralia with local ecological factors, thereby noting where suitable areas can be found for the growth and development of this plant. This is also the basis for proposing planning of the area for growing Ming aralia for the purpose of improving the livelihood of the residents and contributing to biodiversity conservation in Hai Hau district, Nam Dinh province.

2. Methods

2.1. Research area

The Hai Hau district is located in the southeast of the Nam Dinh province (Fig. 1). The district has the same soil and climate characteristics of the Northern delta with flat land, fertile soil, and tropical monsoon climate with cold winters. The population here is unevenly distributed and primarily concentrated in the coastal area [13]. In Hai Hau, agricultural development is the main focus, which makes this area a large granary of the Red river delta. Besides, fisheries, industry, handicrafts, and tourism attract a lot of domestic and foreign investment.

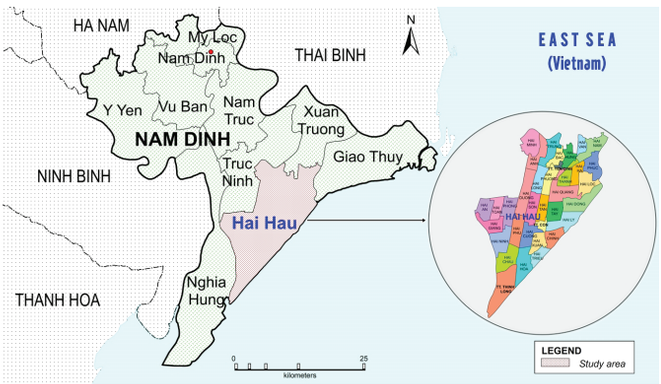

Fig. 1. Location map of the study area.

The climate and soil properties were collected, sorted, systematized, summarized, and analysed using hydro-meteorological data from statistical yearbook of Nam Dinh province [14] and the socio-economic report of Hai Hau district [15].

Characteristics of climate and soil in Hai Hau district, Nam Dinh province:

- *Radiation and daylight*: The average annual hours of sunshine are from 1650 to 1700. The average annual amount of solar radiation is 100 Kcal/cm^2.

- *Temperature*: The average annual temperature is from 23 to 24^{o}C, and the daily temperature amplitude is less than 10^{o}C.

- *Precipitation*: The average annual rainfall is from 1700 to 1800 mm. High rainfall levels mostly occur in July, August, and September accounting for nearly 80% of the total annual rainfall. Highest rainfall level in a day can be up to 200-250 mm.

- *Humidity*: Hai Hau is an area with a relatively high humidity and the average value is between 80 and 85%. The humidity of the area is stable with minor fluctuation. The humidity is highest in February and March at 92% and lowest at 80%, in which there is hot, dry southeast wind.

- *Other weather phenomena*: The study area is influenced by 2 prevailing wind directions - the southeast wind in summer and northeast wind in winter. Every year, Hai Hau is affected by 4-6 storms on average.

- *Soil*: Hai Hau belongs to a young group of soil, mainly alluvial soil with 56.1% natural area formed by the deposition of alluvial materials from the Red river system. The other groups of soils are saline soils (accounting for 19.4%), sandy soils (accounting for 5.7%), and the other groups such as alkaline soils and soils with feralitic products.

2.2. Research object

Biological and ecological characteristics of Ming aralia (*Polyscias fruticosa* (L.) Harms.) were summarized from the following documents: list of plant species in Vietnam [10], Vietnamese Medicinal Plants and Medicinal Herbs [11], Medicinal Plants in Vietnam [12], and An Illustrated Flora of Vietnam [16].

The field investigation process method by N.N. Thin (2007) [17] was applied. This process includes following steps: determining the route and survey points; setting up standard plots (10x10 m); measuring the indicators of Ming aralia, soil, and climate; then to collect, analyse, preserve, and store samples.

Ming aralia (*Polyscias fruticosa*) grows in bushes of 0.5-2 m in height. Small tree, smooth stem, no spines, no hairs, white bark; edematous roots that look like tubers (Fig. 2). Fragrant leaves, 3-pinnate and 20-40 cm long; leaflets with toothed margin; no sheath, leaves are fragrant. The mace-shaped inflorescence is short, about 7-18 mm, consisting of many crowns, with broad leaves that quickly fall off, small green flowers, petals 5, white, stamens 5, and ovary 2 chambers. Flowers bloom in November - December, slightly flattened round fruit 3-4 mm long, 1 mm thick with existing spigot, silvery white colour.

Fig. 2. Morphology of Ming aralia [12, 18].

Alkaloids, glucosides, saponins, flavonoids, tannins, B vitamins, and amino acids including lysine, xystei and methionine, have been found in Ming aralia.

To evaluate the ecological adaptability of Ming aralia (*Polyscias fruticosa*), the adverse ecological conditions for Ming aralia have been studied as follows:

- *Light-humidity:* Ming aralia is a perennial plant that favours moisture, is photophilic, and thrives in medium humid conditions. Ming aralia is also a shade-tolerant plant, but it can grow slower in shade.

- *Temperature-precipitation:* Ming aralia does not require high rainfall. Ming aralia can withstand mild drought and dislikes stagnant water. Ming aralia cannot bear waterlogging, either. The optimal temperature threshold for the growth of Ming aralia is between 22-27^{o}C.

- *Soil:* Ming aralia is a plant with a wide ecological limit as it can live and grow on many types of soil, particularly sandy soil.

2.3. The AHP multi-objective decision making model

Evaluating ecological suitability of Ming aralia includes selecting and classifying criteria, weighting indicators, and summarizing evaluations [3].

Selecting and classifying criteria: Based on previously published documents and the evaluation of experts, we selected the main ecological factor (Xi) as the criterion affecting the development and growth of the research object.

Weighting indicators: To calculate the priority between indicators (based on Saaty's priority scale - Table 1), a matrix is established:

	X_1	X_2	…	X_n
X_1	a_{11}	a_{12}	…	a_{1n}
X_2	a_{21}	a_{22}	…	a_{2n}
..	…	…	…	…
X_n	a_{n1}	a_{n2}	…	a_{nm}

where a_{ij} is the priority between the two indices i and j: $a_{ij}>0$, $a_{ij}=1/a_{ji}$, and $a_{ij}=1$ (with $i=j$).

Table 1. Priority scorecard [3].

Priority level	Level
1	Equal priority
3	Fairly equal priority
5	More priority
7	Very priority
9	Extreme priority
2, 4, 6	Average priority

Then using the above matrix creates a new matrix by dividing each value in the column by the sum of the column:

$$\begin{array}{c} \\ X_1 \\ X_2 \\ .. \\ X_n \end{array} \begin{array}{c} \begin{array}{cccc} X_1 & X_2 & \dots & X_n \end{array} \\ \begin{pmatrix} w_{11} & w_{12} & \dots & w_{1n} \\ w_{21} & w_{22} & \dots & w_{2n} \\ \dots & \dots & \dots & \dots \\ w_{n1} & w_{n2} & \dots & w_{nn} \end{pmatrix} \end{array} \quad w_{ij} = \frac{aij}{\sum_{i=1}^{n} aij}$$

where W_i is the weight of the indicator: $W_i=\frac{\sum_{j=1}^{n} wij}{n}$.

Summarizing evaluation: The consistency index (CR) needs to be calculated and checked for a value to accept the assessment. CR is calculated according to the formula: CR=CI/RI (with CR<0.1 the evaluation is accepted) in which:

$$CI = \frac{\lambda_{max}-n}{n-1} \quad \text{and} \quad \lambda_{max} = \sum_{i=1}^{n} w_i.$$

RI is determined according to Table 2 where n is the number of evaluation criteria.

Table 2. The random index match with number of criteria.

n	1	2	3	4	5	6	7	8	9	10	11	12	13	14	15
RI	0.00	0.00	0.58	0.90	1.12	1.24	1.32	1.41	1.45	1.49	1.51	1.48	1.56	1.57	1.59

2.4. Creating maps

To build multiple layer maps, we use MapInfo 11.5 and ArcGIS 10.0 software following these steps: (1) input and add data, (2) manage and organize data, (3) process and analyse data, and (4) publish output data [19, 20].

2.5. Assessment of ecological suitability

Evaluating the ecological suitability of Ming aralia using a combination of AHP hierarchical analysis and a GIS allows the construction of spatial analyses, and the management, integration, and overlay of information layers [21] with the evaluation formula: $S = \sum_{i=1}^{n} M_i$.

where S is the adaptability index; M_i is the coefficient of adapting to the criteria; and W_i is the weight of the indicators.

3. Results and discussion

3.1. Selection and classification of adaptability of Ming aralia to ecological factors

For Ming aralia in Hai Hau district, the study to select X_i for assessment includes 6 main ecological factors:

X_1 - annual average temperature; X_2 - annual average rainfall; X_3 - annual average humidity; X_4 - the length of cold seasons; X_5 - the length of dry seasons; X_6 - type of soil.

The threshold for ecological suitability of Ming aralia to the ecological and soil conditions X_i (Table 3) is given based on evaluation and meta-analysis.

Table 3. Ecological suitability table of Ming aralia to ecological factors in Hai Hau district.

Factors	Symbols	Value	Measures	Details	Suitable level			
					Highly suitable	*Moderately suitable*	*Marginally suitable*	*Not suitable*
					S1	*S2*	*S3*	*N*
1. Annual average temperature	1	<20	℃	Slightly cold				+
	2	20-22		Cool			+	
	3	22-24		Normal	+			
	4	24-28		Slightly hot		+		
	5	>28		Hot				+
2. Annual average rainfall	s	<1500	mm/year	Small		+		
	m	1500-1800		Average	+			
	l	1800-2000		Slightly heavy			+	
	vl	>2000		Heavy				+
3. Annual average humidity	s	<81	%	Normal			+	
	m	81-83		Average	+			
	h	83-85		Slightly high		+		
	vh	>85		High			+	
4. The length of cold seasons	ls	<2	month/ year	Very short		+		
	s	2-3		Short	+			
	m	>3		Average			+	
5. The length of dry seasons	s	<3	month/ year	Short		+		
	m	3-5		Average	+			
	h	5-6		Long			+	
	vh	>6		Very long				+
6. Type of soil	FL			Fluvisols	+			
	FLSm			Molli Salic Fluvisols		+		
	FLSh			Hapli Fluvisols			+	
	FLSg			Gleyi Salic Fluvisols				+

3.2. Determining the weights of the indicators

The main factors affecting the ecological suitability of Ming aralia in the study area are calculated in correlations using the AHP model through weight values (Table 4). With the value of consistency ratio (CR)=0.02<0.1, the evaluation can be accepted.

Table 4. Table of weight of factors affecting ecological suitability of Ming aralia.

Factor	Annual average temperature	Annual average rainfall	Annual average humidity	The length of cold seasons	The length of dry seasons	Type of soil
Weight	0.304	0.263	0.130	0.101	0.101	0.101

It can be seen that the average annual temperature is the most important factor affecting the growth and development of Ming aralia (30.4%). This is followed by the factors of annual average rainfall (26.3%) and annual average humidity (13%). The factors of length of cold season, length of dry season, and mechanical composition have less influence (a total of 10.1%).

3.3. Developing component maps

The main goal of applying GIS software is to process collected data and arrange it using algorithms to create target maps (Figs. 3-8).

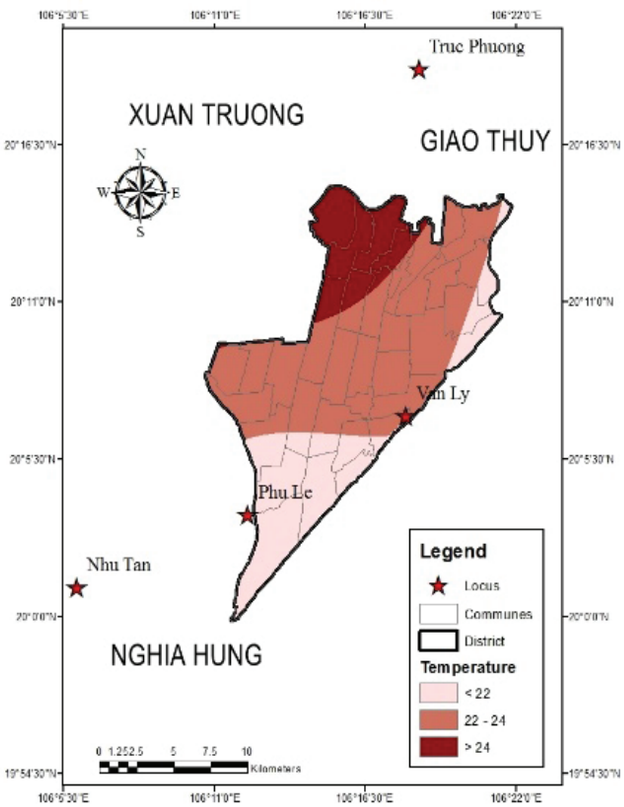

Fig. 3. Annual average temperature map.

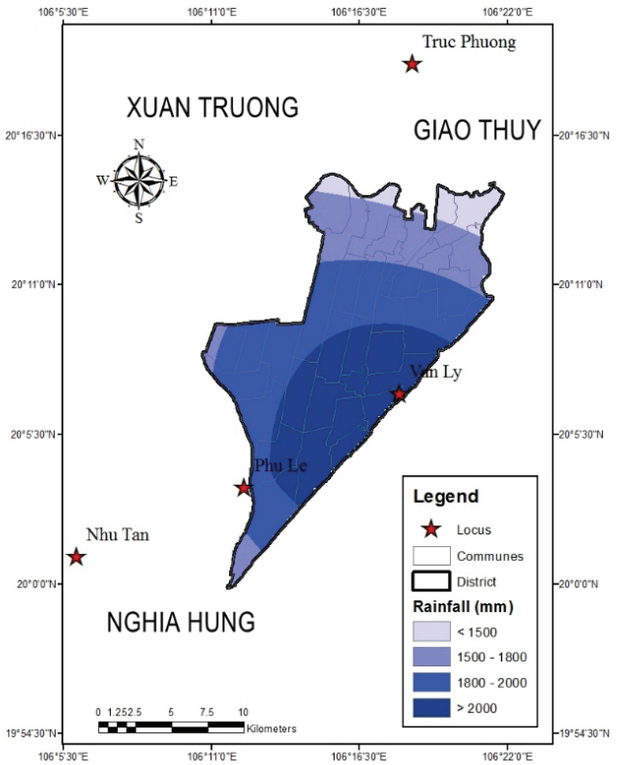

Fig. 4. Annual average rainfall map.

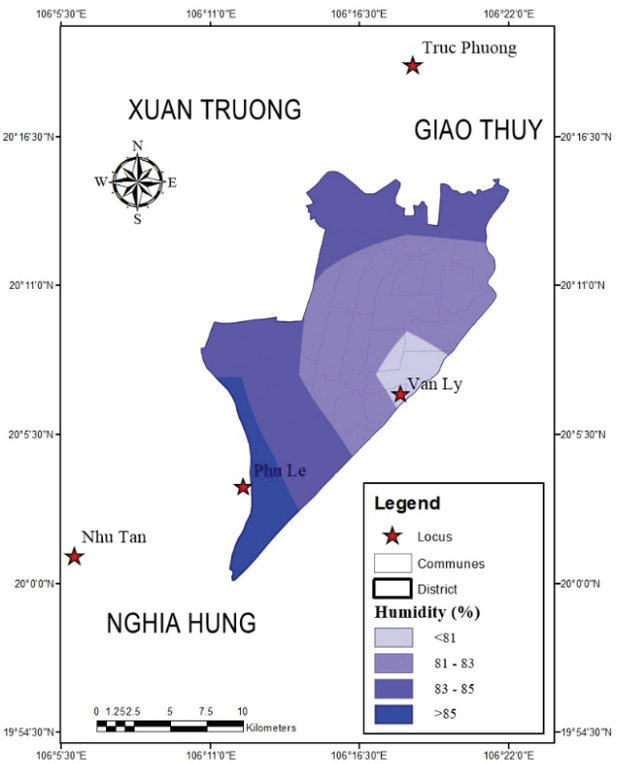

Fig. 5. Annual average humidity map.

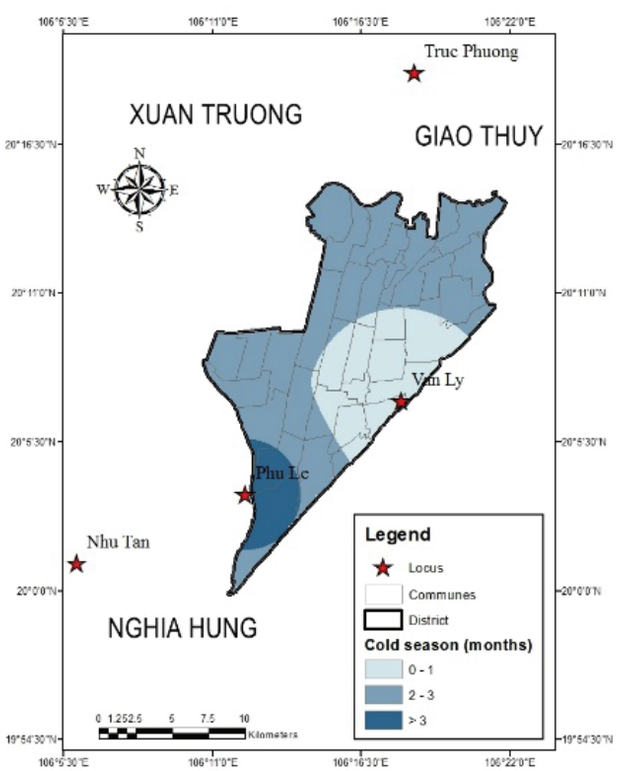

Fig. 6. The length of cold seasons map.

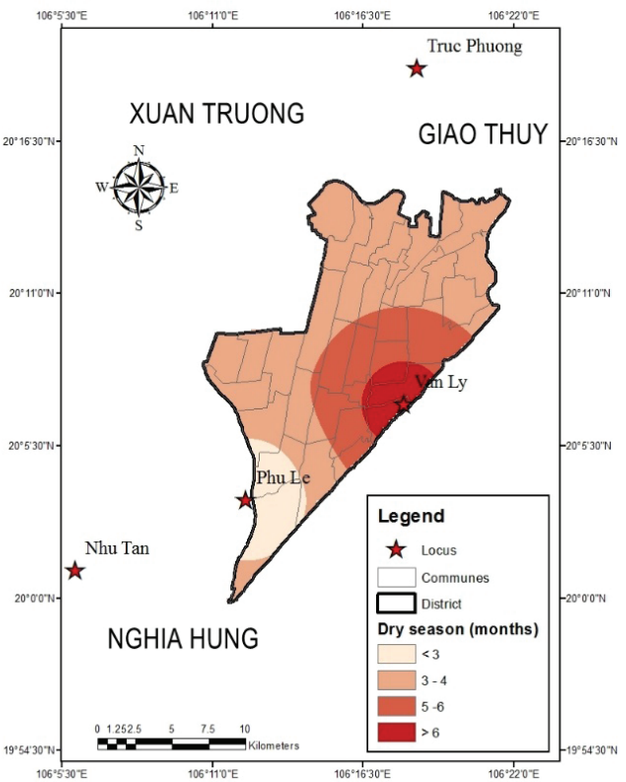

Fig. 7. The length of dry seasons map.

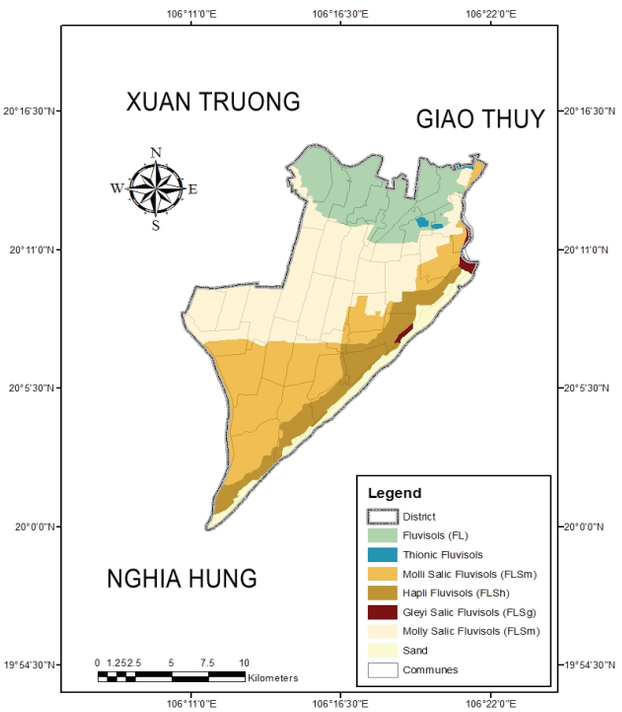

Fig. 8. Type of soil map.

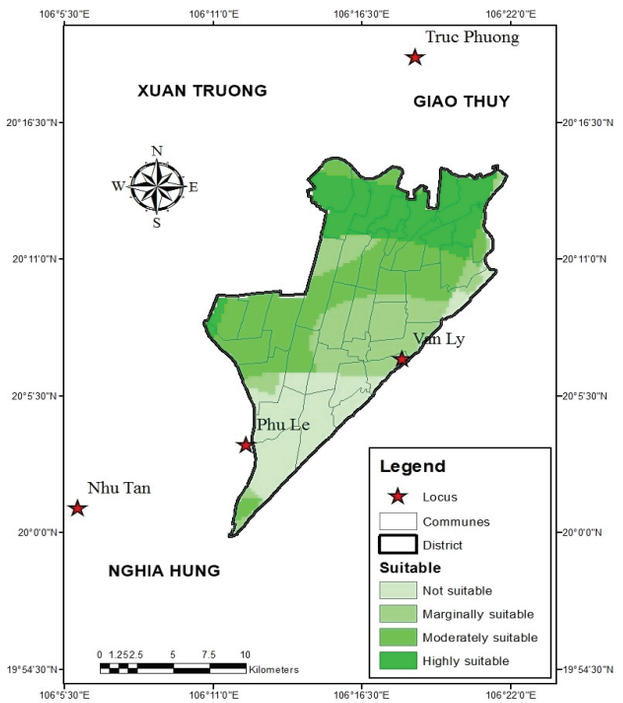

Fig. 9. Suitability level map of Ming aralia in Hai Hau district.

3.4. Evaluation of the ecological suitability of Ming aralia

The ecological suitability is divided into 4 levels based on the average score rate (S): S1 (highly suitable): average suitability score rate is above 80%; S2 (moderately suitable): average suitability score rate from 66 to 80%; S3 (marginally suitable): average suitability score rate from 50 to 65%; N (not suitable): average suitability score rate is less than 50%.

The map of the suitability of Ming aralia in Hai Hau was developed based on applying the AHP model to determine the weights, then overlaying the corresponding map on ArcGIS software (Fig. 9).

The evaluation results by the AHP-GIS method and the evaluation formula show that:

- The highly suitable area (S1) has a total area of 5,781.62 ha, which accounts for 25.3% of the Hai Hau district and is distributed to the north of the district in which the communes of Hai Anh, Hai Bac, Hai Van, Hai Nam, Hai Trung, and Hai Minh are located. The soil in this area is mostly alluvial; the ecological factors are within the moderately suitable - highly suitable threshold. This is a favourable area for the growth, development, and rooting of Ming aralia.

- The moderately suitable area (S2) has a total area of 7,740.75 ha accounting for 33.8% of the Hai Hau district. These regions extend from the east to the southwest of Hai Hau and is located along the communes of Hai Thanh, Hai Long, Hai Duong, Hai Phong, Hai Toan, and Hai An. This area has annual ecological factors, which have a slight influence on Ming aralia.

- The marginally suitable area (S3) has a total area of 5,321.61 ha accounting for 23.3% of Hai Hau. These areas are in Hai Tay and Hai Son communes and these areas contain land plots with small/moderate areas that are isolated or located between the distribution zones of the moderately suitable (S2) and highly suitable (S1) areas. This area has an adverse ecological factor of heavy average annual rainfall.

- The not suitable area (N) has a total area of 4,051.61 ha accounting for 17.5% of Hai Hau and is distributed to the south along the Hai Xuan, Hai Cuong, and Hai Hoa communes, and a small part of the eastern of Hai Hau district. These areas possess mainly saline soils (FLSm and FLSh). The adverse ecological factors are the average annual temperature and the length of the cold season.

Thus, the climatic and soil conditions in Hai Hau district (Nam Dinh province) are suitable for the cultivation and development of Ming aralia as nearly 60% area is assessed as highly suitable and moderately suitable. However, the actual scale of planting Ming aralia in the area is still not high compared to the potential realized through this study. According to the documents summarized above, Ming aralia is easy to grow, easy to care for, and can be harvested from 3 years of age. After harvesting, good stems can be selected for breeding while other parts such as roots, stems, and leaves can be sold in fresh form or processed immediately. Currently, companies and businesses in the Hai Hau district also focus on promoting people to build high-yield Ming aralia farms and to approach GACP standards to produce medicinal herbs. Therefore, the planning of potential areas and the construction of Ming aralia growing areas should be of focus to enhance and ensure local livelihood, which aims to improve living standards and contribute to biodiversity conservation in the Hai Hau district, Nam Dinh province.

Conclusions

Based on the assessment of the adaptability of ecological factors to the growth and development of Ming aralia, a table of ecological suitability of Ming aralia to ecological factors in Hai Hau district, Nam Dinh province has been developed to summarize four suitability levels of highly suitable (S1), moderately suitable (S2), marginally suitable (S3), and not suitable (N).

Using the AHP model, the development of Ming aralia in Hai Hau district, Nam Dinh province has been evaluated under the influence of 6 factors: average annual temperature, average annual rainfall, average annual humidity and relative humidity, length of cold season, length of dry season, and soil mechanical composition with the following weights: 0.034; 0.263; 0.130; 0.101; 0.101; 0.101, respectively. In addition, corresponding component target maps has been established.

Hai Hau, Nam Dinh has the most suitable area for the development of Ming aralia (S1 and S2), which is located in the north of the district with 13,522.37 ha accounting for 59.1% of the study area. The area with high adaptability for growing Ming aralia is fairly large and located along the communes of Hai Anh, Hai Bac, Hai Van, Hai Nam, Hai Trung and Hai Minh. This area has alluvial soil with ecological factors that are highly suitable for the growth, development, and tuber production of Ming aralia. It can be seen that the total area of Hai Hau district is quite large, but the suitable area for growing Ming aralia is mainly concentrated in the northern area of the district because of the complexity of the soil as well as the climatic conditions in the area. However, Ming aralia generates great economic value that can stabilize livelihoods, so potential areas should be expanded in the future.

The method of integrating the AHP hierarchical analysis model into GIS for assessing the adaptability of Ming aralia is an effective approach to local research and the assessment of the ecological suitability of plants for planning in potential regions. The scoring and weighting methods for each ecological factor with quantitative values has partly eliminated the subjectivity in the assessment of plant ecological suitability.

In the future, with the method of integrating the AHP hierarchical analysis model into GIS, the implementation of studies to assess the potential of bioclimatological and soil resources in localities to determine the degree of ecological adaptation while serving as the planner of cultivation areas of medicinal plants is effective and feasible. Enhancing livelihoods, improving lives, promoting sustainable socio-economic development, and creating a premise for the formation of potential areas for the cultivation of high-yielding varieties, species, specialties for each locality will all be gradually brought into reality by using this method.

CRediT author statement

Le Thuy Chau Ngoc, Truong Ngoc Kiem: Data curation, Software, Visualisation, Investigation, Writing original draft preparation, Conceptualization, Methodology, Supervision.

COMPETING INTERESTS

The authors declare that there is no conflict of interest regarding the publication of this article.

REFERENCES

[1] N.C. Huan, N.A. Thinh, P.Q. Tuan (2004), "An integrated ALES-GIS model in landscape evaluation for cultivated crop development in Sa Pa district, Lao Cai province", *VNU Journal of Science: Natural Sciences and Technology*, **4**, pp.43-50 (in Vietnamese).

[2] Y. Chen, J. Yu, K. Shahbaz, et al. (2009), "A GIS-based sensitivity analysis of multi-criteria weighs", *18th World IMACS/MODSIM Congress, Cairns, Australia*, pp.3137-3143.

[3] T.L. Saaty (2001), "Fundamentals of the analytic hierarchy process", *The Analytic Hierarchy Process in Natural Resource and Environmental Decision Making*, Springer, **3**, pp.15-35, DOI: 10.1007/978-94-015-9799-9_2.

[4] H. Alipor, M. Zare, S. Shojaei (2016), "Assessing the degradation of vegetation of arid zones using FAO-UNIP model (case study: Kashan zone)", *Model. Earth Syst. Environ.*, **2**, pp.1-6, DOI: 10.1007/s40808-016-0258-8.

[5] J. Bigelow, Z. Mobaraki (2009), "Land suitability comparison of Ghazvin to cultivate saffron based on the multi-criteria decision methods", *Nat. Geog. Res.*, **66**, pp.101-119.

[6] R.P. Ahmad, R.M. Hamid, S. Akbar, et al. (2020), "Integrated fuzzy, AHP and GIS techniques for land suitability assessment in semi-arid regions for wheat and maize farming", *Ecological Indicators*, **110**, DOI: 10.1016/j.ecolind.2019.105887.

[7] P. Issa, M. Mahboobeh, Z.T. Ali, et al. (2019), "The spatial assessment of suitable areas for medicinal species of Astragalus (Astragalus hypsogeton bunge) using the analytic hierarchy process (AHP) and geographic information system (GIS)", *The Egyptian Journal of Remote Sensing and Space Science*, **22(2)**, pp.193-201, DOI: 10.1016/j.ejrs.2018.02.003.

[8] N.H. Cuong (2018), "Integration of GIS and decision tree in land evaluation for coconut trees in Mo Cay Nam district, Ben Tre province", *VNU Journal of Science: Earth and Environmental Sciences*, **34(1)**, pp.66-76, DOI: 10.25073/2588-1094/vnuees.4218 (in Vietnamese).

[9] N.V. Loi, T.K. Ngoc, P.D. Hung (2020), "Application of GIS, AHP, and FAPH in assessing indigenous cinnamon species suitability in Tra Bong, Quang Ngai", *Hue University Journal of Science: Agriculture and Rural Development*, **129(3D)**, pp.5-19, DOI: 10.26459/hueuni-jard.v129i3D.5713 (in Vietnamese).

[10] Hanoi National University, Vietnam Institute of Science and Technology (2005), *Checklist of Plant Species of Vietnam*, Agriculture Publishing House, 1248pp (in Vietnamese).

[11] D.T. Loi (2004), *Vietnamese Medicinal Plants and Medicinal Herbs*, Medical Publishing House, 1294pp (in Vietnamese).

[12] P.H. Ho (2006), *Medicinal Plants in Vietnam*, Tre Publishing House, 718pp (in Vietnamese).

[13] Department of Natural Resources and Environment of Nam Dinh Province (2016), *Decision 722 / QD-UBND On Approval of Land Use Plan in 2020 Hai Hau District* (in Vietnamese).

[14] Nam Dinh Statistical Office (2013), *Nam Dinh Statistical Yearbook* (in Vietnamese).

[15] Hai Hau District People's Committee (2020), *Report on The Implementation of The Socio-Economic Development Plan in 2019 and Objectives, Tasks and Solutions in 2020* (in Vietnamese).

[16] P.H. Ho (2003), *An Illustrated Flora of Vietnam*, Tre Publishing House, 1027pp (in Vietnamese).

[17] N.N. Thin (2007), *Methods of Plant Research*, Hanoi National University Publishing House, 166pp (in Vietnamese).

[18] WHO/WPRO Manila, Institute of Materia Medica Hanoi (1990), *Medicinal Plants in Vietnam*, Science and Technology Publishing House, 435pp (in Vietnamse).

[19] T.T. Duc (2002), *Basis GIS*, National University Publishing House, 200pp.

[20] N.D. Ky, L.T. Anh, N.C. Huan, et al. (2005), "ALES-GIS integrated model in assessing ecological adaptation to crops (Sample study: Coffee and rubber areas in Dak Lak and Dak Nong provinces)", *Journal of Soil Science*, **23**, pp.97-102 (in Vietnamese).

[21] E. Memarbashi, H. Azadi, A.A. Barati, et al. (2017), "Land-use suitability in northeast Iran: application of AHP-GIS hybrid model", *ISPRS International Journal Geo-Information,* **6(12)**, DOI: 10.3390/ijgi6120396.

Vietnam Journal of Science, Technology and Engineering (VJSTE): Manuscript Template

General Instructions on using this template and submitting a manuscript to VJSTE: Thank you for preparing a manuscript for submission to VJSTE. Using this template, or following the guidelines below, will help us in processing your article.

The structure of different types of articles may vary according to the type of study, and the content of the article.

The following are the detailed main components of the original research and review articles submitted to the journal.

Original research

The original research should have three following parts:

Preliminary section: It includes title, list of all contributing authors with their institutional affiliation, and abstract (160-250 words) with at least 3 keywords.

Title: How to format a science article (replace with your real title)

Author(s): List the author name(s) separated by commas. Use superscript numbers to link affiliations, and symbols *†‡ for author notes. For example, Y. Obsie[1*], S.A. Adem[1, 2]

**Corresponding author(s):* Include the email addresses or telephone numbers of the corresponding author(s). Please use the asterisk (*) symbol for the corresponding author information. This information is at the bottom of the manuscript's first page.

Author's affiliation addresses:

[1]Affiliations should be preceded by superscript numbers corresponding to the author list

[2]For any institutions, please provide the institution name, street, district, city, country

Received ; revised ; accepted

Abstract:
Start your abstract here…
Keywords: **keyword 1, keyword 2, keyword 3…**
Classification number(s): **1.1, 3.4, 5.3, etc.**

Abstract: The abstract should range between 160 and 250 words and be structured in a single paragraph following keywords in a separate line. The abstract should represent the main part of the research manuscript. It should reflect a brief and comprehensive background following the aim of the study (main questions to be addressed), methods used for investigating the problem, a summary of significant findings, main conclusions, and implications of the results.

Keywords: They should come immediately after the abstract and contain 3-7 specific and relevant keywords. They should reflect the research study and the relevant field of research.

Classification numbers: Depend on the Journal's Classification Scheme.

Author(s) are encouraged to write a "Highlights" that summarises the most exciting, interesting points from your manuscript.

Manuscript section: It is the main body of the scientific manuscript including: 1) Introduction; 2) Material(s) and method(s); 3) Results and discussion (separation of these two sections is acceptable); 4) Conclusions; 5) Recommendations/Suggestions/ Implications/Study limitations...(if any). These sections may slightly vary depending on the type of research approach and design used in the research. Each section should be numbered.

All of the Figures, Tables, and Equations should be cited in numerical order.

Figures

Fig. #: (Begin each figure caption with a label, "**Fig. 1.**" for example, as a new paragraph).

Fig. 1. The figure caption should begin with an overall descriptive statement of the figure followed by additional text. They should be immediately after each figure. Figure parts are indicated with capital letters **(A)**. If you prefer, you can place both the actual figures and captions logically through the text near where they are cited rather than at the end of the file (but not both). If a paragraph in the main text begins with the name of a figure, write out "Figure" in full (e.g., <para> "Figure 1 shows...").

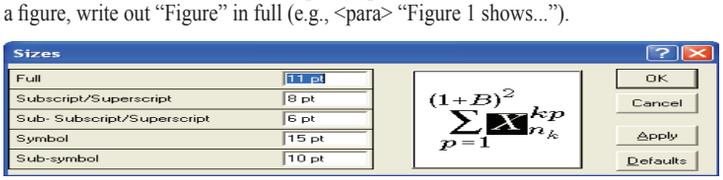

Fig. 1. The figure caption.

Tables

Table #: (Begin each table caption with a label "**Table 1.**", etc. as a new paragraph).

Table 1. Start this caption with a short description of your table. Format tables using the Word Table commands and structures. Do not create tables using spaces or tabs characters.

Table 1. Caption.

a	b	c	d	e
f				
g				
h				

Equations

$$\int_a^b x dx \tag{1}$$

Equations can be included. We do not recommend using the native Word 2007, 2008, 2010 or 2011 equation editor. This can in some cases produce less reliable MathML, the online markup language we use, which may result in display errors. Instead, use the legacy equation editor in Word (Insert menu; select insert object; select word equation) or use MathType (recommended). If you enter equations in simple LaTeX, check that they will convert accurately (Word 2007 and higher can convert simple LaTeX equations).

Closing section: It includes appendices/supplementary materials/data availability statement (if applicable), CRediT author statement (for multiple authors), acknowledgements (if applicable), competing interests, ethics (if any) and a complete list of references corresponding to all the citations given in the text of the manuscript. The appendices/supplementary materials may include data files and other material relevant to the research that should be submitted in separate files if required.

APPENDICES (if any)

The appendices should ideally be under 1000 words (approximately 2 A4 pages) for printing version. With longer appendices, they are only accepted for online publication.

CRediT author statement (for multiple authors)

CRediT offers authors the opportunity to share an accurate and detailed description of their diverse contributions to the published work.

ACKNOWLEDGEMENTS (if applicable)

This section is for the researchers who were funded for the research projects, and it should enclose all sources of financial support.

COMPETING INTERESTS

The author(s) declare(s) that there is no conflict of interest regarding the publication of this article.

REFERENCES

For in-text citation: References should be cited in the bracket with a number [1]. Multiple reference citations are separated by commas [2, 3] or if a series, dashes [4-6]. When citing sources with the author(s) and the year, they should be shortened to the first author's name, followed by et al. (with more than one author) and the year.

For reference list: With less than or equal to three authors, list all the author(s). With more than three authors, the first three should be listed and followed by et al.

References are listed in numerical order, and in the same order in which they are cited in text. The reference list should include all and only those references you have cited in the text. The reference list appears at the end of the article.

The reference consists of: Initial(s) and first/last name of the author(s), author' names separated by commas (Year of publication), "Titles of journal articles or chapter of book", *Title of Journal, Book or Other Publication*, **Volume(Number)** (if any), page numbers (if any), DOI (if any), URL and accessed date (if any) (in its original language if not English).

To cite a website and online/electronic resources, please include the accessed date (day month year).

Example of a reference list:

[1] T. Binzoni, T.S. Leung, D. Boggett, et al. (2003), "Non-invasive laser Doppler perfusion measurements of large tissue volumes and human skeletal muscle blood RMS velocity", *Phys. Med. Biol.*, **48(1)**, pp.2527-2549, DOI: 10.1088/0031-9155-48-15-318.

[2] H.W. Bischoff, H.C. Bold (1963), *Some Soil Algae from Enchanted Rock and Related Algal Species*, University of Texas Publications, 95pp.

[3] R. Busi (2016), "Weedy rice in the Philippines and Vietnam", https://www.aciar.gov.au/publication/technical-publications/weedy-rice-philippines-and-vietnam-final-report, accessed 15 July 2018.

Review articles

They should be different from the original research as they would contain different sections on the literature review. Authors may structure this part as per nature, background, and available literature on the issue argued in the manuscript.

For more detailed instructions, please visit our website: vietnamscience.vn or vietnamscience.vjst.vn

This manuscript template has been used from 2021 onwards.

P-ISSN 2525-2461 • E-ISSN 2615-9937

Vietnam Journal of Science, Technology and Engineering

MARCH 2022 • VOLUME 64 NUMBER 1

EDITORIAL OFFICE

113 Tran Duy Hung Str., Cau Giay Dist., Hanoi, Vietnam

Tel: (84.24) 39436793; Fax: (84.24) 39436794

Email: vjste@most.gov.vn

Website: vietnamscience.vn or vietnamscience.vjst.vn

PUBLICATION LICENCE

No. 459/GP-BTTTT 20th July 2021